

AFRL-ML-WP-TR-1998-4188



**LASER/MATERIALS INTERACTION STUDIES FOR  
ENHANCED SENSITIVITY OF LASER ULTRASONIC  
SYSTEMS**

**MICHAEL J. EHRLICH  
JAMES B. SPICER  
TODD W. MURRAY  
DAVID H. HURLEY**

**JOHNS HOPKINS UNIVERSITY  
DEPARTMENT OF MATERIALS SCIENCE AND ENGINEERING  
102 MARYLAND HALL  
3400 NORTH CHARLES STREET  
BALTIMORE, MD 21218**

**DATED: MAY 1998**

**FINAL REPORT FOR APRIL 1995 THROUGH SEPTEMBER 1998**

19990304 009

**APPROVED FOR PUBLIC RELEASE: DISTRIBUTION IS UNLIMITED**

**MATERIALS AND MANUFACTURING DIRECTORATE  
AIR FORCE RESEARCH LABORATORY  
AIR FORCE MATERIEL COMMAND  
WRIGHT-PATTERSON AFB, OH 45433-7817**

## NOTICE

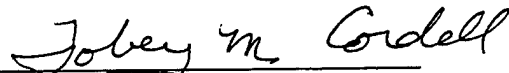
WHEN GOVERNMENT DRAWINGS, SPECIFICATIONS, OR OTHER DATA ARE USED FOR ANY PURPOSE OTHER THAN IN CONNECTION WITH A DEFINITELY GOVERNMENT-RELATED PROCUREMENT, THE UNITED STATES GOVERNMENT INCURS NO RESPONSIBILITY OR ANY OBLIGATION WHATSOEVER. THE FACT THAT THE GOVERNMENT MAY HAVE FORMULATED OR IN ANY WAY SUPPLIED THE SAID DRAWINGS, SPECIFICATIONS, OR OTHER DATA, IS NOT TO BE REGARDED BY IMPLICATION OR OTHERWISE IN ANY MANNER CONSTRUED, AS LICENSING THE HOLDER OR ANY OTHER PERSON OR CORPORATION, OR AS CONVEYING ANY RIGHTS OR PERMISSION TO MANUFACTURE, USE, OR SELL ANY PATENTED INVENTION THAT MAY IN ANY WAY BE RELATED THERETO.

THIS REPORT IS RELEASABLE TO THE NATIONAL TECHNICAL INFORMATION SERVICE (NTIS). AT NTIS, IT WILL BE AVAILABLE TO THE GENERAL PUBLIC, INCLUDING FOREIGN NATIONS.

THIS TECHNICAL REPORT HAS BEEN REVIEWED AND IS APPROVED FOR PUBLICATION.



CURTIS J. FIEDLER, Project Engineer  
Nondestructive Evaluations Branch  
Metals, Ceramics & NDE Division



TOBEY M. CORDELL, Chief  
Nondestructive Evaluations Branch  
Metals, Ceramics & NDE Division

  
GERALD J. PETRAK, Acting Asst Chief  
Metals, Ceramics & NDE Division  
Materials & Manufacturing Directorate

IF YOUR ADDRESS HAS CHANGED, IF YOU WISH TO BE REMOVED FROM OUR MAILING LIST, OR IF THE ADDRESSEE IS NO LONGER EMPLOYED BY YOUR ORGANIZATION, PLEASE NOTIFY, AFRL/MLLP, WRIGHT-PATTERSON AFB OH 45433-7817 AT 59819 TO HELP US MAINTAIN A CURRENT MAILING LIST.

COPIES OF THIS REPORT SHOULD NOT BE RETURNED UNLESS RETURN IS REQUIRED BY SECURITY CONSIDERATIONS, CONTRACTUAL OBLIGATIONS, OR NOTICE ON A SPECIFIC DOCUMENT.

| REPORT DOCUMENTATION PAGE   |  |   | Form Approved<br>OMB No. 0704-0188  |  |
|---|--|---|---|--|
| Public reporting burden for this collection of information is estimated to average 1 hour per response, including the time for reviewing instructions, searching existing data sources, gathering and maintaining the data needed, and completing and reviewing the collection of information. Send comments regarding this burden estimate or any other aspect of this collection of information, including suggestions for reducing this burden, to Washington Headquarters Services, Directorate for Information Operations and Reports, 1215 Jefferson Davis Highway, Suite 1204, Arlington, VA 22202-4302, and to the Office of Management and Budget, Paperwork Reduction Project (0704-0188), Washington, DC 20503.  |  |   |   |  |
| 1. AGENCY USE ONLY (Leave blank)  |  | 2. REPORT DATE<br>MAY 1998                              | 3. REPORT TYPE AND DATES COVERED<br>FINAL REPORT: APRIL 1995 - SEP 1998           |  |
| 4. TITLE AND SUBTITLE<br>LASER/MATERIALS INTERACTION STUDIES FOR ENHANCED SENSITIVITY OF LASER ULTRASONIC SYSTEMS   |  |   | 5. FUNDING NUMBERS<br>C F33615-95-C-5223<br>PE 62102<br>PR 2418<br>TA 40<br>WU 18 |  |
| 6. AUTHOR(S)<br>MICHAEL J. EHRlich, JAMES B. SPICER, TODD W. MURRAY,<br>DAVID H. HURLEY   |  |   |   |  |
| 7. PERFORMING ORGANIZATION NAME(S) AND ADDRESS(ES)<br>JOHNS HOPKINS UNIVERSITY<br>DEPT OF MATERIALS SCIENCE & ENGINEERING<br>102 MARYLAND HALL<br>3400 NORTH CHARLES STREET<br>BALTIMORE, MD 21218  |  |   | 8. PERFORMING ORGANIZATION<br>REPORT NUMBER                                       |  |
| 9. SPONSORING/MONITORING AGENCY NAME(S) AND ADDRESS(ES)<br>MATERIALS AND MANUFACTURING DIRECTORATE<br>AIR FORCE RESEARCH LABORATORY<br>AIR FORCE MATERIEL COMMAND<br>WRIGHT-PATTERSON AFB, OH 45433-7750<br>POC: DR. CURTIS J. FIEDLER, AFRL/MLLP, (937) 255-9797   |  |   | 10. SPONSORING/MONITORING<br>AGENCY REPORT NUMBER<br><br>AFRL-ML-WP-TR-1998-4188  |  |
| 11. SUPPLEMENTARY NOTES   |  |   |   |  |
| 12a. DISTRIBUTION AVAILABILITY STATEMENT<br>APPROVED FOR PUBLIC RELEASE; DISTRIBUTION UNLIMITED   |  |   | 12b. DISTRIBUTION CODE  |  |
| 13. ABSTRACT (Maximum 200 words)<br>Under this program, laser ultrasonic wave generation and propagation in composite materials was studied to improve the sensitivity of laser ultrasonic inspection of composite materials. The obvious advantages of laser-based systems aside, compared to conventional counterparts, the sensitivity of these systems must be improved to yield comparable inspection capabilities. To address sensitivity issues, those factors that are critical to improving the generation efficiency and propagation of laser ultrasound in composite materials were investigated to provide directions for advancing the performance of laser ultrasonics systems. The directions that were identified and pursued included the following: optimization of laser pulse duration for maximum ultrasonic energy transmission, determination of the effects of composite anisotropy and homogeneity on ultrasonic transmission, modification of the laser source to improve detectability using signal processing and investigation of laser ablation damage mechanisms. Owing to inhomogeneity and anisotropy, composite materials behave differently than do traditional aircraft materials such as aluminum. This behavior was assessed to identify the frequency dependant effects on various ultrasonic modes in composites. The effects of pulse duration on ultrasonic generation deficiency were determined; the ability to deliver more energy at the frequencies of interest, that are supported by the composite, greatly improves the transmission of ultrasound through composites. These accomplishments of the program were broadly applicable to laser ultrasonic inspection of composites and directly indicated methods to improve laser ultrasonic system sensitivity. |  |   |   |  |
| 14. SUBJECT TERMS<br>ULTRASONICS, LASER-BASED ULTRASONICS   |  |   | 15. NUMBER OF PAGES<br>346  |  |
|   |  |   | 16. PRICE CODE  |  |
| 17. SECURITY CLASSIFICATION OF REPORT<br>UNCLASSIFIED   | 18. SECURITY CLASSIFICATION OF THIS PAGE<br>UNCLASSIFIED | 19. SECURITY CLASSIFICATION OF ABSTRACT<br>UNCLASSIFIED | 20. LIMITATION OF ABSTRACT<br>SAR   |  |

## Table of Contents

|  |          |
|--|----------|
| <b>Objective</b> .....   | <b>1</b> |
| <b>Introduction</b> .....  | <b>1</b> |
| <b>Summary of Results</b> .....  | <b>3</b> |
| <b>Appendix A</b> ..... “An Investigation of the Anisotropic and Heterogeneous Nature of Laser Generated Ultrasound in Carbon -Fiber-Reinforced Epoxy and Single Crystal Materials.” |          |
| <b>Appendix B</b> ..... “Laser Interactions with Materials: Optimizing the Laser Source for the Generation of Acoustic Waves In Laser Ultrasonic Applications.”                      |          |

**R&D FINAL REPORT:  
LASER/MATERIALS INTERACTION STUDIES FOR  
ENHANCED SENSITIVITY OF LASER ULTRASONIC SYSTEMS**

**Contract No. F33615-95-C-5223**

**April 1998**

**Data Item No. A002**

Objective

The goal of this program was to develop methods to enhance the sensitivity of laser based ultrasonic systems, specifically by studying and addressing the laser/material interaction during generation of ultrasound in materials of interest to the Air Force.

Introduction

The work performed under this program is aimed at enhancing the aircraft inspection capabilities of the Air Force using rapid, non-contact, laser based methods. Areas investigated include optimization of the laser source for efficient ultrasound generation, modulation of the laser source for improved signal-to-noise ratio, and modeling of laser based ultrasound generation and propagation in anisotropic and heterogenous materials.

This work has direct benefit in both the civilian and military sectors. One of the greatest challenges facing the United States today is maintenance of its aging aircraft infrastructure. Civilian and military aircraft are being flown well beyond their design lifetime, and often under adverse conditions. As these fleets are operated in this manner, it becomes imperative to assess the structural integrity of these aircraft and to inspect repaired or reworked areas. Owing to the large number and physical size of aircraft in service, this becomes an extremely difficult task using conventional technology.

Also, new aircraft designs are utilizing composite materials to ever greater extents. Unlike the aluminum alloys in older aircraft, these composite materials may be highly anisotropic and heterogeneous. The defect rate for these new composite structures is significant because of the relative infancy of composite materials processing technology. For this reason, most composite structures are inspected immediately after manufacture. However, owing to material anisotropy and heterogeneity, and the fact that many new composite parts are manufactured with intricate contours, inspection is rarely straightforward and the results are often difficult to interpret.

Laser-based ultrasonic inspection techniques hold promise for overcoming several of the difficulties associated with inspecting both aging and advanced aircraft. Laser based systems for generation and detection of ultrasound have been investigated widely in

academic and industrial laboratories around the world. These promising techniques offer noncontact and remote means for ultrasonic inspection of materials and structures. Since light beams from a laser are all that must come in "contact" with the surface of an object under inspection, prospects for high scan rates and inspection of surfaces with complex contours add to the attractiveness of this technology. In addition to the potential advantages for inspection of manufactured materials and structures in service, laser generation and detection of ultrasound is also being targeted at process control applications where measurements can be made on hot materials or those under high pressure or in otherwise hostile environments, so long as optical access to the material can be gained through an inspection port. Also, since ultrasonic transduction with laser beams can be done in the absence of couplants and without being subjected to the mechanical resonances associated with most contact ultrasonic transducers, laser based methods are capable of sensing ultrasonic vibrations with extreme fidelity, opening possibilities for data interpretation beyond simple time-of-flight and attenuation measurements currently made with conventional piezoelectric ultrasonic transducers.

Unfortunately, laser based ultrasonic systems suffer from considerably poorer sensitivity than their conventional counterparts. The factors affecting performance of the receiver systems are well understood; however, less well understood are those parameters associated with the mechanism for laser generation of the ultrasound. Put simply, the signal-to-noise ratio for a laser ultrasonic system is directly proportional to the power of the receiving laser, the ultrasonic surface displacement, and inversely proportional to the total system bandwidth. The last two of these factors, surface displacement and system bandwidth, pertain almost exclusively to the laser generation side of the system. The ultrasonic signal generated by a laser source depends on the thermal, optical, and elastic properties of the specimen and on the characteristics of the laser source. For a given materials system, the laser source parameters, including temporal profile, spatial profile, energy, and wavelength, can be chosen such that the signal-to-noise ratio of the laser ultrasonic system is maximized.

The work performed under this contract was aimed at gaining a better understanding of the laser generation process in an effort to determine what techniques could be employed to enhance the overall laser ultrasonic system sensitivity. Efforts were directed in four separate areas:

1. Modeling laser generation of ultrasound in the ablative regime.
2. Spatial Modulation of the incident laser light.
3. Temporal modulation of the incident laser light.
4. Modeling of laser generated ultrasound in transversely isotropic materials.

Details and results for each of these efforts are given in the attached Ph.D. dissertations, Appendix A and Appendix B which completely describe all work performed under this contract. These dissertations were written by the students which this contract supported. A brief summary of the results is presented below.

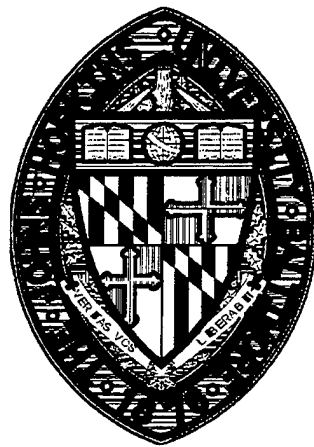
## Summary of Results

1. It is well known that the amplitude of the laser generated ultrasonic waves can be significantly enhanced by increasing the energy in the generation laser pulse such that surface ablation occurs. The amplitude of ultrasonic waves generated in the ablative regime is directly related to the surface vaporization process. Under this program, the laser vaporization process in vacuum was modeled using an implicit finite difference technique. First, the surface pressure resulting from vaporization is calculated. This surface pressure physically generates the ultrasonic waves, and in the model is used as a source term to calculate the ultrasonic wave displacement. Model based calculations were compared to experimentally measured surface displacements in aluminum specimens, showing good agreement for the case where absorption of light in the vapor can be neglected. This model can be used to predict the onset of ablation, as well as the expected surface displacement and ultrasonic signal shape for a given laser irradiance. One of the interesting findings of this work is that strong vaporization occurs only during the time of illumination. Experimentally, it has been found that for highly ablative generation of ultrasound in air, pressure is exerted on the material surface for a significant time after the laser pulse ends. This was previously assumed to be a result of the vaporization process continuing for a substantial time after illumination. However, this effect was not observed in vacuum, and indicates that strong vaporization occurs only during the laser pulse, and that the surface cools quite rapidly when the pulse finishes. The step function time dependence of the forcing function observed in high irradiance laser ablation experiments is apparently due to the presence of a backing gas, and not to surface vaporization.
2. A novel technique for increasing laser ultrasonic system sensitivity through spatial modulation of the incident laser pulse was developed under this program. The method uses a transmission mask to generate chirped surface waves. The laser source is extended in space allowing for a large amount of laser energy to be utilized in the generation process without surface ablation. The received ultrasonic signal is digitally processed using a matched filter, which leads to compression of the signal in time. This technique allows for temporal resolution to be maintained while surface damage is avoided.
3. A linear systems approach for determination of laser pulse length effects on ultrasound generation was developed. This allows for the calculation of the resultant ultrasonic wave displacements given an arbitrary laser pulse temporal profile, provided an experimentally determined reference signal is available. For materials exhibiting strong surface absorption, it was found that there exists a temporal pulse length which optimizes the laser generated signal amplitude while avoiding surface damage. Also, pulse length effects on two composite materials supplied by the Air Force were evaluated.

4. A comprehensive model of laser generated ultrasound in carbon fiber composites was developed. Both the nature of the source and the nature of the material were addressed to construct the appropriate model. Fiber composite materials are inherently elastically anisotropic, and for certain experimental geometries and ultrasonic frequencies, the composite must be considered heterogeneous. The pulsed laser source generates ultrasound with a broad frequency spectrum. This broad spectrum further complicates issues related to the composite's homogeneous/heterogeneous character. The approach taken was to investigate under what experimental conditions would a theory that accounted only for elastic anisotropy and not heterogeneity sufficiently describe the resulting waveform. A transversely isotropic material was chosen in order to simplify the analysis while keeping the salient features of elastic anisotropy. Both a line source and a point source representation of laser-generated ultrasound in materials exhibiting transverse isotropy was developed. Experimental validation of the theory was performed using two transversely isotropic materials, single crystal zinc and unidirectional carbon epoxy. For zinc, the experimentally obtained epicentral and surface wave displacements agree well with theoretical predictions. The carbon epoxy sample exhibits homogeneous behavior when the wave vector is perpendicular to the fiber direction. When the wave vector is aligned with the fiber direction, the wave form appears to be influenced by the inhomogeneous nature of the composite.

**APPENDIX A**

An Investigation of the Anisotropic and Heterogeneous Nature of Laser  
Generated Ultrasound in Carbon-Fiber-Reinforced Epoxy and Single  
Crystal Materials



by

David Howard Hurley

A dissertation submitted to Johns Hopkins University in  
conformity with the requirements  
for the degree of Doctor of Philosophy

Baltimore, Maryland

1997

## ABSTRACT

Laser generated ultrasound in carbon epoxy composites provides an ultrasonic signature which is difficult to interpret owing to the elastic anisotropic and inhomogeneous nature of these materials. In this manuscript, both a line source and a point source representation of laser-generated ultrasound in materials exhibiting transverse isotropy is presented. The bounding plane of the half space is assumed to be the plane of isotropy. Neglecting thermal diffusion, it is shown that in the limit of strong optical absorption, the buried line source is equivalent to applying a shear stress dipole at the bounding surface. A formal solution is found using double (Fourier-Laplace) transforms. The Cagniard-de Hoop technique is used to analytically invert the transform for the epicentral case as well as the surface wave case. Solutions for a sub-surface source and for observation points that are off the epicentral axis are obtained numerically.

Experimental validation of the theory is performed using single crystal zinc and a unidirectional carbon epoxy sample. For the Carbon fiber epoxy sample, the plane of isotropy was found to be perpendicular to the fiber direction. For zinc, the experimentally obtained epicentral and surface wave displacements agree well with theoretical predictions. The carbon epoxy sample exhibits homogeneous behavior when the wave vector is perpendicular to the fiber direction. When the wave vector is aligned with the fiber direction, the wave form appears to be influenced by the inhomogeneous nature of the composite.

## ACKNOWLEDGEMENTS

There are a number of teachers and friends whose support and encouragement have helped bring my academic studies to fruition. First and foremost on this list are my parents. From the days of "Open Highways" through my studies at Hopkins, their support has been unwavering.

While at Hopkins, I have had the advantage of having two advisors. My first advisor, Dr. James Wagner was very influential in bringing me to Hopkins. I greatly value his confidence in me and appreciate his patience and guidance in the laboratory.

For the past three years, Dr. James Spicer has served as my advisor. During this time, Jim has helped enrich my understanding of laser acoustics. Jim is a true scientist who has a special way of approaching problems that I have come to admire and appreciate.

Most graduate students in the Materials Science department deserve some thanks, but there are a few who should be mentioned by name. First I would like to thank Dr. Peter Shull for indulging me in many late night discussions ranging from science to the meaning of life. I would also like to thank Johanna Bernstein for her support during the writing process.

There are two people that deserve my special thanks. Dr. Robert E. Green Jr. furnished single crystal zinc samples and Dr. Chris Bryne provided samples of unidirectional carbon fiber reinforced epoxy. Without these material samples, the completion of my thesis would have been delayed by several months.

Finally, I wish to acknowledge the Department of Airforce Materiel Command, The Wright Laboratory, for their funding of this program.

## TABLE OF CONTENTS

|   |     |
|---|-----|
| ABSTRACT .....  | ii  |
| ACKNOWLEDGEMENTS .....  | iii |
| LIST OF FIGURES .....   | vi  |
| LIST OF TABLES .....  | xi  |
| CHAPTER 1 .....   | 1   |
| (1.1) Literature Review .....   | 3   |
| (1.2) Overview of Presentation .....  | 8   |
| CHAPTER 2 .....   | 10  |
| (2.1) The Optical Problem .....   | 10  |
| (2.2) The Thermal Problem .....   | 21  |
| (2.3) The Elastic Problem .....   | 24  |
| CHAPTER 3 .....   | 35  |
| (3.1) Normal Curves for Some Transversely Isotropic Systems<br>(Two Space Dimensions) .....     | 35  |
| (3.2) Wave-Front Curves for Some Transversely Isotropic Systems<br>(Two Space Dimensions) ..... | 42  |
| CHAPTER 4 .....   | 46  |
| (4.1) Equivalent Boundary Conditions .....  | 46  |
| (4.2) Half Space Subjected to Shear Stress Dipole .....   | 53  |
| (4.3) Solutions along the Epicentral Axis .....   | 64  |
| (4.3.1) .....   | 66  |
| (4.3.2) .....   | 69  |
| (4.4) 3-Dimensional Half-Space .....  | 78  |
| CHAPTER 5 .....   | 86  |
| (5.1) Observation Points off the Symmetry Axis .....  | 86  |
| (5.1.1) Cagniard Path for Hafnium .....   | 90  |
| (5.1.2) Cagniard Path for Beryl .....   | 93  |
| (5.1.3) Cagniard Path for Zinc .....  | 95  |
| (5.1.4) Details of Inversion for Zinc .....   | 97  |
| (5.3) Buried Source .....   | 100 |
| CHAPTER 6 .....   | 111 |

|  |     |
|--|-----|
| (6.1) Experimental Setup -----                       | 111 |
| (6.2) Sample Specification -----                     | 114 |
| CHAPTER 7 -----                                      | 116 |
| (7.1) Regarding the Temporal Transfer Function ----- | 116 |
| (7.2) Back-face Reflection Coefficients -----        | 120 |
| (7.3) Results and Discussion (Zinc) -----            | 121 |
| (7.4) Results and Discussion (Graphite Epoxy) -----  | 126 |
| (7.5) Conclusion -----                               | 139 |
| (7.5.1) Summary of presentation -----                | 139 |
| (7.5.2) Future work -----                            | 140 |
| APPENDIX 1: Program Listings -----                   | 142 |
| REFERENCES -----                                     | 174 |
| VITA -----   | 178 |

## LIST OF FIGURES

|             |   |    |
|-------------|---|----|
| Figure 2.1  | Coordinate system used in discussing reflection at the surface of a Conductor. $E^{(1)}$ represents the incident wave, $E^{(2)}$ represents the transmitted wave and $E^{(3)}$ represents the reflected wave. ----- | 15 |
| Figure 2.2  | Schematic of Pulsed Nd:YAG laser interaction with graphite epoxy. --  | 20 |
| Figure 2.3  | Incident shear wave polarized parallel to cylinder axis. -----  | 25 |
| Figure 2.4  | A plot of scattered power versus wavenumber parameter. -----  | 31 |
| Figure 2.5  | Ideal carbon fiber arrangement in epoxy composite. -----  | 32 |
| Figure 3.1  | Spherical cavity of radius $a$ subjected to internal pressure. -----  | 36 |
| Figure 3.2  | Class I normal curve. ( $\alpha=0.64, \beta=0.64, \gamma=1.2$ ). -----  | 40 |
| Figure 3.3  | Class II normal curve. ( $\alpha=0.64, \beta=0.25, \gamma=0.42$ ). -----  | 40 |
| Figure 3.4  | Class III normal curve. ( $\alpha=0.25, \beta=0.64, \gamma=0.42$ ). -----   | 41 |
| Figure 3.5  | Class IV normal curve. ( $\alpha=0.64, \beta=0.64, \gamma=-1.0$ ). -----  | 41 |
| Figure 3.6  | Class V normal curve. ( $\alpha=4, \beta=6, \gamma=20$ ). -----   | 41 |
| Figure 3.7  | Mapping normal curve to wave front curve. -----   | 43 |
| Figure 3.8  | Class I normal curve. ( $\alpha=0.64, \beta=0.64, \gamma=1.2$ ). -----  | 44 |
| Figure 3.9  | Class II normal curve. ( $\alpha=0.64, \beta=0.25, \gamma=0.42$ ). -----  | 44 |
| Figure 3.10 | Class III normal curve. ( $\alpha=0.25, \beta=0.64, \gamma=0.42$ ). -----   | 44 |
| Figure 3.11 | Class IV normal curve. ( $\alpha=0.64, \beta=0.64, \gamma=-1.0$ ). -----  | 44 |
| Figure 3.12 | Class V normal curve. ( $\alpha=4, \beta=6, \gamma=20$ ). -----   | 45 |
| Figure 4.1  | Problem geometry with source and sink locations. -----  | 48 |
| Figure 4.2  | Integration contour for the vertical displacement, $u_3$ , at the bounding Surface. -----   | 58 |

|            |   |    |
|------------|---|----|
| Figure 4.3 | Theoretical displacement for surface waves generated with a line source in zinc as a function of T. Delta function represented by vertical line at T=1.13. -----  | 63 |
| Figure 4.4 | Theoretical displacement for the epicentral wave generated with a line source in Beryl. -----   | 68 |
| Figure 4.5 | Theoretical displacement for the epicentral wave generated with a line source in an isotropic material (polycrystalline aluminum). -----                          | 68 |
| Figure 4.6 | Cargniard contour for zinc. Solid line represents contour corresponding to $\zeta_1$ and the dashed line represents the contour corresponding to $\zeta_1$ . - 72 |    |
| Figure 4.7 | Theoretical displacement for epicentral wave generated with a line source in zinc as a function of T. -----   | 77 |
| Figure 4.8 | Enlargement of portion of wavefront intersecting the syjjetry axis for Zinc. -----  | 78 |
| Figure 4.9 | Epicentral displacement for laser point-source in a 3-dimensional half-space. -----   | 86 |
| Figure 5.1 | Problem geometry with source and detection locations. -----   | 87 |
| Figure 5.2 | Wave-front curve for Hafnium. -----   | 91 |
| Figure 5.3 | Cagniard path for Hafnium ( $\theta=25^\circ$ ). The dashed line represents the portion of the Cagniard path on the second sheet of the Riemann surface. -----    | 91 |
| Figure 5.4 | Cagniard path for Hafnium ( $\theta=45^\circ$ ). The dashed line represents the portion of the Cagniard path on the second sheet of the Riemann surface. -----    | 92 |
| Figure 5.5 | Cagniard path for Hafnium ( $\theta=47.5^\circ$ ). The dashed line represents the portion of the Cagniard path on the second sheet of the Riemann surface. -----  | 92 |
| Figure 5.6 | Wave-front curve for Beryl. Enlargement of $R_+$ branch shown in insert. -----  | 93 |
| Figure 5.7 | Cagniard path for Beryl ( $\theta=35^\circ$ ). The dashed line represents the portion of the Cagniard path on the second sheet of the Riemann surface. -----      | 94 |

|   |     |
|---|-----|
| Figure 5.8 Cagniard path for Beryl ( $\theta=45^\circ$ ). The dashed line represents the portion of the Cagniard path on the second sheet of the Riemann surface. -----                             | 94  |
| Figure 5.9 Cagniard path for Beryl ( $\theta=48^\circ$ ). The dashed line represents the portion of the Cagniard path on the second sheet of the Riemann surface. -----                             | 95  |
| Figure 5.10 Wave-front curve for Zinc. Enlargement of $R_+$ branch shown in insert. -----   | 96  |
| Figure 5.11 Cagniard path for zinc ( $\theta=10^\circ$ ). The dashed line represents the portion of the Cagniard path on the second sheet of the Riemann surface. -----                             | 96  |
| Figure 5.12 Cagniard path for zinc ( $\theta=35^\circ$ ). Dashed line represents the portion of the Cagniard path on the second sheet of the Riemann surface. -----                                 | 97  |
| Figure 5.13 Cagniard path correspond to Eq. 5.2b. The times, $t_1$ , $t_2$ , and $t_3$ correspond to wave arrivals. -----   | 98  |
| Figure 5.14 Cagniard path correspond to Eq. 5.2b. The times $t_2$ and $t_4$ correspond to wave arrivals. -----  | 99  |
| Figure 5.15 Theoretical displacement for off epicentral waves generated in zinc with a line source. The observation angle is $10^\circ$ . Fig. 16. Problem geometry for a buried line source. ----- | 100 |
| Figure 5.16 Problem geometry for a buried line source. -----  | 101 |
| Figure 5.17 Various Cagniard paths for a buried line-source in Beryl. Fig. 5.18. Epicentral displacement waveforms due to a surface and a buried line source in Beryl. -----                        | 108 |
| Figure 5.18 Epicentral displacement waveforms due to a surface and a buried line source in Beryl. -----   | 109 |
| Figure 5.19 Spatial profile of the displacement at different times produced from a planar temperature source at z-h in a elastic half-space. -----  | 110 |
| Figure 6.1 Experimental setup used for same side detection. A Nd:YAG laser is used to generated the ultrasound and a Michelson interferometer is used to detect the ultrasound. -----               | 112 |
| Figure 6.2 Experimental setup used for opposite side detection. A Nd:YAG laser is used to generated the ultrasound and a Michelson interferometer is used to detect the ultrasound. -----           | 113 |

|             |  |     |
|-------------|--|-----|
| Figure 7.1  | Schematic showing pulse spreading caused by a finite detection spot. Detection is along the epicentral axis. -----   | 117 |
| Figure 7.2  | Schematic showing pulse spreading caused by a finite detection spot. Detection and generation on same side of sample. -----  | 119 |
| Figure 7.3  | Comparison between experiment and theory for surface waves in zinc. -----  | 122 |
| Figure 7.4  | Comparison between experiment and theory for displacements along the epicentral axis. -----  | 123 |
| Figure 7.5  | Comparison between experiment and theory for axial displacements along the epicentral axis resulting from a point source. -----  | 124 |
| Figure 7.6  | Comparison between experiment and theory for axial displacements off the epicentral axis. The observation angle is $10^\circ$ . -----  | 125 |
| Figure 7.7  | Waveform and experimental geometry used for determination of elastic constants. The sample thickness is 12mm. -----  | 127 |
| Figure 7.8  | Waveform and experimental geometry used for determination of elastic constants. The sample thickness is 12mm. -----  | 128 |
| Figure 7.9  | Waveform and experimental geometry used for determination of elastic constants. The sample thickness is 12mm. -----  | 128 |
| Figure 7.10 | Surface wave displacement wave form and experimental geometry. -   | 130 |
| Figure 7.11 | Normal curve for unidirectional carbon fiber epoxy sample. -----   | 131 |
| Figure 7.12 | Wave front curve for unidirectional carbon fiber epoxy sample. -----   | 131 |
| Figure 7.13 | Comparison between experiment and theory for a laser line source in carbon fiber epoxy composite. The fibers were oriented parallel to both the surface and the line source. -----                 | 132 |
| Figure 7.14 | Comparison between experiment and theory for surface waves generated with a laser line source in carbon fiber epoxy composite. The fibers were oriented perpendicular to the sample surface. ----- | 133 |
| Figure 7.15 | Comparison between experiment and theory for the epicentral displacement resulting from a laser line source. Fibers were oriented perpendicular to sample surface. -----                           | 134 |

- Figure 7.16 Comparison between experiment and theory for the epicentral displacement resulting from a laser point source. Fibers were oriented perpendicular to sample surface. ----- 135
- Figure 7.17 Epicentral waves resulting from a laser source with circular symmetry. ----- 136
- Figure 7.18 Epicentral waveform resulting from an ablative point source. The fibers are oriented perpendicular to the sample surface. ----- 137
- Figure 7.19 Comparison of temporal profile between direct longitudinal wave and first reflected longitudinal wave. The signal was produce with an ablative point source. ----- 138

## LIST OF TABLES

|           |  |     |
|-----------|--|-----|
| Table 2.1 | Skin depth versus wavelength for graphite. Extraordinary is denoted by (e) and ordinary is denoted by (o) [33]. -----                                      | 18  |
| Table 2.2 | Location of the absorption peaks for various epoxies [35,36]. Absorption depths are not given since the cell length for spectral data was not given. ----- | 19  |
| Table 4.1 | Shear stress pre-multiplier for various transversely isotropic materials. -----  | 80  |
| Table 5.1 | Location of branch points and Rayleigh pole. -----   | 90  |
| Table 6.1 | Sample size, orientation and detection scheme. -----   | 114 |
| Table 7.1 | A listing of the elastic constants and the density for unidirectional carbon fiber epoxy. -----  | 130 |



## CHAPTER 1

Ultrasonic techniques as probes for characterizing material properties have been used successfully since the Second World War. Ultrasonic testing was first used for locating material flaws in plates, forgings, and welds. Since its genesis, ultrasonic testing has lent itself to an ever-widening array of applications. These applications include characterization of porosity distribution in ceramics, evaluation of microstructural properties, such as grain size in metal, and determination of the stress distribution in load bearing structures.

There is a number of ways to produce ultrasound in a material. Traditionally, ultrasound has been generated by means of a piezoelectric transducer. A disc shaped piezoelectric material, like lead zirconate titanate, changes its dimensions in response to the application of a voltage across its faces. The ultrasonic energy in the transducer is then coupled into the material of interest via a coupling fluid. The primary advantages of piezoelectric transducers are their sensitivity and their ability to generate extremely narrow bandwidth signals. Among the disadvantages of piezoelectric transducers are that they required a couplant, they must be in contact or near contact with the sample, and the transducer must conform to the geometry of the sample's surface.

With the advent of pulsed lasers in the mid 1960s, a new way of generating ultrasound emerged, namely, the generation of ultrasound by irradiating a specimen with a short pulse from a high intensity laser. When a pulsed laser beam is incident on a sample, the material absorbs a small portion of the energy of the incident pulse,

while the remaining energy is reflected or scattered from the sample's surface. The portion of the incident energy that is absorbed gives rise to rapid, localized heating of the sample. This rapid heating in turn generates ultrasound that propagates throughout the material. The primary advantages of laser ultrasound over more conventional methods can be summarized as follows. Since light is being used to transduce the ultrasound, the specimen being examined is not mechanically coupled to the transducer. As a result, a laser can generate ultrasound in specimens with complicated geometries and can remotely generate ultrasound in specimens that are in hazardous environments. In addition, pulsed lasers can generate ultrasound with an extremely large bandwidth.

With its advantages over contact ultrasound, laser ultrasound is being applied to an increasing variety of materials. These materials range from the traditional structural materials like polycrystalline steel to more exotic materials used in the aerospace industry, like carbon epoxy composites. To a large extent, the successful application of laser ultrasound to this range of materials rests in the researcher's ability to correctly predict the temporal and spatial evolution of the displacements resulting from pulsed laser irradiation. With this information, the researcher is then able to ascertain material properties, such as grain size, temperature, porosity, crystal orientation, etc. Theories that assume homogeneity and elastic isotropy work well for untextured polycrystalline materials that have grain sizes that are small compared to the wavelength of the interrogating ultrasonic wave. However, materials that must be considered inhomogeneous and or elastically anisotropic, for example epoxy composites, behave in a markedly different fashion than their isotropic homogeneous

counterparts. The need to predict correctly the ultrasonic disturbance in materials such as carbon fiber epoxy requires the refinement of theories that assume homogeneity and elastic isotropy.

### (1.1) LITERATURE REVIEW

In order to understand the motivation for the following presentation it is necessary to briefly review the existing literature pertaining to laser ultrasonics. The generation of high frequency ultrasonic pulses by absorption of electromagnetic radiation was first demonstrated by White [1] in 1963. Later White [2] used a  $Q$ -switched ruby laser to produce Rayleigh surface waves in piezoelectric and non-piezoelectric materials. The first work to give a quantitative scientific basis to pulsed laser ultrasonics was that of Scruby *et al.* [3]. In this work, a point source model was presented that show good correlation between experiment and theory. In this model, the thermoelastic source was reported to be equivalent to a surface shear stress dipole. The development of the model put forth by Scruby, *et al.* runs parallel to the development by Lamb [4] in his original treatment of transient waves in an elastic half space. Later, Rose [5] gave a systematic derivation for a point-source representation for laser generated ultrasound. In this presentation, Rose showed that by neglecting the effects of heat conduction, the laser source can be approximated by a surface center of expansion (SCOE). In addition, Rose demonstrated that the (SCOE) is equivalent to the shear stress dipole source proposed by Scruby *et al.* [3].

These early attempts at theoretically studying the problem of laser generated ultrasound neglected the effects of heat conduction and sub-surface optical

absorption. As a result, there remained certain features in the displacement waveform, i.e. the longitudinal precursor spike, which were not accounted for by these theories. Lyamshev and Chelnokov [6] included the effect of both optical absorption and thermal conduction. Their results were analytical in nature and hence, confined to addressing certain limiting cases. As a consequence, they did not make mention of the longitudinal precursor spike. Doyle [7] showed that the precursor spike, in the epicentral waveform resulted from thermal diffusion into the material. Doyle distributed point centers of expansion below the surface to model the action of thermal diffusion. The resulting waveform predicted the precursor pulse and was in agreement with existing experimental results. Later, Telschow and Conant [8] more fully addressed the problem of optical absorption by using a previous development by Sve and Miklowitz [9] to model the exponential absorption of the laser energy. The results of this development predicted the existence of a precursor spike and agreed well with experimental results in ceramics. It is interesting to note that unlike the previous work in this area, Telschow and Conant [8] represented the epicentral displacement with a summation of symmetric and asymmetric plate modes.

The discussion so far has been limited to the study of laser ultrasound in isotropic continua. Perhaps Geophysics was the first field of science to recognize the need to study the effects of anisotropy and inhomogeneity on transient elastic phenomenon. In 1977 a paper by Bamford and Crampin [10], a discussion was given with regard to the elastic anisotropic nature of a thin layer of the earth's upper mantle. Later, Martynov and Mikhailenko [11] presented numerical modeling of the propagation of elastic waves in an anisotropic and inhomogeneous half-space. The

basic question they considered is Lamb's problem in a vertically inhomogeneous half-space. In 1983, Crampin *et al.* [12] presented a comprehensive classification of seismic anisotropy. In this classification scheme, Crampin categorizes elastic anisotropy into inherent and extrinsic anisotropy. Inherent anisotropy refers to anisotropy found in homogeneous materials, while extrinsic anisotropy originates from inhomogeneities.

The effects of inherent anisotropy, or crystal anisotropy, has been a subject of mathematical interest since 1949 when Stoneley [13] studied the propagation of Rayleigh surface waves in certain single crystal systems. In particular Stoneley analyzed three specific cases, surface waves propagating in the  $[0\ 0\ 1]$  plane of cubic crystals along the  $[1\ 0\ 0]$  and  $[1\ 1\ 0]$  directions, and in the basal plane of hexagonal crystals. Royer and Dieulesaint [14] extended the work of Stoneley to include the analysis of Rayleigh wave propagation in orthorhombic and tetragonal systems. In their paper, Royer and Dieulesaint demonstrated that the decay rate of the Rayleigh wave disturbance varies strongly as a function of the anisotropy factor. The analysis by Stoneley [13] and Royer and Dieulesaint [14] considered the disturbance to have planar phase fronts. Although a plane wave analysis gives the researcher a great amount of insight into the physical principles of the problem, it assumes that a finite source is separated from an observer by an infinite distance or that the generation source is infinite in extent. In certain instances, a plane wave analysis is a reasonable assumption, while in other instances, the finite geometry of the source must be considered in order to gain a better understanding of the underlying physical principles. In 1963, Kraut [15] extended the work of Lamb [4] by considering a

transversely isotropic elastic half space subjected to a source of finite extent. In this paper, Kraut used the Cagniard-de Hoop method [16-17] to study the resulting displacements in the crystal Beryl. Later in 1970, a book written by Musgrave [18], entitled *Crystal Acoustics*, detailed the mechanics of elastic wave propagation in a variety of single crystals systems. Other researchers [19-22] have further developed the work by Kraut [15] and Musgrave [18]. Mourad *et al.* [21] used the Cagniard-de Hoop method to numerically obtain the solutions to Lamb's problem in an anisotropic half-space. In their paper, Mourad *et al.* assumed that the laser source could be modeled as a shear stress dipole applied at the bounding surface. In addition, Weaver *et al.* [22] have studied the elastodynamic response of a thick transversely isotropic plate to a normal point source applied at the bounding surface. Of particular interest is the work by Payton [23], who has treated a general class of problems for crystals that exhibit transverse isotropy. Payton furnished a detailed analysis of the solution and solution technique for a variety of transient problems in bounded and semi-bounded solids. In addition, Payton gave an explicit set of conditions, related to the elastic parameters of the material, that predict the existence of inflection points on the slowness curve.

An interest in extrinsic anisotropy outside the field of the Geological Sciences was stimulated by the advent of carbon fiber epoxy composites and a need to characterize their material properties. Traditionally, ultrasonic methods that assumed elastic isotropy were used for determining material properties and could not be directly applied to composites. Thus, researchers in the field of ultrasonic material characterization were lead to investigate the effects of inhomogeneity. The early

work by Achenbach [24], on wave propagation in fiber-reinforced composites assumed that the scale on which the composite could be viewed as inhomogeneous was very much smaller than the wavelength of the interrogating ultrasound. Therefore, for a range of ultrasonic frequencies, the composite could be viewed as an anisotropic, homogeneous material. This apparent anisotropy induced by inhomogeneities, i.e. fibers, is best illustrated when considering a unidirectional carbon fiber composite. For unidirectional fiber composites, the fibers are ideally packed with a hexagonal symmetry. This type of ideal symmetry has led researchers [25,26] to model a unidirectional fiber composite as transversely isotropic. In addition to investigating the artifacts of apparent anisotropy in fiber epoxy composites, other researchers [27,28] have considered the attenuative and dispersive effects of viscoelasticity and inhomogeneities. Data *et al.* [27] utilized the stiffness method to study dispersive wave propagation in a laminated anisotropic plate, while Mal and Lih [28], modeled the effects of viscoelasticity and scattering of ultrasonic energy off fiber inhomogeneities by assuming that the stiffness constants,  $C_{ij}$ , were complex.

Now the question naturally arises, should the composite be viewed as elastically anisotropic, inhomogeneous, or both? Before answering this question, the researcher must consider the ultrasonic generation method, the fiber lay-up, fiber orientation relative to the surfaces, the source and receiver location, and the detection method. In this work, only pulsed laser generation is considered. Since the pulse duration of the laser source is roughly 10 ns, a large range of wavelengths is produced, which might require that the composite's inhomogeneous character be recognized. In order

to simplify the problem as much as possible while still retaining the salient features of laser generated ultrasound in fiber composites, the fiber epoxy samples that were examined were all unidirectional. The fibers in the test samples were oriented either parallel or perpendicular to the free surface, which further leads to questions regarding the conditions in which the fiber-reinforced epoxy composite can be considered homogeneous.

### *(1.2) OVERVIEW OF PRESENTATION*

The objective of this work is to gain a better understanding of the response of carbon fiber-reinforced epoxy composites to pulsed laser irradiation. As mentioned previously, epoxy composites are heterogeneous. The effects of these heterogeneities will be the focus of Chapter 2. In this chapter, the source specification will be considered as a function of the beam diameter, pulse duration, and optical frequency of the illumination beam. In addition, the problem of scattering off inhomogeneities is addressed. This chapter is concluded by considering the conditions in which a unidirectional carbon fiber epoxy composite can be considered a transversely isotropic elastic continuum.

Chapter 3 discusses the slowness curves and wave front curves for the various crystals that exhibit transverse isotropy. In Chapter 4, the solutions for a line source and a point source in a transversely isotropic medium are considered. Only same surface and epicentral displacements are considered. These special cases lend themselves to an analytic solution, which affords a detailed analysis of the solution

procedure. This explicit analysis of the solution procedure will aid in the development presented in chapter 5.

Solutions of a more complicated nature in a transversely isotropic half-space are examined in Chapter 5. Off-epicentral displacements for a surface line source as well as epicentral displacements for a buried line source are considered. Knowledge of displacements at positions that are off the symmetry axis are required in order to construct the solution to problems where the source has a finite lateral extent. Consideration of a buried source is a first step in addressing the effects of optical inhomogeneity.

The laser generation and detection system is the subject of Chapter 6. Included in this chapter is the specification of the material samples examined.

In Chapter 7, experimental results are compared with theoretical results for samples of Zinc and unidirectional carbon fiber epoxy composite. Zinc is used as a prototype to ensure that the theory correctly predicts the effects of elastic anisotropy. The presentation will conclude by discussing any discrepancies between theory and experiment and addressing the direction of future work.

## CHAPTER 2

Modeling laser ultrasonics in carbon fiber epoxy composites involves understanding the optical interactions with the sample, as well as the thermal and mechanical response of the sample. This chapter addresses the physical processes involved in laser generated ultrasound as they happen in chronological order. First, a portion of the optical energy incident on the sample is absorbed by the sample. Second, the absorbed optical energy is transferred into thermal energy. Third, a portion of the thermal energy, which is very localized in time and space, is transferred into high frequency acoustic energy. Thus, a rough outline of this chapter could be stated as follows, the optical problem, the thermal problem, and the acoustic problem. The heterogeneous and anisotropic nature of the carbon fiber composite can affect all three problems.

### *(2.1) THE OPTICAL PROBLEM*

The optical problem can be divided into two parts. The first part is concerned with understanding what physical processes are involved when light is absorbed by matter. The second part involves determining the spatial distribution of the absorbed energy.

The interaction of an electromagnetic wave with a material results in two phenomena, which are 1) reflection, and 2) transmission. Photons that are specularly scattered from a material interface without losing energy to the material are referred to as reflected photons. Reflection is a result of photons being absorbed by valence

electrons and being reradiated at the same frequency. In metals at sub-ultraviolet frequencies, the interaction is with quasi-free electrons, while in dielectrics, the interaction is with strongly bound electrons.

Transmission can be divided into two categories. Photons can interact with valence electrons as they pass through a material causing their path to bend in response to a gradient in the refractive index (refraction), or photons can be absorbed by the material having their energy transformed into non-optical forms of energy. Refraction without absorption is realizable only in dielectrics, while the transmogrification of optical energy can happen in dielectrics as well as conductors.

A further classification involves the division of the mechanisms involved in the absorption of optical energy into two broad classes: mechanisms that are linear with the electric field and mechanisms that are non-linear with the electric field. Linear mechanisms, such as the piezoelectric effect, produce acoustic energy with the same frequency as the incident light. Acoustic energy is generated by field linear mechanisms when the incident radiation has a frequency less than the Debye frequency ( $\omega_D \sim 10^{13}$  Hz). Since the optical frequency being considered is always greater than the Debye frequency, the absorption mechanisms that are linear with electric field can be neglected. Therefore, the absorption of optical energy is due to non-linear quadratic effects, such as electrostriction, magnetostriction, and the thermo-optical effect.

Before continuing, the relative contributions of the field quadratic effects need to be considered. The ensuing discussion follows that of Gusev and Karabutov

[29]. Consider a plane electromagnetic wave incident on an isotropic dielectric. The spatial density of forces acting on the dielectric is given by [30],

$$\begin{aligned}
 f_i = & -\frac{\partial p}{\partial x_i} - \frac{\partial}{\partial x_i} \left( \epsilon \frac{\langle E_j E_j \rangle}{8\pi} \right) - \frac{\partial}{\partial x_i} \left( \mu \frac{\langle H_j H_j \rangle}{8\pi} \right) \\
 & + \frac{\partial}{\partial x_i} \left[ \left( \rho \frac{\partial \epsilon}{\partial \rho} \right)_T \frac{\langle E_j E_j \rangle}{8\pi} + \left( \rho \frac{\partial \mu}{\partial \rho} \right)_T \frac{\langle H_j H_j \rangle}{8\pi} \right] + \frac{\epsilon\mu - 1}{4\pi c} \frac{\partial}{\partial t} \langle e_{ijk} E_k H_j \rangle,
 \end{aligned} \tag{2.1}$$

where  $p$  is the pressure in the material,  $\epsilon$  and  $\mu$  are the permittivity and magnetic permeability,  $c$  is the speed of light,  $\rho$  is the density,  $T$  is the temperature,  $E$  and  $H$  are the electric and magnetic fields,  $e_{ijk}$  is the permutation symbol and the angled brackets represent a time average over a period much greater than the period of the electromagnetic wave. The first term on the right hand side of Eq. 2.1 represents the force produced by the photo-thermal effect. The second and third terms in Eq. 2.1 are present if the material is heterogeneous on a length scale proportional to the wavelength of the optical disturbance. The terms in the square brackets represent the electrostrictive and magnetostrictive effect. The Abraham-Lorentz force is expressed by the last term on the right side of Eq. 2.1. This force is a result of a charged particle interacting with its own radiation field.

For diamagnetic and paramagnetic materials, magnetostrictive effect are not significant at optical frequencies [29]. The relative contribution of the Abraham-Lorentz force and the electrostriction force can be expressed by the following ratio,

$$\frac{|f_a|}{|f_{str}|} \sim \frac{\omega a}{c}, \quad (2.2)$$

where  $f_a$  and  $f_{str}$  represent the Abraham-Lorentz and electrostriction force respectively,  $a$  is a characteristic length such as the beam diameter, and  $\omega$  is the frequency of the excited acoustic disturbance. Thus, for a spot size on the order of 1 cm, the Abraham-Lorentz force can be neglected for acoustic disturbances below  $1 \times 10^{10}$  Hz. It can be shown [29], that for most cases, the electrostriction (termed photostriction at optical frequencies) effect becomes significant relative to the photo-thermal effect in transparent media (absorption depth  $> 1$  cm) and at high ultrasonic frequencies. The exceptions to this rule are possible when there exists a substantial time delay ( $\Delta t \sim 1 \mu s$ ) between absorption of the photon and thermalization of the excited electron. The excited valence electron is delocalized, or stripped from its parent atoms, resulting in a change in the interaction energy between the parent atoms. This change in interaction energy gives rise to a non-thermal change in density. Non-thermal laser generation of ultrasound has been reported by a number of researchers [30,31,32]. Dixon, *et al.* [32], demonstrated that non-thermal generation in single crystal silicon is significant for fluences below  $\sim 0.2 \text{ J cm}^{-2}$ . Dharamsi and Hassam [31], give a set of conditions and a list of candidate materials for photostrictive acoustic generation. From their paper it can be inferred that polycrystalline and/or amorphous material would not exhibit photostrictive effects, due to the fact that the excited electron would quickly drift out of the localized region where the band structure lends itself to photostrictive generation.

The focus of this presentation is pulsed Nd:YAG generation in polycrystalline-carbon-fiber epoxies. Using the above discussion, and noting typical values for the pulse duration, beam diameter, and the absorption depth ( $\tau=10$  ns,  $a=1$  cm,  $\alpha=1$  cm), it can be shown that the dominant mechanisms in the absorption of light by a carbon epoxy composite are represented by

$$f_i = -\frac{\partial p}{\partial x_i} - \frac{\partial}{\partial x_i} \left( \epsilon \frac{\langle E_j E_j \rangle}{8\pi} \right) - \frac{\partial}{\partial x_i} \left( \mu \frac{\langle H_j H_j \rangle}{8\pi} \right). \quad (2.3)$$

Graphite epoxy can be considered heterogeneous on length scales corresponding to the spacing between fibers (10  $\mu$ m). Thus, for laser systems operating in the visible or near visible range, only the photo-thermal mechanism needs to be considered.

Determination of the spatial distribution of the absorbed energy involves understanding the influence that the laser parameters have on the absorption of optical energy in the constitutive materials, graphite and epoxy. The most important parameter influencing the absorption characteristics of graphite epoxy is the optical wavelength of the generation beam. The amount of optical energy absorbed and whether it is absorbed in the epoxy or in the fiber is a function of optical wavelength. Thus, to investigate the nature of pulsed laser interaction in graphite epoxy in a general sense, the optical frequency of the generation beam should be left arbitrary. In Fig. 2.1, a schematic of a plane electromagnetic wave of arbitrary frequency incident on a partially absorbing optically isotropic material is shown. The

propagation direction is perpendicular to the interface and hence, there is no need to distinguish between fields that are parallel and perpendicular to the plane of incidence. The incident electric field propagating in the  $x_3$  direction and polarized along  $x_1$ , is represented as

$$E_1^{(1)} = \hat{x}_1 E_0^{(1)} e^{i(k_3^{(1)} x_3 - \omega t)}, \quad (2.4)$$

where  $E_0^{(1)}$  is the amplitude of the wave,  $\omega$  is the frequency. The wavenumber is expressed as

$$k_3^{(1)} = \frac{n^{(1)} \omega}{c}, \quad (2.5)$$

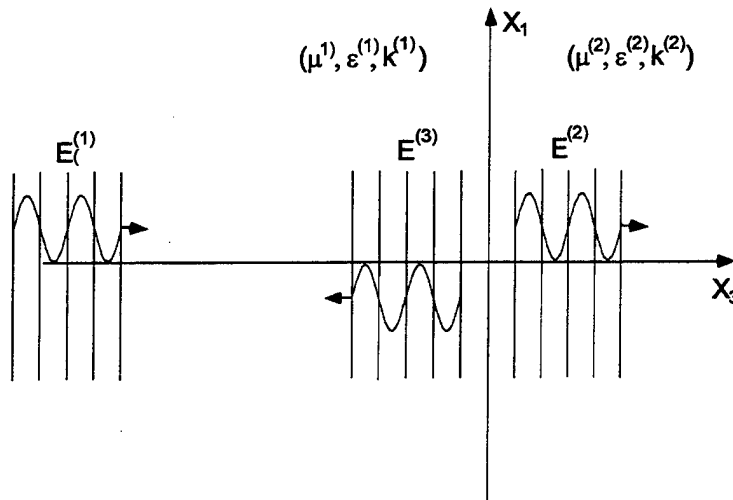


**Fig. 2.1.** Coordinate system used in discussing reflection at the surface of a conductor.  $E^{(1)}$  represents the incident wave,  $E^{(2)}$  represents the transmitted wave and  $E^{(3)}$  represents the reflected wave.

where  $n^{(1)}$  is the index of refraction in medium one, and  $c$  is the speed of light. The reflected and transmitted electric fields have the form,

$$\begin{aligned} E_1^{(2)} &= \hat{x}_1 E_0^{(2)} e^{i(k_3^{(2)} x_3 - \omega t)}, \\ E_1^{(3)} &= \hat{x}_1 E_0^{(2)} e^{i(-k_3^{(1)} x_3 - \omega t)}, \end{aligned} \quad (2.6)$$

where

$$\begin{aligned} k_3^{(2)} &= \alpha^{(2)} + i\beta^{(2)}, \\ \alpha^{(2)} &= \omega \left[ \frac{\mu^{(2)} \varepsilon^{(2)}}{2} \left( \sqrt{1 + \frac{\sigma^{(2)}}{\omega \varepsilon^{(2)}}} + 1 \right) \right]^{1/2}, \\ \beta^{(2)} &= \omega \left[ \frac{\mu^{(2)} \varepsilon^{(2)}}{2} \left( \sqrt{1 + \frac{\sigma^{(2)}}{\omega \varepsilon^{(2)}}} - 1 \right) \right]^{1/2}. \end{aligned} \quad (2.7)$$

In Eq. 2.1,  $\mu^{(2)}$ ,  $\varepsilon^{(2)}$ , and  $\sigma^{(2)}$  represent the frequency dependent, permeability, permittivity, and the conductivity in medium 2. The wavevector in medium 2 is complex and hence the amplitude of the electromagnetic wave is damped exponentially as it travels in medium 2. The wave amplitude is attenuated by a factor of  $1/e$  as it travels a distance  $x_3 = 1/\beta$ . This is generally written as  $\delta$  and is referred to as the skin depth. The boundary conditions giving the equality of the tangential components of  $E$  and  $H$  at the plane  $x_3 = 0$  leads to the following expressions for the reflectivity and transmissivity,

$$R = \frac{|E_0^{(2)}|}{|E_0^{(1)}|} = \left| \frac{1 - \left( \mu^{(1)} / \mu^{(2)} \right) \left( 1 / 2\pi n^{(1)} \right) \left( \lambda \alpha^{(2)} + i\lambda \beta^{(2)} \right)}{1 + \left( \mu^{(1)} / \mu_2 \right) \left( 1 / 2\pi n^{(1)} \right) \left( \lambda \alpha_2 + i\lambda \beta_2 \right)} \right|, \quad (2.8)$$

$$T = \frac{|E_0^{(3)}|}{|E_0^{(1)}|} = \left| \frac{2}{1 + \left( \mu^{(1)} / \mu^{(2)} \right) \left( 1 / 2\pi n^{(1)} \right) \left( \lambda \alpha^{(2)} + i\lambda \beta^{(2)} \right)} \right|.$$

Equation 2.8 demonstrates that if the product  $\lambda\beta^{(2)} \gg 1$ ,  $R \sim 1$ . Good conductors approach this limit when the optical frequency is less than the plasma frequency. For polished metals irradiated by visible light, the reflectivity can be greater than 90%. In contrast,  $\lambda\beta^{(2)} \ll 1$  for most ceramics and polymers in the visible portion of the spectrum. As a result, polymers and ceramics only absorbed weakly in the visible region of the spectrum.

When considering the amplitude of a photothermally generated acoustic disturbance, the spatial extent is as important as the amount of energy absorbed. Let generation in a conductor using a visible laser source serve as an example. While only a small percentage of the incident light is absorbed, its spatial extent is confined to a skin depth,  $\delta \sim 10$  nm. The localized nature of the absorbed energy leads to large thermal gradients and hence large acoustic amplitudes. In comparison, a poor conductor such as epoxy, confines the absorbed energy to a skin depth,  $\delta \sim 10$  mm. The relatively large spatial extent of the absorbed energy leads to small temperature gradients and small acoustic amplitudes.

First consider the variation of the product  $\lambda\beta^{(2)}$  with wavelength for graphite. Graphite consist of molecular sheets of carbon atoms. Within the plane of the

molecular sheets, there are three covalent bonds and one delocalized metallic bond. The sheets are bound together by Van der Waals forces. The delocalized bond gives rise to metallic-like character for electronic properties in the plane of the sheets. Thus,  $\lambda\beta^{(2)} \gg 1$  for polycrystalline graphite fibers at frequencies below the plasma frequency. At frequencies above the plasma frequency, the skin depth of the material relative to the optical wavelength increases substantially. In Table 2.1 a list of the skin depths for single crystal graphite at various commercially available laser wavelengths is given. Graphite is birefringent, and hence, the index of refraction and the skin depth depend on the polarization direction relative to the materials crystallographic axes. Electromagnetic waves polarized parallel and perpendicular to the optic axis are termed ordinary and extraordinary respectively. Table 2.1 shows that the skin depth for both the ordinary and extraordinary rays is on the order of 10-100 nm in the visible and near IR portion of the spectrum.

**Table 2.1.** Skin depth versus wavelength for graphite. Extraordinary is denoted by (e) and ordinary is denoted by (o) [33].

| WAVELENGTH ( $\mu\text{M}$ ) | POTENTIAL LASER SYSTEM | ABSORPTION DEPTH (NM) |
|------------------------------|------------------------|-----------------------|
| 0.2638                       | (1/4 Nd:YAG)           | 15.8 (o)              |
| 0.3542                       | (1/3 Nd:YAG)           | 41.4 (o), 81.6 (e)    |
| 0.5391                       | (1/2 Nd:YAG)           | 64.1 (o)              |
| 0.6880                       | (Ruby)                 | 60.5 (o)              |
| 1.069                        | (Nd:YAG)               | 82.2 (o)              |
| 10.64                        | (CO <sub>2</sub> )     | $5.6 \times 10^7$ (e) |

It should be noted that graphite does not exhibit metallic character for 10.6  $\mu\text{m}$  radiation that is polarized perpendicular to the optic axis.

In contrast to graphite, epoxies are poor conductors and do not exhibit metallic character. Epoxies are a family of thermosetting polymer resins with excellent mechanical, dimensional stability, adhesive properties, and heat resistance. The binding force, which holds the individual atoms in the polymer resin together, is covalent. Table 2.2 gives the location of the absorption peaks for two commercially available epoxies. Epoxies, like most polymers, absorb weakly in the visible region and have strong absorption peaks in the ultraviolet and infrared portions of the spectrum. Unlike graphite, absorption in polymers is not associated with contributions from delocalized electrons. Absorption in the ultraviolet is associated with electronic transitions between molecular orbitals while absorption in the infrared is associated with vibrational, translational and rotational motion of the molecules. Experimental results demonstrating the combined absorption spectrum for graphite epoxy composites were presented by Dubois *et al.* [34].

**Table 2.2.** Location of the absorption peaks for various epoxies [35,36]. Absorption depths are not given since the cell length for spectral data was not given.

| LOCATION OF SPECTRA PEAK | TRADE NAME OR CHEMICAL NAME | PERCENT TRANSMISSION |
|--------------------------|-----------------------------|----------------------|
| 211 (nm)                 | chalcone epoxy              | 12                   |
| 3.50 ( $\mu\text{m}$ )   | Den <sup>®</sup> 438        | 46                   |
| 7.63 ( $\mu\text{m}$ )   | Den <sup>®</sup> 438        | 4                    |
| 8.06 ( $\mu\text{m}$ )   | Den <sup>®</sup> 438        | 2                    |
| 10.99 ( $\mu\text{m}$ )  | Den <sup>®</sup> 438        | 34                   |

Their data showed that the graphite epoxy laminates absorb strongly in the infrared region of the spectrum from 5.5  $\mu\text{m}$  to 10  $\mu\text{m}$  radiation. These results illustrate that

the absorption characteristics of the graphite epoxy in the infrared are dominated by the epoxy.

Owing to the fact that graphite and epoxy have vastly different optical properties, the way in which optical energy is absorbed by the composite is a strong function of the illumination wavelength. For instance, pulsed CO<sub>2</sub> generation would result in the majority of the absorbed optical energy being deposited in the epoxy rather than the fibers. Conversely, illumination with a laser system emitting visible radiation would result in the absorbed energy being deposited in the fibers.

For pulsed Nd:YAG generation, tables 2.1 and 2.2 demonstrate that the graphite fibers absorb the majority of the transmitted energy. Figure 2.3 illustrates the notable features of Nd:YAG pulsed irradiation in graphite epoxy.

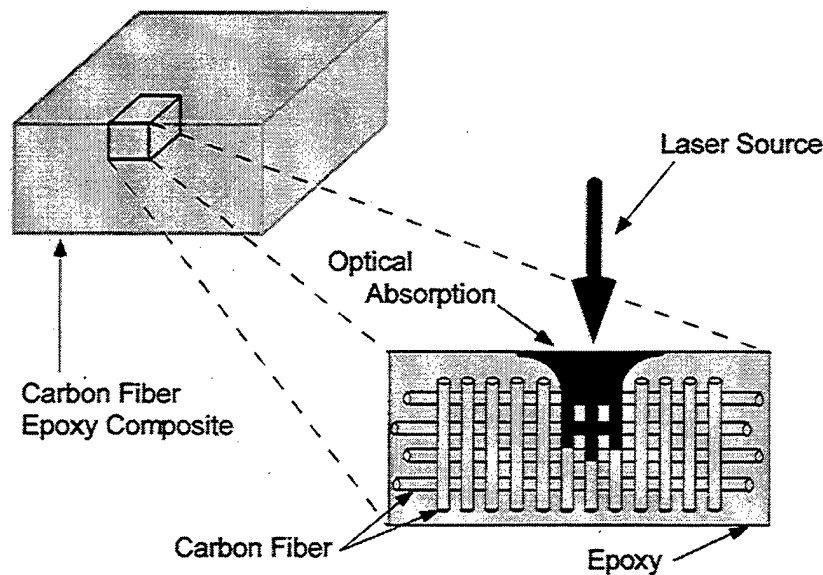


**Fig. 2.2.** Schematic of Pulsed Nd:YAG laser interaction with graphite epoxy.

For a large illumination area relative to the fiber spacing, the optical energy is absorbed over a network of fibers with a complicated composite geometry. Thus, solving the optical problem exactly with its complex system of boundary conditions would be a formidable task. As an alternative, two special cases can be considered which greatly simplify the optical problem. The first case assumes that all the optical energy is absorbed at a point located on the surface of the material. This could be realized by bringing the first layer of fibers to the samples surface and then focusing the generation beam to a small spot. The second case assumes that all the energy is deposited at a point buried beneath a thin layer of epoxy. Considering a buried source is perhaps the first step in modeling inhomogeneity due to variations in optical properties.

## (2.2) *THERMAL PROBLEM*

The assumption that all the optical energy is absorbed at a point greatly simplifies the thermal problem as it did in the optical problem. The thermal problem involves predicting the spatial and temporal distribution of the temperature field. Immediately after the absorption of the optical energy, thermal energy is conducted into a thermally heterogeneous anisotropic material. To make matters more complicated; the transient nature of the problem couples the temperature field to the strain field via the strain rate. The thermal problem starts by considering the fully coupled equations of thermoelasticity,

$$\begin{aligned}
C_{ijkl}u_{l,kj} - B_{ij}T_{,i} &= \rho u_{i,t} , \\
k_{ij}T_{,ij} - Q &= \rho CT_{,t} - \rho TB_{ij}\epsilon_{ij,t} ,
\end{aligned}
\tag{2.9}$$

where  $C_{ijkl}$  is the elastic stiffness tensor,  $u_i$  are the displacements,  $B_{ij}$  is the thermal pressure coefficient,  $T$  is the temperature,  $\rho$  is the density,  $k_{ij}$  is the thermal conductivity,  $Q$  is the heat generation term,  $C$  is the specific heat at constant strain, and  $\epsilon_{ij}$  is the strain tensor. Hetnarski [37] and Nowacki [38] considered the influence of coupling between the strain and the temperature fields. Their results showed that for the general problem of a concentrated heat source in an infinite thermoelastic space, the coupling between the strain and temperature fields is negligible. If the strain rate contribution to the temperature is neglected, the heat conduction equation can be written as

$$k_{ij}T_{,ij} - \rho CT_{,t} = -Q(x_1, x_2, x_3, t) . \tag{2.10}$$

For a buried laser point source,  $Q$  can be represented as follows:

$$\begin{aligned}
Q &= q_0 \delta(x_1) \delta(x_2) \delta(x_3 - a) \delta(t) , \\
q_0 &= E(1 - R) ,
\end{aligned}
\tag{2.11}$$

where  $q_0$  is the absorbed heat,  $E$  is the energy of the laser pulse, and  $R$  is the reflectivity of the sample surface. Before considering the solution to the heat

conduction equation, Eq. 2.10, the conditions under which thermal diffusion can be neglected are examined. Rose [5], states that a point-source representation for the radiation from a localized source is adequate for  $\lambda \gg l$ , where  $\lambda$  is the ultrasonic wavelength and  $l$  is the largest characteristic length relating to the source region. Ready [39] has shown that the source is effectively localized within a region,  $0 \leq l \leq \omega + (4kt)^{1/2}$ , where  $\omega$  is the laser beam radius,  $k$  is the coefficient of thermal conductivity and  $t$  is the time interval of interest. Considering laser generation in graphite, it can be shown [5] that a point-source representation is a fair assumption for a frequency/spot-size product that is less than 1000 MHz- $\mu\text{m}$ . Thus, for a laser pulse with a 10 ns pulse duration and a spot size of 20  $\mu\text{m}$ , it is reasonable to neglect the effects of thermal diffusion. The temperature distribution in the absence of thermal diffusion is represented as

$$T = T_0 \delta(x_1) \delta(x_2) \delta(x_3 - a) H(t) ,$$

$$T_0 = \frac{q_0}{\rho C} ,$$
(2.12)

As a result of neglecting thermal diffusion, the thermally anisotropic and heterogeneous nature of the problem need not be considered.

### (2.3) THE ELASTIC PROBLEM

In a similar manner to the optical and thermal problem, the heterogeneous and anisotropic elastic character of carbon fiber epoxy is addressed in this section. First, the effects of heterogeneities are examined by considering a plane shear wave interacting with an infinite cylinder. This simple model affords an estimate of the dependence of the scattered power on the ultrasonic wavelength. Next the anisotropic elastic character of carbon fiber epoxy is discussed. This chapter is concluded by presenting a stiffness tensor representative of the symmetry imposed by a unidirectional fiber arrangement.

Diffraction of elastic waves is a subject that has been addressed by several authors, [40-42]. In this section, one of the simplest examples of elastic wave diffraction is treated. Consider a harmonic shear wave polarized parallel to the axis of an infinite cylinder as shown in Fig. 2.4. The incident wave propagates in the matrix along the  $x_1$ -axis and is given by

$$u_1^{(i)} = u_2^{(i)} = 0, \quad u_3^{(i)} = u_0 \exp[i(k^{(1)}x_1 - \omega t)], \quad k^{(1)} = \frac{c^{(1)}}{\omega}, \quad (2.13)$$

where  $u_3^{(i)}$  is the displacement of the incident wave and  $c^{(1)}$  is the phase velocity in the material surrounding the cylinder. Since the incident wave is polarized parallel to the cylinder axis (SH), the scattered wave is also a SH wave.

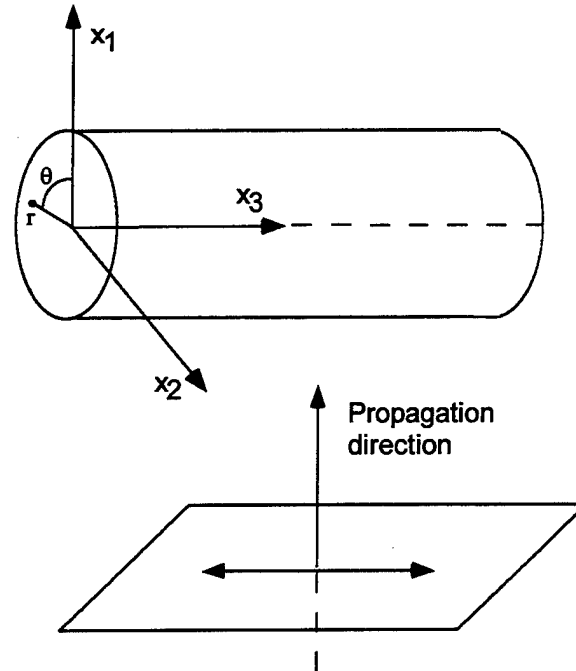


**Fig. 2.3.** Incident shear wave polarized parallel to cylinder axis.

It should be noted, since the motion is antiplane shear, the solution of this problem lends itself to the eigenfunction expansion method. If the problem involved shear and longitudinal waves, the integral equation technique would be used rather than eigenfunction expansion method. The displacement of the wave after interaction with the cylinder,  $u_3^{(d)}$ , satisfies the wave equation in cylindrical coordinates,

$$\left( \frac{\partial^2}{\partial r^2} + \frac{1}{r} \frac{\partial}{\partial r} + \frac{1}{r^2} \frac{\partial^2}{\partial \theta^2} \right) u_3^{(d)} = \frac{1}{c_2} \frac{\partial^2 u_3^{(d)}}{\partial t^2} . \quad (2.14)$$

The solutions of Eq. 2.14 are of the form,

$$u_3^{(d)} = R(r)\Theta(\theta)e^{-i\omega t} . \quad (2.15)$$

Substitution of Eq. 2.15 into Eq. 2.14 and separating variables gives

$$r^2 \frac{\partial^2 R}{\partial r^2} + r \frac{\partial R}{\partial r} + (k^2 r^2 - n^2) R = 0, \quad \frac{\partial^2 \Theta}{\partial \theta^2} + n^2 \Theta = 0 . \quad (2.16)$$

Noting that  $\Theta$  must be periodic with period  $2\pi$ , the solution to this problem is

$$u_3^{(d)} = u_0 \sum_{n=0}^{\infty} (A_n H_n^1(k^{(1)}r) + B_n H_n^2(k^{(1)}r)) \cos(n\theta) e^{-i\omega t} , \quad (2.17)$$

where  $H_n^1$  and  $H_n^2$  are the first and second Hankel functions of order  $n$ . The displacement  $u_3^{(d)}$ , is composed of a scattered wave and a refracted wave ( $r < a$ ). The functions  $H_n^2$  are the appropriate solutions for the outwardly propagating scattered wave. The domain of the refracted wave includes  $r=0$ , thus,  $J_n$  are the appropriate solutions for the refracted wave. The solution now can be written as

$$\begin{aligned}
u_3^{(d)} &= u_3^{(s)} + u_3^{(r)} , \\
u_3^{(s)} &= u_0 \sum_{n=0}^{\infty} A_n H_n^1(k^{(1)}r) \cos(n\theta) e^{-i\omega t} , \\
u_3^{(r)} &= -u_0 \sum_{n=0}^{\infty} C_n J_n(k^{(2)}r) \cos(n\theta) e^{-i\omega t} ,
\end{aligned} \tag{2.18}$$

where  $u_3^{(s)}$  and  $u_3^{(r)}$  represent the scattered wave and the refracted wave respectively.

The wavevector in the fiber is defined as

$$k^{(2)} = \frac{\omega}{c^{(2)}} , \tag{2.19}$$

where  $c^{(2)}$  is the phase velocity in the fiber. The amplitudes,  $A_n$  and  $B_n$ , are obtained by satisfying the boundary conditions. The boundary conditions require the continuity of the displacements and stresses at the surface of the cylinder,

$$u_3^{(i)} + u_3^{(s)} = u_3^{(r)} , \quad \mu^{(1)} \frac{\partial}{\partial r} (u_3^{(i)} + u_3^{(s)}) = \mu^{(2)} \frac{\partial u_3^{(r)}}{\partial r} , \quad \text{at } r = a . \tag{2.20}$$

Since the scattered and refracted waves are in cylindrical coordinates, it is necessary to express  $u_3^{(i)}$  in cylindrical coordinates. Using the series expansion,

$$\begin{aligned}
e^{(ikr \cos \theta)} &= \sum_{n=0}^{\infty} \varepsilon_n i^n J_n(kr) \cos(n\theta) , \\
\varepsilon_0 &= 1, \quad \varepsilon_i = 2 \quad \text{for } n = 1, 2, \dots ,
\end{aligned} \tag{2.21}$$

$u_3^{(i)}$  can be expressed in cylindrical coordinates as,

$$\begin{aligned} u_3^{(i)} &= U(r, \theta) e^{i\omega t} = u_0 e^{-ik^{(1)}r \cos \theta} e^{i\omega t}, \\ u_3^{(i)} &= u_0 \sum_{n=0}^{\infty} \epsilon_n i^n J_n(k^{(1)}r) \cos(n\theta) e^{i\omega t}. \end{aligned} \quad (2.22)$$

Substituting Eqs.2.18 and Eq.2.22 into Eqs.2.20 gives

$$\begin{aligned} A_n &= \left(-i^n \epsilon_n / D_n\right) \left[ \mu^{(2)} k^{(2)} J_n(k^{(1)}a) \frac{\partial J_n(k^{(2)}a)}{\partial r} - \mu^{(1)} k^{(1)} \frac{\partial J_n(k^{(1)}a)}{\partial r} J_n(k^{(2)}a) \right], \\ C_n &= \left(-i^n \epsilon_n / D_n\right) \mu^{(1)} k^{(1)} \left[ \frac{\partial J_n(k^{(1)}a)}{\partial r} H_n^1(k^{(1)}a) - \frac{\partial H_n^1(k^{(1)}a)}{\partial r} J_n(k^{(1)}a) \right], \\ D_n &= \mu^{(2)} k^{(2)} H_n^1(k^{(1)}a) \frac{\partial J_n(k^{(2)}a)}{\partial r} - \mu^{(1)} k^{(1)} \frac{\partial H_n^1(k^{(1)}a)}{\partial r} J_n(k^{(2)}a). \end{aligned} \quad (2.23)$$

The effect that the fiber has on the acoustic wave can be gauged by considering the scattered energy relative to the energy of the incident wave. The power flux per unit length along the cylinder is given by

$$\mathbf{P} = \oint_C \tau_{kl} n_k \frac{\partial u_l}{\partial t} ds, \quad (2.24)$$

where  $C$  is the contour along the circumference of the cylinder. The time mean value of the power flux for harmonic waves is given by

$$\langle \mathbf{P} \rangle = \oint_C \langle \mathbf{P}_k \rangle \mathbf{n}_k ds, \quad (2.25)$$

where the angled brackets represent the time average over one period. The average power flux per unit area is given by

$$\begin{aligned} \langle \mathbf{p}_k \rangle &= \left\langle \bar{t}_{kl} \frac{\partial \bar{u}_l}{\partial t} \right\rangle, \\ \bar{t}_{kl} &= \bar{t}_{kl} e^{i\omega t}, \quad \bar{u}_l = \bar{u}_l e^{i\omega t}, \\ \langle \mathbf{p}_k \rangle &= -\frac{1}{4} i\omega (\bar{t}_{kl} \bar{u}_l^* - \bar{t}_{kl}^* \bar{u}_l), \end{aligned} \quad (2.26)$$

where quantities with an overbar represent the spatial part of the stress and the displacement, and an asterisk denotes the complex conjugate of a quantity. The average power flux per unit area of the incident wave can be written as

$$\langle \mathbf{p}_l^{(i)} \rangle = -\frac{1}{2} \omega \mu^{(1)} \mathbf{k}^{(1)} |\bar{u}_0|^2. \quad (2.27)$$

The average power flux per unit area of the scattered wave can be written as

$$\langle P_1^{(s)} \rangle = -\frac{1}{4} i \omega k^{(1)} \mu^{(1)} |u_0|^2 \sum_{n=0}^{\infty} \sum_{m=0}^{\infty} \left[ A_n A_m^* \frac{\partial H_n^1(k^{(1)}r)}{\partial r} H_m^{*1}(k^{(1)}r) - A_n^* A_m \frac{\partial H_n^{*1}(k^{(1)}r)}{\partial r} H_m^1(k^{(1)}r) \right] \cos n\theta \cos m\theta. \quad (2.28)$$

At large distances from the fiber ( $R \gg \lambda$ ), the Hankel functions take on the following form,

$$H_n^1(kR) \sim \sqrt{2/(\pi kR)} e^{i[kR - (n+1/2)(\pi/2)]},$$

$$\frac{\partial H_n^1(kR)}{\partial r} \sim i H_n^1(kR). \quad (2.29)$$

Using Eqs. 2.25, 2.27, 2.28, and 2.29, an expression representing the scattering cross section of the fiber can be written as

$$\gamma = \frac{\langle P \rangle}{\langle P_1^{(i)} \rangle} = \frac{2}{k^{(1)}} \left( 2A_0 A_0^* + \sum_{n=1}^{\infty} A_n A_n^* \right). \quad (2.30)$$

Before continuing, the acoustic impedance mismatch between the fiber and the matrix must be specified. If the matrix and the fiber have the same elastic constants, then from Eqs. 2.23, the amplitude of the scattered wave is zero and the acoustic disturbance passes through the fiber unaffected. In contrast if  $\mu^{(2)} \rightarrow \infty$  or  $\mu^{(2)} \rightarrow 0$ , Eqs. 2.23 would reduce to the case of a rigid cylinder or a cylindrical cavity respectively. In order to keep the salient features of elastic wave scattering by a

cylindrical obstacle while considerably simplifying the analysis, the shear modulus of the fiber is assumed to be zero ( $\mu^{(2)}=0$ ).

A plot of scattered power versus wavenumber parameter is plotted in Fig. 2.4. The power per unit length of the cylinder is normalized with respect to the power in the incident beam whose width is equal to the diameter of the cylinder.

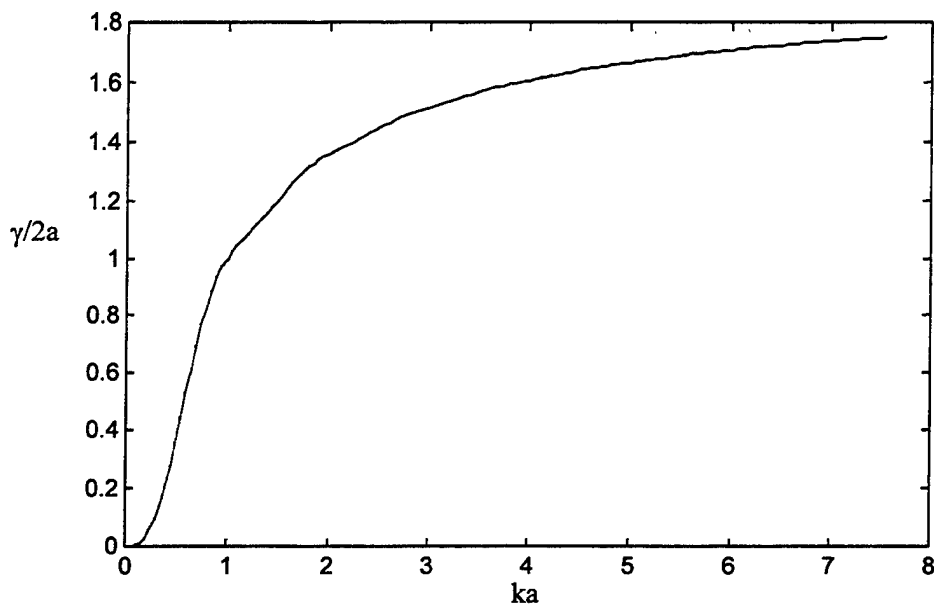


**Fig. 2.4.** A plot of scattered power versus wavenumber parameter.

For wavelengths that are small compared to the cylinder radius, the power in the scattered beam is twice the power contained in the incident beam. This is due to the fact that the scattered wave contains forward and backward propagation components. The backward propagating component is the reflected wave and the forward propagation component destructively interferes with the undisturbed portion of the incident wave. The forward-scattered wave is referred to as the shadow-forming

wave. Figure 2.4 demonstrates that if the acoustic wavelength is large relative to the cylinder radius, then the wave passes by the cavity essentially unaffected. The relevant experimental parameters in this case are the laser pulse duration and the acoustic velocity in the material. For a 10 ns pulse duration and an acoustic velocity ranging from 1 - 10 mm/ $\mu$ s, the smallest acoustic wavelength ranges from 10 - 100  $\mu$ m. Thus, for a fiber spacing of 10  $\mu$ m, only the highest frequencies will suffer scattering losses.

The emphasis of the remaining portion of this presentation involves the effect of elastic anisotropy on the character of laser generated ultrasound in graphite epoxy. Scattering effects will be neglected by replacing the graphite epoxy by an idealized homogeneous elastically anisotropic material. In the limit of homogeneity, this idealized material will have a crystal symmetry analogue related to the way the fibers are arranged in the composite. This is best illustrated by considering a unidirectional graphite fiber epoxy composite illustrated in Fig. 2.5.

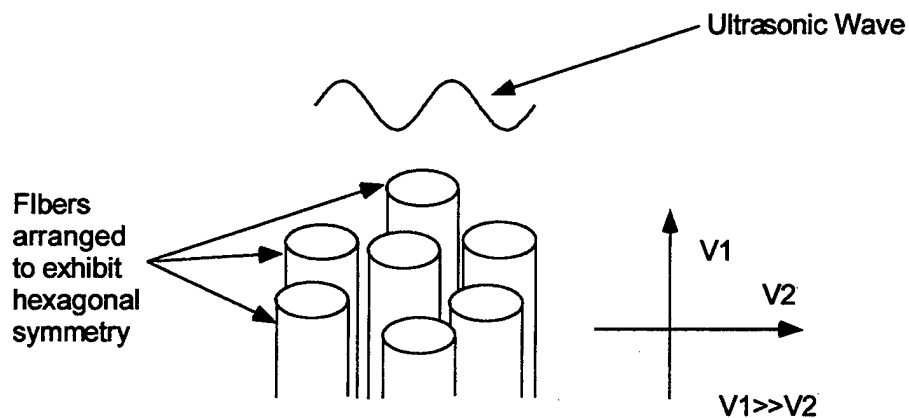


**Fig. 2.5.** Ideal carbon fiber arrangement in epoxy composite.

From mechanical considerations, the fibers are packed as tightly as possible. Ideally, the highest volume fraction of fibers to epoxy is obtained when the fibers are arranged with hexagonal symmetry as shown in Fig. 2.5. Since the fibers are assumed to have hexagonal symmetry, the stiffness tensor is that of a hexagonal crystal,

$$c_{ij} = \begin{bmatrix} c_{11} & c_{12} & c_{13} & \bullet & \bullet & \bullet \\ c_{12} & c_{11} & c_{13} & \bullet & \bullet & \bullet \\ c_{13} & c_{13} & c_{33} & \bullet & \bullet & \bullet \\ \bullet & \bullet & \bullet & c_{44} & \bullet & \bullet \\ \bullet & \bullet & \bullet & \bullet & c_{44} & \bullet \\ \bullet & \bullet & \bullet & \bullet & \bullet & c_{66} \end{bmatrix}, \quad (2.31)$$

where the matrix notation or reduced notation has been used to represent the stiffness tensor. The equations of motion for a laser source in a transversely isotropic material can now be written explicitly as

$$\begin{aligned} \beta u_{1,11} + \delta u_{1,22} + u_{1,33} - u_{1,\tau\tau} + (\beta - \delta)u_{2,12} + \kappa u_{3,13} &= S_1, \\ (\beta - \delta)u_{1,12} + \delta u_{2,11} + \beta u_{2,22} + u_{2,33} - u_{2,\tau\tau} + \kappa u_{3,23} &= S_2, \\ \kappa u_{1,13} + \kappa u_{2,23} + u_{3,11} + u_{3,22} + \alpha u_{3,33} - u_{3,\tau\tau} &= S_3, \end{aligned} \quad (2.32)$$

$$\begin{aligned} S_1 &= B_{11} T_0 \delta'(x_1) \delta(x_2) \delta(x_3 - a) H(t), \\ S_2 &= B_{11} T_0 \delta(x_1) \delta'(x_2) \delta(x_3 - a) H(t), \\ S_3 &= B_{33} T_0 \delta(x_1) \delta(x_2) \delta'(x_3 - a) H(t), \end{aligned}$$

where  $\alpha$ ,  $\beta$ ,  $\kappa$ ,  $\delta$  and  $\tau$  are defined as

$$\alpha = \frac{c_{33}}{c_{44}}, \beta = \frac{c_{11}}{c_{44}}, \kappa = (1 + \alpha\beta - \gamma)^{1/2}, \delta = \frac{1}{2}(\beta - c_{12}/c_{44})$$

$$\gamma = 1 + \alpha\beta - \left(\frac{c_{13}}{c_{44}} + 1\right)^2, \tau = t\left(\frac{c_{44}}{\rho}\right)^{1/2} \quad (2.33)$$

The ratios of the elastic constants introduced in Eq. 2.33 are convenient groupings that are later used to determine the character of the slowness curve and wave-front curve. The construction and analysis of these curves is the subject of Chapter 3. The statement of the problem is completed by stating the traction free boundary conditions,

$$\tau_{13} = \frac{\partial u_3}{\partial x_1} + \frac{\partial u_1}{\partial x_3} = 0,$$

$$\tau_{23} = \frac{\partial u_3}{\partial x_2} + \frac{\partial u_2}{\partial x_3} = 0,$$

$$\tau_{33} = (\kappa - 1)\left(\frac{\partial u_1}{\partial x_1} + \frac{\partial u_2}{\partial x_2}\right) + \alpha \frac{\partial u_3}{\partial x_3}.$$
(2.34)

### CHAPTER 3

The solution of for an unbounded isotropic material in the presence of a spherically symmetric cavity source, shown in Fig. 3.1, has been thoroughly treated by a number of authors [40-42]. When the source is spherically symmetric, elastic isotropy greatly simplifies the solution for two reasons. First, isotropy leads to spherical phase fronts which in turn leads to a solution that is independent of angle,  $\varphi$  and  $\phi$ . Second, shear and longitudinal motions are not coupled in isotropic materials; thus, the solution procedure is greatly aided by the use of displacement potentials. In contrast, an elastically anisotropic material does not have spherical phase fronts and shear and longitudinal motions are coupled. Before seeking the solution to Eqs. 2.33, subjected to the boundary conditions given in Eq. 2.35, it is prudent to investigate the differences in behavior between an isotropic and a anisotropic full-space subjected to an acoustic disturbance. These differences are most conveniently exemplified by considering the phase front and wave front shapes.

#### *(3.1) NORMAL CURVES FOR SOME TRANSVERSELY ISOTROPIC SYSTEMS (TWO SPACE DIMENSIONS)*

Consider a time-harmonic plane wave propagating in a transversely isotropic elastic solid. The equation of motion, given explicitly in Eq. 2.33, can be written in index form as

$$\bar{c}_{ijkl}u_{l,kj} - u_{i,\tau\tau} = 0, \quad (3.1)$$

where  $\bar{c}_{ijkl} = c_{ijkl} / c_{2323}$ , and  $\tau$  is defined in Eq. 2.34. The displacement wave has the following form,

$$u_i = A d_i e^{\left[ i\omega \left( x_p q_p - \frac{\tau}{v^{(2)}} \right) \right]}, \quad (3.2)$$

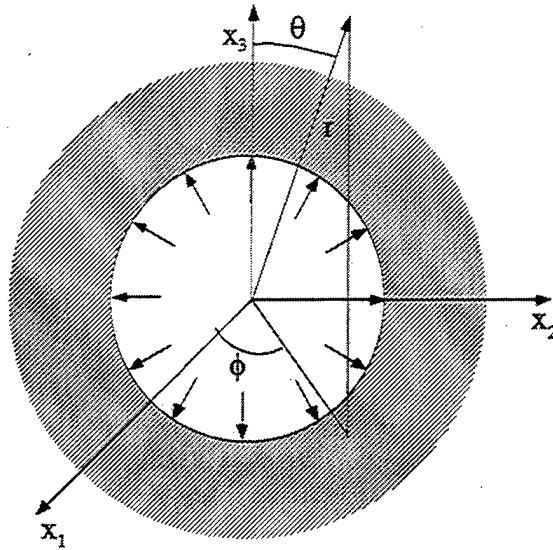


Fig. 3.1. Spherical cavity of radius  $a$  subjected to internal pressure.

where  $\omega$  is the frequency,  $A$  is the amplitude,  $q_p$  are the components of the components of the slowness vector, and  $v^{(4)}$  is given as

$$v^{(2)} = \sqrt{\frac{c_{2323}}{\rho}}. \quad (3.3)$$

Substitution of Eq. 3.2 into Eq. 3.1 gives

$$\left( \bar{c}_{ijkl} q_j q_l - \delta_{ik} \right) d_k = 0 , \quad (3.4)$$

where  $\delta_{ik}$  is the Kronecker delta. For a nontrivial solution the determinant of the coefficients of  $d_k$  must vanish, which gives

$$\left| \bar{c}_{ijkl} q_j q_l - \delta_{ik} \right| = 0 . \quad (3.5)$$

The slowness vector may be rewritten as

$$q_j = \frac{k_j}{\omega} = \frac{p_j}{v} , \quad (3.6)$$

where  $v$  is the phase velocity, and  $p_j$  is the direction cosine of the wavevector,  $k$ .

Using Eq. 3.6, Eq. 3.5 can be expressed as

$$\left| \Gamma_{ik} - v^2 \delta_{ik} \right| = 0, \quad \Gamma_{ik} = c_{ijkl} p_j p_l . \quad (3.7)$$

The constants  $\Gamma_{ik}$  are known as the Christoffel stiffnesses. From the properties of the stiffness tensor,  $C_{ijkl}$ , it follows that the eigenvalues of  $\Gamma_{ik}$  are real and positive and

their corresponding eigenvectors are orthonormal. The three eigenvalues of  $\Gamma_{ik}$  represent the phase velocities and are termed  $c_1$ ,  $c_2$ , and  $c_3$ . For the general anisotropic case, the phase velocities depend on the components of  $p_i$  (i.e. the propagation direction). However, for an isotropic material, there are only two unique phase velocities, which are also independent of propagation direction.

A polar plot of the phase velocities as a function of propagation angle is called a normal curve or slowness curve. For isotropic materials, the normal curves in two dimensions are circular, while the normal curves for anisotropic materials are non-circular. Consider the slowness curve for a material that is transversely isotropic. Let the coordinate axes coincide with the crystallographic axes. Using the form of the stiffness tensor given by Eq. 2.32, Eq. 3.7 reduces to

$$\left[ p_3^2 + \delta(p_1^2 + p_2^2) - v^2 \left[ \alpha p_3^4 + \gamma p_3^2(p_1^2 + p_2^2) + \beta(p_1^2 + p_2^2)^2 + (\alpha + 1)p_3^2 v^2 - (\beta + 1)(p_1^2 + p_2^2)v^2 + v^4 \right] \right] = 0, \quad (3.8)$$

where  $\alpha$ ,  $\beta$ ,  $\delta$ ,  $\gamma$ , and  $\kappa$  were defined in Eq. 2.34. The direction cosines in Eq. 3.8 can be written as

$$p_1 = vr \cos(\varphi), \quad p_2 = vr \sin(\varphi), \quad p_3 = vs, \quad (3.9)$$

where  $\varphi$  is to be identified with the azimuthal angle shown in Fig. 3.1. Using Eq. 3.9, Eq. 3.8 can be rewritten as

$$\begin{aligned} & \left[ s^2 + \delta r - 1^2 \right] \left[ \alpha s^4 + \gamma s^2 r^2 + \beta r^4 - (\alpha + 1) s^2 \right. \\ & \left. - (\beta + 1) r^2 + 1 \right] = 0 . \end{aligned} \quad (3.10)$$

Notice that Eq. 3.10 does not depend  $\varphi$ , a consequence of transverse isotropy. In order to graphically display the normal curve it is convenient to use polar coordinates defined by

$$s = R \cos \Theta , \quad r = R \sin \Theta . \quad (3.11)$$

Equation 3.10 now can be written as

$$\begin{aligned} & A(\Theta)R^4 - B(\Theta)R^2 + 1 = 0 , \\ & A(\Theta) = \alpha \cos^4 \Theta + \gamma \cos^2 \Theta \sin^2 \Theta + \beta \sin^4 \Theta , \\ & B(\Theta) = (\alpha + 1)\cos^2 \Theta + (\beta + 1)\sin^2 \Theta . \end{aligned} \quad (3.12)$$

Solving for R gives

$$R_{\pm}(\Theta) = \left[ \frac{B(\Theta) \pm \sqrt{B(\Theta)^2 - 4A(\Theta)}}{2A(\Theta)} \right]^{1/2} . \quad (3.13)$$

It is evident from the preceding development that the shape of the normal curve is a function of the elastic constants. The distinguishing features of the normal curves are the number and location of the inflection points. According to Payton [23], five classifications exist for transversely isotropic continua for which the normal curve is free of double points ( $B(\Theta)^2 - 4A(\Theta) = 0$ ). The five classes are represented graphically in Figs. 1-5.

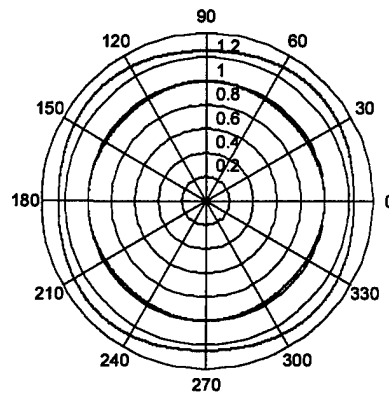


**Fig. 3.2.** Class I normal curve. ( $\alpha=0.64$ ,  $\beta=0.64$ ,  $\gamma=1.2$ )

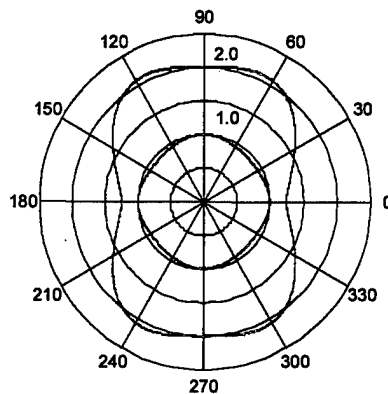


**Fig. 3.3.** Class II normal curve. ( $\alpha=0.64$ ,  $\beta=0.25$ ,  $\gamma=0.42$ )

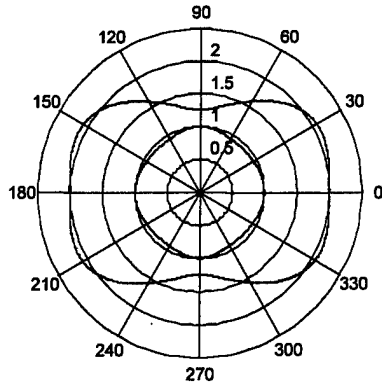


**Fig. 3.4** Class III normal curve. ( $\alpha=0.25$ ,  $\beta=0.64$ ,  $\gamma=0.42$ )

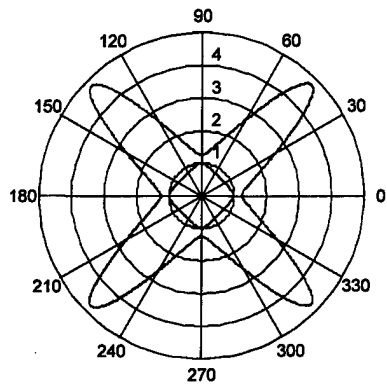


**Fig. 3.5.** Class IV normal curve. ( $\alpha=0.64$ ,  $\beta=0.64$ ,  $\gamma=-1.0$ )

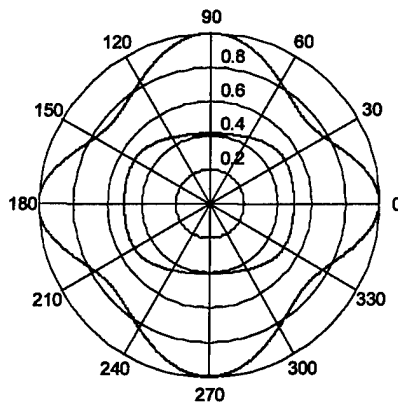


**Fig. 3.6.** Class V normal curve. ( $\alpha=4$ ,  $\beta=6$ ,  $\gamma=20$ )

The  $R_+$  branch of the class I normal curves has no inflection points. Class II and III normal curves have two inflection points on the  $R_+$  branch, intersecting the  $x_1$  and  $x_2$  axis respectively. The  $R_+$  branch of the class IV and V normal curves has four inflection points. The significance of the location of the inflection points will become apparent when considering the shape of the wave front.

*(3.2) WAVE-FRONT CURVES FOR SOME TRANSVERSELY ISOTROPIC SYSTEMS (TWO SPACE DIMENSIONS)*

Energy flows in a direction normal to the wave front and thus, it is the wave front that is of experimental interest. For isotropic material, the energy flux vector and the normal to the slowness curve coincide, while for an anisotropic material, the two vectors may or may not coincide depending on the propagation direction. Many authors have developed methods for constructing wave-front curve and the energy flux vector [23,41,43]. It suffices for this presentation to briefly describe the method given by Duff [43] for construction of the wave front. This method consists of mapping a point on the normal curve to a point on the wave-front curve. Consider a segment of the normal curve denoted  $N$ , shown in Fig. 3.7.

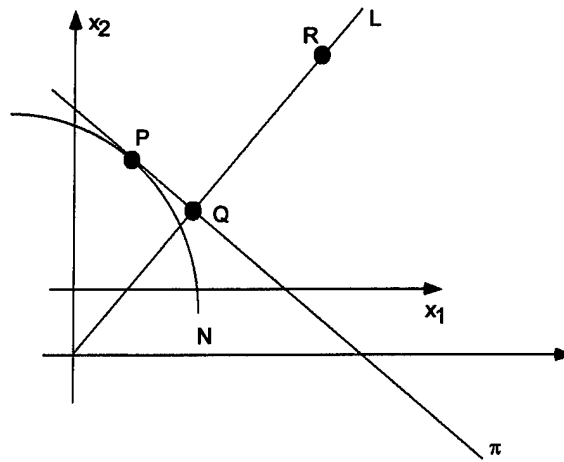


Fig. 3.7. Mapping normal curve to wave front curve.

Let  $\pi$  be a tangent line to  $N$  at  $P$ , and let  $L$  be a line normal to  $\pi$ . Point  $Q$  is located at the intersection of line  $P$  and  $L$ , and  $R$  is a point on line  $L$ . The distance from the origin to  $R$  is the inverse of the distance from the origin to  $Q$ . Point  $R$  is identified with a point on the wave front. A proof of this construction is given by Payton [23].

Wave-front curves corresponding to the normal curves given earlier are shown in Figs. 3.8-3.12.

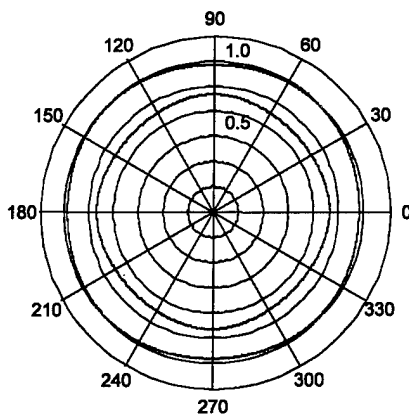
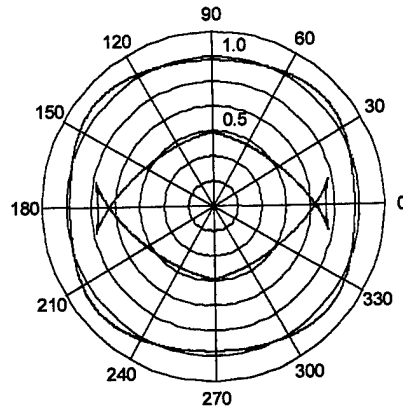
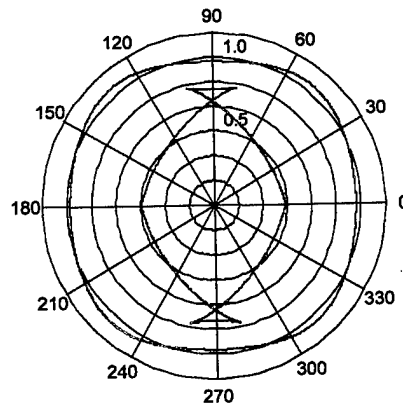


Fig. 3.8. Class I normal curve. ( $\alpha=0.64$ ,  $\beta=0.64$ ,  $\gamma=1.2$ )



**Fig. 3.9.** Class II normal curve. ( $\alpha=0.64$ ,  $\beta=0.25$ ,  $\gamma=0.42$ )



**Fig. 3.10.** Class III normal curve. ( $\alpha=0.25$ ,  $\beta=0.64$ ,  $\gamma=0.42$ )

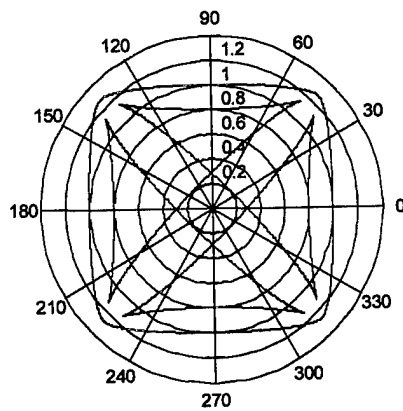


**Fig. 3.11.** Class IV normal curve. ( $\alpha=0.64$ ,  $\beta=0.64$ ,  $\gamma=-1.0$ )

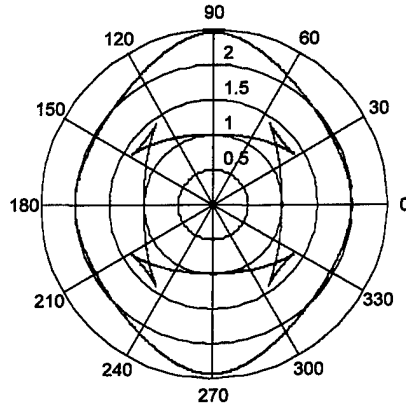


**Fig. 3.12.** Class V normal curve. ( $\alpha=4$ ,  $\beta=6$ ,  $\gamma=20$ )

The triangular portions or cusp in the wave front, lacunas, corresponding to the  $R_+$  branch, are artifacts of the normal curve inflection points. Much work has been devoted to understanding the consequences of the cuspidal portions of the wave fronts in anisotropic materials [23,44]. One of the more obvious consequences is that more than two wave arrivals exist in directions that intersect triangular portions of the wave front. For example, consider a material with a class two normal curve. An observer located along the  $x_3$  axis will experience 3 wave arrivals. The first arrival corresponds to the  $R_-$  branch of the slowness curve and the second and third arrivals correspond to the  $R_+$  branch of the slowness curve. Now consider a material with a class three normal curve. An observer along the  $x_3$  axis experiences only two arrivals, which is the case had the material been elastically isotropic. Thus, the observation direction in combination with the elastic constants dictate the behavior of the acoustic disturbance.

## CHAPTER 4

This chapter starts by developing a set of boundary conditions, which are equivalent to a thermoelastic point-source located at the bounding surface of a transversely isotropic 2-dimensional half-space. Since the inhomogeneous source term appears in the boundary conditions, implementing an equivalent set of boundary conditions is very convenient analytically. Theoretical expressions representing the out of plane displacements for waves propagation along the free surface, and waves propagation along the axis of material symmetry are presented. It is shown that for the epicentral case, the form of the solution depends strongly on the nature of the material anisotropy. The free surface and epicentral cases lend themselves to an analytic solution, which affords a detailed analysis of the solution procedure. The analysis presented in this chapter aids in the solution of problems of a more complicated nature presented in chapter 5.

### (4.1) *EQUIVALENT BOUNDARY CONDITIONS*

In order to correctly evaluate the elastic boundary conditions, Rose [5] considers the center of expansion to be buried some distance below the free surface. The source is then brought to the surface where it is shown to be equivalent to a shear stress dipole applied at the bounding surface. For an anisotropic half space, the procedure presented by Rose [5], is long and cumbersome owing to the fact that the shear and longitudinal deformations cannot be uncoupled.

As an alternative to considering a buried point-source, a method of images, Nowacki [38], will be used to aid in the development of a set of boundary conditions that are equivalent to a laser line-source located at the bounding surface. To understand the method of images, consider an infinite elastic medium. The medium is subjected to two line sources of opposite polarity as shown in Fig 4.1. The line source for this development is the 2-dimensional analogue of the source specification given in Eq. 2.33. The plane of separation formed by the  $x_2$  and  $x_3$  coordinate axis, is midway between the two sources and is perpendicular to the line joining the two sources. It should be noted that since the crystallographic axes coincide with the coordinate axes, the plane of separation is also a plane of isotropy. This type of arrangement will result in a nonzero shear stress state, and a zero normal stress state at the plane of separation. If we apply at the separation plane, a shear stress of opposite sign to the shear stress resulting from the source-sink combination, a stress-free state will be obtained at the separation plane. With the aid of the uniqueness theorem relating to a system of linear differential equations, the separation plane can now be identified with the stress free bounding surface of an elastic half space. It should be noted that no net thermal energy is transferred to the sample since the source and sink are of equal magnitude and opposite polarity. As a consequence, the total strain energy remains constant. This can be understood by noticing that the sink has reduced the strain energy of the system relative to a reference state by an amount equal to the increase in the strain energy of the system produced by the source.

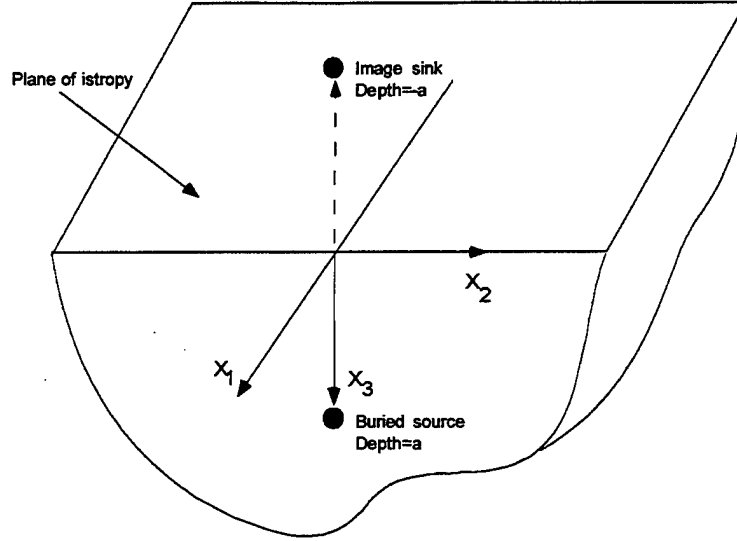


**Fig. 4.1.** Problem geometry with source and sink locations.

The elastic equations of motions in two dimensions are written as follows:

$$\begin{aligned} \beta u_{2,22} + u_{2,33} - u_{2,\tau\tau} + \kappa u_{3,23} &= F_{x_2(\text{real})} + F_{x_2(\text{image})} , \\ \kappa u_{2,23} + u_{3,22} + \alpha u_{3,33} - u_{3,\tau\tau} &= F_{x_3(\text{real})} + F_{x_3(\text{image})} , \end{aligned} \quad (4.1)$$

where the source-sink specification are given by

$$\begin{aligned} F_{x_2(\text{real})} &= F_2 \delta'(x_2) \delta(x_3 - a) H(\tau) , \\ F_{x_2(\text{image})} &= -F_2 \delta'(x_2) \delta(x_3 - a) H(\tau) , \\ F_{x_3(\text{real})} &= F_3 \delta(x_2) \delta'(x_3 - a) H(\tau) , \\ F_{x_3(\text{image})} &= -F_3 \delta(x_2) \delta'(x_3 - a) H(\tau) , \\ \delta'(x_i) &= \frac{d\delta(x_i)}{dx} , \end{aligned} \quad (4.2)$$

where  $F_2$  and  $F_3$  are

$$\begin{aligned} F_2 &= \frac{B_{22}T_0}{C_{44}}, \\ F_3 &= \frac{B_{33}T_0}{C_{44}}. \end{aligned} \quad (4.3)$$

The transformed equations of motion are expressed as

$$\begin{aligned} [-\beta\eta^2 - k^2 - s^2] \bar{u}_2(\eta, k, s) - \eta\kappa k \bar{u}_3(\eta, k, s) &= \frac{i\eta F_2}{s} (e^{-ika} - e^{ika}), \\ -\eta\kappa k \bar{u}_2(\eta, k, s) + [-\eta^2 - \alpha k^2 - s^2] \bar{u}_3(\eta, k, s) &= \frac{ikF_3}{s} (e^{-ika} - e^{ika}), \end{aligned} \quad (4.4)$$

where a bar denotes a transformed displacement. The Fourier-Laplace transform operator is defined as

$$\bar{u}_{2/3}(\eta, k, s) = \int_{-\infty}^{\infty} \int_{-\infty}^{\infty} \int_0^{\infty} u_{2/3}(x_2, x_3, \tau) e^{-(i\eta x_2 + ikx_3 + s\tau)} d\eta dk d\tau. \quad (4.5)$$

Now the equations can be uncoupled algebraically giving:

$$\begin{aligned}\bar{u}_2(\eta, \mathbf{k}, s) &= \frac{i\eta}{s} \left[ \frac{(F_2(\eta^2 + \alpha k^2 + s^2) - F_3 \kappa k^2)(e^{iak} - e^{-iak})}{\alpha k^4 + k^2((\alpha + 1)s^2 + \gamma \eta^2) + (\beta \eta^4 + (\beta + 1)s^2 \eta^2 + s^4)} \right], \\ \bar{u}_3(\eta, \mathbf{k}, s) &= \frac{ik}{s} \left[ \frac{(F_3(\beta \eta^2 + k^2 + s^2) - F_2 \eta^2 \kappa)(e^{iak} - e^{-iak})}{\alpha k^4 + k^2((\alpha + 1)s^2 + \gamma \eta^2) + (\beta \eta^4 + (\beta + 1)s^2 \eta^2 + s^4)} \right].\end{aligned}\quad (4.6)$$

The denominator in Eq. 4.6 can be identified with the equation for the slowness surface. Dependence on  $x_3$  is recovered using partial fractions and a table of integral transforms. The result is given by

$$\begin{aligned}\bar{u}_2(\eta, \mathbf{x}_3, s) &= \frac{i\eta}{2s(k_3^2 - k_1^2)} \left[ \frac{F_2(\eta^2 + s^2 + \alpha k_1^2) - F_3 \kappa k_1^2}{k_1} N_1(x_3) \right] - \\ &\quad \frac{i\eta}{2s(k_3^2 - k_1^2)} \left[ \frac{F_2(\eta^2 + s^2 + \alpha k_3^2) - F_3 \kappa k_3^2}{k_3} N_3(x_3) \right] \\ \bar{u}_3(\eta, \mathbf{x}_3, s) &= \frac{1}{2s(k_3^2 - k_1^2)} \left[ \frac{F_3(\beta \eta^2 + k_1^2 + s^2) - F_2 \eta^2 \kappa}{k_1} \left( \frac{d(N_1(x_3))}{dx_3} \right) \right] - \\ &\quad \frac{1}{2s(k_3^2 - k_1^2)} \left[ \frac{F_3(\beta \eta^2 + k_3^2 + s^2) - F_2 \eta^2 \kappa}{k_3} \left( \frac{d(N_3(x_3))}{dx_3} \right) \right]\end{aligned}\quad (4.7)$$

$$N_1(x_3) = e^{-k_1|x_3-a|} - e^{-k_1|x_3+a|}, \quad N_3(x_3) = e^{-k_3|x_3-a|} - e^{-k_3|x_3+a|},$$

where  $(k_1)^2$  and  $(k_3)^2$  are defined as the two roots of the biquadratic equation representing the slowness surface. It should be noted that the roots to the slowness surface can be complex. Borrowing notation used by Payton [23], crystals that exhibit elastic transverse isotropy can be divided into three categories according to the behavior of the displacements of these crystal classes along the symmetry axis.

These categories are listed below

- (i)  $(\alpha + \beta) < \gamma < (1 + \alpha\beta)$  ,  
(ii)  $(\beta + 1) < \gamma < (\alpha + \beta)$  and  $(\gamma^2 - 4\alpha\beta) < 0$  ,  
(iii)  $\gamma < (\beta + 1)$  and  $(\gamma^2 - 4\alpha\beta) < 0$  also  $\beta > \alpha$  .

(4.8)

For crystals belonging to the first category in Eq. 4.8, the roots of the slowness equation are purely imaginary. In addition, there are no cusps in the wave-front curves for class (i) crystals. The crystals belonging to categories (ii) and (iii) have complex roots and the wave-front curves for these crystals have cuspidal triangles. For class (iii) crystals, the triangular portion of the wave-front is centered on the symmetry axis. It will be shown, that for class (i) crystals, the solutions along the free surface or in the epicentral direction behave in a similar manner to isotropic materials. However, the evolution of the solution for class (ii) and (iii) crystals differs profoundly from their isotropic counterparts. It should be noted that this classification scheme given in this chapter, denoted by lower case Roman numerals, is different than the one presented in the previous chapter, denoted by upper case Roman numerals.

Notice that the displacement in the  $x_3$  direction contains the 1<sup>st</sup> derivative of  $N(x_3)$  and as a consequence, the sign of the displacement changes as an observer passes the source. This sign change is tantamount to a discontinuity. The  $x_2$  displacement is not discontinuous at the source as a function of  $x_3$ . In preparation for evaluating the stresses at the mid-plane between the source and sink, the displacement and the derivatives of displacements in Eq. 4.7 can be written as

$$\begin{aligned}
\bar{u}_2|_{x_3=0} &= \bar{u}_{3,3}|_{x_3=0} = 0, \\
\lim_{a \rightarrow 0} \left( \bar{u}_{2,3}|_{x_3=0} \right) &= \frac{i\eta}{s} (F_3 \kappa - F_2 \alpha), \\
\lim_{a \rightarrow 0} \left( \bar{u}_3|_{x_3=0} \right) &= \frac{-F_3}{s}.
\end{aligned} \tag{4.9}$$

Next the normal and shear stresses at the plane  $x_3 = 0$  are evaluated, giving

$$\begin{aligned}
\bar{\sigma}_{33}(\eta, 0, s) &= \alpha \bar{u}_{3,3}|_{x_3=0} + i\eta(\kappa - 1) \bar{u}_2|_{x_3=0} = 0, \\
\lim_{a \rightarrow 0} (\bar{\sigma}_{23}(\eta, 0, s)) &= \lim_{a \rightarrow 0} \left( \bar{u}_{2,3}|_{x_3=0} + i\eta \bar{u}_3|_{x_3=0} \right) = \frac{-i\eta}{s} (F_3 + F_2 \alpha - F_3 \kappa),
\end{aligned} \tag{4.10}$$

For isotropic medium,  $(1 + \alpha - \kappa) = 2$ .

Thus, the source and sink annihilate as they are moved to the plane of separation, leaving only a shear stress contribution at the  $x_3 = 0$  plane. A stress free condition can be achieved at the  $x_3 = 0$  plane, by applying a shear stress at the bounding surface of opposite sign to the one listed in Eq. 15. The equivalent shear stress boundary condition becomes

$$\begin{aligned}
(\sigma_{23})_{x_3=0} &= \tilde{F} \delta'(x_2) H(\tau) , \\
(\sigma_{33})_{x_3=0} &= 0 , \\
\tilde{F} &= (F_3 + F_2 \alpha - F_3 \kappa) .
\end{aligned} \tag{4.11}$$

#### (4.2) HALF SPACE SUBJECTED TO SHEAR STRESS DIPOLE

Now, a line source representation for laser generated ultrasound will be presented using the equivalent boundary conditions listed in Eq. 4.11. The equations of motion are written as

$$\begin{aligned}
\beta u_{2,22} + u_{2,33} - u_{2,\tau\tau} + \kappa u_{3,23} &= 0 , \\
\kappa u_{2,23} + u_{3,22} + \alpha u_{3,33} - u_{3,\tau\tau} &= 0 .
\end{aligned} \tag{4.12}$$

The transformed equations of motion are:

$$\begin{aligned}
\left[ -\beta \eta^2 + \frac{\partial^2}{\partial x_3} - s^2 \right] \left( \bar{u}_2(\eta, k, s) \right) + i \eta \kappa \left( \frac{\partial \bar{u}_3(\eta, k, s)}{\partial x_3} \right) &= 0 , \\
\eta \kappa \left( \frac{\partial \bar{u}_2(\eta, k, s)}{\partial x_3} \right) + \left[ -\eta^2 + \alpha \frac{\partial^2}{\partial x_3^2} - s^2 \right] \left( \bar{u}_3(\eta, k, s) \right) &= 0 .
\end{aligned} \tag{4.13}$$

Solutions to the system of homogenous differential equations are of the form:

$$\begin{aligned}
\bar{u}_2(\eta, x_3, s) &= A_1 e^{ik_1 x_3} + A_2 e^{ik_3 x_3} , \\
\bar{u}_3(\eta, x_3, s) &= A_3 e^{ik_1 x_3} + A_4 e^{ik_3 x_3} ,
\end{aligned} \tag{4.14}$$

where  $k_{1/3}$  are the physical roots to the slowness curve. Next, the following substitution will be made so as to facilitate the Cagniard [16] inversion technique:

$$k = s\zeta, \quad \eta = s\omega, \quad (4.15)$$

The denominator of Eq. 4.6 will be rewritten using the above substitutions,

$$\alpha\bar{\zeta}^4 + \bar{\zeta}^2((\alpha+1) + \gamma\omega^2) + (\beta\omega^4 + (\beta+1)\omega^2 + 1) = 0. \quad (4.16)$$

The four roots to the slowness curve may be written as

$$\begin{aligned} i\bar{\zeta}_1(\omega) &= \frac{[-((\alpha+1) - \gamma\omega^2) - \sqrt{\phi(\omega)}]^{1/2}}{\sqrt{2\alpha}} = i\zeta_1(\omega), \\ \bar{\zeta}_2(\omega) &= -\bar{\zeta}_1(\omega), \\ i\bar{\zeta}_3(\omega) &= \frac{[-((\alpha+1) + \gamma\omega^2) + \sqrt{\phi(\omega)}]^{1/2}}{\sqrt{2\alpha}} = i\zeta_3(\omega), \\ \bar{\zeta}_4(\omega) &= -\bar{\zeta}_3(\omega), \\ \phi(\omega) &= [\gamma\omega^2 + (\alpha+1)]^2 - 4\alpha[\beta\omega^4 + (\beta+1)\omega^2 + 1]. \end{aligned} \quad (4.17)$$

As a consequence of the branch cut locations that will be introduced shortly, we have

$$\zeta_1 > 0, \quad \zeta_3 > 0, \quad \zeta_2 < 0, \quad \zeta_4 < 0. \quad (4.18)$$

The coefficients  $A_3$  and  $A_4$  are not independent but are related by the fact that the above displacements must solve the equations of motion. By substituting both solutions into the transformed equations of motion, it can be shown:

$$\begin{aligned} A_1 &= A_3 \left[ \frac{\alpha \zeta_1^2 - \omega^2 - 1}{i\kappa\omega\zeta_1} \right], \\ A_2 &= A_4 \left[ \frac{\alpha \zeta_3^2 - \omega^2 - 1}{i\kappa\omega\zeta_3} \right]. \end{aligned} \quad (4.19)$$

The coefficients  $A_3$  and  $A_4$  are found by requiring the expressions for the displacement in Eq. 4.14 to satisfy the boundary conditions in Eq. 4.11,

$$\begin{aligned} A_3 &= \frac{\tilde{F}\zeta_1}{s(\zeta_1 - \zeta_3)D} \left[ \omega^2 \left[ \alpha \zeta_3^2 + (\kappa - 1)\omega^2 + (\kappa - 1) \right] \right] \\ A_4 &= \frac{-\tilde{F}\zeta_3}{s(\zeta_1 - \zeta_3)D} \left[ \omega^2 \left[ \alpha \zeta_1^2 + (\kappa - 1)\omega^2 + (\kappa - 1) \right] \right] \end{aligned} \quad (4.20)$$

$$D = \left[ 2(1 - \kappa)(\omega^4 + \omega^2) - (\gamma\omega^2 + \alpha)(\omega^2 + 1) - \alpha\zeta_1\zeta_3 \right]$$

where  $D$  is the Rayleigh denominator.

## (4.3) SOLUTIONS ALONG THE BOUNDING SURFACE

For displacements along  $x_3=0$ , the Cagniard integration path is along the imaginary  $\omega$  axis. This can be shown in detail by considering the  $u_3$  displacement for  $x_3=0$ . Operating on the  $u_3$  displacement with the inverse Fourier, and noting that  $\tilde{u}_3$  is even in  $\omega$ , gives

$$\bar{u}_3(x_2, 0, s) = \text{Re} \frac{1}{\pi} \int_0^{+\infty} \tilde{u}_3(\omega, s) d\omega ,$$

$$\tilde{u}_3(s, \omega) = \frac{-\tilde{F} \omega^2}{D} \left[ \alpha \zeta_1 \zeta_3 + (1 - \kappa)(\omega^2 + 1) \right] e^{i s \omega |x_2|} , \quad (4.21)$$

Cagniard Path  $\rightarrow i\omega|x_2| = \tau = \text{real} .$

The Cagniard path is the imaginary  $\omega$  axis. Before the Cagniard inversion can be performed, the branch points and singularities associated with  $\bar{u}_3$  must be identified.

Branch points for  $\xi(\omega)$  may arise in two distinct ways:

- 1.)  $\phi(\omega) = 0 ,$
  - 2.)  $\gamma\omega^2 + (\alpha + 1) \pm \sqrt{\phi(\omega)} = 0 .$
- (4.22)

Presently, only the inversion of  $u_3$  is being considered. Since  $u_3$  is an even function of  $\sqrt{\phi(\omega)}$ , branch points arising from (1) need not be considered. As a consequence, the solution technique for solutions along the bounding surface is the same for class

(i), class (ii) and class (iii) materials. If  $u_2$ , which is odd in  $\sqrt{\phi(\omega)}$ , were being examined and the crystal under consideration belonged to class (ii) or class (iii), then the branch points arising from (1) would be involved in the solution. The branch points originating from (2) are

$$\omega = \pm \frac{i}{\sqrt{\beta}}, \quad \omega = \pm i. \quad (4.23)$$

The branch cuts which make  $\zeta_1$ , and  $\zeta_3$  single-valued in the  $\omega$ -plane are shown in Fig. 4.2 and can be defined as

$$\begin{aligned} \text{for } \omega &= \frac{i}{\sqrt{\beta}}, \\ \sqrt{\omega^2 + 1/\beta} &= (R_1 R_2)^{1/2} e^{i(\theta_1 + \theta_2)/2}, \\ R_{1/2} &= |\omega \mp i / \sqrt{\beta}|, \\ \theta_{1/2} &= \arg(\omega \mp i / \sqrt{\beta}), \end{aligned} \quad (4.24)$$

or  $\omega = i$ ,

$$\begin{aligned} \sqrt{\omega^2 + 1} &= (R_3 R_4)^{1/2} e^{i(\theta_3 + \theta_4)/2}, \\ R_{3/4} &= |\omega \mp i|, \\ \theta_{3/4} &= \arg(\omega \mp i). \end{aligned}$$

The product,  $\zeta_1 \zeta_3$ , plays an important role in the Cagniard inversion process for  $u_3$ . With the branch cut so defined, the product,  $\zeta_1 \zeta_3$ , exhibits the following behavior along the imaginary  $\omega$  axis:

$$\begin{aligned}
 \zeta_1 \zeta_3 &= \sqrt{\frac{\beta(1/\beta - \omega^2)(1 - \omega^2)}{\alpha}} && \text{for } 0 \leq \omega_2 \leq 1/\sqrt{\beta}, \\
 \zeta_1 \zeta_3 &= i \sqrt{\frac{\beta(\omega^2 - 1/\beta)(1 - \omega^2)}{\alpha}} && \text{for } 1/\sqrt{\beta} \leq \omega_2 \leq 1, \\
 \zeta_1 \zeta_3 &= -\sqrt{\frac{\beta(\omega^2 - 1/\beta)(\omega^2 - 1)}{\alpha}} && \text{for } \omega_2 \geq 1.
 \end{aligned} \tag{4.25}$$

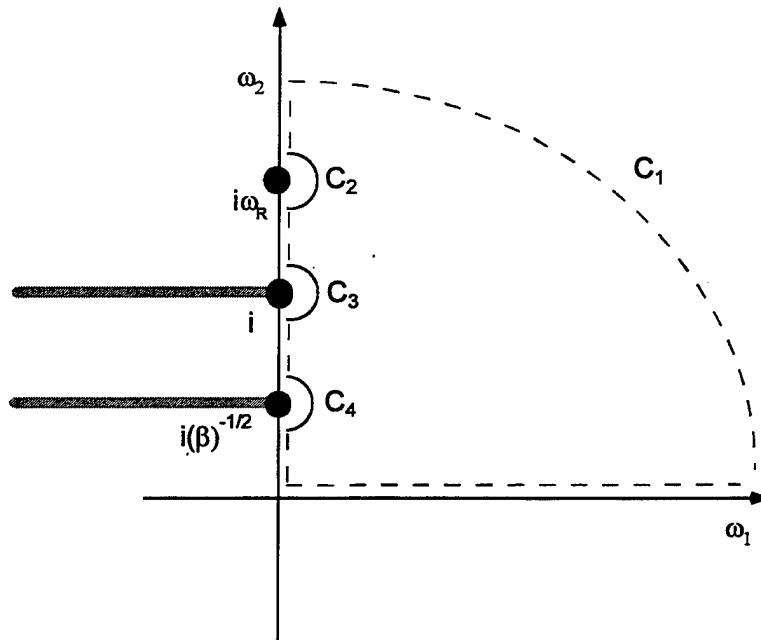


**Fig. 4.2.** Integration contour for the vertical displacement,  $u_3$ , at the bounding surface.

The singularities in the function  $D(\omega)$  will now be discussed. The branch points singularities for this function have been discussed above. Only pole singularities in

$D(\omega)$  need to be considered. After squaring and simplifying, the equation for  $D(\omega)=0$  yields:

$$\begin{aligned} a^2\omega^2 + a(a+2\alpha)\omega^4 + \alpha(2a+\alpha-\beta)\omega^2 + \alpha(\alpha-1) &= 0, \\ a &= 2\kappa - 2 + \gamma. \end{aligned} \quad (4.26)$$

The roots of interest will lie on the positive imaginary axis. The remaining roots will lie on the nonphysical sheets of the Riemann surface. The (Rayleigh) root of Eq. 4.26 will be denoted by  $D(\omega_r)=0$ . Now the integration contour and the subsequent inversion of the integral in Eq. 4.21 may be performed. Fig 4.2 shows the complex  $\omega$  plane along with the integration contour. The real axis is the Fourier inversion path and the imaginary axis is the Cagniard inversion path. Since the contour does not enclose any singularities, by Cauchy's theorem the closed path integral will vanish. The Fourier inversion may be written formally with the aid of Eq. 4.21 as

$$\text{Re} \left\{ \begin{aligned} &\int_0^{+\infty} \tilde{u}_3(s, \omega_1) d\omega + \int_{C_1} +P \int_{-\infty}^1 \tilde{u}_3(s, i\omega_2) id\omega + \left\{ \pi i (\text{residue @ } \omega = i\omega_r) \right\} + \\ &\int_{C_3} + \int_{1/1}^{1/\sqrt{\beta}} \tilde{u}_3(s, i\omega_2) id\omega + \int_{C_4} + \int_{1/\sqrt{\beta}}^0 \tilde{u}_3(s, i\omega_2) id\omega \end{aligned} \right\} = 0, \quad (4.27)$$

$$\tilde{u}_3(s, \omega) = \frac{-\tilde{F}\omega^2}{D} \left[ \alpha\zeta_1\zeta_3 + (1-\kappa)(\omega^2 + 1) \right] e^{i s \omega |x_3|},$$

where the first integral in Eq. 4.27 corresponds to the Fourier inversion path. The  $P$  in front of the third integral indicates that this integral is to be interpreted as a Cauchy

principal value integral. Before evaluating the second integral, the asymptotic expression for the transformed displacement as  $\omega \rightarrow \infty$  must be investigated:

$$\bar{u}_3(\eta, 0, s) \approx -\tilde{F} \frac{(\sqrt{\alpha\beta} + 1 - \kappa)}{s(2(1 - \kappa) - \gamma)}. \quad (4.28)$$

Thus,

$$\lim_{\omega \rightarrow \infty} (\omega \bar{u}_3(\omega)) = \left[ \omega s \left( -\tilde{F} \frac{i(\sqrt{\alpha\beta} + 1 - \kappa)}{2(1 - \kappa) - \gamma} \right) e^{i s \omega |y|} \right] = 0 \quad (4.29)$$

The above relation can be shown by considering that along  $C_1$ ,  $\omega$  has an imaginary component and as a consequence, the real part of the argument of the exponential is negative and increasing negatively. From Jordan's lemma, the second integral is zero. From Eq. 4.25, the product,  $\zeta_1 \zeta_3$ , is real for  $\omega \geq 1$  and  $0 \leq \omega \leq 1/\sqrt{\beta}$  and since  $D$  is an even function of  $\omega$ , the integrands associated with the 3rd and 8th integrals on the left hand side of Eq. 4.27 are imaginary. As a consequence,

$$\operatorname{Re} \left( \mathcal{P} \int_{\infty}^1 \tilde{u}_3(i\omega) i d\omega \right) = \operatorname{Re} \left( \int_{1/\sqrt{\beta}}^0 \tilde{u}_3(i\omega) i d\omega \right) = 0. \quad (4.30)$$

Using L'Hopital's Rule, it can be shown that

$$\lim_{\varepsilon \rightarrow 0} \left\{ \tilde{u}_3(i + \varepsilon e^{i\theta}) \right\} = \text{finite} . \quad (4.31)$$

In addition,

$$\lim_{\varepsilon \rightarrow 0} \left\{ \tilde{u}_3(i/\sqrt{\beta} + \varepsilon e^{i\theta}) \right\} = \text{finite} . \quad (4.32)$$

From Eq. 4.31 and Eq. 4.32, it follows that the 5th and 7th integrals on the left hand side of Eq. 4.27 are zero. The Fourier inversion for the out of plane displacement can now be written as:

$$\bar{u}_3(x_2, x_3, s) = \text{Re} \left\{ \pi i \psi_r \right\} + \int_1^{1/\sqrt{\beta}} \tilde{u}_3(i\omega) i d\omega , \quad (4.33)$$

$$\psi_r = \text{residue}(\tilde{u}(i\omega_r)) .$$

The residue associated with the simple pole at  $\omega = i\omega_r$  can be calculated with the aid of L'Hopital's rule:

$$\psi_r = \lim_{\omega \rightarrow i\omega_r} \left( (\omega - i\omega_r) \tilde{u}(\omega) \right) = \frac{X(\omega_r)}{\left( dD(\omega)/d\omega \right)_{\omega = i\omega_r}} , \quad (4.34)$$

where  $\psi_r$  can be written explicitly as

$$\psi_r = i s \omega_r \tilde{F} \left\{ \frac{(1 - \omega_r) [-2(1 - \kappa) \omega_r^2 + \gamma \omega_r^2 - \alpha + 1 - \kappa]}{D'(i \omega_r)} \right\} e^{-s \omega_r |y|},$$

$$dD(i \omega_r) / d\omega = 4(1 - \kappa)(-2\omega_r^2 + 1) - 2(-2\gamma + \gamma + \alpha) -$$

$$\frac{\alpha(\beta + 1) - 2\alpha\beta\omega_r^2}{(1 - \omega_r^2) [-2(1 - \kappa)\omega_r^2 + \gamma\omega_r^2 - \alpha]}.$$
(4.35)

Before performing the Laplace inversion of Eq. 4.33, it should be noted that the integrand of the second integral is complex. The real part of the integrand can be written as

$$\operatorname{Re}\{\bar{u}_3(i\omega)\} = \frac{-\tilde{F} \omega^2 \alpha \zeta_1 \zeta_3 [(1 - \kappa)(1 + 2\omega^2) - (\alpha + \gamma\omega^2)]}{[2(1 - \kappa)\omega^2 - \gamma\omega^2 - \alpha]^2 (1 + \omega^2) - \alpha(\beta\omega^2 + 1)}.$$
(4.36)

The Laplace inversion is further simplified by introducing the following change of variables:

$$\tau = \omega |x_2|,$$

$$d\omega = \frac{d\tau}{|x_2|}.$$
(4.37)

Now Eq. 4.33 will be operated on with the inverse Laplace operator giving

$$u_3(x_2, 0, \tau) = \tilde{F}(G(\tau)), \quad (4.38)$$

$$G(\tau) = \bar{\psi}_r \delta(\tau - \omega_r |x_2|) + \frac{g(\tau)}{|x_2| \pi} \left[ H(\tau - |x_2|/\sqrt{\beta}) - H(\tau - |x_2|) \right],$$

where  $g(\tau)$  is given by

$$g(\tau) = \frac{\tilde{F} T^2 \alpha \zeta_1 \zeta_3 \left[ (1 - \kappa)(1 - 2T^2) - (\alpha - \gamma T^2) \right]}{\left[ -2(1 - \kappa)T^2 + \gamma T^2 - \alpha \right]^2 (1 - T^2) + \alpha(\beta T^2 - 1)}, \quad (4.39)$$

$$T = \frac{\tau}{|x_2|}.$$

A typical displacement waveform generated using Eq. 4.37 is shown in Fig. 4.3.

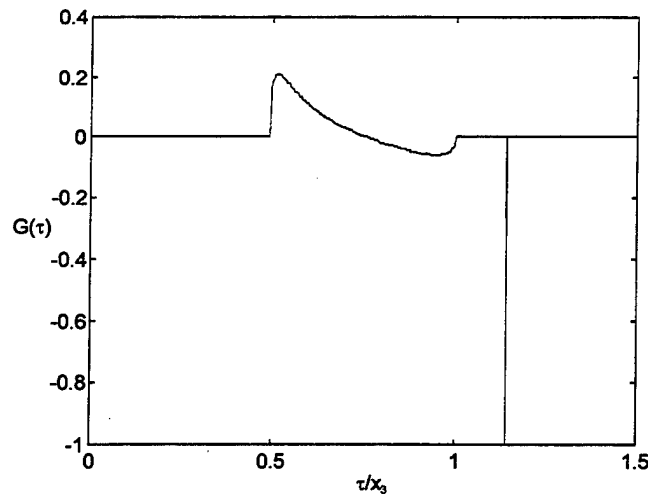


**Fig. 4.3.** Theoretical displacement for surface waves generated with a line source in zinc as a function of  $T$ . Delta function represented by vertical line at  $T=1.13$ .

Figure 4.3 demonstrates that the surface-skimming wave turns on at the longitudinal velocity and turns off at the shear wave velocity. The latter arriving Rayleigh wave

travels as a Dirac Delta function. The characteristics of the waveform for class (i), class (ii), and class (iii) materials are similar. The similarity is due to the fact that the contributions from the branch point corresponding to (1) in Eq. 4.22 do not effect the solution for the vertical displacement. The corresponding similarity for the in-plane displacement components does not exist. It should be noted, according to Eq. 4.38, the Rayleigh wave travels without geometric attenuation, while the surface-skimming wave, represented by  $g(\tau)$ , decreases in amplitude inversely with the distance from the source. This can be understood by first noting that the source doesn't allow energy to flow in the  $x_1$  direction. Thus since the Rayleigh wave is confined to the surface, the amplitude must remain constant. Conversely, the bulk wave, represented by  $g(\tau)$ , isn't confined to the surface, therefore, the amplitude must decrease with propagation distance.

#### (4.3) SOLUTIONS ALONG EPICENTRAL AXIS

Solutions along the epicentral axis form another class of solutions that can be inverted using the Cagniard technique. The location of the Cagniard path in the complex plane depends on the category of crystal being investigated, (see Eq. 4.8). For materials belonging to category (i), the Cagniard path is along the real  $\omega$  axis. For class (ii) and (iii) materials, the Cagniard path is off the real  $\omega$  axis. The formal solution for the vertical displacement along the epicentral axis is given as

$$\begin{aligned}\bar{u}_3(0, x_3, s) &= \frac{1}{2\pi} \int_{-\infty}^{\infty} \tilde{u}_3(\eta, x_3, s) s d\omega, \\ \tilde{u}_3(\eta, x_3, s) &= A_3 e^{-\zeta_1 x_3 s} + A_4 e^{-\zeta_3 x_3 s}.\end{aligned}\quad (4.40)$$

The coefficients,  $A_3$  and  $A_4$ , are defined in Eq. 4.20. Since the roots to the slowness equations,  $\zeta_1$ , and  $\zeta_3$  are even functions of  $\omega$ ,  $\bar{u}_3(\eta, x_3, s)$  is even in  $\omega$ , thus

$$\bar{u}_3(0, x_3, s) = \frac{1}{\pi} \operatorname{Re} \left\{ \int_0^{\infty} A_3 e^{-\zeta_1 x_3 s} s d\omega + \int_0^{\infty} A_4 e^{-\zeta_3 x_3 s} s d\omega \right\}.\quad (4.41)$$

In what follows it will be convenient to make the following substitution,

$$\begin{aligned}\varpi &= \omega^2, \\ \bar{u}_3(0, x_3, s) &= \frac{1}{\pi} \operatorname{Re} \{ I_1 + I_3 \}, \\ I_1 &= \int_0^{\infty} \bar{A}_3 e^{-\zeta_1 x_3 s} d\varpi, \quad I_3 = \int_0^{\infty} \bar{A}_4 e^{-\zeta_3 x_3 s} d\varpi, \\ \bar{A}_{3/4} &= \frac{A_{3/4} s}{2\sqrt{\varpi}}\end{aligned}\quad (4.42)$$

The substitution given in Eq. 4.42 consolidates the branch cuts along the real and imaginary axes so they both lie on the real axis. The expressions for the slowness surface given in Eq. 4.17 now take the form,

$$\begin{aligned}
\zeta_1(\omega) &= \frac{[-((\alpha+1)+\gamma\omega) - \sqrt{\phi(\omega)}]^{1/2}}{\sqrt{2\alpha}}, \\
\zeta_2(\omega) &= -\zeta_1(\omega), \\
\zeta_3(\omega) &= \frac{[-((\alpha+1)s + \gamma\omega) + \sqrt{\phi(\omega)}]^{1/2}}{\sqrt{2\alpha}}, \\
\zeta_4(\omega) &= -\zeta_3(\omega), \\
\phi(\omega) &= [\gamma\omega + (\alpha+1)]^2 - 4\alpha[\beta\omega^2 + (\beta+1)\omega + 1].
\end{aligned} \tag{4.43}$$

The Cagniard path for the first integral in Eq. 4.41 is defined by

$$\begin{aligned}
\zeta_1(\omega)x_3 &= \tau, \\
\tau &= \text{real and positive}.
\end{aligned} \tag{4.44}$$

#### (4.3.1) SOLUTION FOR CLASS (i) MATERIALS

For class (i) materials, the above condition on  $\tau$  is met for real  $\omega$ , giving the positive real  $\omega$  axis as the Cagniard contour. Squaring Eq. 4.43 twice and solving for  $\omega$  in terms of  $\tau$  gives

$$\begin{aligned}\varpi_{1/3} &= \frac{-B \pm \sqrt{B^2 - 4AC}}{2A}, \\ A &= \beta, \\ B &= \beta + 1 - \gamma \left( \frac{\tau^2}{x_3^2} \right), \\ C &= 1 - (\alpha + 1) \left( \frac{\tau^2}{x_3^2} \right) - \alpha \left( \frac{\tau^4}{x_3^4} \right).\end{aligned}\tag{4.45}$$

Changing variables from  $\varpi$  to  $\tau$  results in

$$\bar{u}_3(0, x_3, s) = \frac{1}{\pi} \operatorname{Re} \left\{ \int_1^{\infty} \bar{A}_3 e^{-s\tau} \frac{\partial \varpi_3}{\partial \tau} d\tau + \int_{1/\sqrt{\alpha}}^{\infty} \bar{A}_4 e^{-s\tau} \frac{\partial \varpi_1}{\partial \tau} d\tau \right\}.\tag{4.46}$$

Operating on the expression for the vertical displacement given in Eq. 4.46 with the inverse Laplace operator gives

$$\bar{u}_3(0, x_3, \tau) = \frac{1}{\pi} \operatorname{Re} \left[ \bar{A}_3 \frac{\partial \varpi_3}{\partial \tau} H(\tau - 1) + \bar{A}_4 \frac{\partial \varpi_1}{\partial \tau} H(\tau - 1/\sqrt{\alpha}) \right].\tag{4.47}$$

The displacement waveform, for Beryl, shown in Fig. 4.4 has characteristics similar to the displacement waveform for an isotropic material, Fig. 4.5. Both waveforms show the presence of two distinct wave arrivals. However, a close comparison between Fig. 4.4 and 4.5 show that the decay of the pulse tails is somewhat altered by the introduction of anisotropy.

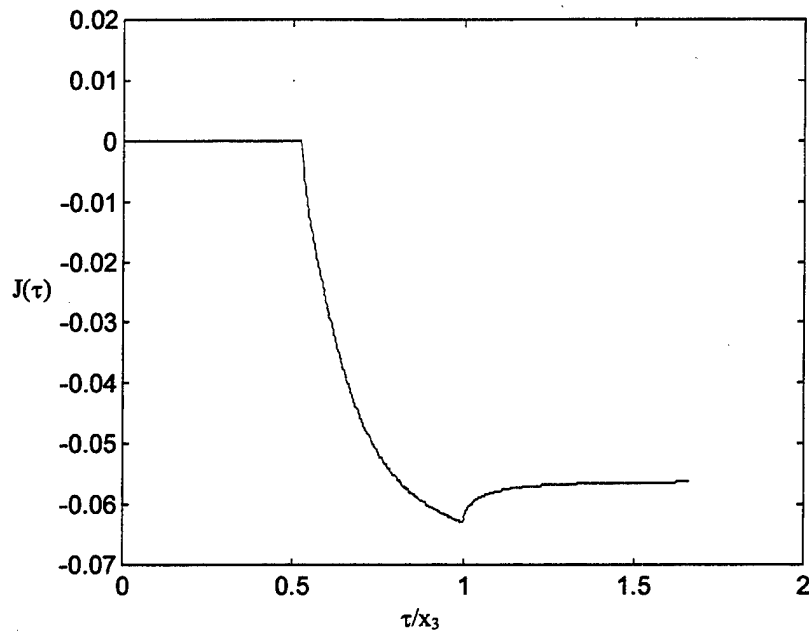


**Fig. 4.4.** Theoretical displacement for the epicentral wave generated with a line source in Beryl.

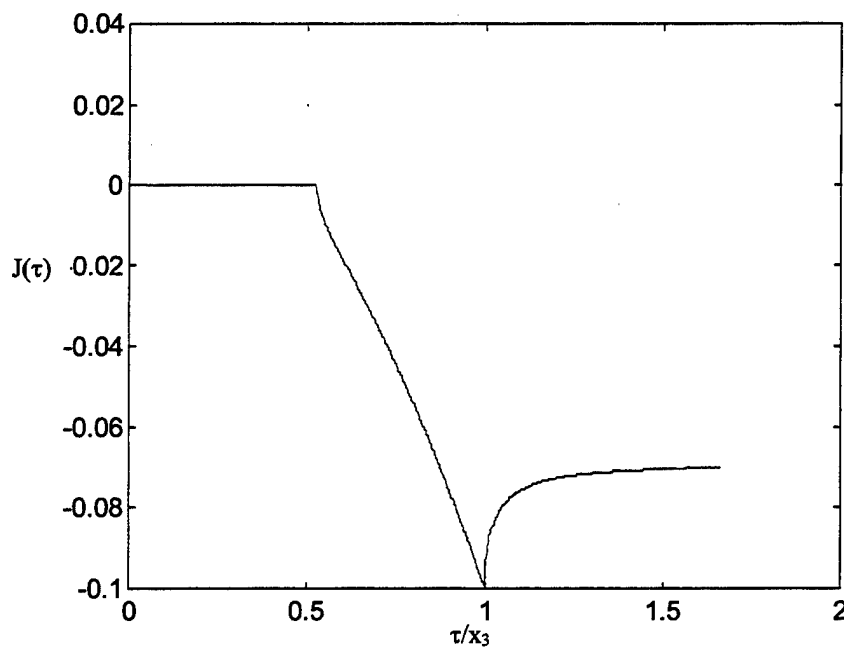


**Fig. 4.5.** Theoretical displacement for the epicentral wave generated with a line source in an isotropic material (polycrystalline aluminum).

## (4.3.2) SOLUTION FOR CLASS (ii) AND (iii) MATERIALS

For class (ii) and (iii) materials, the Cagniard path no longer lies on the real  $\omega$  axis. Before embarking on the solution for these materials, the location of the branch points must be investigated. As was the case for solutions along  $x_3=0$ , branch points associated with  $\zeta(\omega)$  may occur in two ways,

$$\begin{aligned} 1.) \quad \phi(\omega) &= 0, \\ 2.) \quad \gamma\omega + (\alpha + 1) \pm \sqrt{\phi(\omega)} &= 0. \end{aligned} \tag{4.48}$$

In contrast to the surface wave case, the expression for  $\bar{u}_3$  for the epicentral case is an odd function of  $\sqrt{\phi(\omega)}$ , and as a consequence, the branch points arising from (1), Eq. 4.44, need to be considered in addition to the branch points arising from (2). The expression for  $\sqrt{\phi(\omega)}$  may be rewritten as

$$\sqrt{\phi(\omega)} = \sqrt{(\gamma^2 - 4\alpha\beta)(\omega - \omega_+)(\omega - \omega_-)}, \tag{4.49}$$

where

$$\omega_{\pm} = \frac{-[\gamma(\alpha + 1) - 2\alpha(\beta + 1)] \mp \sqrt{4[\alpha(\alpha + \beta - \gamma)(\alpha + \alpha\beta - \gamma)]}}{(\gamma^2 - 4\alpha\beta)}. \tag{4.50}$$

Thus  $\sqrt{\phi(\omega)}$  will have branch points on the real  $\omega$  axis at  $\omega = \omega_{\pm}$ . Branch points arising from (2) are located on the real  $\omega$  axis  $\omega = -1$  and  $\omega = -1/\beta$ . If we take zinc, for example,  $\zeta_1$  will have branch points at  $\omega = \omega_-$  and  $\omega = \omega_+$  while  $\zeta_3$  will have branch points at  $\omega = \omega_-$ ,  $\omega = \omega_+$ ,  $\omega = -1$ , and  $\omega = -1/\beta$ . The Cagniard path for the first integral is again defined by Eq. 4.44, but  $\omega$  is now a complex variable given by

$$\omega = \omega_1 + i\omega_2 . \quad (4.51)$$

Substituting Eq. 4.51 into Eq. 4.44, and squaring twice to eliminate the radicals and equating the real and imaginary part of the equation gives

$$\begin{aligned} \gamma\tau^2\omega_1 + (\alpha+1)\tau^2 - \alpha\tau^4 &= \beta(\omega_1^2 - \omega_2^2) + (\beta+1)\omega_1 + 1 , \\ \gamma\tau^2\omega_2 &= 2\beta\omega_1\omega_2 + (\beta+1)\omega_2 . \end{aligned} \quad (4.52)$$

The second equation of Eqs. 4.52 is satisfied if  $\omega_2=0$ . Since the branch points, for class (ii) and (iii) materials, lie on the real axis, the first of Eqs. 4.52 imposes the additional constraint

$$\begin{aligned} \omega_- \leq \omega_1 \leq \omega_+ & \quad \text{for } \zeta_1(\omega) , \\ -1/\beta \leq \omega_1 \leq \omega_+ & \quad \text{for } \zeta_3(\omega) . \end{aligned} \quad (4.53)$$

If  $\varpi_2 \neq 0$ , then  $\varpi_2$  and  $\varpi_1$  can be expressed in terms of the parameter  $T_3$  as follows

$$\begin{aligned}\varpi_1(T_3) &= \frac{\gamma\tau^2 - (\beta+1)}{2\beta}, \\ \varpi_2(T_3) &= \frac{\sqrt{4\alpha\beta - \gamma^2}(\tau^2 - \tau_-^2)(\tau^2 - \tau_+^2)}{2\beta},\end{aligned}\tag{4.54}$$

where

$$\tau_{\pm}^2 = \frac{-[\gamma(\beta+1) - 2\beta(\alpha+1)] \pm \sqrt{4\beta(\alpha+\beta-\gamma)(1+\alpha\beta-\gamma)}}{(4\alpha\beta - \gamma^2)}.\tag{4.55}$$

The parametric expressions given in Eq. 4.54 map out a hyperbola in the complex  $\varpi$  plane that intersects the real  $\varpi$  axis at

$$\varpi_{\pm} = \frac{\gamma(\alpha+1) - 2\alpha(\beta+1) \pm \sqrt{\frac{\gamma^2}{\beta}(\alpha+\beta-\gamma)(\alpha+\alpha\beta-\gamma)}}{(4\alpha\beta - \gamma^2)}.\tag{4.56}$$

Using zinc as an example, the Cagniard paths for  $\zeta_1$ , and  $\zeta_2$  are shown in Fig. 4.6.

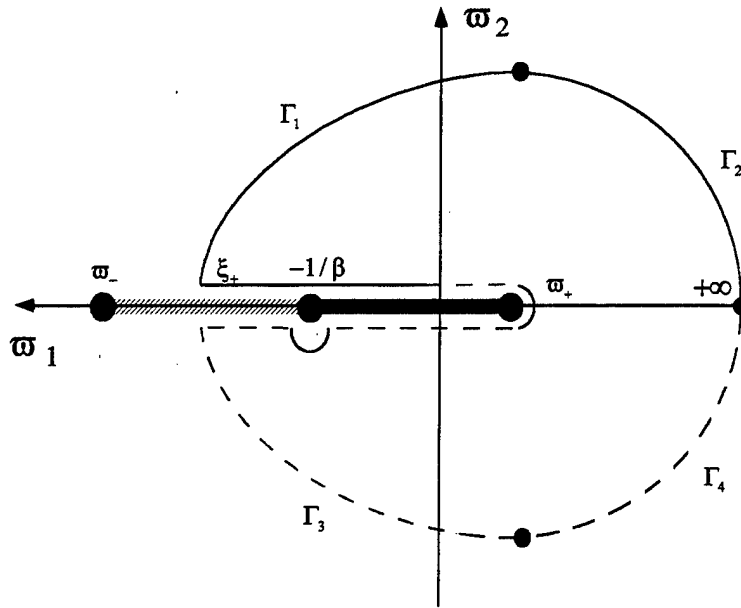


**Fig 4.6.** Cargniard contour for zinc. Solid line represents contour corresponding to  $\zeta_1$  and the dashed line represents the contour corresponding to  $\zeta_1$ .

The expression for  $I_1$  listed in Eq. 4.42 may be rewritten as

$$\begin{aligned}
 I_1 &= \int_{\tau_0}^{\tau_+} I_{11} + \int_{\Gamma_1} I_{11} + \int_{\Gamma_2} I_{11} , \\
 I_{11} &= \bar{A}_3 e^{-s\tau} \frac{\partial \omega}{\partial \tau} , \\
 \tau_0 &= \sqrt{\frac{(\alpha+1) - \sqrt{(\alpha+1)^2 - 4\alpha}}{2}} .
 \end{aligned} \tag{4.57}$$

Investigation of the first integral in Eq. 4.57 shows

$$\int_{\tau_0}^{\tau_+} I_{11} = \int_{\tau_0}^{\tau_+} \bar{A}_3 e^{-s\tau} \frac{\partial \varpi}{\partial \tau} d\tau ,$$

$$\varpi(\tau) = \xi(\tau) = (-)\text{real} ,$$

$$\bar{A}_3 = (\text{imaginary}) .$$
(4.58)

Thus,  $I_{11}$  is purely imaginary and does not contribute to the epicentral displacement.

The second integral in Eq. 4.57 can be written as

$$\int_{\Gamma_1} I_{11} = \int_{\Gamma_1} \bar{A}_3 e^{-s\tau} \frac{\partial \varpi}{\partial \tau} d\tau ,$$

$$\varpi \text{ is taken along } \Gamma_1 .$$
(4.59)

The third integral in Eq. 4.57 vanishes, since

$$\int_{\Gamma_2} I_{11} \rightarrow 0 \text{ as } |\varpi| \rightarrow \infty .$$
(4.60)

This completes the inversion for the  $\zeta_1$  portion of the Cagniard contour. The contour for  $\zeta_1$  is represented in Fig. 4.6 by the dashed line. The expression for  $I_3$  given in Eq. 4.42 may be rewritten as

$$\begin{aligned}
I_3 &= \int_{\tau_0}^{\tau_e} I_{33} + \oint_{\omega_+} I_{33} + \int_{\tau_e}^{\tau_0} I_{33} + \int_{\tau_0}^{\tau_+} I_{33} + \int_{\Gamma_3} I_{33} + \int_{\Gamma_4} I_{33} , \\
I_{33} &= \bar{A}_4 e^{-s\tau} \frac{\partial \varpi}{\partial \tau} d\tau , \\
\tau_e &= \sqrt{\frac{-B + \sqrt{B^2 - 4\alpha C}}{2\alpha}} , \\
B &= -(\omega_+ \gamma + \alpha + 1) , \\
C &= \omega_+^2 \beta + \omega_+ (\beta + 1) + 1 .
\end{aligned} \tag{4.61}$$

Before continuing with the inversion of  $I_3$ , the character of  $\sqrt{\phi(\varpi)}$  as the contour passes to the lower half plane at  $\omega_+$  must be investigated. The expression,  $\sqrt{\phi(\varpi)}$ , can be written as

$$\begin{aligned}
\sqrt{\phi(\varpi)} &= \sqrt{|\phi(\varpi)|} e^{i\theta/2} , \\
\theta &= \arg(\phi(\varpi)) .
\end{aligned} \tag{4.62}$$

As the contour travels around the branch point,  $\theta$  changes by  $2\pi$  causing the real part  $\sqrt{\phi(\varpi)}$  to change sign. As the contour continues from  $\omega_+$  to  $\tau_0$ , the imaginary part of  $\sqrt{\phi(\varpi)}$  remains zero and as a consequence,  $\sqrt{\phi(\varpi)} \rightarrow -\sqrt{\phi(\varpi)}$  as the contour proceeds to the lower half plane. Thus, after transversing the branch point at  $\omega_+$ ,  $\zeta_3 \rightarrow \zeta_1$  and  $\bar{A}_4 \rightarrow \bar{A}_3$ . The first integral in Eq. 4.61 can be written as

$$\int_{\tau_e}^{\tau_0} I_{33} = \int_{\tau_e}^{\tau_0} \bar{A}_4 e^{-s\tau} \frac{\partial \varpi}{\partial \tau} d\tau , \tag{4.63}$$

where the expression for  $\varpi(\tau)$  along the real axis is obtained by solving the first of Eqs. 4.51,

$$\begin{aligned}\varpi_2 &= 0, \\ \varpi_1 &= \frac{-B \pm \sqrt{B^2 - 4AC}}{2A}, \\ A &= \beta, \\ B &= \beta + 1 - \gamma T^2, \\ C &= 1 + \alpha T^4 - (\alpha + 1)T^2.\end{aligned}\tag{4.64}$$

Since the portion of the real  $\varpi$  axis of interest is to the right of  $\varpi_+$ , the positive sign in front of the radical in Eq. 4.64 will be taken. The second integral in Eq. 4.61 is zero since,

$$\oint_{\varpi_+} I_{33} \rightarrow 0 \text{ as } |\varpi| \rightarrow 0.\tag{4.65}$$

The third integral in Eq. 4.61 can be written as

$$\int_{\tau_e}^{\tau_o} I_{33} = - \int_{\tau_e}^{\tau_o} A_3 e^{-s\tau} \frac{\partial \varpi}{\partial \tau} d\tau,$$

$\varpi$  is taken along real axis .

(4.66)

The fourth integral in Eq. 4.61 does not contribute to the epicentral displacement since

$$\int_{\tau_0}^{\tau_+} I_{33} = - \int_{\tau_0}^{\tau_+} \bar{A}_3 e^{-s\tau} \frac{\partial \varpi}{\partial \tau} d\tau ,$$

$$\varpi(\tau) = \xi(\tau) = (-)\text{real} , \quad (4.67)$$

$$\bar{A}_3 = (\text{imaginary}) .$$

The fifth integral in Eq. 4.61 is written as

$$\int_{\Gamma_3} I_{33} = - \int_{\Gamma_3} \bar{A}_4 e^{-s\tau} \frac{\partial \varpi}{\partial \tau} d\tau , \quad (4.68)$$

$\varpi$  is taken along  $\Gamma_3$  .

The last integral in Eq. 4.61 vanishes since

$$\int_{\Gamma_2} I_{11} \rightarrow 0 \text{ as } |\varpi| \rightarrow \infty . \quad (4.69)$$

Applying the inverse Laplace transform operator to Eq. 4.57 and Eq. 4.61 gives

$$u(0, x_3, \tau) = \bar{A}_4 \left( \frac{\partial \varpi_{1 \rightarrow 2}}{\partial \tau} \right) \{H(\tau - \tau_e) - H(\tau - \tau_0)\} +$$

$$\bar{A}_3 \left( \frac{\partial \varpi_{2 \rightarrow 3}}{\partial \tau} \right) \{H(\tau - \tau_L) - H(\tau - \tau_e)\} + \bar{A}_4 \left( \frac{\partial \varpi_{3 \rightarrow 4}}{\partial \tau} \right) \{H(\tau - \tau_p)\} . \quad (4.70)$$

A plot of the theoretical epicentral displacement for zinc is given in Fig 4.7. The character of the epicentral waveform for zinc is considerably different that it's isotropic counterpart, shown in Fig. 4.4. The arrivals of the various waves in Fig. 4.7 is best understood by referencing the portion of the wavefront curve that pierces the symmetry axis, Fig. 4.8. The first wave arrival corresponds to the longitudinal branch of the wavefront curve. The solution gives zero for the portion of the wave the corresponds to the interior of the cuspidal triangle. The majority of the acoustic

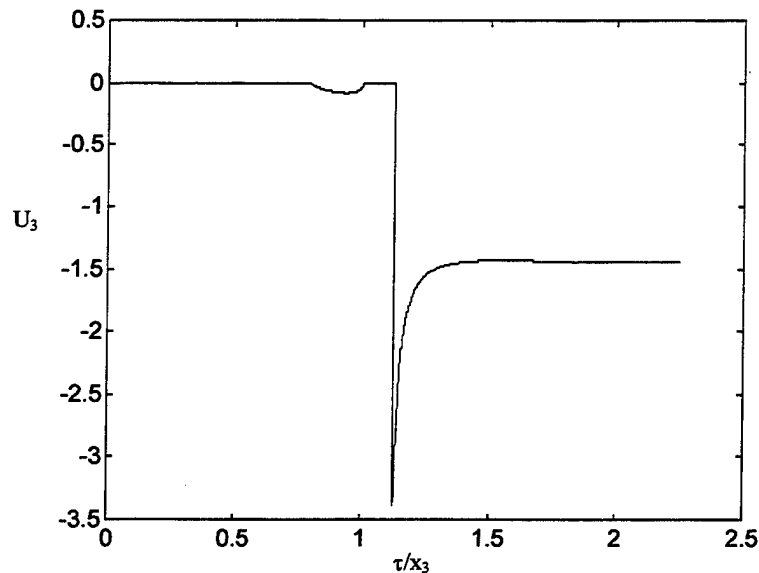


**Fig. 4.7.** Theoretical displacement for epicentral wave generated with a line source in zinc as a function of  $T$ .

energy arrives in the form of a reciprocal square root singularity at a time corresponding to the apex of the cuspidal triangle. The presence of the square root singularity in the epicentral waveform for zinc is an artifact of the conical point on the wavefront and is commonly referred to as phonon focusing, [45].

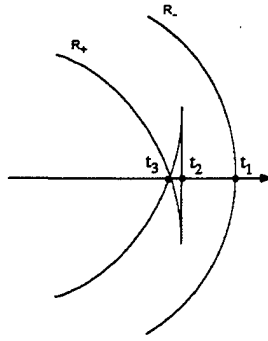


**Fig. 4.8.** Enlargement of portion of wavefront intersecting the symmetry axis for zinc.

#### (4.4) 3-DIMENSIONAL HALF-SPACE

The procedure for finding the equivalent boundary conditions for the 3-dimensional case follows the 2-dimensional case. The transformed solution for the 3-dimensional equations of motions, 2.33, is given by

$$\begin{aligned} \bar{u}_1(\chi, \eta, x_3, s) &= \frac{i\chi}{2s(k_3^2 - k_1^2)} \left[ \frac{F_2(t^2 + s^2 + \alpha k_1^2) - F_3 \kappa k_1^2}{k_1} N_1(x_3) \right] - \\ & \frac{i\chi}{2s(k_3^2 - k_1^2)} \left[ \frac{F_2(t^2 + s^2 + \alpha k_3^2) - F_3 \kappa k_3^2}{k_3} N_3(x_3) \right], \\ \bar{u}_2(\chi, \eta, x_3, s) &= \frac{i\eta}{2s(k_3^2 - k_1^2)} \left[ \frac{F_2(t^2 + s^2 + \alpha k_1^2) - F_3 \kappa k_1^2}{k_1} N_1(x_3) \right] - \\ & \frac{i\eta}{2s(k_3^2 - k_1^2)} \left[ \frac{F_2(t^2 + s^2 + \alpha k_3^2) - F_3 \kappa k_3^2}{k_3} N_3(x_3) \right], \\ \bar{u}_3(\chi, \eta, x_3, s) &= \frac{1}{2s(k_3^2 - k_1^2)} \left[ \frac{F_3(\beta t^2 + k_1^2 + s^2) - F_2 t^2 \kappa}{k_1} \left( \frac{d(N_1(x_3))}{dx_3} \right) \right] - \\ & \frac{1}{2s(k_3^2 - k_1^2)} \left[ \frac{F_3(\beta t^2 + k_3^2 + s^2) - F_2 t^2 \kappa}{k_3} \left( \frac{d(N_3(x_3))}{dx_3} \right) \right], \\ N_1(x_3) &= e^{-ik_1|x_3-a|} + e^{-k_1|x_3+a|}, \end{aligned} \quad (4.71)$$

where,  $\chi$  is the Fourier transform parameter for the  $x_1$  coordinate and  $t^2 = \chi^2 + \eta^2$ . The equivalent stress boundary conditions are obtained by substituting the displacement equations, Eq. 4.71, into Eq. 2.35, and evaluating the stresses at the bounding surface.

$$\begin{aligned} (\sigma_{13})_{x_3=0} &= \tilde{F} \delta'(x_1) \delta(x_2) H(\tau) , \\ (\sigma_{23})_{x_3=0} &= \tilde{F} \delta'(x_2) \delta(x_1) H(\tau) , \\ (\sigma_{33})_{x_3=0} &= 0 , \\ \tilde{F} &= (F_3 + F_2 \alpha - F_3 \kappa) . \end{aligned} \tag{4.72}$$

The stresses given in Eq. 4.72 has the same functional form as the equivalent stress boundary conditions given by Rose [5]. The pre-multiplier,  $\tilde{F}$ , is a function of the elastic constants for the anisotropic case and independent of the elastic constants for the isotropic case. The value of  $\tilde{F}$  for various materials is given in Table 4.1.

**Table 4.1.** Shear stress pre-multiplier for various transversely isotropic materials.

| CRYSTAL   | $\alpha$                      | $\beta$ | $\gamma$ | $\tilde{F}$ |
|-----------|-------------------------------|---------|----------|-------------|
| Beryl     | 3.62                          | 4.11    | 11.81    | 2.60        |
| Ice       | 4.57                          | 4.26    | 13.51    | 2.93        |
| Titanium  | 3.88                          | 3.47    | 8.31     | 2.40        |
| Zinc      | 1.57                          | 4.17    | 2.40     | 0.30        |
| Cadmium   | 2.62                          | 5.95    | 6.80     | 0.49        |
| Isotropic | $\alpha = \beta = \gamma / 2$ |         |          | 2           |

The solution procedure for a 3-dimensional half-space with the boundary conditions given by Eq. 4.72 starts by considering transformed homogeneous equations of motion

$$\begin{aligned}
 & \left[ -\beta\chi - \delta\eta + D^2 - s^2 \right] \bar{u}_1 - (\beta - \delta)\chi\eta\bar{u}_2 + i\kappa\chi D\bar{u}_3 = 0 , \\
 & -(\beta - \delta)\chi\eta\bar{u}_1 + \left[ -\delta\chi - \beta\eta + D^2 - s^2 \right] \bar{u}_2 + i\eta\kappa D\bar{u}_3 = 0 , \\
 & i\kappa\chi D\bar{u}_1 + i\eta\kappa D\bar{u}_2 + \left[ -\chi^2 - \eta^2 + \alpha D^2 - s^2 \right] \bar{u}_3 = 0 , \\
 & D = \frac{\partial}{\partial x_3} .
 \end{aligned} \tag{4.73}$$

The solutions to the homogeneous equations of motion will have the form

$$\bar{u}_i = B_i e^{ikx_3} . \tag{4.74}$$

Substituting Eq. 4.74 into Eq. 4.73 gives the matrix equation

$$A \bullet B = 0 , \tag{4.75}$$

where

$$A = \begin{bmatrix}
 -\beta\chi - \delta\eta - k^2 - s^2 & -(\beta - \delta)\chi\eta & -\kappa\chi k \\
 -(\beta - \delta)\chi\eta & -\delta\chi - \beta\eta - k^2 - s^2 & -\eta\kappa k \\
 -\kappa\chi k & -\eta\kappa k & -\chi^2 - \eta^2 - \alpha k^2 - s^2
 \end{bmatrix} . \tag{4.76}$$

For a non-trivial solution to exist, the determinate of [A] must vanish giving

$$\left[ k^2 + \delta(\chi^2 + \eta^2) + s^2 \right] \left[ \alpha k^4 + k^2((\alpha + 1)s^2 + \gamma(\chi^2 + \eta^2)) + \beta(\chi^2 + \eta^2)^2 + (\beta + 1)(\chi^2 + \eta^2)s^2 + s^4 \right] = 0. \quad (4.77)$$

The six roots of Eq. 4.76 are written as

$$\begin{aligned} k_1 &= \frac{\left[ -(\alpha + 1)s^2 - \gamma(\chi^2 + \eta^2) + \sqrt{\phi(\chi, \eta)} \right]^{1/2}}{\sqrt{2\alpha}}, \\ k_2 &= -k_1, \\ k_3 &= \frac{\left[ -(\alpha + 1)s^2 - \gamma(\chi^2 + \eta^2) - \sqrt{\phi(\chi, \eta)} \right]^{1/2}}{\sqrt{2\alpha}}, \\ k_4 &= -k_3, \\ \phi(\chi, \eta) &= \left[ \gamma(\chi^2 + \eta^2) + (\alpha + 1) \right]^2 - 4\alpha \left[ \beta(\chi^2 + \eta^2)^2 + (\beta + 1)(\chi^2 + \eta^2) + 1 \right]. \end{aligned} \quad (4.78)$$

It will be shown that along the Cagniard Path, the k-roots satisfy

$$\begin{aligned} \text{Im}(k_i) &< 0, & i = 1, 3, 5 \\ \text{Im}(k_i) &> 0, & i = 2, 4, 6. \end{aligned} \quad (4.79)$$

Thus,  $k_2$ ,  $k_4$  and  $k_6$  represent the physical roots. Using the first two equations in Eq.

4.75, the eigenvectors for  $k_2$  and  $k_4$  are given as follows

$$\begin{aligned}
B_1(k_\alpha) &= B_3(k_\alpha) \bar{A}_{13}(k_\alpha) , \\
B_2(k_\alpha) &= B_3(k_\alpha) \bar{A}_{23}(k_\alpha) , \\
\bar{A}_{13}(k_\alpha) &= \frac{[A_{12}(k_\alpha)A_{23}(k_\alpha) - A_{13}(k_\alpha)A_{22}(k_\alpha)]}{[A_{22}(k_\alpha)A_{11}(k_\alpha) - A_{21}(k_\alpha)A_{12}(k_\alpha)]} , \\
\bar{A}_{23}(k_\alpha) &= \frac{[A_{21}(k_\alpha)A_{13}(k_\alpha) - A_{23}(k_\alpha)A_{11}(k_\alpha)]}{[A_{22}(k_\alpha)A_{11}(k_\alpha) - A_{21}(k_\alpha)A_{12}(k_\alpha)]} , \\
\alpha &= 1, 2 .
\end{aligned} \tag{4.80}$$

The second two equations of Eq. 4.75 are used to define the eigenvector corresponding to  $k_6$  since the first two equations are linearly independent for  $k_6$ . The resulting eigenvector is given by

$$\begin{aligned}
B_1(k_6) &= B_2(k_6) \bar{A}_{12}(k_6) , \\
B_3(k_6) &= 0 , \\
\bar{A}_{12}(k_6) &= \frac{[A_{32}(k_6)A_{23}(k_6) - A_{33}(k_6)A_{22}(k_6)]}{[A_{23}(k_6)A_{31}(k_6) - A_{21}(k_6)A_{33}(k_6)]} .
\end{aligned} \tag{4.81}$$

It should be noted that  $B_3(k_6)=0$  stems from the fact that  $u_3$  satisfies a fourth order differential equation while  $u_1$  and  $u_2$  require a sixth order operator to describe their motion. The component  $B_3(k_i)$  is found by satisfying the boundary conditions.

Using Eq. 4.80 and Eq. 4.81 in Eq. 4.72 gives

$$\begin{aligned}
B_3(k_2)[i\chi + \bar{A}_{13}(k_2)] + B_3(k_4)[i\chi + \bar{A}_{13}(k_4)] &= \frac{i\chi \tilde{F}}{s}, \\
B_3(k_2)[i\eta + \bar{A}_{23}(k_2)] + B_3(k_4)[i\eta + \bar{A}_{23}(k_4)] &= \frac{i\eta \tilde{F}}{s}, \\
B_3(k_2)[(\kappa-1)[i\chi \bar{A}_{13}(k_2) + i\eta \bar{A}_{23}(k_2)] + i\alpha k_2] + \\
B_3(k_4)[(\kappa-1)[i\chi \bar{A}_{13}(k_4) + i\eta \bar{A}_{23}(k_4)] + i\alpha k_4] &= 0.
\end{aligned} \tag{4.82}$$

It appears that there are three equations for two unknowns in Eq. 4.82, but a closer investigation reveals that the first two equations are colinear. Solving Eq. 4.82 for  $B_3(k_2)$  and  $B_3(k_4)$  gives

$$\begin{aligned}
A_3 &= \frac{\tilde{F} k_2 t^2}{(k_2 - k_4) D} \left[ \alpha k_4^2 + (\kappa - 1) t^2 + (\kappa - 1) \right] \\
A_4 &= \frac{\tilde{F} k_4 t^2}{(k_2 - k_4) D} \left[ \alpha k_2^2 + (\kappa - 1) t^2 + (\kappa - 1) \right] \\
D &= \left[ 2(1 - \kappa)(t^4 + t^2 s^2) - (\gamma t^2 + \alpha s^2)(t^2 + s) + \alpha k_2 k_4 \right].
\end{aligned} \tag{4.83}$$

Notice that the expressions for  $B_3(k_2)$  and  $B_3(k_4)$  have the same functional form as  $A_3$  and  $A_4$  given in Eq. 4.20 with  $\eta$  replaced by  $t$ . The formal solution for the axial displacement is given by

$$u_3(x_1, x_2, x_3, s) = \frac{1}{(2\pi)^2} \int_{-\infty}^{\infty} \int_{-\infty}^{\infty} (B_3(k_2) e^{ik_2 x_3} + B_3(k_4) e^{ik_4 x_3}) d\eta d\chi. \tag{4.84}$$

In anticipation of the Cagniard inversion method, the following substitution of variables,

$$\chi = sw \cos(\varphi) , \quad \eta = sw \sin(\varphi) , \quad (4.85)$$

leads to

$$u_3(x_1, x_2, x_3, s) = \frac{1}{(2\pi)^2} \int_0^\infty s^2 w dw \int_0^{2\pi} (B_3(k_2)e^{ik_2x_3} + B_3(k_4)e^{ik_4x_3}) d\varphi . \quad (4.86)$$

Since the integrand is independent of  $\varphi$ , a consequence of the source symmetry and the transverse isotropy of the material, the representation of the axial displacement in Eq. 4.85 can be reduce to the evaluation of a single integral,

$$u_3(x_1, x_2, x_3, s) = \frac{1}{(2\pi)} \int_0^\infty (B_3(k_2)e^{ik_2x_3} + B_3(k_4)e^{ik_4x_3}) s^2 w dw d\varphi . \quad (4.87)$$

A detailed implementation of Cagniard's method can be avoided by noting that the integrand for the 3-dimensional case, Eq. 4.86, is obtained by multiplying the 2-dimensional analogue by the product of the Laplace and Fourier transform parameters. The multiplication by the Laplace transform parameter is tantamount to taking a temporal derivative. The solution procedure now becomes obvious. First multiply the transformed solution for the 2-dimensional case by the Fourier transform

parameter and find the inverse. The temporal derivative of the inverse is now associated with the solution for the 3-dimensional case. The above procedure has been carried out for axial displacement in the epicentral direction resulting from a laser point source in zinc. Figure 4.9 shows the results of this procedure.

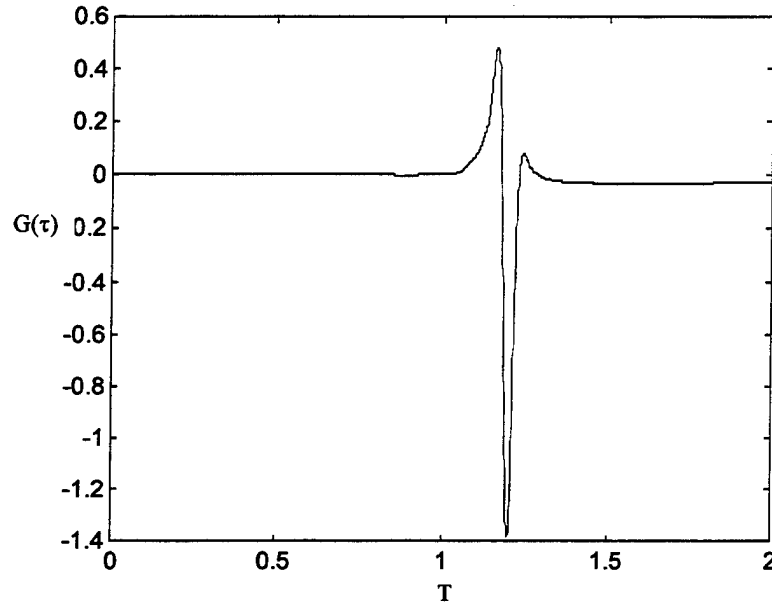


**Fig. 4.9.** Epicentral displacement for laser point-source in a 3-dimensional half-space.

A close examination of the waveform reveals that there is a small amount of energy arriving at the quasi-longitudinal velocity. It is interesting to note that the portion of the waveform corresponding to the interior of the lacuna is no longer zero.

Mathematically, this is an artifact of having to multiply the 2-dimensional analogue by the product of the Laplace and Fourier transform parameters to obtain the 3-dimensional solution.

## CHAPTER 5

This chapter is dedicated to solutions that must be obtained numerically. The idealized nature of the source and the specific location of the observation point made the analytical results in Chapter 4 possible. If the source considered is located beneath the surface and/or if the observation point is off the symmetry axis, then the solution must be obtained numerically. The numerical nature of the solution follows from the fact that the Cagniard path must be obtained numerically. This chapter considers two specific numerical problems. The first problem entails a surface line-source and observation points that are off the symmetry axis. The second problem involves displacements along the symmetry axis due to a buried line-source.

### *(5.1) OBSERVATION POINTS OFF THE SYMMETRY AXIS*

Consider the inverse of Eq. 4.14 for observation points that are neither along the symmetry axis nor on the bounding surface. The geometry of the problem is shown in Fig. 5.1. The bounding surface coincides with the plane of isotropy. The source is a surface line-source. The observation angle,  $\theta$ , is defined as the angle between the symmetry axis and a line joining the source and observation point.

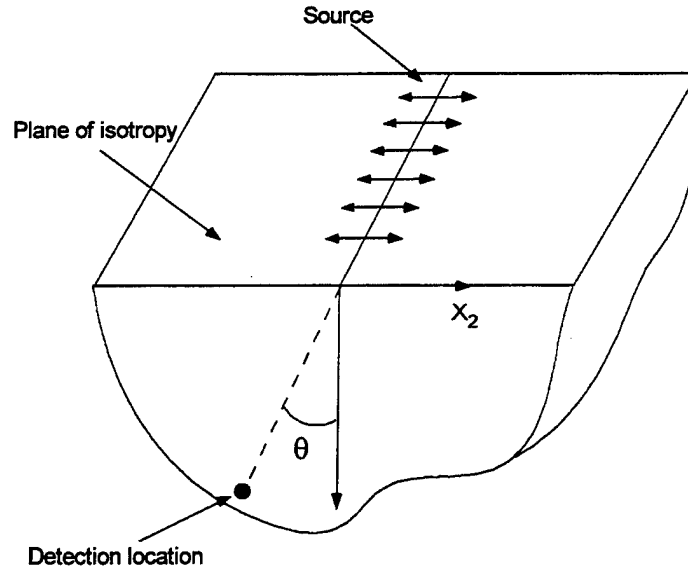


**Fig. 5.1.** Problem geometry with source and detection locations.

Formally, the inverse of Eq. 4.14 is written as

$$\bar{u}_3(x_2, x_3, s) = \frac{1}{\pi} \operatorname{Re} \int_0^{\infty} (A_3 e^{-\zeta_1 x_3 s} + A_4 e^{-\zeta_3 x_3 s}) e^{i s \omega |x_2|} s d\omega . \quad (5.1)$$

The Cagniard paths for Eq. 5.1 are defined by

$$\begin{aligned} \text{a) } \zeta_1 x_3 - i\omega |x_2| &= \tau , \\ \text{b) } \zeta_3 x_3 - i\omega |x_2| &= \tau , \end{aligned} \quad (5.2)$$

$\tau = \text{real and positive} .$

The parametric equations representing the Cagniard path are obtained by substituting Eqs. 4.17 into Eqs. 5.2 and squaring twice to eliminate the radicals. This procedure yields a fourth order equation for  $\omega$  of the form,

$$\begin{aligned}
 A(\theta)\omega^4 + B(\theta, T)\omega^3 + C(\theta, T)\omega^2 + D(\theta, T)\omega + E(\theta, T) &= 0, \\
 A(\theta) &= F(\theta) + 4\alpha\beta - \gamma^2, \\
 B(\theta, T) &= \frac{8i\alpha T \sin(\theta)F(\theta)}{\cos^2(\theta)}, \\
 C(\theta, T) &= 2F(\theta)G(\theta, T) - 16\frac{\alpha^2 T^2 \sin^2(\theta)}{\cos^4(\theta)} - 2(\alpha + 1)\gamma + 4\alpha(\beta + 1), \\
 D(\theta, T) &= \frac{8i\alpha T \sin(\theta)G(\theta, T)}{\cos^2(\theta)}, \\
 E(\theta, T) &= G(\theta, T) - (\alpha + 1)^2 + 4\alpha, \\
 F(\theta) &= -\left(\frac{2\alpha \sin^2(\theta) + \gamma \cos^2(\theta)}{\cos^2(\theta)}\right)^2, \\
 G(\theta, T) &= \frac{2\alpha T^2 - (1 + \alpha)\cos^2(\theta)}{\cos^2(\theta)}.
 \end{aligned} \tag{5.3}$$

Equation 5.3 has four complex roots,  $\Theta_1, \Theta_2, \Theta_3,$  and  $\Theta_4$ , which occur in complex conjugate pairs. The roots labeled  $\Theta_1$  and  $\Theta_3$  correspond to the physical sheets of the Riemann surface. For the special case of an isotropic solid,  $\alpha = \beta = \gamma/2$ , Eq. 5.3 can be factored into two second order equations that can be solved analytically. For the general anisotropic case, the roots of Eq. 5.3 must be found numerically. The program CAGNIARD was used to find the roots to Eq. 5.3. The computer code along with a complete description is given in Appendix A.

It was found that the character of the Cagniard paths was dictated to a large extent by the location of the lacunas relative to the observation direction. Thus, all crystals belonging to a particular class (I-V) will have Cagniard paths with similar characteristics. Discussing the Cagniard paths as a function of observation angle for all the crystals that exhibit transverse isotropy would be a difficult task. Instead three representative examples will be discussed. The first example is Hafnium. It was chosen because the wave-front curve for Hafnium does not have any lacunas. The remaining examples, Beryl and Zinc, have lacunas off the symmetry axis and aligned with the symmetry axis, respectively. Before discussing the Cagniard paths in detail, the location of the branch points and singularities associated with  $\bar{u}_3$  will be identified. From Eq. 4.22, the branch points for  $\zeta(\omega)$  arise in two distinct ways,

$$\begin{aligned} 1) \quad & \phi(\omega) = 0, \\ 2) \quad & \gamma\omega^2 + (\alpha + 1) \pm \sqrt{\phi(\omega)} = 0. \end{aligned} \tag{5.4}$$

The branch points originating from (1) are

$$\omega_{\pm} = \pm \sqrt{\frac{\gamma(\alpha + 1) - 2\alpha(\beta + 1) \pm 2\sqrt{\alpha(\alpha + \beta - \gamma)(1 + \alpha\beta - \gamma)}}{4\alpha\beta - \gamma^2}}, \tag{5.5}$$

while the branch points originating from (2) are given by

$$\omega = \frac{i}{\sqrt{\beta}}, \quad \omega = i. \quad (5.6)$$

The only pole singularity associated with  $\bar{u}_3$  is the Rayleigh pole, the physical root of Eq. 4.26. With the aid of Table 4.1, the branch points resulting from (1) and (2) and the location of the Rayleigh pole for the example crystals are listed in Table 5.1.

**Table 5.1.** Location of branch points and Rayleigh pole.

| Crystal | $\omega_+$       | $\omega_-$       | $\omega=i$ | $\omega=i/\sqrt{\beta}$ | $i\omega_R$ |
|---------|------------------|------------------|------------|-------------------------|-------------|
| Hafnium | 0.4026 - 0.7261i | 0.4026 + 0.7261i | i          | 0.5547I                 | 1.0465i     |
| Beryl   | 0.1915 - 0.5063i | 0.1915 + 0.5063i | i          | 0.4933I                 | 1.0719I     |
| Zinc    | 0.1260           | 1.0007I          | i          | 0.4897I                 | 1.1386i     |

### (5.1.1) CAGNIARD PATH FOR HAFNIUM

The wave-front curve for Hafnium, class (I), is shown in Fig 5.2. The wavefront for the  $R_+$  branch, like an isotropic material, has no cusp. Since the wavefront curve for Hafnium has similar characteristics with the wavefront curve for an isotropic material, it is also expected that the Cagniard paths will have similar characteristics. Figures 5.3-5.5 illustrate the dependence of the Cagniard path on the detection angle,  $\theta$ . The path shown in Fig. 5.3 is for a detection angle of  $25^\circ$ . For a detection angle of  $45^\circ$ , Fig. 5.4 shows that the integration contour corresponding to the  $R_+$  branch is deformed by the branch

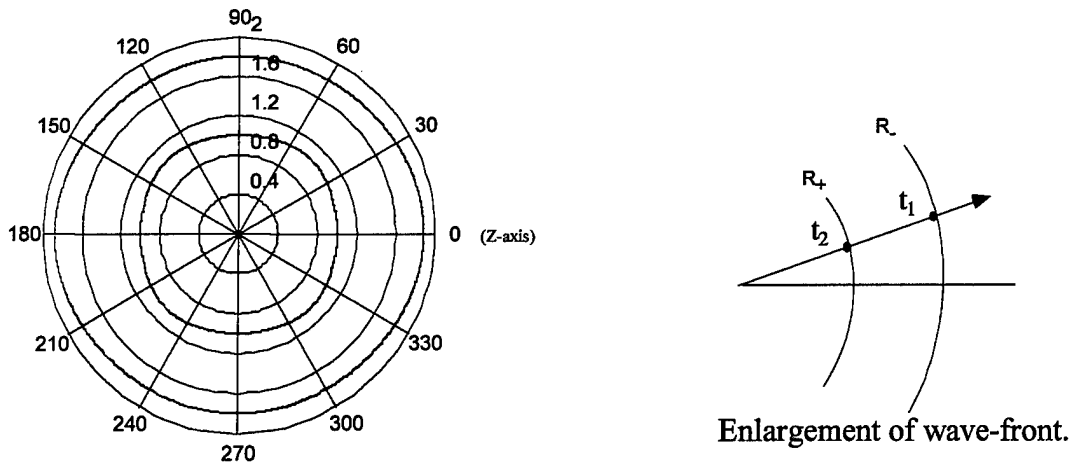


**Fig. 5.2.** Wave-front curve for Hafnium.

cut starting at  $\omega = i/\sqrt{\beta}$ . In Figure 5.5, the Cagniard path encircles the branch points,  $\omega_-$  and  $-\omega_+$ . It should be noted that the behavior of the Cagniard path in Figs. 5.4, and 5.5 is not seen in isotropic materials since the branch points corresponding to isotropic materials are purely imaginary.

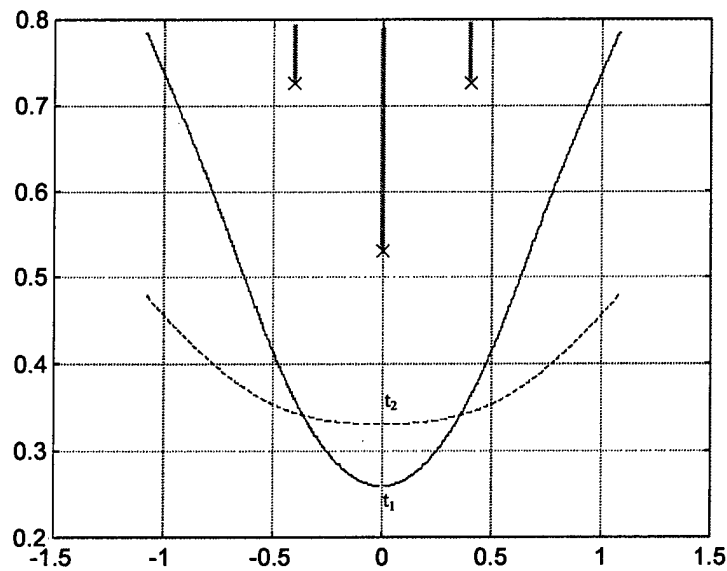


**Fig. 5.3.** Cagniard path for Hafnium ( $\theta=25^\circ$ ). The dashed line represents the portion of the Cagniard path on the second sheet of the Riemann surface.

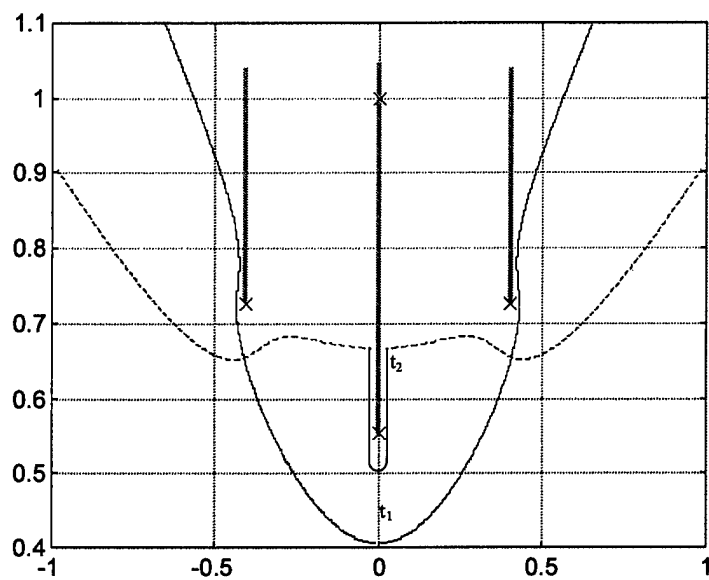


**Fig. 5.4.** Cagniard path for Hafnium ( $\theta=45^\circ$ ). The dashed line represents the portion of the Cagniard path on the second sheet of the Riemann surface.

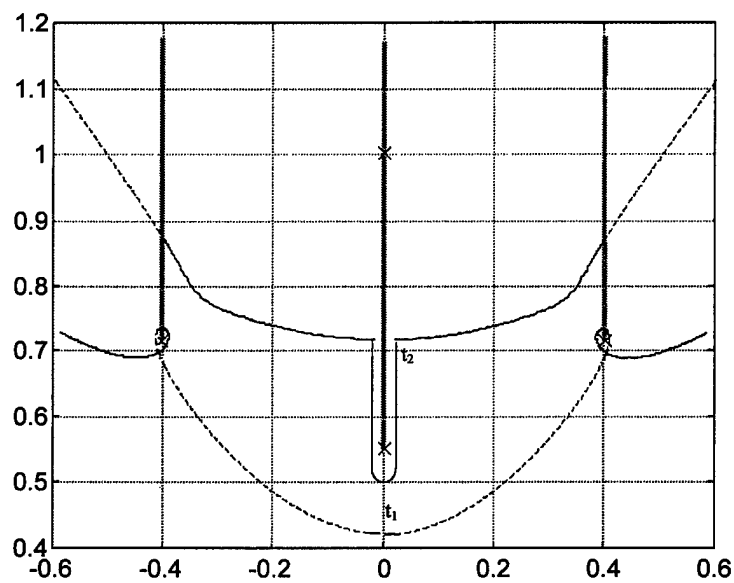


**Fig. 5.5.** Cagniard path for Hafnium ( $\theta=47.5^\circ$ ). The dashed line represents the portion of the Cagniard path on the second sheet of the Riemann surface.

## (5.1.2) CAGNIARD PATH FOR BERYL

In Fig. 5.6 the wave-front curve for Beryl is shown. Figure 5.6 demonstrates that, for Beryl, three natural subdivisions exist. The first division corresponds to the angular region between the z-axis and the inside vertex of the lacuna. Observation directions that intersect the lacuna make up the second division. The third division corresponds to an angular region between the outside vertex of the lacuna and the y-axis.

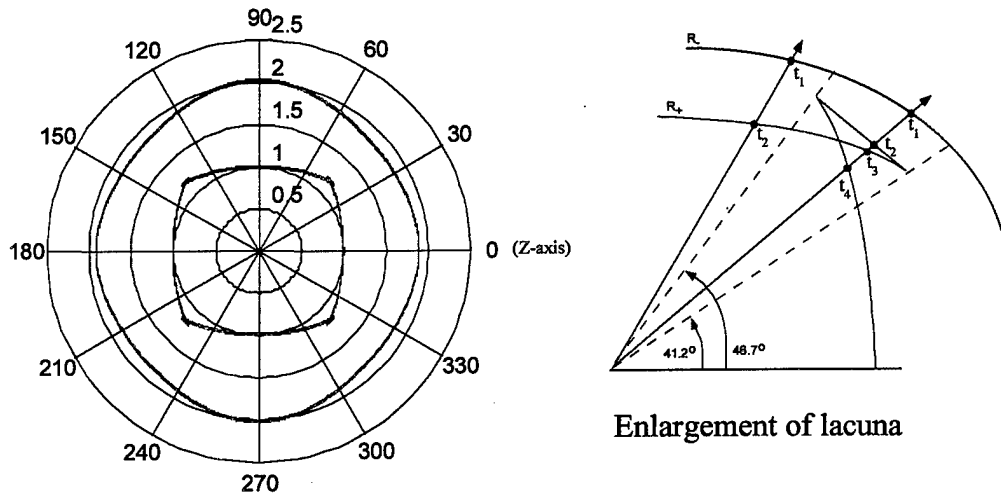


**Fig. 5.6.** Wave-front curve for Beryl. Enlargement of  $R_+$  branch shown in insert.

Numerical values for the angular boundaries of these divisions are given below.

- (i)  $0^\circ \leq \theta < 41.2^\circ$ ,
  - (ii)  $41.2^\circ \leq \theta < 46.7^\circ$ ,
  - (iii)  $46.7^\circ \leq \theta < 90^\circ$ .
- (5.7)

Figures 5.7-5.9 illustrate the dependence of the Cagniard path on the detection angle.

The path shown in Fig. 5.7 is for an angle of  $30^\circ$ , which lies in region (i). Figures 5.8 and 5.9 are for detection angles that lie in regions (ii) and (iii) respectively.

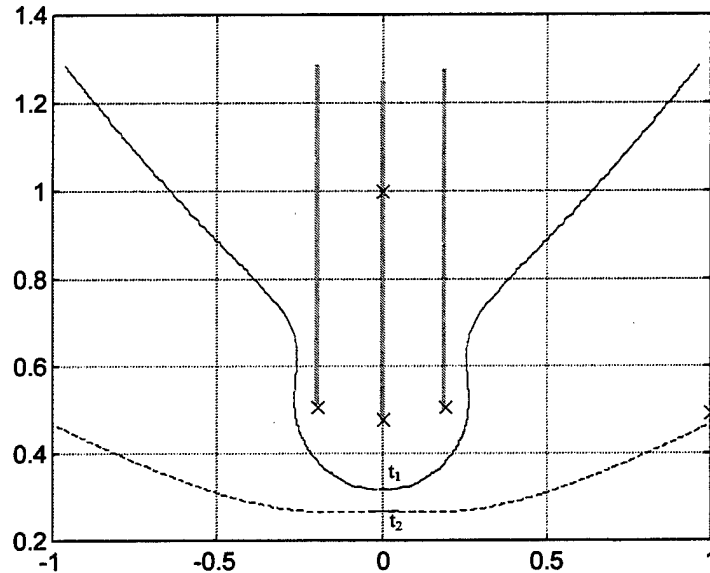


**Fig. 5.7.** Cagniard path for Beryl ( $\theta=35^\circ$ ). The dashed line represents the portion of the Cagniard path on the second sheet of the Riemann surface.

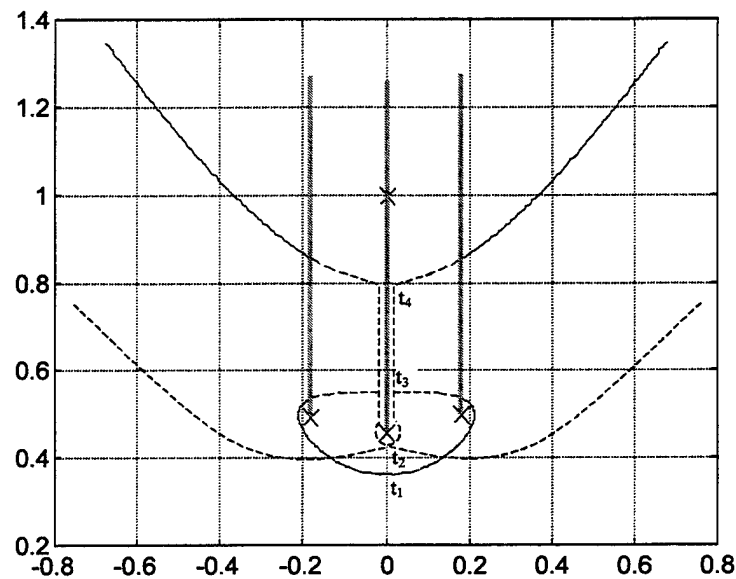


**Fig 5.8.** Cagniard path for Beryl ( $\theta=45^\circ$ ). The dashed line represents the portion of the Cagniard path on the second sheet of the Riemann surface

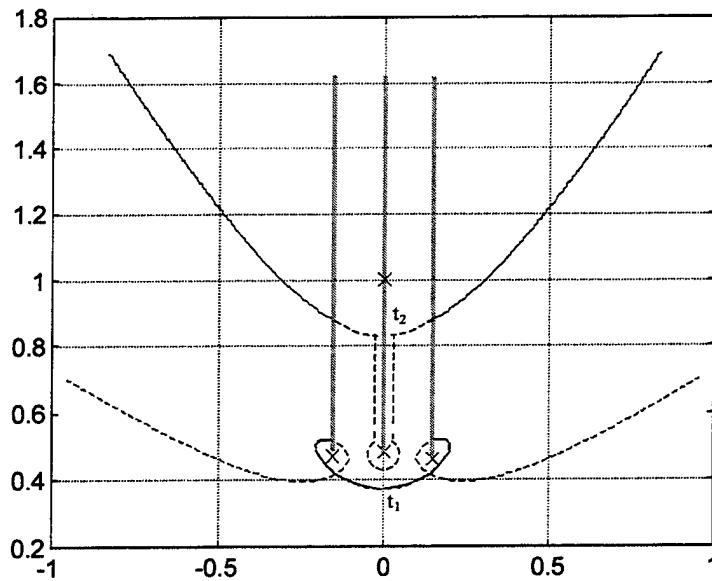


**Fig 5.9.** Cagniard path for Beryl ( $\theta=48^\circ$ ). The dashed line represents the portion of the Cagniard path on the second sheet of the Riemann surface.

### (5.1.3) CAGNIARD PATH FOR ZINC

The wavefront for zinc, class (IV), is shown in Fig. 5.10. The lacunas in the  $R_+$  branch are centered along the symmetry axis and along the bounding surface. The lacunas that intersect the bounding surface are very small and must be viewed under magnification. Figure 5.11 shows the Cagniard path for an observation angle that intersects the lacuna along the symmetry axis while Fig. 5.12 shows the Cagniard path for an angular region outside the lacuna.

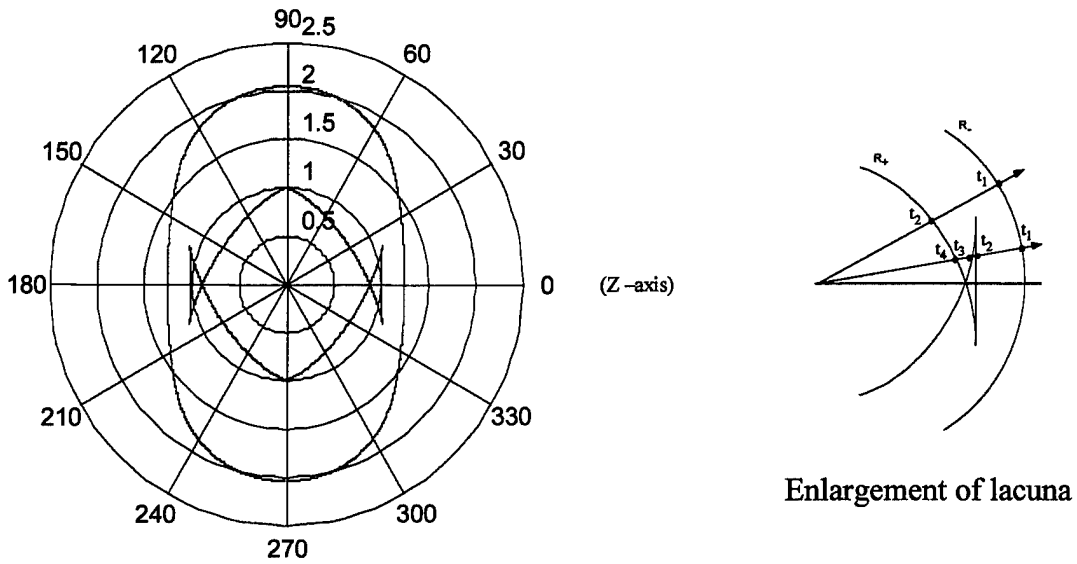


Fig. 5.10. Wave-front curve for Zinc. Enlargement of  $R_+$  branch shown in insert.

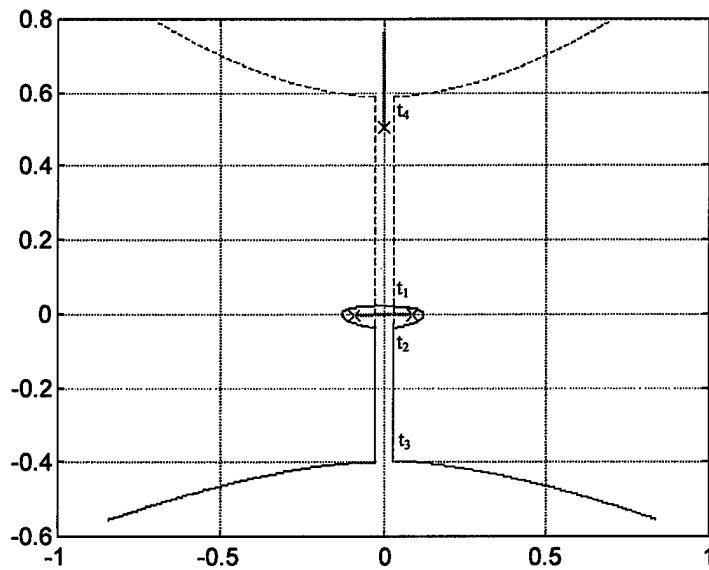
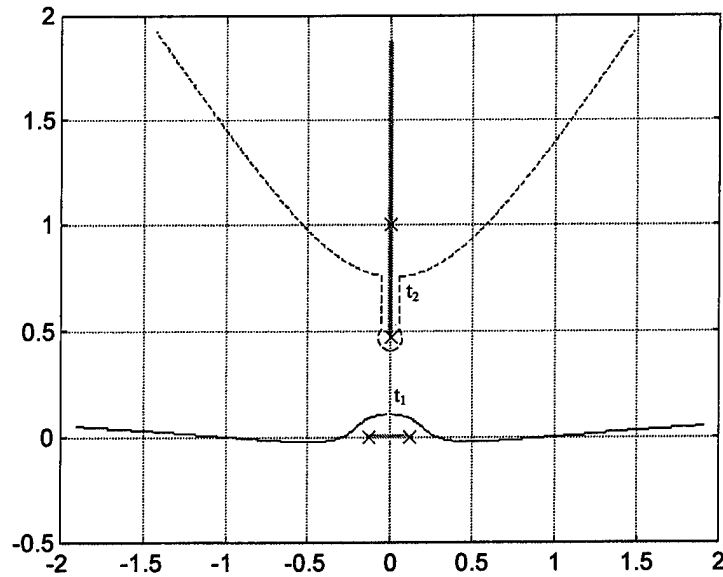


Fig. 5.11. Cagniard path for zinc ( $\theta=10^\circ$ ). The dashed line represents the portion of the Cagniard path on the second sheet of the Riemann surface.



**Fig. 5.12.** Cagniard path for zinc ( $\theta=35^\circ$ ). Dashed line represents the portion of the Cagniard path on the second sheet of the Riemann surface.

#### (5.1.4) DETAILS OF INVERSION FOR ZINC

With the Cagniard path numerically defined, the inversion of the transformed displacements, Eq. 5.1, may be performed. In this section, a detailed analysis of the inversion for the off-epicentral vertical displacement for zinc is given. Figures 5.13 and 5.14 show an enlarged view of the integration contours for zinc when the observation angle is  $10^\circ$ . The Cagniard path plotted in Fig. 5.13 corresponds to Eq. 5.2a while the Cagniard path plotted in Fig. 5.14 corresponds to Eq. 5.2b. In order to keep the notation consistent with previous chapters, Eq. 5.1 is rewritten as

$$\bar{u}_3(\omega, x_3, s) = \frac{1}{\pi} \operatorname{Re}\{I_1 + I_3\}, \quad (5.8)$$

$$I_1 = \int_0^{\infty} A_3 e^{-s(\zeta_1 x_3 + i\omega|x_2|)} s d\omega, \quad I_3 = \int_0^{\infty} A_4 e^{-s(\zeta_3 x_3 + i\omega|x_2|)} d\omega.$$

With the aid of Cauchy's theorem and the change of variables given in Eq. 5.2, the Fourier inversion corresponding to  $I_1$  and  $I_3$  in Eq. 5.8 can be written as

$$I_1 = \int_{t_1}^{t_2} I_{11} + \int_{t_2}^{t_3} I_{11} + \int_{\Gamma_1} I_{11},$$

$$I_3 = \int_{t_2}^{t_4} I_{33} + \int_{\Gamma_2} I_{33}, \quad (5.9)$$

$$I_{11} = A_3 e^{-s\tau} s \frac{\partial \omega}{\partial \tau} d\tau,$$

$$I_{33} = A_4 e^{-s\tau} s \frac{\partial \omega}{\partial \tau} d\tau.$$

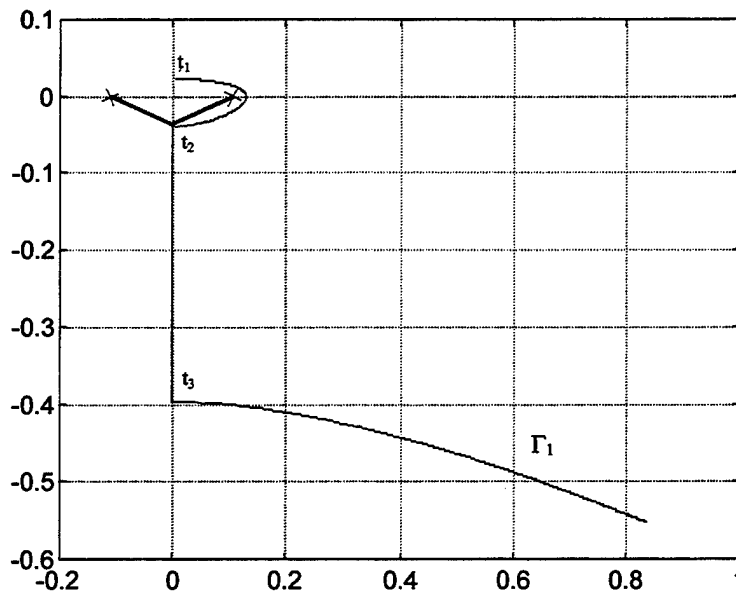
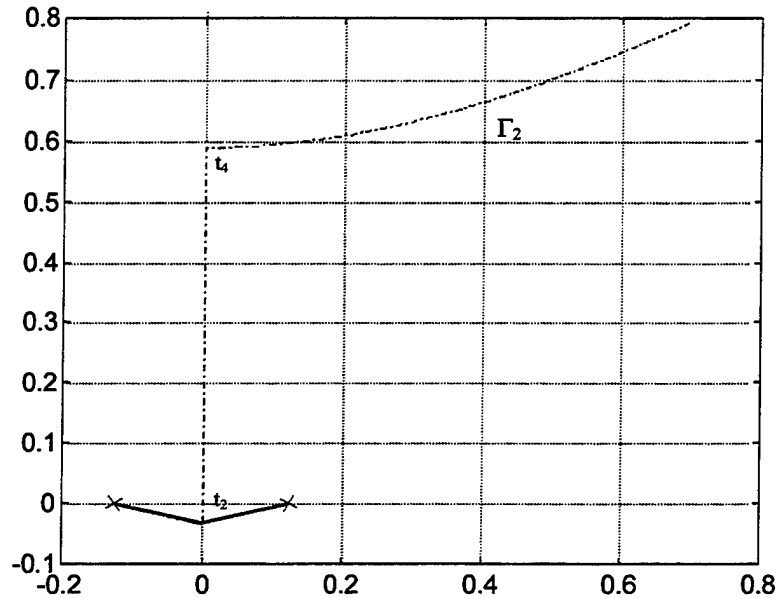


Fig. 5.13. Cagniard path correspond to Eq. 5.2b. The times,  $t_1$ ,  $t_2$ , and  $t_3$  correspond to wave arrivals.

It should be noted that the portion of the contour along the imaginary axis does not contribute to the displacement since the integrand is totally imaginary. Applying the inverse Laplace transform operator to Eq. 5.8 gives

$$u(x_2, x_3, \tau) = [H(\tau - t_1) - H(\tau - t_2)]A_3 \frac{\partial \omega(t_1 \rightarrow t_2)}{\partial \tau} + H(\tau - t_3)A_3 \frac{\partial \omega(\Gamma_1)}{\partial \tau} + H(\tau - t_4)A_4 \frac{\partial \omega(\Gamma_2)}{\partial \tau} . \quad (5.10)$$



**Fig.5.14.** Cagniard path correspond to Eq. 5.2b. The times  $t_2$  and  $t_4$  correspond to wave arrivals.

The off epicentral vertical displacement in zinc for a detection angle of  $10^\circ$  is shown in Fig. 5.15. The characteristics of the waveform shown in Fig. 5.15 are similar to the epicentral waveform shown in Fig. 4.7. The primary difference is the splitting of wave resulting from the conical portion of the slowness surface. Figure 5.10 shows that for observation points along the symmetry axis, the two conical pulses travel at the same velocity, while for points off the epicentral axis, the two conical pulses travel at different velocities.

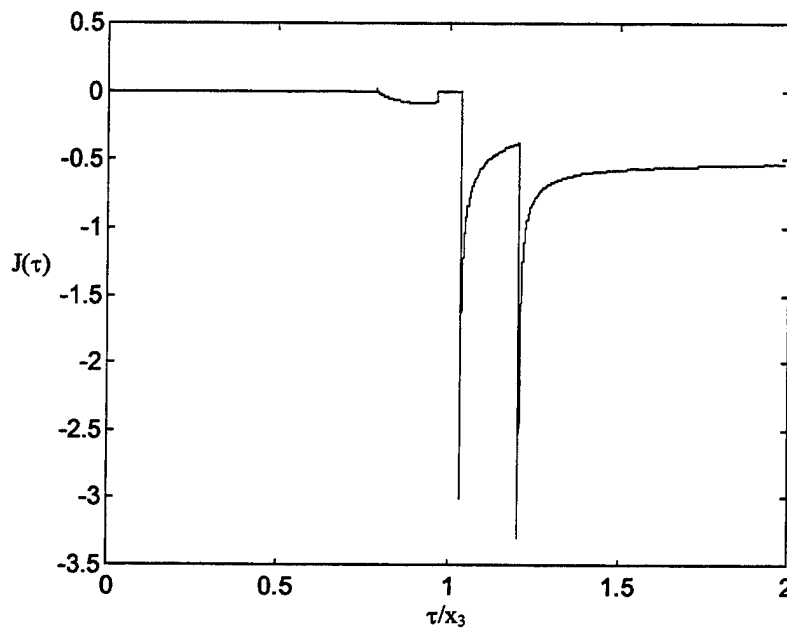


**Fig. 5.15.** Theoretical displacement for off epicentral waves generated in zinc with a line source. The observation angle is  $10^\circ$ .

## (5.2) BURIED SOURCE

Spatial variations in the mechanical and optical properties of a composite material can have a pronounced effect on the acoustic signature resulting from pulsed laser irradiation. The purpose of this section is to address the effects of optical

heterogeneity. The solution for a point source located on the bounding surface can serve as a Green's function for modeling the effects lateral variations in optical properties. However, a buried source must be considered in order to develop a Green's function suitable for modeling arbitrary absorption characteristics in two dimensions. Hence, the focus of this section is modeling the effects of sub-surface absorption. The problem geometry, shown in Fig. 5.16, involves a buried line source in a transversely isotropic half-space where the bounding plane is a plane of isotropy.

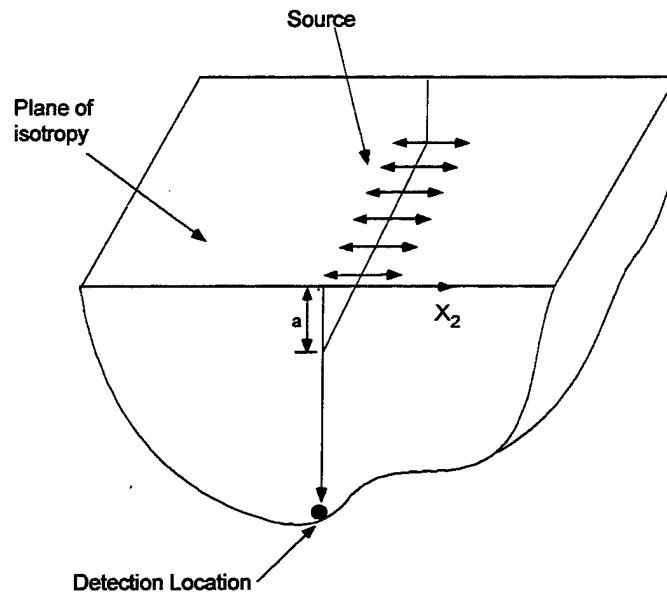


**Fig. 16.** Problem geometry for a buried line source.

The equations of motion for this problem are given as

$$\begin{aligned} \beta u_{2,22} + u_{2,33} - u_{2,\tau\tau} + \kappa u_{3,23} &= F_2 \delta'(x_2) \delta(x_3 - a) H(\tau) , \\ \kappa u_{2,23} + u_{3,22} + \alpha u_{3,33} - u_{3,\tau\tau} &= F_3 \delta(x_2) \delta'(x_3 - a) H(\tau) . \end{aligned} \quad (5.11)$$

The stress free boundary conditions are stated as follows:

$$\begin{aligned}\sigma_{33}(x_2, 0, \tau) &= \alpha \bar{u}_{3,3}|_{x_3=0} + (\kappa - 1) \bar{u}_{2,2}|_{x_3=0} = 0, \\ \sigma_{23}(x_2, 0, \tau) &= \bar{u}_{2,3}|_{x_3=0} + \bar{u}_{3,2}|_{x_3=0} = 0.\end{aligned}\quad (5.12)$$

The solution proceeds with the aid of integral transform techniques. The transformed equations of motion are expressed as

$$\begin{aligned}[-\beta\eta^2 - k^2 - s^2] (\bar{u}_2(\eta, x_3, s)) - \eta\kappa k (\bar{u}_3(\eta, x_3, s)) &= \frac{i\eta F_2}{s} e^{ika}, \\ -\eta\kappa k (\bar{u}_2(\eta, x_3, s)) + [-\eta^2 - \alpha k^2 - s^2] (\bar{u}_3(\eta, x_3, s)) &= \frac{ikF_3}{s} e^{ika},\end{aligned}\quad (5.13)$$

where a bar denotes a transformed displacement. The Fourier-Laplace transform operator is defined as

$$\bar{u}_{2/3}(\eta, k, s) = \int_{-\infty}^{\infty} \int_0^{\infty} u_{2/3}(x_2, x_3, \tau) e^{-(i\eta x_2 + ikx_3 + s\tau)} d\eta dk d\tau. \quad (5.14)$$

The following substitution is made so as to facilitate the Cagniard inversion technique:

$$k = is\zeta, \quad \eta = s\omega. \quad (5.15)$$

The homogeneous solution of Eq. 5.13 is given by

$$\begin{aligned}\bar{u}_2^{(H)} &= A_1 e^{-\zeta_1 x_3} + A_2 e^{-\zeta_3 x_3}, \\ \bar{u}_3^{(H)} &= A_3 e^{-\zeta_1 x_3} + A_4 e^{-\zeta_3 x_3}.\end{aligned}\quad (5.16)$$

where  $\zeta_{1/3}$  are the physical roots to the slowness equation. The relation between the coefficients, given in Eq. 4.19, will be restated here for convenience,

$$\begin{aligned}A_1 &= A_3 \bar{A}_3 = A_3 \left[ \frac{\alpha \zeta_1^2 - \omega^2 - 1}{i \kappa \omega \zeta_1} \right], \\ A_2 &= A_4 \bar{A}_4 = A_4 \left[ \frac{\alpha \zeta_3^2 - \omega^2 - 1}{i \kappa \omega \zeta_3} \right].\end{aligned}\quad (5.17)$$

A formal expression for the particular solution is obtained by algebraically uncoupling Eqs. 5.13,

$$\begin{aligned}\bar{u}_2(\omega, \zeta, s) &= \frac{i\omega}{s^2} \left[ \frac{(F_2(\omega^2 - \alpha \zeta^2 + 1) + F_3 \kappa \zeta^2) e^{-as\zeta}}{\alpha \zeta^4 - \zeta^2((\alpha + 1) + \gamma \omega^2) + (\beta \omega^4 + (\beta + 1)\omega^2 + 1)} \right], \\ \bar{u}_3(\omega, \zeta, s) &= \frac{-\zeta}{s^2} \left[ \frac{(F_3(\beta \omega^2 - \zeta^2 + 1) - F_2 \omega^2 \kappa) e^{-as\zeta}}{\alpha \zeta^4 - \zeta^2((\alpha + 1) + \gamma \omega^2) + (\beta \omega^4 + (\beta + 1)\omega^2 + 1)} \right].\end{aligned}\quad (5.18)$$

Dependence on  $x_3$  is recovered by using a table of partial fractions,

$$\begin{aligned}
 \bar{u}_2^{(P)}(\omega, x_3, s) &= R_1(\omega, \zeta, s)N_1(x_3) + R_3(\omega, \zeta, s)N_3(x_3) , \\
 \bar{u}_3^{(P)}(\omega, x_3, s) &= S_1(\omega, \zeta, s)[d(N_1(x_3))/dx_3] + S_3(\omega, \zeta, s)[d(N_3(x_3))/dx_3] , \\
 R_1(\omega, \zeta, s) &= \frac{\omega}{2s(\zeta_1^2 - \zeta_3^2)} \left[ \frac{F_2(\omega^2 + 1 - \alpha\zeta_1^2) + F_3\kappa\zeta_1^2}{\zeta_1} \right] , \\
 R_3(\omega, \zeta, s) &= \frac{-i\omega}{2s(\zeta_1^2 - \zeta_3^2)} \left[ \frac{F_2(\omega^2 + 1 - \alpha\zeta_3^2) + F_3\kappa\zeta_3^2}{\zeta_3} \right] , \\
 S_1(\omega, \zeta, s) &= \frac{i}{2s^2(\zeta_3^2 - \zeta_1^2)} \left[ \frac{F_3(\beta\omega^2 - \zeta_1^2 + 1) - F_2\omega^2\kappa}{\zeta_1} \right] , \\
 S_3(\omega, \zeta, s) &= \frac{-i}{2s^2(\zeta_3^2 - \zeta_1^2)} \left[ \frac{F_3(\beta\omega^2 - \zeta_3^2 + 1) - F_2\omega^2\kappa}{\zeta_3} \right] ,
 \end{aligned} \tag{5.19}$$

$$N_1(x_3) = e^{-s\zeta_1 |x_3 - a|} , N_3(x_3) = e^{-s\zeta_3 |x_3 - a|} .$$

The coefficients  $A_3$  and  $A_4$  are determined by requiring that the solution to Eq. 5.11, homogeneous and particular, satisfy the boundary conditions, Eq. 5.12,

$$\begin{aligned}
 A_3 &= \frac{\text{Det (M)}}{D} , \\
 A_4 &= \frac{\text{Det (O)}}{D} ,
 \end{aligned} \tag{5.20}$$

where  $D$  is the Rayleigh denominator given in Eq. 4.20, and  $M$  and  $O$  are given by

$$\begin{aligned}
\mathbf{M} &= \begin{bmatrix} M_{11} & M_{12} \\ M_{21} & M_{22} \end{bmatrix}, \quad \mathbf{O} = \begin{bmatrix} O_{11} & O_{12} \\ O_{21} & O_{22} \end{bmatrix}, \\
M_{11} &= -\left[ \alpha \left( S_1 s^2 \zeta_1^2 e^{-s\zeta_1 a} + S_2 s^2 \zeta_3^2 e^{-s\zeta_3 a} \right) + i s \omega (\kappa - 1) \left( R_1 e^{-s\zeta_1 a} + R_3 e^{-s\zeta_3 a} \right) \right], \\
M_{12} &= -\alpha s \zeta_3 + i s \omega (\kappa - 1) \bar{A}_4, \\
M_{21} &= -\left[ \left( R_1 s \zeta_1 e^{-s\zeta_1 a} + R_2 s \zeta_3 e^{-s\zeta_3 a} \right) + i s \omega \left( S_1 s \zeta_1 e^{-s\zeta_1 a} + S_3 s \zeta_3 e^{-s\zeta_3 a} \right) \right], \\
M_{22} &= -\bar{A}_4 \zeta_3 s + i s \omega, \\
O_{11} &= -\alpha s \zeta_1 + i s \omega (\kappa - 1) \bar{A}_3, \\
O_{12} &= -\left[ \alpha \left( S_1 s^2 \zeta_1^2 e^{-s\zeta_1 a} + S_2 s^2 \zeta_3^2 e^{-s\zeta_3 a} \right) + i s \omega (\kappa - 1) \left( R_1 e^{-s\zeta_1 a} + R_3 e^{-s\zeta_3 a} \right) \right], \\
O_{21} &= -\bar{A}_3 \zeta_1 s + i s \omega, \\
O_{22} &= -\left[ \left( R_1 s \zeta_1 e^{-s\zeta_1 a} + R_2 s \zeta_3 e^{-s\zeta_3 a} \right) + i s \omega \left( S_1 s \zeta_1 e^{-s\zeta_1 a} + S_3 s \zeta_3 e^{-s\zeta_3 a} \right) \right],
\end{aligned} \tag{5.21}$$

where  $\bar{A}_{3/4}$  are defined in Eq. 5.17. Explicit expressions for the coefficients in Eq. 5.20 were obtained using a symbolic manipulator, and are not given in this manuscript due to length considerations.

In order to gain a clear understanding of the Cagniard inversion procedure for a buried line-source, where the observation point is beneath the source, the solution is re-written as

$$\begin{aligned}
\bar{u}_2(\omega, x_3, s) &= R_1(DS) + R_3(DL) + SS_1 + LL_1 + SL_1 + LS_1, \\
\bar{u}_3(\omega, x_3, s) &= -is\zeta_1 S_1(DS) - is\zeta_3 S_3(DL) + SS_3 + LL_3 + SL_3 + LS_3, \\
DL &= e^{-s\zeta_3(x_3-a)}, \\
DS &= e^{-s\zeta_1(x_3-a)}, \\
SS_i &= SSC_i e^{-s(\zeta_1 a + \zeta_1 x_3)}, \\
LL_i &= LLC_i e^{-s(\zeta_3 a + \zeta_3 x_3)}, \\
SL_i &= SLC_i e^{-s(\zeta_1 a + \zeta_3 x_3)}, \\
LS_i &= LSC_i e^{-s(\zeta_3 a + \zeta_1 x_3)}, \\
i &= 1, 3,
\end{aligned} \tag{5.22}$$

where DS, DL, SS, LL, SL, LS, stand for direct shear, direct longitudinal, shear reflected as shear, longitudinal reflected as longitudinal, shear reflected as longitudinal, and longitudinal reflected as shear respectively.

It is interesting to note that if the material considered is isotropic, the DS, SS, and SL components of the waveform are identically zero. The vanishing of these components can be best understood by considering the symmetry of the source and the material. If the source has zero curl and if the material is thermally and elastically isotropic, then the terms  $R_1$  and  $S_1$ , given in Eq. 5.19, vanish.

$$\begin{aligned}
e_{ijk} F_{k,j}^{(\text{source})} &= 0, \\
F_2 &= F_3, \\
\zeta_1^2 &= (\omega^2 + 1), \quad \zeta_3^2 = ((\alpha\omega^2 + 1)/\alpha), \\
R_1 &= S_1 = 0.
\end{aligned} \tag{5.23}$$

The various Cagniard paths corresponding to the inversion of Eq. 5.21 can be written as

$$\begin{aligned}
 \text{a) } & \zeta_1 x_3 - \zeta_1 a = \tau , \\
 \text{b) } & \zeta_3 x_3 - \zeta_3 a = \tau , \\
 \text{c) } & \zeta_1 x_3 + \zeta_1 a = \tau , \\
 \text{d) } & \zeta_1 x_3 + \zeta_1 a = \tau , \\
 \text{e) } & \zeta_1 x_3 + \zeta_3 a = \tau , \\
 \text{f) } & \zeta_3 x_3 + \zeta_1 a = \tau , \\
 & \tau = \text{real and positive} .
 \end{aligned}
 \tag{5.24}$$

The Cagniard paths labeled a, b, c, and d in Eq. 5.24 can be obtained analytically, while the Cagniard paths labeled e and f must be obtained numerically. As was the case for solutions along the epicentral axis, Section 4.3, the character of the Cagniard paths, specified in Eq. 5.24, is dictated by the class to which the crystal belongs, (i-iii). For materials belonging to class (i), the Cagniard paths are purely real, while the Cagniard paths for class (ii) and class (iii) materials are complex. It would be a formidable task to describe the Cagniard paths, corresponding to a buried-source, for all materials that exhibit transverse isotropy. In addition, it is of little utility to study solutions for buried sources in strongly absorbing transversely isotropic materials, such as zinc and titanium. The author has chosen Beryl to serve as an example crystal. Beryl is weakly absorbing in the visible and near infrared region of the spectrum, thus exhibiting the effects of sub-surface absorption. In Fig. 5.17., the Cagniard paths for Beryl are plotted versus a dimensionless time parameter,  $T = \tau/x_3$ .

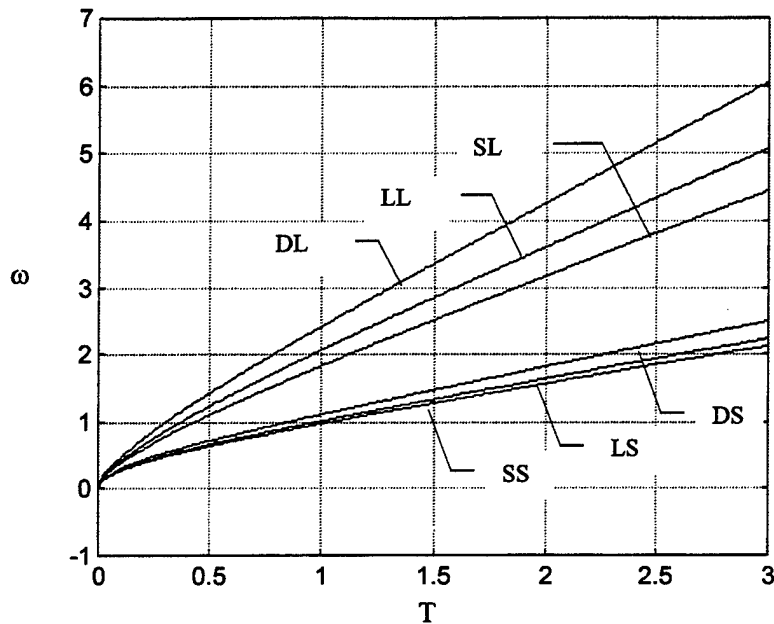


**Fig. 5.17.** Various Cagniard paths for a buried line-source in Beryl.

The ratio of the observation depth to the source depth,  $R_{x/a}$ , was set to 10 to ensure that all the Cagniard paths could be easily discerned. Figure 5.18 shows the epicentral displacement due to a buried line-source and a surface line source in Beryl. A value of 5000 for  $R_{x/a}$  was used to generate the data in Fig. 5.18. Thus, if the sample thickness is 1 cm, the source depth would be 2  $\mu\text{m}$ . The notable difference between the surface source and a buried source waveforms is the presence of a precursor spike that arrives at the longitudinal velocity.

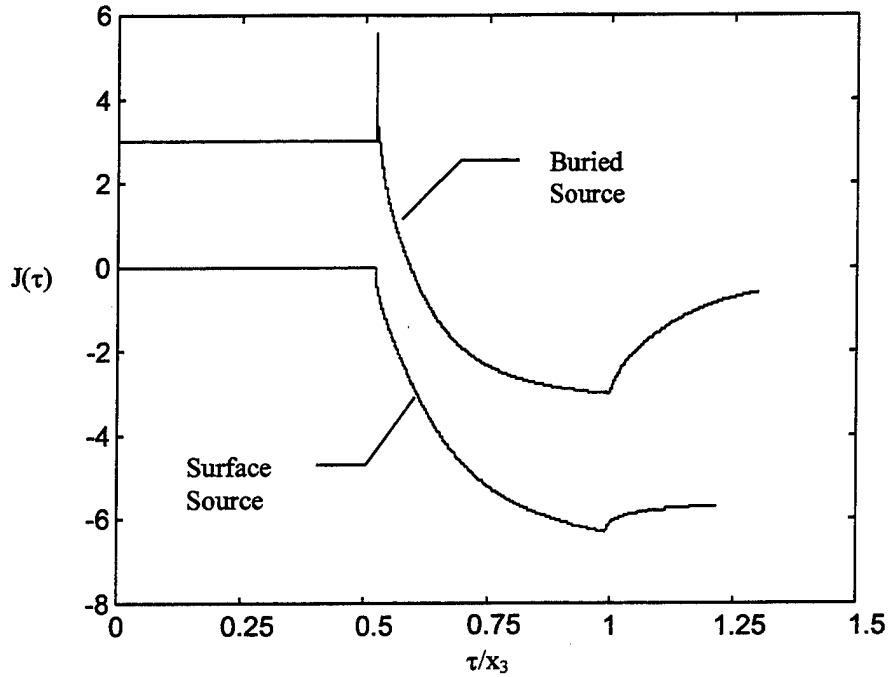


**Fig. 5.18.** Epicentral displacement waveforms due to a surface and a buried line source in Beryl.

The physical origin of this precursor was described by Telschow and Conant [8] and can be easily understood by considering plane wave with a step profile generated some distance beneath the free surface of an elastic half space. The wave will consist of forward and backward propagation components as shown in Fig. 5.19. The forward propagation wave has a positive displacement while the backward propagating wave has a negative displacement. At  $t=h/c$ , the negative displacement wave front strikes the surface and is reflected. Because the surface is stress free, the reflected wave is also a negative displacement wave. At  $t=2h/c$ , the negative displacement of all the particles in the region  $z<h$  has doubled. As the wave front of the reflected wave propagates further into the half-space, its negative displacement cancels the positive displacement previously caused by the forward propagating wave. The net result is

that for  $t > 2h/c$ , the material in the region  $z < h$  has moved as a rigid body in the negative  $z$  direction, while in the region  $z > h$ , a displacement "block" of length  $2h$  propagates toward infinity with velocity  $c$ .

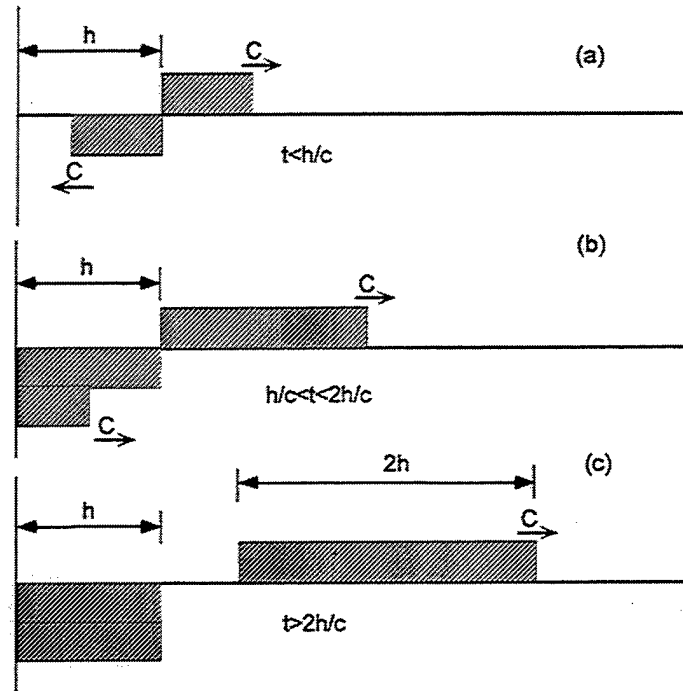


**Fig. 5.19.** Spatial profile of the displacement at different times produced from a planar temperature source at  $z=h$  in an elastic half-space.

## CHAPTER 6

There are many methods used for laser generation and laser detection of ultrasound. Laser generation of ultrasound is usually achieved with a Q-switched or long-pulsed laser. The influence of the laser parameters, wavelength and pulsed duration, on the generation of ultrasound was addressed in Chapter Two. Laser detection of ultrasound includes interferometric, beam deflection, and acousto-optic techniques [46]. Techniques that rely on coupling between the acoustic and optic fields have the advantage of probing the sample's interior. The major drawback is that acousto-optic techniques require high coupling coefficients and transparent samples. Beam deflection techniques are inexpensive, but they require highly reflective surfaces and the sensitivity is a function of the experimental geometry (i.e. angle of incidence, spot size, etc.). Interferometric techniques have poor sensitivity compared to piezoelectric devices, and usually require some form of electronic feedback to insure peak sensitivity. However, interferometric detection does offer a number of advantages such as, high spatial resolution without compromising sensitivity, measurements that are directly related to laser wavelength, detection off rough surfaces, and a flat broadband frequency response.

### (6.1) *EXPERIMENTAL SETUP*

The experimental data sets reproduced in this manuscript were generated using a Nd:YAG Q-switched laser. The laser was a Continuum model Surelite II, operating at 1.064  $\mu\text{m}$ . The transverse spatial profile was Gaussian and the temporal

pulse length was approximately 10 ns. The energy per pulse could be varied between 5 mJ and 600 mJ. The ultrasonic disturbance was detected with a skew-stabilized Michelson interferometer operating at 632.8 nm (see appendix A1). The upper limit of the bandwidth was determined to a large extent by the frequency response of the photodetectors in the interferometer. The photodetectors were manufactured by EG&G (product designation FFD-040) and have a specified upper bandwidth limit of 150 MHz into a 50  $\Omega$  load. The lower limit of the bandwidth, estimated at 1 kHz, was dictated by the characteristics of the stabilization circuit.

There were two basic experimental configuration used, generation and detection on the same side of the sample, Fig. 6.1, and generation and detection on the opposite side of the sample, Fig. 6.2.

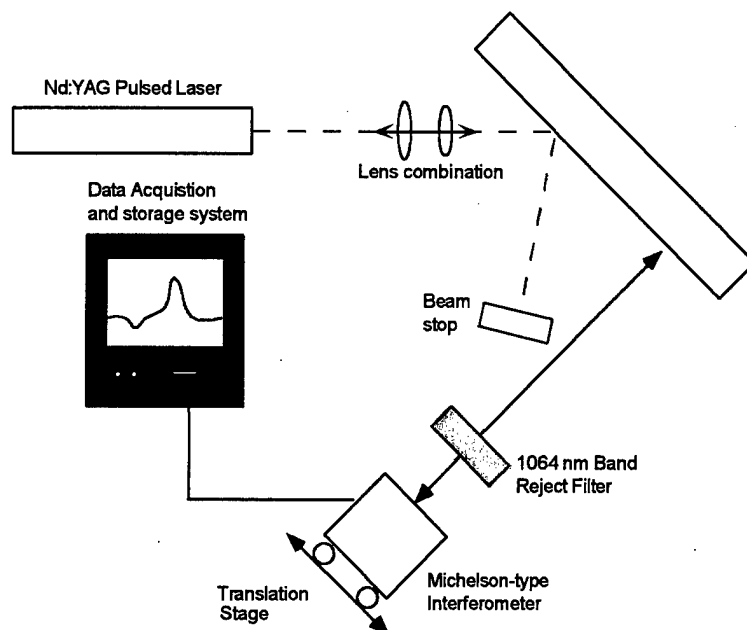


**Fig. 6.1.** Experimental setup used for same side detection. A Nd:YAG laser is used to generated the ultrasound and a Michelson interferometer is used to detect the ultrasound.

For same side detection, care had to be taken so as not to saturate the photodiodes in the interferometer with light from the Nd:YAG laser that had scattered off the sample surface. A beam stop was used to collect the specular component of the scattered light while a 1064 nm band reject filter was used to block the remaining scattered light from reaching the photodiodes.

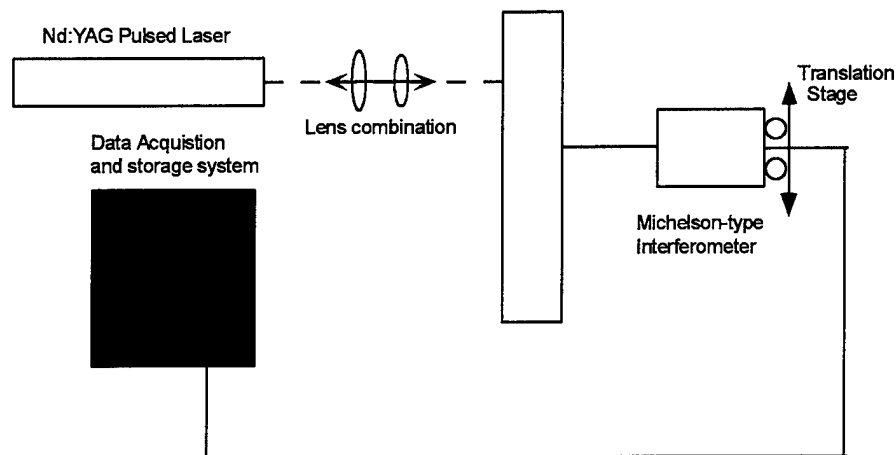


**Fig. 6.2.** Experimental setup used for opposite side detection. A Nd:YAG laser is used to generate the ultrasound and a Michelson interferometer is used to detect the ultrasound.

Two source configurations were used to test the theoretical prediction, a point source and a line source. For a point source, a single convex lens was used to focus the generation beam. Using a piece of laser burn paper, the beam diameter at the sample's surface was estimated to be 200  $\mu\text{m}$ . In order to approximate an infinite line source, a convex/concave lens combination was used as a telescope to expand the beam while a cylindrical lens was then used to focus the generation beam to a line.

The approximate line dimensions, as measured from a piece of laser burn paper, where 20mm x 0.2mm.

### (6.2) SAMPLE SPECIFICATION

As mentioned earlier in this manuscript, the materials that were studied experimentally were samples of single crystal zinc and unidirectional carbon fiber epoxy composites. Table 6.1 list the sample geometry and orientation for the experiments described in this manuscript.

**Table 6.1.** Sample size, orientation and detection scheme.

| MATERIAL  | SIZE (mm)  | ORIENTAION                | DETECTION SCHEME |
|-----------|------------|---------------------------|------------------|
| Zinc      | r=30, d=60 | c-axis $\perp$ surface    | Same side        |
| Zinc      | r=30, d=10 | c-axis $\perp$ surface    | Opposite side    |
| Composite | 6 x 6 x 1  | fibers $\perp$ surface    | Same side        |
| Composite | 6 x 6 x 2  | fiber $\parallel$ surface | Opposite side    |
| Composite | 6 x 6 x 2  | fibers $\perp$ surface    | Same side        |
| Composite | 6 x 6 x 2  | fiber $\parallel$ surface | Opposite side    |
| Composite | 6 x 6 x 3  | fibers $\perp$ surface    | Same side        |

The zinc samples were grown from the melt by Dr. Robert E. Green Jr. The zinc specimens were cleaved along basal planes and then polished using Buehler Carbimet paper to produce a mirror like surface. The crystal orientation was determined using x-ray diffraction. The polished surface was perpendicular to the x-ray beam resulting in a diffraction pattern that had six-fold symmetry, confirming that the polished surface coincided with the basal plane. The cylindrical zinc sample had a radius of 15mm and a length of 60mm for same side detection, while sample used for detection of epicentral waves had a radius of 15mm and a length of 10mm.

The carbon fiber epoxy composite samples were cut from a thick specimen of carbon fiber epoxy made by Dr. Chris Byrne. The prepreg was produced by Fiberite, product designation Hy-E 2048A1A. The carbon fiber, designation 20 A, is a high tensile strength pitch based fiber and the resin, designation 948A1, is a short-cure-time epoxy resin. The composite samples were cut to have a plate-like geometry with the plate surface measuring 6 cm x 6 cm. The plates were cut to have a thickness of 1cm, 2cm, or 3cm. The fibers were oriented either parallel or perpendicular to the plate surface. Further discussion regarding experimental parameters or material specification will be given in the next chapter where the experimental and theoretical results are compared.

## CHAPTER 7

In the present chapter, theory will be compared to experimental results obtained from samples of single crystal zinc and unidirectional graphite epoxy. In Chapters 4 and 5, analytical and numerical results were developed for a source with a delta function temporal profile in a half space. Before a direct comparison between experiment and theory can be made, the temporal transfer function representing the experimental setup must be addressed as well as reflection off the back surface of the sample.

### (7.1) REGARDING THE TEMPORAL TRANSFER FUNCTION

The effects of a laser pulse with finite duration and the frequency response of the interferometer can be modeled using the Duhamel formula as follows:

$$u(x_i, t) = u_\delta(x_i, t) \otimes P(t) \otimes C(t) \otimes E(t), \quad (7.1)$$

where  $\otimes$  represents the convolution operation,  $u_\delta$  is the solution for a source that has a delta function temporal profile,  $P(t)$  is the temporal profile of the laser pulse,  $C(t)$  is the delta function response of the interferometer, and  $E(t)$  represents temporal broadening due to a detection spot with finite size. The temporal profile of the laser is expressed as [47].

$$P(t) = \left( \frac{2t^3}{\tau^4} \right) e^{-\frac{t^2}{\tau^2}}, \quad (7.2)$$

where  $\tau$  is the laser pulse width,  $\sim 10$  ns. The exact functional form of  $C(t)$  is not known by the author but the frequency response of the interferometer is determined to a large extent by the frequency response of the photodetectors in the interferometer ( $\Delta\beta = 150$  MHz). The function  $E(t)$  is representative of the finite transit time of the acoustic wave across the detection spot. Thus, the form of  $E(t)$  depends on detection scheme, (i.e. same side or opposite side detection). Figure 7.1 demonstrates the effects of a finite detection spot for detection along the symmetry axis.

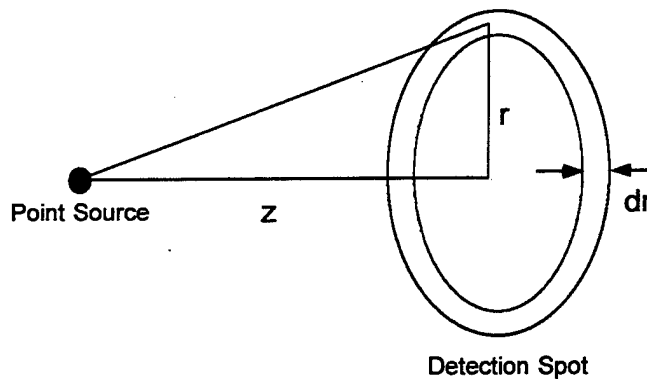


**Fig. 7.1** Schematic showing pulse spreading caused by a finite detection spot. Detection is along the epicentral axis.

Since the detection spot has finite size, acoustic energy emanating from a point source arrives at different portions of the detection spot at different times. For detection along the symmetry axis,  $E(t)$  is given by

$$E(t) = A \int 2\pi e^{(-r^2/N^2)} r dr = -\pi AN^2 e^{(-r^2/N^2)}, \quad (7.3)$$

where A is a normalization constant and N, the pulse width, is related to the radius of the beam at half intensity,  $r_{HM}$ , as follows:

$$N = r_{HM} \sqrt{\frac{-1}{\ln(1/2)}}. \quad (7.4)$$

By expressing time as

$$t = \frac{r(\sqrt{\bar{z}^2 + 1} - \bar{z})}{v}, \quad (7.5)$$

$$\bar{z} = z/r,$$

where v is the acoustic velocity, the expression for E(t) can be rewritten as

$$E(t) = \pi AN^2 e^{(-t^2/\bar{N}^2)}, \quad (7.6)$$

$$\bar{N} = N \sqrt{(2\bar{z}^2 + 1 - 2\bar{z}\sqrt{\bar{z}^2 + 1})},$$

where  $\bar{N}$  is the modified pulse width. For example,  $\bar{N}=10\text{ns}$  for a detection spot with a FWHM of 1mm, and an acoustic velocity of 3 mm/ $\mu\text{s}$ . It should be noted that it was assumed that the amplitude of the acoustic disturbance was constant across the detection spot. This assumption is valid for large values of  $\bar{z}$ .

In order to develop  $E(t)$  for same side detection, consider a surface wave with plane phase fronts that are perpendicular to the free surface as shown in fig. 7.2.

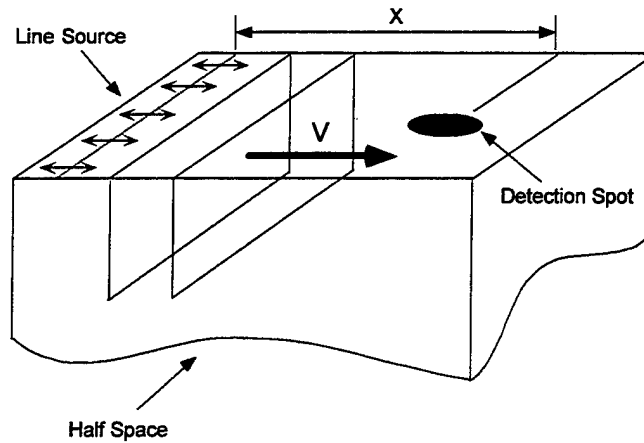


**Fig. 7.2** Schematic showing pulse spreading caused by a finite detection spot. Detection and generation on same side of sample.

For same side detection,  $E(t)$  takes the form,

$$E(t) = Ae^{(-t^2/\bar{N}^2)}, \quad (7.7)$$

where  $\bar{N}$  for same side detection is defined by

$$\bar{N} = \frac{r_{HM}}{v} \sqrt{\frac{-1}{\ln(1/2)}}. \quad (7.8)$$

For a detection spot with a FWHM of 1mm and an acoustic velocity of  $3 \text{ mm}/\mu\text{s}$ ,  $\bar{N}=0.20 \mu\text{s}$ . It should be noted that while this is an exact treatment for a line source, it serves as an approximation for a point source. For a point source, the approximation becomes more accurate as the source/receiver distance increases.

For detection of surface waves, the temporal broadening of the signal is dominated by  $E(t)$ , while  $E(t)$  and  $P(t)$  have similar pulse widths for detection along the epicentral axis. In this manuscript, broadening effects were modeled by convolving the theoretical displacement with a Gaussian having the appropriate pulse width. This is a good approximation for same side detection but perhaps only a fair approximation for detection along the epicentral axis. Since the form of  $C(t)$  not known, including  $P(t)$  in Eq. 7.1 would not necessarily enhance the comparison between theory and experiment.

### *(7.2) BACK-FACE REFLECTION COEFFICIENTS*

Bulk waves, with velocity  $v$ , propagating in a sample with a plate-geometry experience reflections off the traction free surfaces of the sample. Each time the wave reflects off the plate surface, the amplitude and temporal character of the wave is modified. The modification to the wave is described by reflection coefficients, which are a function of observation angle. Solutions that are germane for a plate with two parallel traction free boundaries,  $x_3=0$ ,  $x_3=h$ , can be obtained from solutions for a half-space given in Chapter 4 and Chapter 5 with the aid of the appropriate reflection coefficients. As an example, consider the transformed

displacement due to a laser line source at the back surface of the plate. The out-of-plane displacement for  $h/v > t > 2h/v$  is given by,

$$u_{bs}(\eta, h, s) = (A_3 + SS_{3h}A_3 + SL_{3h}A_3)e^{-\zeta_1 h} + (A_4 + LL_{3h}A_4 + LS_{3h}A_4)e^{-\zeta_3 h}, \quad (7.9)$$

where  $A_{3/4}$  are defined in Eq. 4.20, and the reflection coefficients for the back surface are obtained following the procedure preceding Eq. 5.21. Ideally this development should be used when comparing experiment and theory since the displacement at the back surface is a superposition of the incident wave and the reflected wave. For the isotropic case, Rose [5] shows that along the epicentral direction, reflection primarily alters the amplitude of the reflected wave. It is assumed that a similar result holds for an anisotropic material. Since the emphasis in this manuscript is to compare the temporal character between experiment and theory, the effect of reflection off the back surface will not be taken into account.

### (7.3) RESULTS AND DISCUSSION (ZINC)

In Fig. 7.3 a comparison between theory and experiment for same side detection is presented for single crystal zinc (c-axis perpendicular to surface). The experimental curve is single shot data and the source/receiver separation was 9.1 mm. The theoretical result in Fig. 7.3 is convolved with a Gaussian function ( $\bar{N}=310$  ns) in order to mimic broadening effects. The first disturbance turns on and off at times corresponding to the arrival of the longitudinal wave and shear wave

respectively. The largest disturbance corresponds to the Rayleigh pole and is in the form of a traveling delta function.

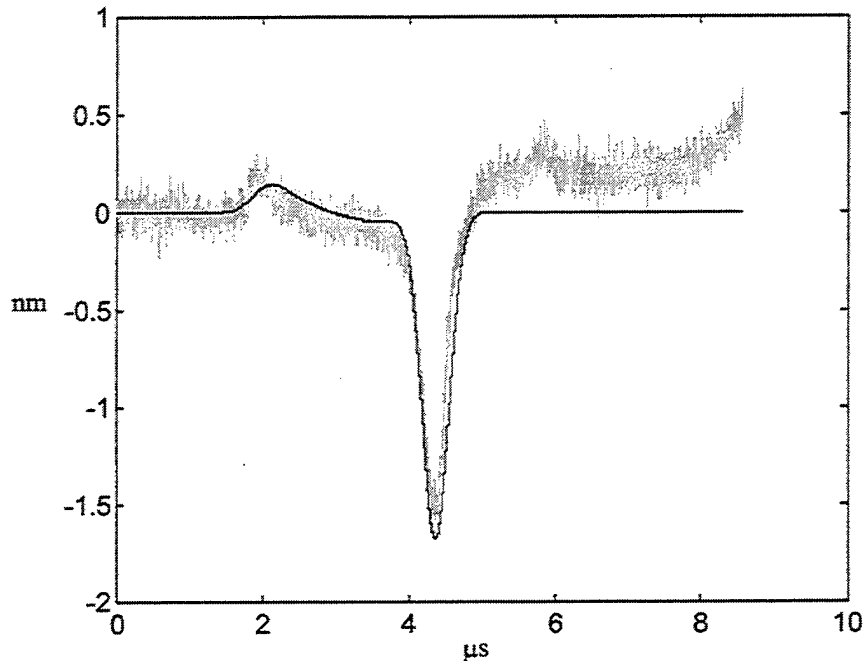


Fig. 7.3. Comparison between experiment and theory for surface waves in zinc.

The amplitude of the theoretical curve was scaled to match the experimental amplitude. Since the data was single shot, comparison of theoretical and experimental amplitudes allows an estimate of the optical reflection coefficient. The theoretical amplitude, given in Eq. 4.38, is expressed by

$$A_{\text{Rayleigh}} = \bar{F} \Psi_r q_0 \left( \frac{1}{N\sqrt{\pi}} \right) \sqrt{C_{44}/\rho}, \quad (7.10)$$

$$\bar{F} = \frac{1}{\rho C} \left[ \frac{B_{33}}{C_{44}} (1 - \kappa) + \frac{B_{22}}{C_{44}} \alpha \right],$$

where  $q_0$  represents the linear energy density. The data shown in Fig. 7.3 was produced by a 37 mJ pulse distributed over 1 cm. Scaling the theoretical amplitude of the Rayleigh wave to match the experimental data, the reflectivity at the sample's surface was estimated to be 90%, which is comparable to published values for zinc. It should be noted that the accuracy of these results decreases as the aspect ratio, the ratio between the line source length and the source receiver distance, decreases.

Figure 7.4 compares theory and experiment for displacement along the epicentral axis for a sample of single crystal zinc (c-axis perpendicular to free surface).

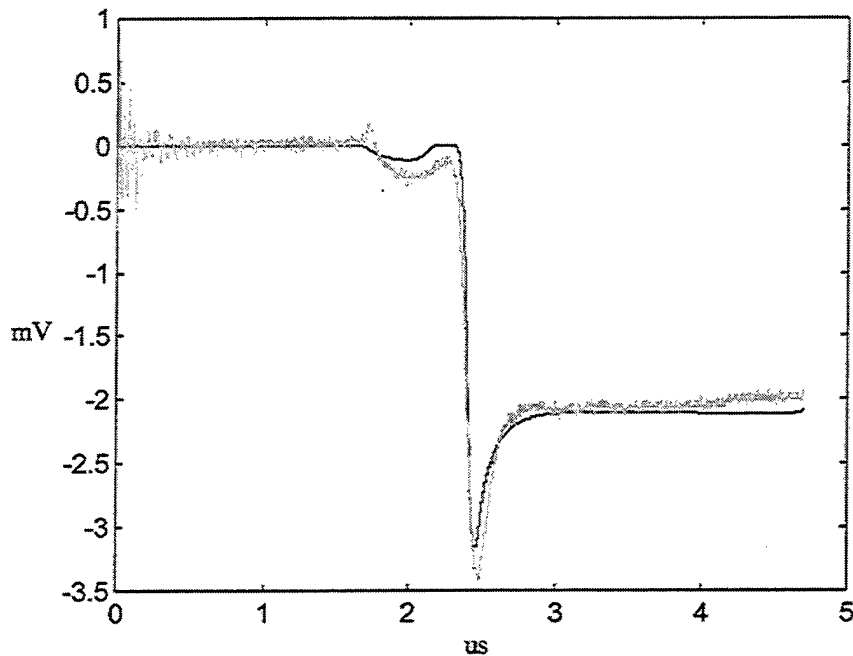


**Fig. 7.4.** Comparison between experiment and theory for displacements along the epicentral axis.

The source/receiver distance was 5mm and the signal was averaged 25 times to improve the signal-to-noise ratio. Again, the theoretical result was convolved with a Gaussian ( $\bar{N}=20$  ns). Zinc is a class three crystal and as a result, the displacement

character differs markedly from its isotropic counterpart. In a fashion similar to that of the surface wave case, the first disturbance turns on and off at times corresponding to the arrival of the longitudinal wave,  $t_l$ , and shear wave,  $t_s$ , respectively. After  $t_s$ , the displacement is identically zero until the arrival of the majority of the acoustic energy at  $t_+$ . The disturbance that arrives at  $t_+$  results from a reciprocal square root singularity and is referred to as phonon focusing [45].

Figure 7.5 shows a comparison between experiment and theory for axial displacements along the epicentral axis for a point source in zinc (c-axis perpendicular to surface).

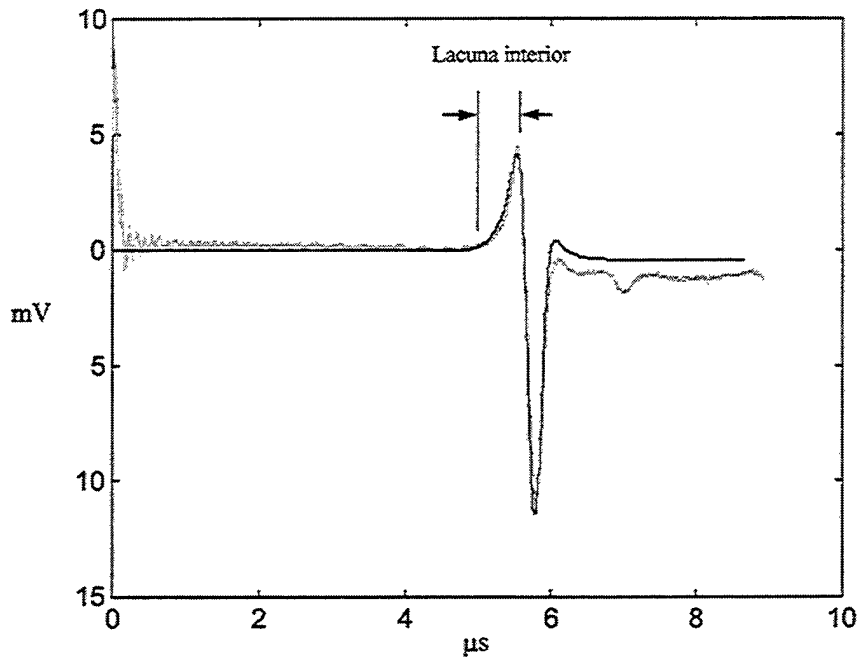


**Fig. 7.5.** Comparison between experiment and theory for axial displacements along the epicentral axis resulting from a point source.

The theoretical result shown in Fig. 7.5 was convolved with a Gaussian pulse ( $\bar{N}=20$  ns). The experimental data in Fig. 7.5 confirms that, unlike a line source, the waveform for a point source corresponding to the interior of the lacuna is non-zero.

A comparison between experiment and theory for observation off the symmetry axis,  $\theta=10^\circ$ , is shown in Fig. 7.6 (c-axis perpendicular to surface). The source is a surface line source. The experimental data was average 25 times to improve the signal-to-noise ratio and the theoretical result was convolved with a Gaussian ( $\bar{N}=20$  ns) to mimic broadening effects. The experimental data in Fig. 7.6 clearly shows the splitting of the wave caused by the conical portion of the slowness surface.

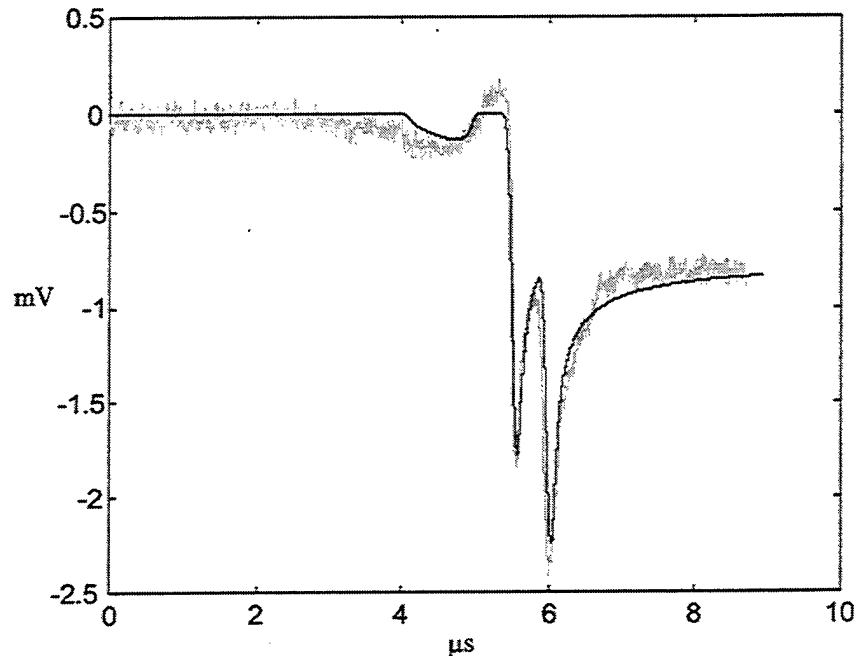
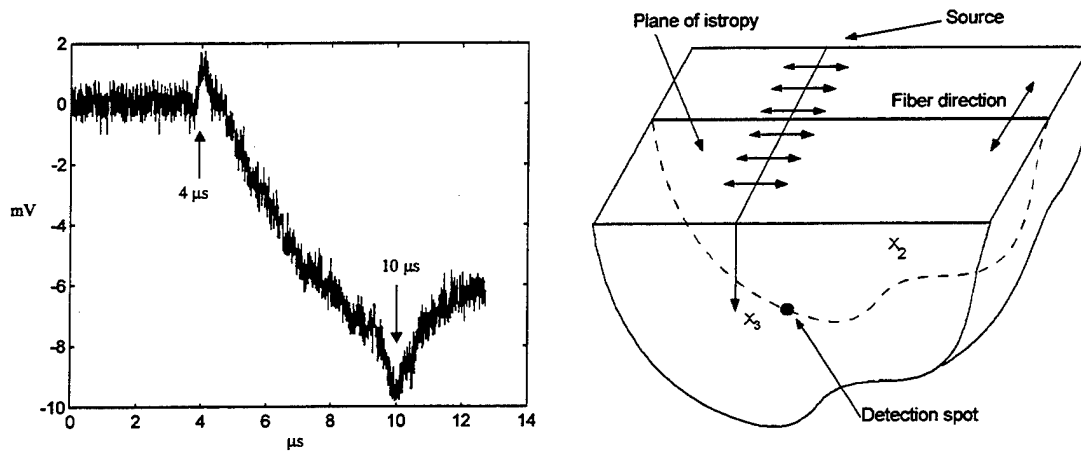


Fig. 7.6. Comparison between experiment and theory for axial displacements off the epicentral axis. The observation angle is  $10^\circ$ .

#### (7.4) RESULTS AND DISCUSSION (GRAPHITE EPOXY)

Before predicting the displacement waveforms caused by a laser source in unidirectional carbon fiber epoxy composites, the elastic constants must be determined. As was mentioned in chapter 2, unidirectional carbon fiber epoxy is transversely isotropic, hence, there are five unknown elastic constants. There are a number of ultrasonic techniques currently used to determine the elastic constants in anisotropic materials. Most of these techniques involve comparing the theoretical and experimentally obtained slowness curves. T.T. Wu and Z.H. Ho [25], have determined the elastic constants in unidirectional graphite epoxy by numerically fitting the theoretical slowness curves to the slowness curve obtained experimentally. This method has two drawbacks. First, the researcher must identify wave front arrivals as a function of angle in a very complicated waveform. Second, since the theoretical slowness surface is matched to the experimental slowness surface through an iterative method, a numerical algorithm must be used. The method proposed in this manuscript for determining the elastic constants involves measuring five acoustic velocities.

Figure 7.7 shows an epicentral waveform resulting from a laser line source in a sample of carbon fiber epoxy composite. As shown on the right hand side of Fig. 7.7, the fibers are parallel to the surface and to the source. Since the displacements and the derivative of the displacements parallel to the line source vanish, the problem reduces to the isotropic case.



**Fig. 7.7.** Waveform and experimental geometry used for determination of elastic constants. The sample thickness is 12mm.

The relation between the elastic constants and the acoustic velocity for this experimental setup is given by

$$v_L = \sqrt{\frac{C_{11}}{\rho}}, \quad v_s = \sqrt{\frac{C_{66}}{\rho}} = \sqrt{\frac{(C_{11} - C_{12})}{\rho}}. \quad (7.11)$$

In Fig. 7.8, the waveform resulting from a laser point source is given. The fibers are parallel to the surface. The first arrival corresponds to the longitudinal wave and the second and third arrivals correspond to the fast and slow shear waves respectively.

Equation 7.12 gives the relation between the elastic constants and the various acoustic velocities.

$$v_L = \sqrt{\frac{C_{11}}{\rho}}, \quad v_{S1} = \sqrt{\frac{C_{44}}{\rho}}, \quad v_{S2} = \sqrt{\frac{C_{66}}{\rho}}. \quad (7.12)$$

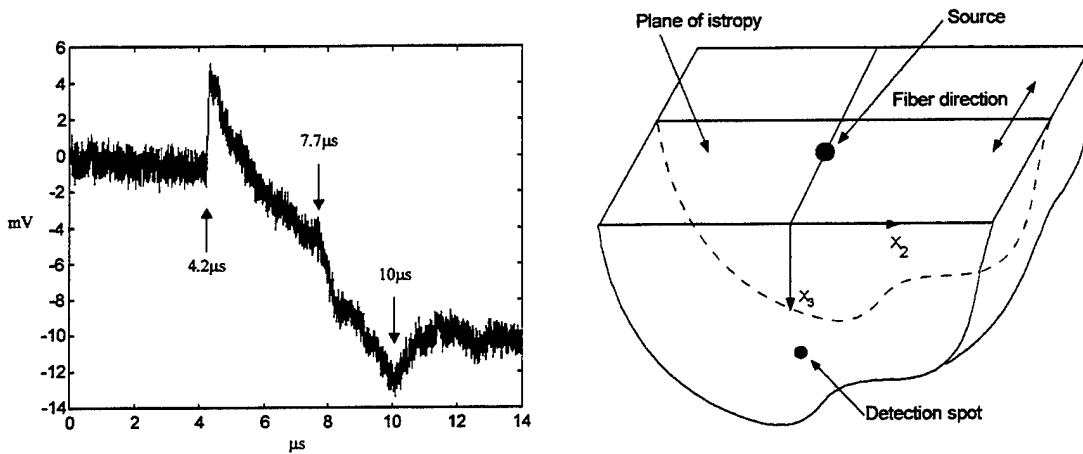


**Fig. 7.8.** Waveform and experimental geometry used for determination of elastic constants. The sample thickness is 12mm.

Figure 7.9 shows the epicentral waveform resulting from a laser line source. The fibers are perpendicular to the sample surface. There are two reflections of the longitudinal wave before the arrival of the shear wave at  $v_s = (C_{44}/\rho)^{1/2}$ . The magnitude of the shear wave at the wave front is proportional to the noise level, thus using the arrival of the shear wave for this experimental setup to determine  $C_{44}$  would be difficult.

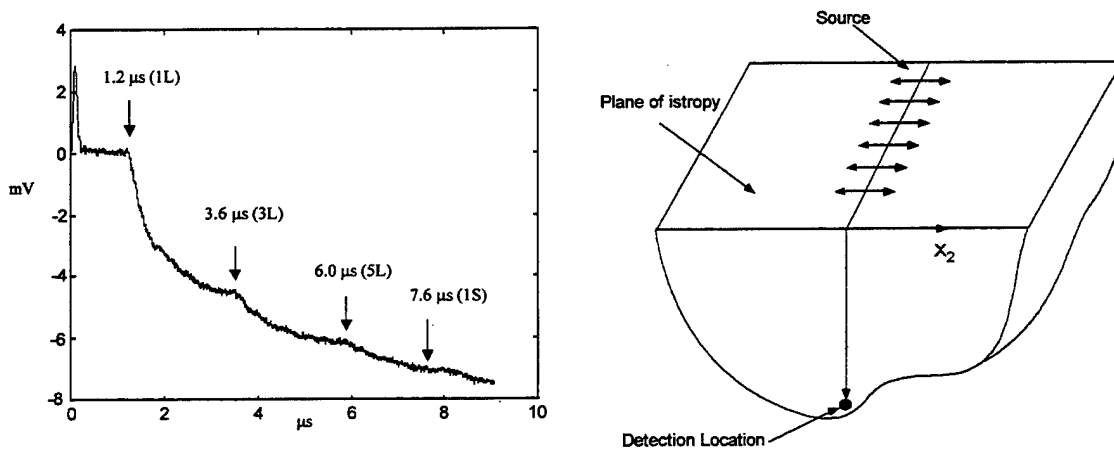


**Fig. 7.9.** Waveform and experimental geometry used for determination of elastic constants. The sample thickness is 12mm.

Equation 7.12 gives the relation between the elastic constant,  $C_{33}$ , and the velocity of the longitudinal wave for the experimental geometry given in Fig. 7.9.

$$v_L = \sqrt{\frac{C_{33}}{\rho}}. \quad (7.12)$$

The remaining elastic constant,  $C_{13}$ , can be determined by measuring the Rayleigh velocity in a direction perpendicular to the fibers. The roots of the Rayleigh equations are uniquely determined by knowledge of the Rayleigh velocity,  $C_{11}$ ,  $C_{33}$ , and  $C_{44}$ . They are obtained by solving

$$D = [2(1 - \kappa)(\omega^4 + \omega^2) - (\gamma\omega^2 + \alpha)(\omega^2 + 1) - \alpha\zeta_1\zeta_3] = 0, \quad (7.13)$$

where  $\alpha$ ,  $\gamma$ , and  $\kappa$  are defined by Eq. 3.33, and  $\omega$  is the slowness. In Fig. 7.10 the out-of-plane surface displacement resulting from a laser line source is plotted. The fibers are perpendicular to the surface, giving the surface as the plane of isotropy. The first wave to arrive is a bulk wave traveling at the longitudinal velocity. The later arriving negative spike is the Rayleigh wave. Since the Rayleigh wave travels without dispersion, the Rayleigh velocity can be obtained by measuring the transit time between two detection spots. For more accurate time of flight results, two signals obtained at different detection spots could be autocorrelated.

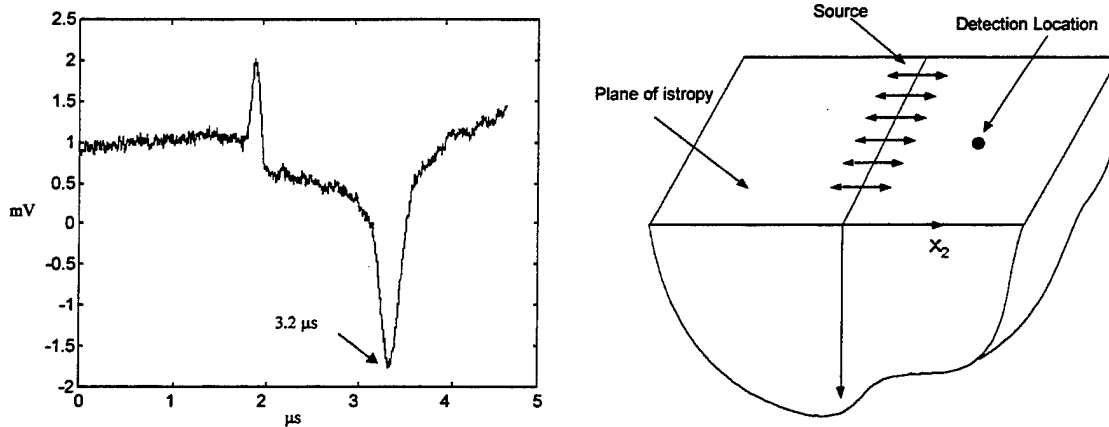


**Fig. 7.10.** Surface wave displacement wave form and experimental geometry.

The measured Rayleigh velocity for the experimental geometry given in Fig. 7.10, 1.54 mm/μs, is only marginally smaller than the shear wave velocity, 1.56 mm/μs, an artifact of the extreme anisotropy exhibited by the unidirectional carbon fiber epoxy composite sample. Table 7.1 lists the material properties of the carbon fiber epoxy composite, including the elastic constants.

**Table 7.1.** A listing of the elastic constants and the density for unidirectional carbon fiber epoxy.

|                                    |                                    |                                    |
|------------------------------------|------------------------------------|------------------------------------|
| $C_{11}=1.56 \times 10^{11}$ dynes | $C_{12}=1.06 \times 10^{11}$ dynes | $C_{13}=2.17 \times 10^{11}$ dynes |
| $C_{33}=16.6 \times 10^{11}$ dynes | $C_{44}=0.42 \times 10^{11}$ dynes | $\alpha=39.5$                      |
| $\beta=3.7$                        | $\gamma=109$                       | $\rho=1.73$ g/cm <sup>2</sup>      |

In Figs. 7.11 and 7.12, the slowness curves and the wavefront curves are plotted using the elastic constants listed in Table 7.1. Notice that the shear branch of the

wave front curve has a cuspidal triangle that does not intersect an axis of material symmetry, thus, the elastic character is defined by class V (see chapter 3).

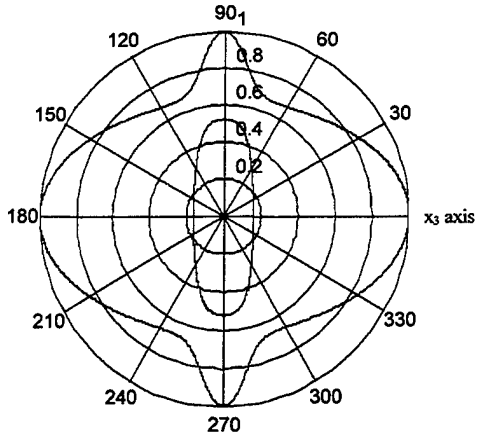


**Fig. 7.11.** Normal curve for unidirectional carbon fiber epoxy sample.

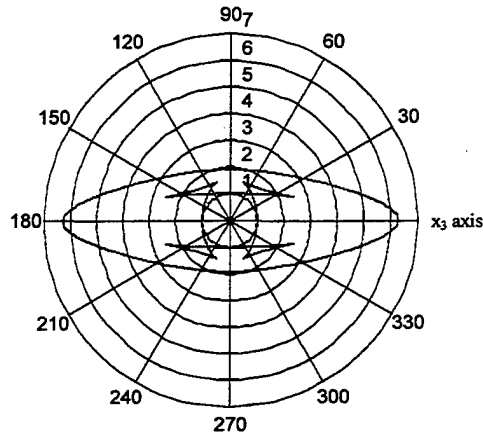


**Fig. 7.12.** Wave front curve for unidirectional carbon fiber epoxy sample.

Now that the elastic constants have been determined, comparison between experiment and theory can be made. Figure 7.132 compares experimental and

theoretical epicentral waveforms resulting from a laser line source oriented parallel to the fiber direction in a sample of carbon fiber epoxy composite. The theoretical signal was convolved with a Gaussian pulse ( $\bar{N}=20\text{ns}$ ) to account for pulse broadening effects. In addition, the experimental signal shown in Fig. 7.13 was signal averaged 25 times to improve the signal-to-noise ratio. As was the case for Fig. 7.7, this problem reduces to the isotropic case since the fibers are parallel to both the surface and the line source. The close comparison between experiment and theory for this experimental setup further bolsters the claim of transverse isotropy.

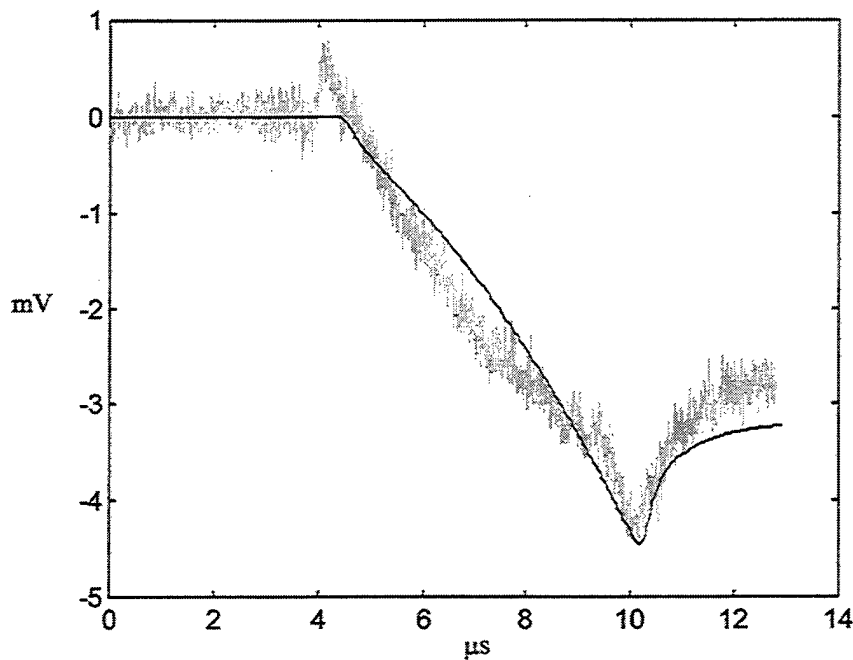


**Fig. 7.13.** Comparison between experiment and theory for a laser line source in carbon fiber epoxy composite. The fibers were oriented parallel to both the surface and the line source.

Figure 7.14 shows a comparison between experiment and theory for surface waves in a unidirection carbon fiber sample. The waves were generated with a laser line source and the fibers were oriented perpendicular to the sample surface.

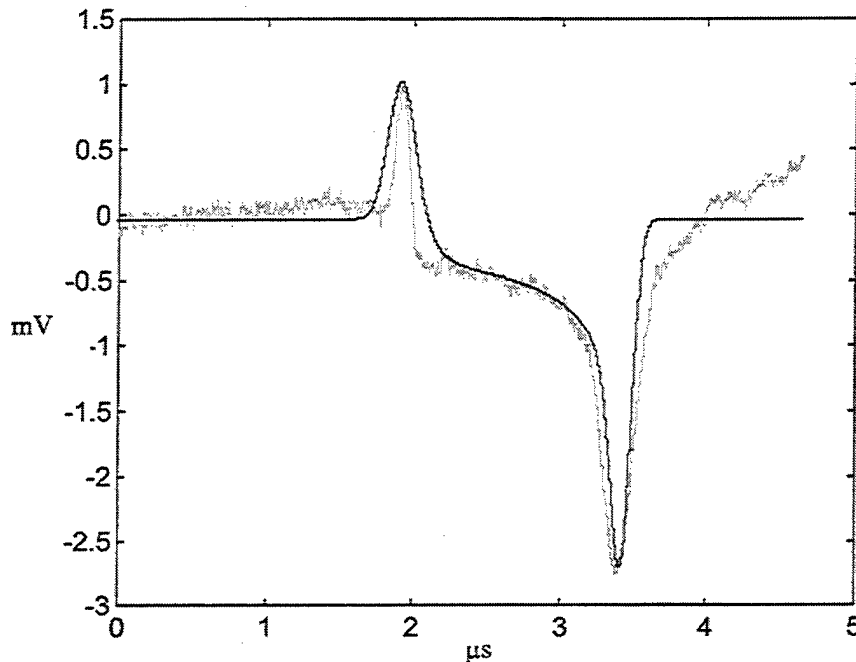


**Fig. 7.14.** Comparison between experiment and theory for surface waves generated with a laser line source in carbon fiber epoxy composite. The fibers were oriented perpendicular to the sample surface.

The theoretical signal was convolved with a Gaussian pulse ( $\bar{N}=200\text{ns}$ ) to model the effects of pulse broadening. It is of interest to note that the early arriving positive spike has a pulse width that is more narrow than that predicted by theory while the later arriving Rayleigh spike has a pulse width that is slightly wider than that predicted by theory. A possible explanation of this phenomenon will be given later in this chapter.

The experimental epicentral waveform is compared with theory in Fig. 7.15. The signal was generated with a laser line source and the fibers were oriented

perpendicular to the surface. The direct longitudinal wave arrives at  $1.2 \mu\text{s}$  followed by two reflected longitudinal waves and the direct shear wave arriving at  $7.6 \mu\text{s}$ . Since two reflected longitudinal waves arrive at the detector before the shear arrival, a direct comparison between theory and experiment is not possible for this case.

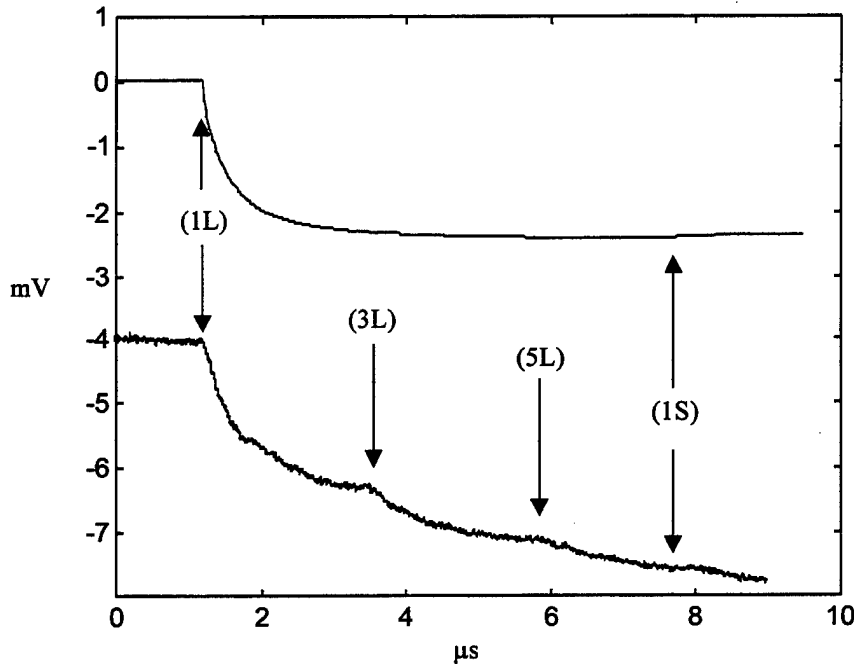


**Fig. 7.15.** Comparison between experiment and theory for the epicentral displacement resulting from a laser line source. Fibers were oriented perpendicular to sample surface.

Nevertheless, Fig. 7.15 illustrates the similarity between experiment and theory for the portion of the wave before the arrival of the first reflected longitudinal wave (3L). In addition, it should be noted that the theoretical curve confirms the fact that the magnitude of the shear wave is very small compared to the longitudinal wave.

Figure, 7.16 shows a comparison between experiment and theory for epicentral displacement resulting from a laser point source. The fibers were oriented perpendicular to the sample surface. To facilitate a direct comparison, only the

portion of the wave arriving before the first reflected longitudinal arrival is plotted.

The theoretical curve has been convolved with a Gaussian pulse ( $\bar{N}=20$  ns) to mimic the effect of temporal broadening.

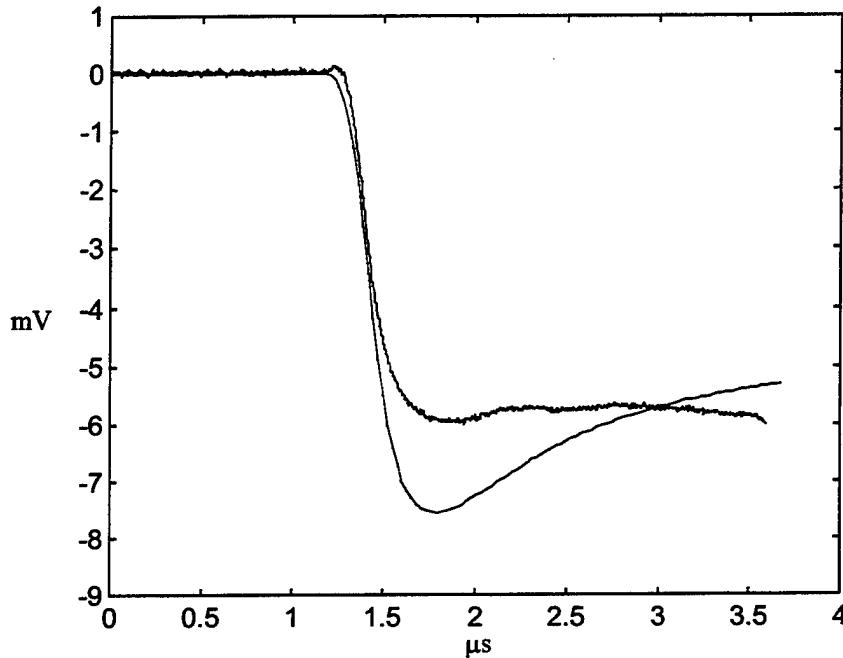


**Fig. 7.16.** Comparison between experiment and theory for the epicentral displacement resulting from a laser point source. Fibers were oriented perpendicular to sample surface.

The experimental data suggest a step profile for the displacement while the theoretical data shows the displacement record reaching a maximum value and then dropping back to a steady state value. It was first thought that the discrepancy between experiment and theory for the point source case was a result of the finite dimension of the source.

In Fig. 7.17, a sequence of epicentral waves is plotted with the source diameter as a parameter. The radius at half maximum of the detection spot varied from 0.18 cm to 0.14 cm.

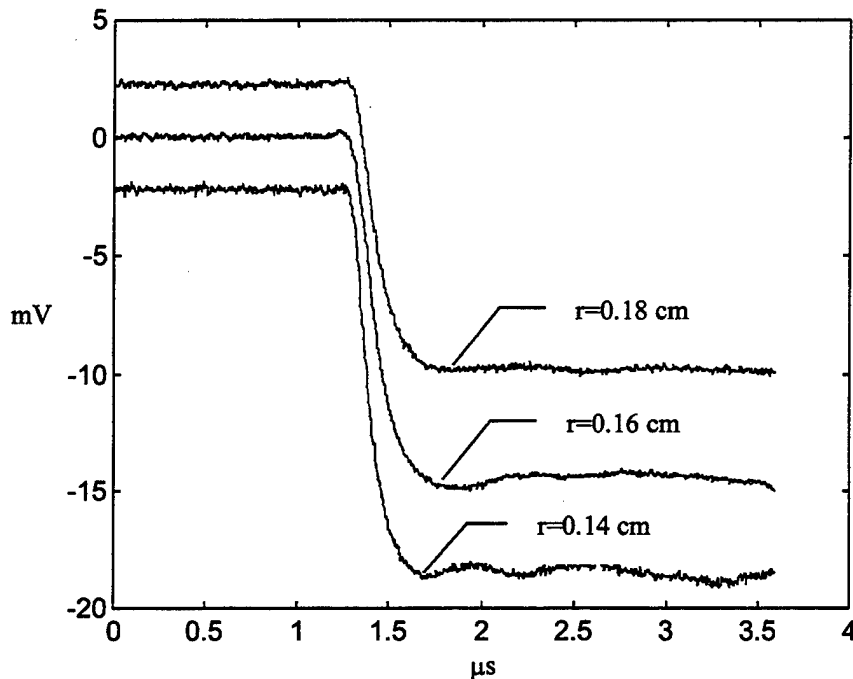


**Fig. 7.17.** Epicentral waves resulting from a laser source with circular symmetry.

Figure 7.17 illustrates that as the source radius decreases, the displacement waveform starts to develop a rippled structure. This structure may be caused by wave guiding effects. It would be instructive to continue the sequence shown in Fig. 7.17 to smaller source radii, but as the spot size decreases it becomes more difficult to generate a detectable signal without ablating the material. In Fig. 7.18, an epicentral waveform resulting from an ablative source is plotted. The generation spot size used to generate the data in this figure was approximately 50  $\mu\text{m}$ .

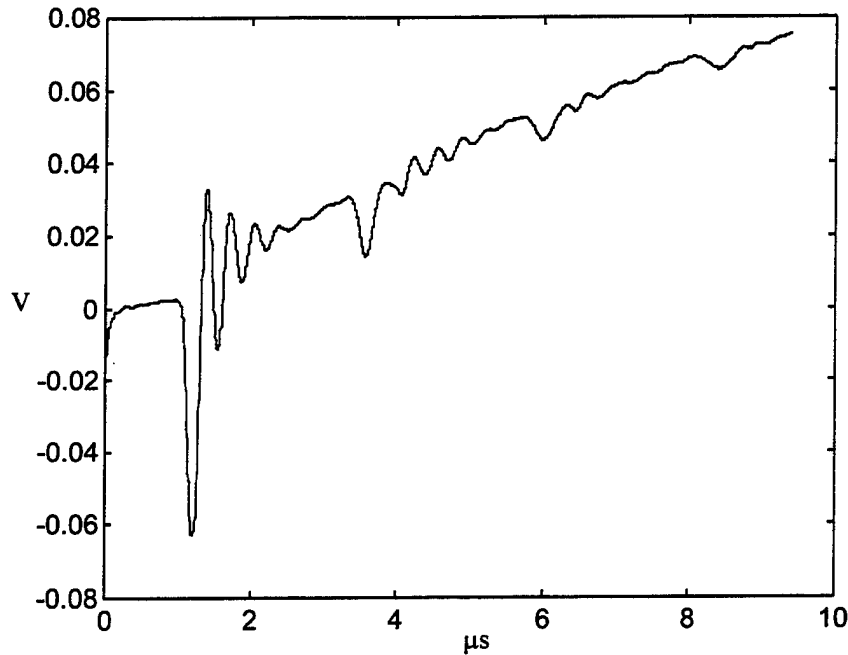


**Fig. 7.18.** Epicentral waveform resulting from an ablative point source. The fibers are oriented perpendicular to the sample surface.

If the ringing exhibited by the waveform in Fig. 7.18 is a result of wave-guiding effects, then the temporal character of the waveform should change with propagation distance. In Fig. 7.19, the temporal profiles of the direct longitudinal wave and the first reflected longitudinal wave (Fig. 7.18) are compared.

The data shown in Fig. 7.19 tends to support the idea that the epicentral waveforms in unidirectional carbon fiber epoxy composite undergo the effects of dispersion. Questions regarding the origin of these dispersive effects are left for future work. One can speculate that the dispersive effects are an artifact of the material's heterogeneous character. In addition, it appears that the magnitude of the dispersive effect is a function of observation direction. For observation directions where the wave vector is perpendicular to the fiber direction, theory and experiment agreed well. One could further speculate that the dispersive effect in unidirectional

carbon epoxy composite is a function of the particle motion. This might also account for the discrepancy in pulse widths between experiment and theory shown in Fig. 7.14. The particle motion for the Rayleigh wave is retrograde elliptical while the surface skimming bulk wave is polarized either parallel or perpendicular to the wave vector.

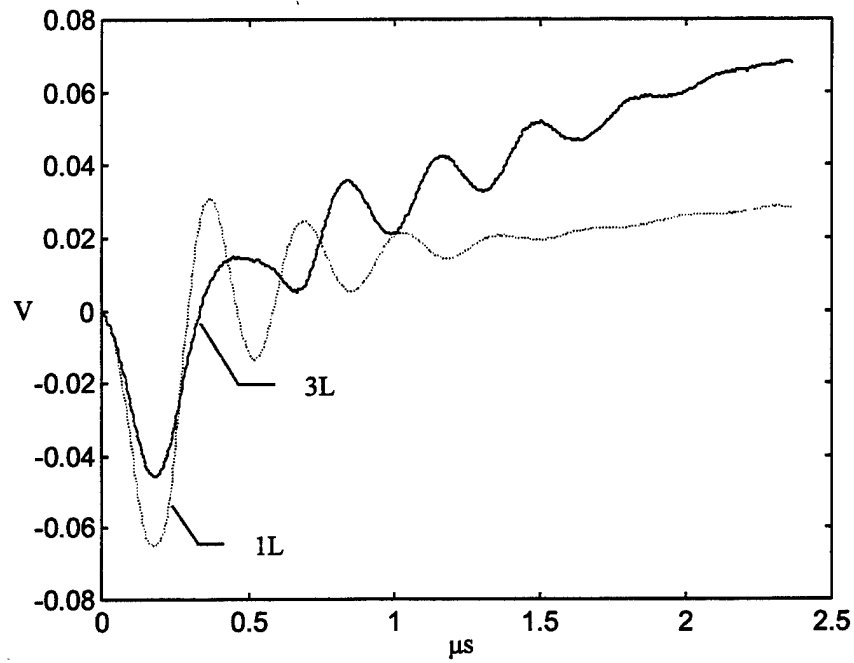


**Fig. 7.19.** Comparison of temporal profile between direct longitudinal wave and first reflected longitudinal wave. The signal was produce with an ablative point source.

## *(7.4) CONCLUSIONS*

### *(7.4.1) SUMMARY OF PRESENTATION*

In this manuscript an investigation of laser-generated ultrasound in unidirectional carbon-fiber-reinforced epoxy was given. An elastodynamic theory that accounted for the elastic anisotropic nature of carbon-fiber epoxy was presented. It was found that the unidirectional carbon-fiber-reinforced samples could be modeled as transversely isotropic in planes perpendicular to the fiber direction. In the theoretical development, the effect of thermal diffusion was neglected and it was assumed that all the absorbed laser energy was deposited along a line or at a point located either beneath the sample surface or on the sample surface. A surface source is applicable in cases where the laser energy is absorbed within the first few nanometers of the exposed surface while a buried source is applicable for sub-surface absorbers such as embedded carbon fibers in an epoxy matrix.

A formal solution of the problem was found using double (Fourier-Laplace) transforms. The Cagniard-de Hoop technique was used to analytically invert the transformed solution for the epicentral case as well as for the surface wave case. Solutions for a sub-surface source and for observation points that are off the epicentral axis were obtained numerically.

Experimental validation of the theory was performed using single crystal zinc and a unidirectional carbon epoxy sample. Zinc was used as a prototype to ensure that the theory correctly predicts the effects of elastic anisotropy. Like unidirectional carbon-fiber-reinforced epoxy, zinc is also transversely isotropic along planes perpendicular to the c-axis. The zinc samples were cut to have the free

surface coincide with a plane of isotropy. Theoretical and experimental results for zinc agreed well for all the cases considered (displacements along the surface, epicentral direction and off-epicentral direction).

The carbon-fiber samples were cut so that the fibers were perpendicular to the surface, thus giving the free surface as a plane of isotropy. It was found that the carbon-fiber epoxy samples exhibit homogeneous behavior when the wave vector is perpendicular to the fiber direction. When the wave vector is aligned with the fiber direction, as was the case for displacements along the epicentral axis, the waveform exhibits the effects of frequency-dependent dispersion. It was speculated that these dispersive effects are an artifact wave-guiding resulting from the material's heterogeneous character.

#### (7.4.2) *FUTURE WORK*

Before concluding, it is appropriate to discuss the direction of future work related to the material presented in this manuscript. The first area for future work would be to consider other crystal symmetries. In this manuscript, only materials that exhibited transverse isotropy were considered. In order to correctly model the effects of elastic anisotropy in carbon-fiber-reinforced epoxies that have fiber lay-ups other than unidirectional, additional crystal symmetries must be considered.

The effects of heterogeneities must also be more thoroughly addressed. Experimental results suggested that wave-guiding by the carbon fibers in unidirectional carbon-fiber epoxy influences the displacement waveform along the epicentral axis. One of two methods could be used to model the effects of heterogeneities. The more heuristic approach would be to incorporate the effects of

heterogeneities, using first principles, into the model from the beginning. Perhaps the more realistic approach would be to apply a transfer function to the theoretical solution so that it matches the experimental results. The transfer function would account for frequency dependent attenuation and frequency dependent dispersion. This approach is phenomenological and as a result it would shed little light on the true nature of acoustic wave propagation through a heterogeneous material.

## APPENDIX 1: PROGRAM LISTINGS

**Program Burdis**

% This m-file put together the displacement arrays defined in Burline.m in the correct  
 % temporal order. For example, the buried shear mode converted to a longitudinal wave  
 % can arrive before the direct shear depending upon the value of  $x_3/a$ . Burline.m must  
 % be called before this program.

```
tsx=sort(txx);
for n=1:6
[i,yn(n)]=min(abs(txx(n)-tsx));
end
```

```
for n=1:6
[i,yy(n)]=min(abs(yn-n));
end
```

% Assigning the derivatives of the Cagniard path to the various columns of the  
 % variable d.

```
d(1,:)=d1x1;
d(2,:)=d3x3;
d(3,:)=db1x1;
d(4,:)=db3x3;
d(5,:)=d3x1;
d(6,:)=d1x3;
```

% The derivatives of the Cagniard paths are put in the correct temporal order, (dd).  
 % For example d(1,:) might correspond to shear branch mode converted as a longitudinal  
 % branch. This branch will arrive before or after other branches depending on the value  
 % of  $x_3$ .

```
for n=1:6
ug=yn(n)
dd(n,:)=d(yy(n),:);
end
```

```
maxjj=round(maxj+tsx(1)/delt)-1;
```

```
for xxx=1:maxjj
```

```
t=delt*(xxx-1);
```

```
if t<=tsx(1)
```

```

dis(xxx)=0;
y1=xxx;

elseif t>tsx(1) & t<=tsx(2)
dis(xxx)=(dd(1,xxx-y1));
dis1=imag(dis);
y2=xxx;

elseif t>tsx(2) & t<=tsx(3)
dis(xxx)=(dd(1,xxx-y1)+(dd(2,xxx-y2)));
dis2=imag(dis);
y3=xxx;

elseif t>tsx(3) & t<=tsx(4)
dis(xxx)=(dd(1,xxx-y1)+(dd(2,xxx-y2)+(dd(3,xxx-y3)));
dis3=imag(dis);
y4=xxx;

elseif t>tsx(4) & t<=tsx(5)
dis(xxx)=(dd(1,xxx-y1)+(dd(2,xxx-y2)+(dd(3,xxx-y3)+(dd(4,xxx-y4)));
dis4=imag(dis);
y5=xxx;

elseif t>tsx(5) & t<=(tsx(6)+1)
dis(xxx)=(dd(1,xxx-y1)+(dd(2,xxx-y2)+(dd(3,xxx-y3)+(dd(4,xxx-y4)+(dd(5,xxx-
y5)));
dis5=imag(dis);
y6=xxx;

else
dis(xxx)=(dd(1,xxx-y1)+(dd(2,xxx-y2)+(dd(3,xxx-y3)+(dd(4,xxx-y4)+(dd(5,xxx-
y5)+(dd(6,xxx-y6)));
dis6=imag(dis);
end
end

```

**Program Cagn1x1**

```
% This m-file defines the cagniard path for w1x1,w3x3,wb1x1, and wb3x3. The
% Cagniard path for these expressions is obtained analytically (without resorting to root
% finding methods). The m-file cagn3x1 is called to numerically find the w3x1 and
% w1x3 paths
```

```
function [w3x1,w1x3,w1x1,w3x3,wb1x1,wb3x3,txx]=cagn1x1
(alpha,beta,delta,X3,delt,maxj);
```

```
[w3x1,w1x3,txx]=cagn3x1 (alpha,beta,delta,X3,delt,maxj);
```

```
for hh=1:4
txx(1)=(1+X3);
txx(2)=(1+X3)/sqrt(alpha);
txx(3)=X3-1;
txx(4)=(X3-1)/sqrt(alpha);
t=txx(hh);
```

```
% Loop for finding roots at each time step
```

```
if hh==1
```

```
for jj=1:maxj
```

```
tau=t+(jj-1)*delt; % increment time
```

```
% Define coefficients for quadratic formula
```

```
C = (tau^2-1/2*(alpha+1)/alpha*(X3+1)^2)^2-1/4*((alpha+1)^2-
4*alpha)/alpha^2*(X3+1)^4;
B = -(tau^2-1/2*(alpha+1)/alpha*(X3+1)^2)*delta/alpha*(X3+1)^2-
1/4*(2*(alpha+1)*delta-4*alpha*(beta+1))/alpha^2*(X3+1)^4;
A = 1/4*delta^2/alpha^2*(X3+1)^4-1/4*(delta^2-4*alpha*beta)/alpha^2*(X3+1)^4;
```

```
% Apply quadratic formula to find roots
```

```
w1x1(jj)=sqrt((-B-sqrt(B^2-4*A*C))/(2*A));
end
```

```
elseif hh==2
```

```
for jj=1:maxj
```

```

tau=t+(jj-1)*delt; % increment time

% Define coefficients for quadratic formula

C = (tau^2-1/2*(alpha+1)/alpha*(X3+1)^2)^2-1/4*((alpha+1)^2-
4*alpha)/alpha^2*(X3+1)^4;
B = -(tau^2-1/2*(alpha+1)/alpha*(X3+1)^2)*delta/alpha*(X3+1)^2-
1/4*(2*(alpha+1)*delta-4*alpha*(beta+1))/alpha^2*(X3+1)^4;
A = 1/4*delta^2/alpha^2*(X3+1)^4-1/4*(delta^2-4*alpha*beta)/alpha^2*(X3+1)^4;

% Apply quadratic formula to find roots

w3x3(jj)=sqrt((-B+sqrt(B^2-4*A*C))/(2*A));
end

elseif hh==3

for jj=1:maxj

tau=t+(jj-1)*delt; % increment time

% Define coefficients for quadratic formula

C = (tau^2-1/2*(alpha+1)/alpha*(X3-1)^2)^2-1/4*((alpha+1)^2-
4*alpha)/alpha^2*(X3-1)^4;
B = -(tau^2-1/2*(alpha+1)/alpha*(X3-1)^2)*delta/alpha*(X3-1)^2-
1/4*(2*(alpha+1)*delta-4*alpha*(beta+1))/alpha^2*(X3-1)^4;
A = 1/4*delta^2/alpha^2*(X3-1)^4-1/4*(delta^2-4*alpha*beta)/alpha^2*(X3-1)^4;

% Apply quadratic formula to find roots

wb1x1(jj)=sqrt((-B-sqrt(B^2-4*A*C))/(2*A));
end

elseif hh==4

for jj=1:maxj

tau=t+(jj-1)*delt; % increment time

```

% Define coefficients for quadratic formula

$C = (\tau^{2-1/2}(\alpha+1)/\alpha(X3-1)^2)^2 - 1/4 * ((\alpha+1)^2 - 4\alpha)/\alpha^2(X3-1)^4;$

$B = -(\tau^{2-1/2}(\alpha+1)/\alpha(X3-1)^2) * \delta/\alpha(X3-1)^2 - 1/4 * (2 * (\alpha+1) * \delta - 4 * \alpha * (\beta+1))/\alpha^2(X3-1)^4;$

$A = 1/4 * \delta^2/\alpha^2(X3-1)^4 - 1/4 * (\delta^2 - 4 * \alpha * \beta)/\alpha^2(X3-1)^4;$

% Apply quadratic formula to find roots

$wb3x3(jj) = \text{sqrt}((-B + \text{sqrt}(B^2 - 4 * A * C))/(2 * A));$

end

end

end

**Program Cagn3x1**

% This m-file defines the Cagniard paths corresponding to w1x3 and w3x1.  
 % This program utilizes Muller's Method to find the roots. This program  
 % is basically the same as cagn77.m

```
function [w3x1,w1x3,txx]=cagn3x1 (alpha,beta,delta,X3,delt,maxj);
```

```
wst1=.0010;
txx(1)=1+X3/sqrt(alpha);
txx(2)=1/sqrt(alpha)+X3;
txx(5)=txx(1);
txx(6)=txx(2);
```

% loop for shear reflected as long and long reflected as shear

```
for ggg=1:2
```

```
if ggg==1
```

```
clear wr
```

% Define starting omega values with a little uncertainty added on either side  
 % so as to insure that root finding technique converges on root. If the exact root is  
 % given as the first guess, then root finding technique blows up.

```
wr(1)=wst1-(0+.02*j);
wr(2)=wst1*j;
wr(3)=wst1+(.1+.02*j);
t=txx(1);
```

% Loop for finding roots at each time step

```
for jj=1:maxj
tau=t+(jj-1)*delt; % increment time
```

% Define Kraut's Coefficients

```
psi1=(alpha+1)^2-4*alpha;
psi2=1/4*(alpha+1)^2/alpha^2-1/4*((alpha+1)^2-4*alpha)/alpha^2;
psi3=tau^2-1/2*(alpha+1)/alpha*(X3^2+1);
psi4=2*(alpha+1)*delta-4*alpha*(beta+1);
psi5=1/2*(alpha+1)*delta/alpha^2-1/4*(2*(alpha+1)*delta-
4*alpha*(beta+1))/alpha^2;
```

```

psi6=-(tau^2-1/2*(alpha+1)/alpha*(X3^2+1))*delta/alpha*(X3^2+1)-
1/4*(2*(alpha+1)*delta-4*alpha*(beta+1))/alpha^2*(1-X3^2)^2-
4*X3^2*(1/2*(alpha+1)*delta/alpha^2-1/4*(2*(alpha+1)*delta-
4*alpha*(beta+1))/alpha^2);
psi7=delta^2-4*alpha*beta;
psi8=1/4*delta^2/alpha^2-1/4*(delta^2-4*alpha*beta)/alpha^2;
psi9=1/4*(delta^2-4*alpha*beta)/alpha^2*(1-
X3^2)^2+1/4*delta^2/alpha^2*(X3^2+1)^2-4*X3^2*(1/4*delta^2/alpha^2-
1/4*(delta^2-4*alpha*beta)/alpha^2);
phi1=1/4*(alpha+1)^2/alpha^2-1/4*psi1/alpha^2;
phi2=psi3^2-4*X3^2*(1/4*(alpha+1)^2/alpha^2-1/4*psi1/alpha^2)-
1/4*psi1/alpha^2*(1-X3^2)^2;
phi3=-psi3*delta/alpha*(X3^2+1)-1/4*psi4/alpha^2*(1-X3^2)^2-4*X3^2*psi5;
rho1=psi3^2-4*X3^2*phi1-1/4*psi1/alpha^2*(1-X3^2)^2;
w8=psi9^2-4*X3^2*(1-X3^2)^2*psi7/alpha^2*(1/4*delta^2/alpha^2-
1/4*psi7/alpha^2);
w6=-4*X3^2*(1-X3^2)^2*psi4/alpha^2*(1/4*delta^2/alpha^2-1/4*psi7/alpha^2)-
4*X3^2*(1-X3^2)^2*psi7/alpha^2*psi5+2*phi3*psi9;
w4=-4*X3^2*(1-X3^2)^2*psi1/alpha^2*(1/4*delta^2/alpha^2-1/4*psi7/alpha^2)-
4*X3^2*(1-X3^2)^2*psi4/alpha^2*psi5-4*X3^2*(1-
X3^2)^2*psi7/alpha^2*phi1+2*rho1*psi9+phi3^2;
w2=-4*X3^2*(1-X3^2)^2*psi1/alpha^2*psi5-4*X3^2*(1-
X3^2)^2*psi4/alpha^2*phi1+2*rho1*phi3;
w0=rho1^2-4*X3^2*(1-X3^2)^2*psi1/alpha^2*phi1;

eps=1;          % set remainder high so as to enter root finding routine

if jj ~= 1      % For first iteration fill first three omega guesses
    wr(1)=wr(kk-1);
    wr(2)=wr(kk-2);
    wr(3)=wr(kk-3);
end
kk=3;

while abs(eps) > .00000000000001 % loop until remainder is less than this value

% follow algorithm found in "Numerical Recipes"

rpt3=w8*wr(kk)^8+w6*wr(kk)^6+w4*wr(kk)^4+w2*wr(kk)^2+w0;
rpt2=w8*wr(kk-1)^8+w6*wr(kk-1)^6+w4*wr(kk-1)^4+w2*wr(kk-1)^2+w0;
rpt1=w8*wr(kk-2)^8+w6*wr(kk-2)^6+w4*wr(kk-2)^4+w2*wr(kk-2)^2+w0;
q=(wr(kk)-wr(kk-1))/(wr(kk-1)-wr(kk-2));
A=q*rpt3-q*(1+q)*rpt2+q^2*rpt1;
B=(2*q+1)*rpt3-(1+q)^2*rpt2+q^2*rpt1;
C=(1+q)*rpt3;

```

```

numm1=B+sqrt(B^2-4*A*C);
numm2=B-sqrt(B^2-4*A*C);

if abs(numm1) > abs(numm2)
    numm=numm1;
else
    numm=numm2;
end
rptt(jj)=rpt3;
wr(kk+1)=wr(kk)-(wr(kk)-wr(kk-1))*(2*C/numm);
eps=wr(kk+1)-wr(kk);
kk=kk+1;
end
m(jj)=kk;

w3x1(jj)=wr(kk);
end

else

clear wr

% Define starting omega values with a little uncertainty added on either side
% so as to insure that root finding technique converges on root. If the exact root is
% given as the first guess, then root finding technique blows up.

wr(1)=wst1-(0+.02*j);
wr(2)=wst1*j;
wr(3)=wst1+(.1+.02*j);
t=txx(2);

% Loop for finding roots at each time step

for jj=1:maxj
    tau=t+(jj-1)*delt; % increment time

% Define Kraut's Coefficients

% follow alorythm found in "Numerical Recipies"

rpt3=(w8*wr(kk)^8+w6*wr(kk)^6+w4*wr(kk)^4+w2*wr(kk)^2+w0)/w8;
rpt2=(w8*wr(kk-1)^8+w6*wr(kk-1)^6+w4*wr(kk-1)^4+w2*wr(kk-1)^2+w0)/w8;
rpt1=(w8*wr(kk-2)^8+w6*wr(kk-2)^6+w4*wr(kk-2)^4+w2*wr(kk-2)^2+w0)/w8;

```

```

q=(wr(kk)-wr(kk-1))/(wr(kk-1)-wr(kk-2));
A=q*rpt3-q*(1+q)*rpt2+q^2*rpt1;
B=(2*q+1)*rpt3-(1+q)^2*rpt2+q^2*rpt1;
C=(1+q)*rpt3;

numm1=B+sqrt(B^2-4*A*C);
numm2=B-sqrt(B^2-4*A*C);

if abs(numm1) > abs(numm2)
    numm=numm1;
else
    numm=numm2;
end
rptt(jj)=rpt3;
wr(kk+1)=wr(kk)-(wr(kk)-wr(kk-1))*(2*C/numm);
eps=wr(kk+1)-wr(kk);
kk=kk+1;
end
m(jj)=kk;

w1x3(jj)=wr(kk);
end
end
end

```

**Program Burline**

```

% This m-file defines the Cagniard paths for a buried line source in a group (i)
% transversely isotropic material. The various paths have the following designation.
% wb1x1 - direct shear
% wb3x3 - direct longitudinal
% w1x1 - shear reflected as shear
% w3x3 - long reflected as long
% w3x1 - long reflected as shear
% w1x3 - shear reflected as long

% Burline.m calls cagn1x1 which calculates the wb1x1, wb3x3, w1x1,w3x3 from
% analytical expressions, and calculates w1x3 and w3x1 by calling cagn3x1.m

% Define elastic constants
alpha=2;
beta=2;
gamma=4;
kappa=sqrt(1+alpha.*beta-gamma);

delt=.3;      % delta time
X3=1000;     % x3 divided by source depth
Maxj=3500;

F2=1;
F3=1;
delta=gamma;

[w3x1,w1x3,w1x1,w3x3,wb1x1,wb3x3,txx]=cagn1x1(alpha,beta,delta,X3,delt,maxj);

% Calculate the derivatives of the displacement

for hj1=2:(maxj)
    dw1x1(hj1)=(w1x1(hj1)-w1x1(hj1-1))/delt;
    dwb1x1(hj1)=(wb1x1(hj1)-wb1x1(hj1-1))/delt;
    dw3x3(hj1)=(w3x3(hj1)-w3x3(hj1-1))/delt;
    dwb3x3(hj1)=(wb3x3(hj1)-wb3x3(hj1-1))/delt;
    dw1x3(hj1)=(w1x3(hj1)-w1x3(hj1-1))/delt;
    dw3x1(hj1)=(w3x1(hj1)-w3x1(hj1-1))/delt;
end
dw1x1(1)=dw1x1(2);
dwb1x1(1)=dwb1x1(2);
dw3x3(1)=dw3x3(2);
dwb3x3(1)=dwb3x3(2);

```

```
dw1x3(1)=dw1x3(2);
dw3x1(1)=dw3x1(2);
```

```
% This section puts together the displacement via the Cagniard method corresponding to
% each Cagniard path discussed above. The coefficients c1, and c3 were obtained using
% Maple. The expressions were cut and pasted from Maple.
```

```
for iui=1:6;
if iui==1
```

```
omega=wb1x1;
c3 = 1./2.*2.^(1./2).*(1./alpha.*(alpha+1+gamma.*omega.^2-
((gamma.*omega.^2+alpha+1).^2-
4.*alpha.*(beta.*omega.^4+(beta+1).*omega.^2+1)).^(1./2))).^(1./2);
c1 =
1./2.*2.^(1./2).*(1./alpha.*(alpha+1+gamma.*omega.^2+((gamma.*omega.^2+alpha
+1).^2-4.*alpha.*(beta.*omega.^4+(beta+1).*omega.^2+1)).^(1./2))).^(1./2);
M1 = i./(2.*c3.^2-2.*c1.^2).*(F3.*(beta.*omega.^2-c1.^2+1)-
F2.*omega.^2.*kappa)/c1;
db1x1=-c1.*M1.*dwb1x1;
```

```
elseif iui==2
```

```
omega=wb3x3;
c3 = 1./2.*2.^(1./2).*(1./alpha.*(alpha+1+gamma.*omega.^2-
((gamma.*omega.^2+alpha+1).^2-
4.*alpha.*(beta.*omega.^4+(beta+1).*omega.^2+1)).^(1./2))).^(1./2);
c1 =
1./2.*2.^(1./2).*(1./alpha.*(alpha+1+gamma.*omega.^2+((gamma.*omega.^2+alpha
+1).^2-4.*alpha.*(beta.*omega.^4+(beta+1).*omega.^2+1)).^(1./2))).^(1./2);
M2 = i./(2.*c1.^2-2.*c3.^2).*(F3.*(beta.*omega.^2-c3.^2+1)-
F2.*omega.^2.*kappa)/c3;
db3x3 = -c3.*M2.*dwb3x3;
```

elseif iui==3

omega=w1x1;

c3 =

$$1./2.*2.^{(1./2)}.*(1./\alpha.*(\alpha+1+\gamma.*\omega.^2-((\gamma.*\omega.^2+\alpha+1).^2-4.*\alpha.*(\beta.*\omega.^4+(\beta+1).*\omega.^2+1)).^{(1./2)})).^{(1./2)});$$

c1 =

$$1./2.*2.^{(1./2)}.*(1./\alpha.*(\alpha+1+\gamma.*\omega.^2+((\gamma.*\omega.^2+\alpha+1).^2-4.*\alpha.*(\beta.*\omega.^4+(\beta+1).*\omega.^2+1)).^{(1./2)})).^{(1./2)});$$

EE31 =

$$\begin{aligned} & -1./2.*i.*(c3.*\alpha.*c1.^2.*\omega.^4.*F2.*\kappa- \\ & c3.*\alpha.*c1.^2.*\omega.^4.*\kappa.*F3.*\beta+c3.*\alpha.*c1.^4.*\omega.^2.*\kappa. \\ & *F3-2.*c3.*\omega.^6.*\kappa.*F2-3.*c3.*\omega.^4.*\kappa.*F2- \\ & c3.*\omega.^4.*F2.*\alpha.*c1.^2+c3.*\omega.^4.*F3.*\kappa.*c1.^2+c3.*\omega.^2.* \\ & F2+2.*c3.*\omega.^4.*F2- \\ & c3.*\omega.^2.*F2.*\alpha.*c1.^2+c3.*\omega.^2.*F3.*\kappa.*c1.^2- \\ & c3.*\omega.^2.*\kappa.^2.*F3.*c1.^2+c3.*\omega.^6.*F2+c3.*\alpha.*c1.^2.*F3.*\beta. \\ & *\omega.^2- \\ & c3.*\alpha.*c1.^2.*\omega.^2.*\kappa.*F3+c3.*\omega.^6.*\kappa.^2.*F2+c3.*\omega.^4 \\ & 4.*\kappa.^3.*F3.*c1.^2-\kappa.*\omega.^4.*c1.*F3.*\beta- \\ & c3.*\omega.^2.*\kappa.*F2+c3.*\alpha.*c1.^2.*F3-c3.*\alpha.*c1.^4.*F3- \\ & 2.*c3.*\omega.^4.*\kappa.^2.*F3.*c1.^2+c3.^3.*\omega.^2.*\kappa.^2.*\alpha.*F3.*c1. \\ & ^2+c3.^3.*\omega.^2.*\kappa.*\alpha.*F2+c3.*\omega.^4.*\kappa.^2.*F2+2.*\kappa.*\omega \\ & ^2.*c1.^3.*F3+\kappa.^2.*\omega.^4.*c1.*F2- \\ & \kappa.*\omega.^2.*c1.*F3+c3.^3.*\omega.^4.*\kappa.*\alpha.*F2- \\ & 2.*\omega.^6.*c1.*F2.*\kappa+\omega.^4.*c1.*F3+\omega.^4.*\kappa.*c1.^3.*F2.*\alpha \\ & a-\omega.^4.*\kappa.^2.*c1.^3.*F3+\omega.^6.*c1.*F2-... \\ & \omega.^4.*c1.^3.*F2.*\alpha- \\ & c3.^3.*\omega.^4.*\alpha.*F2+\kappa.*\omega.^2.*c1.^3.*F2.*\alpha- \\ & \kappa.^2.*\omega.^2.*c1.^3.*F3-\kappa.*\omega.^2.*c1.*F2- \\ & \alpha.*c3.^2.*\omega.^4.*c1.*F2+\alpha.^2.*c3.^2.*\omega.^2.*c1.^3.*F2- \\ & \alpha.*c3.^2.*\omega.^2.*c1.^3.*F3.*\kappa- \\ & \alpha.*c3.^2.*\omega.^2.*c1.*F2+\omega.^6.*c1.*F3.*\beta- \\ & \omega.^4.*c1.^3.*F3+\omega.^2.*c1.*F3- \\ & \alpha.*c3.^2.*\omega.^4.*c1.*F3.*\beta+\alpha.*c3.^2.*\omega.^2.*c1.^3.*F3+\alpha.* \\ & c3.^2.*\omega.^4.*c1.*F2.*\kappa-\alpha.*c3.^2.*\omega.^2.*c1.*F3- \\ & c3.^3.*\alpha.^2.*c1.^2.*F3.*\beta.*\omega.^2+c3.^3.*\alpha.^2.*c1.^4.*F3- \\ & c3.^3.*\alpha.^2.*c1.^2.*F3+c3.^3.*\omega.^2.*\alpha.^2.*F2.*c1.^2- \\ & c3.^3.*\omega.^2.*\alpha.*F3.*\kappa.*c1.^2- \\ & c3.^3.*\omega.^2.*\alpha.*F2+c3.*\alpha.*c1.^2.*\omega.^4.*F3.*\beta- \\ & c3.*\alpha.*c1.^4.*\omega.^2.*F3+c3.*\alpha.*c1.^2.*\omega.^2.*F3+\omega.^4.*c1.*F \end{aligned}$$

$3 \cdot \beta \cdot \omega^2 \cdot c_1^3 \cdot F_3 - 3 \cdot \omega^4 \cdot c_1 \cdot F_2 \cdot \kappa + 2 \cdot \omega^4 \cdot c_1 \cdot F_2 \cdot \omega \cdot c_1^3 \cdot F_2 \cdot \alpha + \omega^2 \cdot c_1 \cdot F_2 \cdot \omega^6 \cdot \kappa \cdot c_1 \cdot F_3 \cdot \beta + 2 \cdot \omega^4 \cdot \kappa \cdot c_1^3 \cdot F_3 + \omega^6 \cdot \kappa \cdot c_1^2 \cdot F_2 \dots$   
 $\omega^4 \cdot \kappa \cdot c_1 \cdot F_3) \cdot \kappa / (c_1 - c_3)^2 / (c_1 + c_3) / (-$   
 $\alpha \cdot c_1^2 + \alpha \cdot c_1^2 \cdot \kappa \cdot \omega^2 + c_1^2 \cdot \kappa \cdot \alpha + \alpha^2 \cdot c_1^2 \cdot c_3^2 - \alpha \cdot c_1^2 \cdot \omega^2 + c_3 \cdot \kappa \cdot \alpha \cdot c_1 + 1 -$   
 $\kappa + \alpha \cdot c_3^2 \cdot \kappa \cdot \omega^2 + \omega^4 -$   
 $\omega^2 \cdot \alpha \cdot c_3^2 + \omega^4 \cdot \kappa^2 - 2 \cdot \kappa \cdot \omega^4 -$   
 $3 \cdot \kappa \cdot \omega^2 + 2 \cdot \omega^2 -$   
 $\alpha \cdot c_3^2 + \omega^2 \cdot \kappa^2 + c_3^2 \cdot \kappa \cdot \alpha);$

$d1x1 = EE31 \cdot dw1x1;$

elseif iui==4

$\omega = w1x3;$

$c3 =$

$1/2 \cdot 2^{(1/2)} \cdot (1/\alpha \cdot (\alpha + 1 + \gamma \cdot \omega^2 -$   
 $((\gamma \cdot \omega^2 + \alpha + 1)^2 -$   
 $4 \cdot \alpha \cdot (\beta \cdot \omega^4 + (\beta + 1) \cdot \omega^2 + 1))^{(1/2)}))^{(1/2)};$

$c1 =$

$1/2 \cdot 2^{(1/2)} \cdot (1/\alpha \cdot (\alpha + 1 + \gamma \cdot \omega^2 + ((\gamma \cdot \omega^2 + \alpha + 1)^2 -$   
 $4 \cdot \alpha \cdot (\beta \cdot \omega^4 + (\beta + 1) \cdot \omega^2 + 1))^{(1/2)}))^{(1/2)};$

EE33 =

$-1/2 \cdot i \cdot (\kappa \cdot \omega^4 \cdot c_1 \cdot F_3 \cdot \beta -$   
 $2 \cdot \kappa^2 \cdot \omega^4 \cdot c_1 \cdot F_2 + \kappa \cdot \omega^2 \cdot c_1 \cdot F_3 + 4 \cdot \omega^6 \cdot c_1 \cdot F_2 \cdot$   
 $\kappa \cdot \omega^4 \cdot c_1 \cdot F_3 -$   
 $2 \cdot \omega^6 \cdot c_1 \cdot F_2 + 2 \cdot \kappa \cdot \omega^2 \cdot c_1 \cdot F_2 + 4 \cdot \alpha \cdot c_3^2 \cdot \omega^4 \cdot c_1 \cdot$   
 $F_2 + 4 \cdot \alpha \cdot c_3^2 \cdot \omega^2 \cdot c_1 \cdot F_2 - \omega^6 \cdot c_1 \cdot F_3 \cdot \beta -$   
 $\omega^2 \cdot c_1 \cdot F_3 - 4 \cdot \alpha \cdot c_3^2 \cdot \omega^4 \cdot c_1 \cdot F_2 \cdot \kappa -$   
 $\omega^4 \cdot c_1 \cdot F_3 \cdot \beta + 6 \cdot \omega^4 \cdot c_1 \cdot F_2 \cdot \kappa - 4 \cdot \omega^4 \cdot c_1 \cdot F_2 -$   
 $2 \cdot \omega^2 \cdot c_1 \cdot F_2 + \omega^6 \cdot \kappa \cdot c_1 \cdot F_3 \cdot \beta -$   
 $2 \cdot \omega^6 \cdot \kappa^2 \cdot c_1 \cdot F_2 + \omega^4 \cdot \kappa \cdot c_1 \cdot F_3 -$   
 $3 \cdot \omega^4 \cdot \kappa \cdot c_1 \cdot F_3 \cdot c_3^2 -$   
 $c_3^2 \cdot \alpha \cdot c_1 \cdot F_3 \cdot \beta \cdot \omega^2 + c_3^4 \cdot \alpha \cdot c_1 \cdot F_3 - c_3^2 \cdot \alpha \cdot c_1 \cdot F_3 -$   
 $\omega^4 \cdot \kappa^3 \cdot c_1 \cdot F_3 \cdot c_3^2 + 2 \cdot \omega^2 \cdot \kappa^2 \cdot c_1 \cdot F_3 \cdot c_3^2 -$   
 $3 \cdot \omega^2 \cdot \kappa \cdot c_1 \cdot F_3 \cdot c_3^2 + c_3^4 \cdot \alpha \cdot \omega^2 \cdot \kappa \cdot c_1 \cdot F_3 + c_3^2 \cdot$   
 $\alpha \cdot \omega^4 \cdot \kappa \cdot c_1 \cdot F_3 \cdot \beta + 3 \cdot \omega^4 \cdot \kappa^2 \cdot c_1 \cdot F_3 \cdot c_3^2 + c_3^2 \cdot$   
 $\alpha \cdot \omega^2 \cdot \kappa \cdot c_1 \cdot F_3 + \omega^2 \cdot c_1 \cdot F_3 \cdot c_3^2 -$   
 $c_3^6 \cdot \alpha^2 \cdot c_1 \cdot F_3 + \omega^4 \cdot c_1 \cdot F_3 \cdot c_3^2 + c_3^4 \cdot \alpha^2 \cdot c_1 \cdot F_3 \cdot \beta \cdot$   
 $\omega^2 + \dots$

$$\begin{aligned}
& c3.^4.*alpha.^2.*c1.*F3-c3.^4.*alpha.*omega.^2.*kappa.^2.*c1.*F3- \\
& 2.*c3.^2.*alpha.*omega.^2.*kappa.*c1.*F2- \\
& 2.*c3.^4.*omega.^2.*alpha.^2.*c1.*F2).*kappa./((c1-c3).^2./((c1+c3)./(- \\
& alpha.*c1.^2+alpha.*c1.^2.*kappa.*omega.^2+c1.^2.*kappa.*alpha+alpha.^2.*c1.^2. \\
& *c3.^2-alpha.*c1.^2.*omega.^2+c3.*kappa.*alpha.*c1+1- \\
& kappa+alpha.*c3.^2.*kappa.*omega.^2+omega.^4- \\
& omega.^2.*alpha.*c3.^2+omega.^4.*kappa.^2-2.*kappa.*omega.^4- \\
& 3.*kappa.*omega.^2+2.*omega.^2- \\
& alpha.*c3.^2+omega.^2.*kappa.^2+c3.^2.*kappa.*alpha);
\end{aligned}$$

$$d1x3 = EE33.*dw3x1;$$

elseif iui==5

$$omega=w3x1;$$

$$c3 =$$

$$\begin{aligned}
& 1./2.*2.^{(1/2)}.*(1./alpha.*(alpha+1+gamma.*omega.^2- \\
& ((gamma.*omega.^2+alpha+1).^2- \\
& 4.*alpha.*(beta.*omega.^4+(beta+1).*omega.^2+1)).^{(1/2)})).^{(1/2)};
\end{aligned}$$

$$c1 =$$

$$\begin{aligned}
& 1./2.*2.^{(1/2)}.*(1./alpha.*(alpha+1+gamma.*omega.^2+((gamma.*omega.^2+alpha \\
& +1).^2-4.*alpha.*(beta.*omega.^4+(beta+1).*omega.^2+1)).^{(1/2)})).^{(1/2)};
\end{aligned}$$

$$EE41 =$$

$$\begin{aligned}
& 1./2.*i.*(4.*c3.*alpha.*c1.^2.*omega.^4.*F2.*kappa- \\
& c3.*alpha.*c1.^2.*omega.^4.*kappa.*F3.*beta- \\
& c3.*alpha.*c1.^4.*omega.^2.*kappa.*F3-4.*c3.*omega.^6.*kappa.*F2- \\
& 6.*c3.*omega.^4.*kappa.*F2- \\
& 4.*c3.*omega.^4.*F2.*alpha.*c1.^2+3.*c3.*omega.^4.*F3.*kappa.*c1.^2+2.*c3.*om \\
& ega.^2.*F2+4.*c3.*omega.^4.*F2- \\
& 4.*c3.*omega.^2.*F2.*alpha.*c1.^2+3.*c3.*omega.^2.*F3.*kappa.*c1.^2- \\
& 2.*c3.*omega.^2.*kappa.^2.*F3.*c1.^2+2.*c3.*omega.^6.*F2+c3.*alpha.*c1.^2.*F3. \\
& *beta.*omega.^2- \\
& c3.*alpha.*c1.^2.*omega.^2.*kappa.*F3+2.*c3.*omega.^6.*kappa.^2.*F2+c3.*omeg \\
& a.^4.*kappa.^3.*F3.*c1.^2-2.*c3.*omega.^2.*kappa.*F2+c3.*alpha.*c1.^2.*F3- \\
& c3.*alpha.*c1.^4.*F3- \\
& 3.*c3.*omega.^4.*kappa.^2.*F3.*c1.^2+2.*c3.*omega.^4.*kappa.^2.*F2- \\
& omega.^4.*c3.*F3.*c1.^2+omega.^6.*c3.*F3.*beta+omega.^4.*c3.*F3+2.*omega.^2 \\
& .*alpha.^2.*c1.^4.*c3.*F2+2.*c1.^2.*alpha.*c3.*F2.*omega.^2.*kappa- \\
& c1.^4.*alpha.^2.*c3.*F3.*beta.*omega.^2+c1.^4.*alpha.*omega.^2.*kappa.^2.*c3.*F \\
& 3-omega.^4.*kappa.*c3.*F3-omega.^2.*kappa.*c3.*F3-c1.^4.*alpha.^2.*c3.*F3+...
\end{aligned}$$

$c1.^6.*alpha.^2.*c3.*F3-omega.^4.*kappa.*c3.*F3.*beta-$   
 $omega.^6.*kappa.*c3.*F3.*beta+omega.^4.*c3.*F3.*beta-$   
 $omega.^2.*c3.*F3.*c1.^2+omega.^2.*c3.*F3).*kappa./(c1-c3).^2./(c1+c3)./(-$   
 $alpha.*c1.^2+alpha.*c1.^2.*kappa.*omega.^2+c1.^2.*kappa.*alpha+alpha.^2.*c1.^2.$   
 $*c3.^2-alpha.*c1.^2.*omega.^2+c3.*kappa.*alpha.*c1+1-$   
 $kappa+alpha.*c3.^2.*kappa.*omega.^2+omega.^4-$   
 $omega.^2.*alpha.*c3.^2+omega.^4.*kappa.^2-2.*kappa.*omega.^4-$   
 $3.*kappa.*omega.^2+2.*omega.^2-$   
 $alpha.*c3.^2+omega.^2.*kappa.^2+c3.^2.*kappa.*alpha);$

$d3x1=EE41.*dw1x3;$

elseif iui==6

omega=w3x3;

c3 =

$1./2.*2.^{(1./2)}.*(1./alpha.*(alpha+1+gamma.*omega.^2-$   
 $((gamma.*omega.^2+alpha+1).^2-$   
 $4.*alpha.*(beta.*omega.^4+(beta+1).*omega.^2+1)).^{(1./2)})).^{(1./2)};$

c1 =

$1./2.*2.^{(1./2)}.*(1./alpha.*(alpha+1+gamma.*omega.^2+((gamma.*omega.^2+alpha$   
 $+1).^2-4.*alpha.*(beta.*omega.^4+(beta+1).*omega.^2+1)).^{(1./2)})).^{(1./2)};$

EE43 =

$1./2.*i.*(-c3.*alpha.*c1.^2.*omega.^4.*F2.*kappa+2.*c3.*omega.^6$   
 $. *kappa.*F2+3.*c3.*omega.^4.*kappa.*F2+c3.*omega.^4.*F2.*alpha.*c1.^2-$   
 $c3.*omega.^2.*F2-2.*c3.*omega.^4.*F2+c3.*omega.^2.*F2.*alpha.*c1.^2-$   
 $c3.*omega.^6.*F2-c3.*omega.^6.*kappa.^2.*F2+c3.*omega.^2.*kappa.*F2-$   
 $c3.^3.*omega.^2.*kappa.*alpha.*F2-c3.*omega.^4.*kappa.^2.*F2-$   
 $kappa.^2.*omega.^4.*c1.*F2-$   
 $c3.^3.*omega.^4.*kappa.*alpha.*F2+2.*omega.^6.*c1.*F2.*kappa-$   
 $omega.^4.*kappa.*c1.^3.*F2.*alpha-$   
 $omega.^6.*c1.*F2+omega.^4.*c1.^3.*F2.*alpha+c3.^3.*omega.^4.*alpha.*F2-$   
 $kappa.*omega.^2.*c1.^3.*F2.*alpha+kappa.*omega.^2.*c1.*F2+alpha.*c3.^2.*omeg$   
 $a.^4.*c1.*F2-$   
 $alpha.^2.*c3.^2.*omega.^2.*c1.^3.*F2+alpha.*c3.^2.*omega.^2.*c1.^3.*F3.*kappa+$   
 $alpha.*c3.^2.*omega.^2.*c1.*F2-alpha.*c3.^2.*omega.^4.*c1.*F3.*beta-$   
 $alpha.*c3.^2.*omega.^4.*c1.*F2.*kappa-alpha.*c3.^2.*omega.^2.*c1.*F3-$   
 $c3.^3.*omega.^2.*alpha.^2.*F2.*c1.^2+c3.^3.*omega.^2.*alpha.*F3.*kappa.*c1.^2+$   
 $c3.^3.*omega.^2.*alpha.*F2+c3.*alpha.*c1.^2.*omega.^4.*F3.*beta+c3.*alpha.*c1.$   
 $^2.*omega.^2.*F3+...$   
 $3.*omega.^4.*c1.*F2.*kappa-2.*omega.^4.*c1.*F2+omega.^2.*c1.^3.*F2.*alpha-$   
 $omega.^2.*c1.*F2-omega.^6.*kappa.^2.*c1.*F2-omega.^4.*kappa.*c1.*F3.*c3.^2-$

$c3.^2.*alpha.*c1.*F3.*beta.*omega.^2+c3.^4.*alpha.*c1.*F3-c3.^2.*alpha.*c1.*F3-$   
 $omega.^4.*kappa.^3.*c1.*F3.*c3.^2+omega.^2.*kappa.^2.*c1.*F3.*c3.^2-$   
 $omega.^2.*kappa.*c1.*F3.*c3.^2-$   
 $c3.^4.*alpha.*omega.^2.*kappa.*c1.*F3+c3.^2.*alpha.*omega.^4.*kappa.*c1.*F3.*$   
 $beta+2.*omega.^4.*kappa.^2.*c1.*F3.*c3.^2+c3.^2.*alpha.*omega.^2.*kappa.*c1.*$   
 $F3-omega.^6.*c3.*F3.*beta-$   
 $omega.^4.*c3.*F3+omega.^4.*kappa.*c3.*F3+omega.^2.*kappa.*c3.*F3+omega.^4.$   
 $*kappa.*c3.*F3.*beta+omega.^6.*kappa.*c3.*F3.*beta-omega.^4.*c3.*F3.*beta-$   
 $omega.^2.*c3.*F3-$   
 $omega.^2.*alpha.*c1.^2.*c3.^3.*F3+omega.^2.*kappa.^2.*c3.^3.*F3+c1.*alpha.*c3.$   
 $^4.*omega.^2.*F3-$   
 $2.*omega.^2.*c3.^3.*F3.*kappa+omega.^4.*c3.^3.*F3+omega.^2.*c3.^3.*F3-$   
 $c1.^3.*alpha.^2.*c3.^4.*F3+omega.^4.*kappa.^2.*c3.^3.*F3-$   
 $2.*omega.^4.*c3.^3.*F3.*kappa-$   
 $c1.^3.*omega.^2.*kappa.^2.*alpha.*F3.*c3.^2+c1.^3.*alpha.^2.*c3.^2.*F3+...$   
 $c1.^3.*alpha.^2.*c3.^2.*F3.*beta.*omega.^2).*kappa./((c1-c3).^2./((c1+c3)./(-$   
 $alpha.*c1.^2+alpha.*c1.^2.*kappa.*omega.^2+c1.^2.*kappa.*alpha+alpha.^2.*c1.^2.$   
 $*c3.^2-alpha.*c1.^2.*omega.^2+c3.*kappa.*alpha.*c1+1-$   
 $kappa+alpha.*c3.^2.*kappa.*omega.^2+omega.^4-$   
 $omega.^2.*alpha.*c3.^2+omega.^4.*kappa.^2-2.*kappa.*omega.^4-$   
 $3.*kappa.*omega.^2+2.*omega.^2-$   
 $alpha.*c3.^2+omega.^2.*kappa.^2+c3.^2.*kappa.*alpha);$

d3x3=EE43.\*dw3x3;

end  
end

**Program Cagniard**

% This function defines the 3 relevant portions of the Cagniard Path for  
 % off epicentral observation points. It returns WRR, the Cagniard Path. Updated

```
th=10*pi/180; % Theta
a=1.57; % Payton's alpha
b=4.17; % Payton's beta
g=2.4; % Payton's gama
delt=.00025; % Root finding step size
maxj=4800; % Maximum number of steps
x3=1; % Define source receiver separation, x3, in mm.
```

```
wm=-(g*(a+1)-2*a*(b+1)-2*(a*(a+b-g)*(1+a*b-g))^(.5))/(g^2-4*a*b);
wp=-(g*(a+1)-2*a*(b+1)+2*(a*(a+b-g)*(1+a*b-g))^(.5))/(g^2-4*a*b);
```

% You can either call CAGN88 first in which case it will return wst1,txx,th  
 % or you can manually add these constants.

% Test for isotropy. If isotropic, then wavefronts are spherical and wave arrival times are  
 % easily defined, else call cagn88 to obtain wave arrival times (txx) and corresponding  
 % omega values (wst1). Wst1 and txx values tell this program where to start the finding  
 % roots. It is very important that txx and wst1 values are as accurate as possible  
 % to avoid root finding program skipping to another portion of the Cagniard path.

```
if a==b
txx=[1/sqrt(a) 1];
wst1=[sin(th)/sqrt(a) sin(th)];
else
[wst1,txx,th] = cagn88(th,a,b,g);
end;
```

% Look for two or four Cagniard Branches. This depends on if observation direction

```

% intersects lacuna.

[ii.oo]=size(txx);
for df=1:oo

% Define delta time

delt=delt/x3;
s=sin(th);
c=cos(th);
eth=s^4+b/a*c^4+g/a*s^2*c^2;

clear wr

% Define starting omega values with a little uncertainty added on either side
% so as to insure that root finding technique converges on root. If the exact root is
% given as the first guess, then root finding technique blows up.

wr(1)=(wst1(df)-.02)*j;
wr(2)=(wst1(df))*j;
wr(3)=(wst1(df)+.02)*j;
t=txx(df)+delt/16;

% Loop for finding roots at each time step

for jj=1:maxj
tau=t+(jj-1)*delt; % increment time

% Define Kraut's Coefficients

aath=-b;
ath=i*b*((2*tau*s/eth)*(2*s^2+g/a*c^2));
bth=b*((tau^2/eth)*(6*s^2+g/a*c^2)-(c^2/eth)*(c^2*(b/a+1/a)+s^2*(1/a+1)));
cth=-i*b*((2*tau*s/eth)*(2*tau^2-c^2*(1/a+1)));
dth=-b*((tau^2/eth)*(tau^2-c^2*(1/a+1))+c^4/(a*eth));

eps=1; % set remainder high so as to enter root finding routine

if jj ~= 1 % For first iteration fill first three omega guesses
wr(1)=wr(kk-1);
wr(2)=wr(kk-2);
wr(3)=wr(kk-3);
end
kk=3;
% loop until remainder is less than this value

```

```
while abs(eps) > .0000000000001
```

```
% follow algorithm found in "Numerical Recipies"
```

```
rpt3=aath*wr(kk)^4+ath*wr(kk)^3+bth*wr(kk)^2+cth*wr(kk)+dth;
rpt2=aath*wr(kk-1)^4+ath*wr(kk-1)^3+bth*wr(kk-1)^2+cth*wr(kk-1)+dth;
rpt1=aath*wr(kk-2)^4+ath*wr(kk-2)^3+bth*wr(kk-2)^2+cth*wr(kk-2)+dth;
q=(wr(kk)-wr(kk-1))/(wr(kk-1)-wr(kk-2));
A=q*rpt3-q*(1+q)*rpt2+q^2*rpt1;
B=(2*q+1)*rpt3-(1+q)^2*rpt2+q^2*rpt1;
C=(1+q)*rpt3;
```

```
numm1=B+sqrt(B^2-4*A*C);
numm2=B-sqrt(B^2-4*A*C);
```

```
if abs(numm1) > abs(numm2)
    numm=numm1;
else
    numm=numm2;
end
```

```
rptt(jj)=rpt3;
wr(kk+1)=wr(kk)-(wr(kk)-wr(kk-1))*(2*C/numm);
eps=wr(kk+1)-wr(kk);
kk=kk+1;
```

```
end
```

```
m(jj)=kk;
wrr(jj,df)=wr(kk);
```

```
end
end
```

**Program Cagn88**

% This function finds the wave arrival times for a particular angle and  
 % also finds the correspond omega values. This info must be used in "CAGNAIRD"  
 % Type the next line exactly but replace (th) with a number. Function returns  
 % what is in square brackets only.

```
function [wst1,txx,th] = cagn88(th,a,b,g);
```

% Define theta array and build first quadrant of slowness surface  
 % (eqns. 2.2.6, 2.2.4, 1.5.26, 1.5.27 in Payton)

% If theta equals zero, we can blistfully skip thru many hoops, (i.e. the energy  
 % propagation direction equals the normal to the slowness surface making  
 % life much easier.

```
if th == 0
```

```
th1=0;
ath=a*((cos(th1)).^4)+g*((cos(th1)).^2).*((sin(th1)).^2)+b*((sin(th1)).^4);
bth=(a+1)*((cos(th1)).^2)+(b+1)*((sin(th1)).^2);
rplus=sqrt((bth+sqrt(bth.^2-4*ath))./(2*ath));
rminus=sqrt((bth-sqrt(bth.^2-4*ath))./(2*ath));
pp=rplus.*cos(th1);
qp=rplus.*sin(th1);
pm=rminus.*cos(th1);
qm=rminus.*sin(th1);
rp=sqrt(pp.^2+qp.^2);
rm=sqrt(pm.^2+qm.^2);
txx=[rm rp];
wst1=[0 0];
```

```
else
```

```
th1=[0:.01:90]*pi/180;
ath=a*((cos(th1)).^4)+g*((cos(th1)).^2).*((sin(th1)).^2)+b*((sin(th1)).^4);
bth=(a+1)*((cos(th1)).^2)+(b+1)*((sin(th1)).^2);
rplus=sqrt((bth+sqrt(bth.^2-4*ath))./(2*ath));
rminus=sqrt((bth-sqrt(bth.^2-4*ath))./(2*ath));
pp=rplus.*cos(th1);
qp=rplus.*sin(th1);
pm=rminus.*cos(th1);
qm=rminus.*sin(th1);
rp=sqrt(pp.^2+qp.^2);
rm=sqrt(pm.^2+qm.^2);
c2=(cos(th1)).^2;
s2=(sin(th1)).^2;
```

```

k1=2*a*(b+1)-g*(a+1);
k2=2*b*(a+1)-g*(b+1);

```

```

% This segment fills arrays for remaining 3 quadrants

```

```

ty=size(rp);
ty=ty(2);
rpp(1:1:ty)=rp;
rpp(ty+1:1:2*ty)=rp(ty:-1:1);
rpp(2*ty+1:1:3*ty)=rp;
rpp(3*ty+1:1:4*ty)=rp(ty:-1:1);
rmm(1:1:ty)=rm;
rmm(ty+1:1:2*ty)=rm(ty:-1:1);
rmm(2*ty+1:1:3*ty)=rm;
rmm(3*ty+1:1:4*ty)=rm(ty:-1:1);

```

```

% This segment calculates the wavefront shape

```

```

% (tang is the theta that goes with rrr for the wavefront and tangg with rrrr)

```

```

for h=2:(ty-1);
    qpn=(pp(h+1)-pp(h-1));
    qpd=(qp(h+1)-qp(h-1));
    qmn=(pm(h+1)-pm(h-1));
    qmd=(qm(h+1)-qm(h-1));

    if qpn>0 & qpd>0
        tang(h)=atan(-qpn/qpd);
        tangg(h)=atan(-qmn/qmd);
    elseif qpn>0 & qpd<0
        tang(h)=(pi/2)+atan(qpn/qpd);
        tangg(h)=(pi/2)+atan(qmn/qmd);
    elseif qpn<0 & qpd<0
        tang(h)=pi+atan(-qpn/qpd);
        tangg(h)=pi+atan(-qmn/qmd);
    elseif qpn<0 & qpd>0
        tang(h)=atan(-qpn/qpd);
        tangg(h)=atan(-qmn/qmd);
    end
    thp=abs(th1(h)-tang(h));
    thpp=abs(th1(h)-tangg(h));
    adj=rpp(h)*cos(thp);
    adjj=rmm(h)*cos(thpp);
    rrr(h)=1/adj;
    rrrr(h)=1/adjj;
end

```

```

% Check to see if the desired theta value falls within a cuspidal triangle

oi=1; % counting index
i=1; % counting index

sgn=1; % set sign equal to 1 so as not to enter nested if loop during first loop

% The idea here is to build the derivative of tang and look for zeros, zeros correspond
% to critical angles. Then the critical angles are put in ascending order. If theta
% of interest falls within these angles then four wave arrivals must be considered.

for i=1 : 8998
ddtang(i+1)=(tang(i+1)-tang(i));
if i == 1
ddtang(1)=ddtang(2);
end
i=i+1;
sgn=sign(ddtang(i))*sign(ddtang(i-1));
if sgn ~=1
    py(oi)=i;
    oi=oi+1;
end
end

if oi == 1
tcrit=pi/2;
else
tcrit=sort(tang(py));
end

% The idea here, for a given th (must specify th when you call function),
% is to find the tang and tangg value that is closest to th and relate this to
% the corresponding rrr and rrrr values (for one th value, there are 3 rrr values and
% and one rrrr value, ie 3 wave arrivals) There is only one corresponding tangg value
% since the longitudinal branch is always convex and possilby 3 tang values since the
% branch is locally concave. So after the first corresponding tang value is found
% eliminate this from the array and look for the next and then repeat this process.

if th < abs(tcrit(1)) | g == (b+1) & (g^2-4*a*b) < 0

thdif1=abs(th-abs(tang));
thdif2=abs(th-abs(tangg));
[i1,y11]=min(thdif2);
[i2,y22]=min(thdif1);
thdif3=thdif1([1:y22-30 y22+30:length(thdif2)]); % eliminate 60 values around first

```

```

[i3,y33]=min(thdif3); % min so as not to land near
                        % previous min

thdif4=thdif3([1:y33-30 y33+30:length(thdif3)]); % eliminate 60 values around first
[i4,y44]=min(thdif4); % min so as not to land near
                        % previous min

y4=y11;
y1=y22;
y2=y33;
y3=y44;

% Put these min values in order of size (ie cronological order of wave arrivals)

if y1 < y2 & y2 < y3
y2=y2+59;
y3=y3+118;
elseif y1 < y3 & y3 < y2
y3=y3+59;
y2=y2+59;
elseif y2 < y1 & y1 < y3
y3=y3+59;
elseif y2 < y3 & y3 < y1
y3=y3+59;
elseif y3 < y1 & y1 < y2
y2=y2+59;
elseif y3 < y2 & y2 < y1
y2=y2+59;
end

% gives the wave arrival times

t1=1/rrr(y4);
t2=1/rrr(y2);
t3=1/rrr(y3);
t4=1/rrr(y1);

txx=sort([t1 t4 t3 t2]);

```

% The idea here is for a given time of arrival to find the corresponding omega value.

% The point at which the Cagniard path becomes purely imaginary corresponds to a  
 % wave arrival. Procedure consists of substituting a wave arrival time into eqn. 4.41 in  
 % Kraut and fluxing thru real omega values until a root is found (ie omega value  
 % where Cagniard path becomes purely imaginary. Newton's method is  
 % not used since we are cruising around a complex surface. Instead an omega array is  
 % populated and a search for a min value ensues.

```
s=sin(th);
c=cos(th);
eth=s^4+b/a*c^4+g/a*s^2*c^2;
```

% For loop for each wave arrival

```
for df=1:4
tau1=txx(df);
```

% Fill omega array. Make sure that omega array spans kissing root.

```
dwr=0.001;
wr=[-1.2:dwr:1.2]*j;
swr=size(wr);
swr=swr(2);
```

% Coefficients for Cagniard Path (eqn. 4.42-4.47 in Kraut)

```
aath=-b;
ath=j.*b.*((2.*tau1.*s./eth).*(2.*s.^2+g./a.*c.^2));
bth=b.*((tau1.^2./eth).*(6.*s.^2+g./a.*c.^2)-
(c.^2./eth).*(c.^2.*(b./a+1./a)+s.^2.*(1./a+1)));
cth=j.*b.*((2.*tau1.*s./eth).*(2.*tau1.^2-c.^2.*(1./a+1)));
dth=b.*((tau1.^2./eth).*(tau1.^2-c.^2.*(1./a+1))+c.^4./(a.*eth));
```

% Remainder

```
rpt3(df,1:swr)=aath.*wr.^4+ath.*wr.^3+bth.*wr.^2+cth.*wr+dth;
rpt3(df,1:swr)=real(rpt3(df,1:swr));
```

% Find min value "This routine is really screwed up!  
 % The idea here is to find the kissing roots. First the derivative is found.  
 % Then the min value of the derivative is found (drpt3) and compared against the min  
 % value of the function itself (rpt3). DRPT3 can equal zero more than once but the value  
 % of interest is the omega value where DRPT3 and RPT3 both equal zero.

```
for eee = 1:swr-1
```

```

drpt3(df,eee)=(rpt3(df,eee+1)-rpt3(df,eee))/(dwr);
end
drpt3(df,eee+1)=drpt3(df,eee);
[i,y]=min(abs(rpt3(df,:).*drpt3(df,:)))

wst1(df)=imag(wr(y));
end

else

thdif1=abs(th-abs(tang));
thdif2=abs(th-abs(tangg));
[i1,y1]=min(thdif2);
[i2,y2]=min(thdif1);

% gives the wave arrival times

t2=1/rrr(y2);
t1=1/rrr(y1);

txx=sort([t1 t2]);

% The idea here is for a given time of arrival to find the corresponding omega value.
% The point at which the Cagniard path becomes purely imaginary corresponds to a wave
% arrival. Procedure consists of substituting a wave arrival time into eqn. 4.41 in
% Kraut and fluxing thru real omega values until a root is found (ie omega value
% where Cagniard path becomes purely imaginary. Newton's method is
% not used since we are cruising around a complex surface. Instead an omega array is
% populated and a search for a min value insues.

s=sin(th);
c=cos(th);
eth=s^4+b/a*c^4+g/a*s^2*c^2;

% For loop for each wave arrival

for df=1:2
tau1=txx(df);

% Fill omega array. Make sure that omega array spans kissing root.

```

```

dwr=0.001;
wr=[-1.2:dwr:1.2]*j;
swr=size(wr);
swr=swr(2);

```

```
% Coefficients for Cagniard Path (eqn. 4.42-4.47 in Kraut)
```

```

aath=-b;
ath=j.*b.*((2.*tau1.*s./eth).*(2.*s.^2+g./a*c.^2));
bth=b.*((tau1.^2./eth).*(6.*s.^2+g./a*c.^2)-
(c.^2./eth).*(c.^2.*(b./a+1./a)+s.^2.*(1./a+1)));
cth=j.*b.*((2.*tau1.*s./eth).*(2.*tau1.^2-c.^2.*(1./a+1)));
dth=b.*((tau1.^2./eth).*(tau1.^2-c.^2.*(1./a+1))+c.^4./(a.*eth));

```

```
% Remainder
```

```

rpt3(df,1:swr)=aath.*wr.^4+ath.*wr.^3+bth.*wr.^2+cth.*wr+dth;
rpt3(df,1:swr)=real(rpt3(df,1:swr));

```

```
% Find min value "This routine is really screwed up!
```

```
% The idea here is to find the kissing roots. First the derivative is found.
```

```
% Then the min value of the derivative is found (drpt3) and compared against the min
```

```
% value of the function itself (rpt3). DRPT3 can equal zero more than once but the value
```

```
% of interest is the omega value wher DRPT3 and RPT3 both equal zero.
```

```

for eee = 1:swr-1
drpt3(df,eee)=(rpt3(df,eee+1)-rpt3(df,eee))/(dwr);
end
drpt3(df,eee+1)=drpt3(df,eee);
[i,y]=min(abs(rpt3(df,:).*drpt3(df,:)));

```

```

wst1(df)=imag(wr(y));
end
end
end

```

**Program Diss2**

```
% This m-file calculates the displacement resulting from a laser line source.
% The theoretical expression obtained via the Cagniard inversion routine is convolved
% with a Gaussian to mimic a finite source and detection spot as well as limited
% bandwidth. The elastic constants used are those for graphite epoxy.
```

```
% Load experimental data
```

```
load test11
load un29
test11=test11+4.4e-3;
```

```
% Enter material constants
```

```
a=39.5;           % Ratio of c33/c44
b=3.67;          % Ratio of c11/c44
g=109;          % Payton's gamma
k=(1+a*b-g)^.5; % Payton's kappa
rho=1.73;       % density in cgs units
wr=1.008;      % Rayleigh root
y=5;           % Source receiver separation in mm
t=[0:.002:4.56]; % time array (microsec)
v444=1.50;     % velocity in mm/microsec
tau=t*v444;    % time in mm
tt=tau/y;
delta=.002*v444/y; % Integration delta for convolution
[jmax,imax]=size(t);
```

```
% Build displacement for surface skimming longitudinal wave (sslw)
```

```
rad=(a*(b*tt.^2-1).*(1-tt.^2)).^5;
num=tt.^2.*rad.*((1-k).*(1-2*tt.^2)-(a-g*tt.^2));
den=(-2*(1-k)*tt.^2+g*tt.^2-a).^2.*(1-tt.^2)+a*(b*tt.^2-1);
disp=(num)./(den*pi);
```

```
% Incorporate step functions that turn (sslw) on and off
```

```
for i=1:(imax);
    if tt(i) < (1/sqrt(b))
        dis(i)=0;

        elseif tt(i) > 1
            dis(i)=0;
```

```

else
dis(i)=disp(i);
end
end;

```

```
% Build displacement for Rayleigh wave (delta function)
```

```

dprime1=4*(1-k)*(-2*wr^2+1)-2*(-2*g*wr^2+g+a);
dprime2=(a*(b+1)-2*a*b*wr^2)/((1-wr^2)*(-2*(1-k)*wr^2+g*wr^2-a));
dprime=dprime1-dprime2;
dnum=wr*(1-wr^2)*(-2*(1-k)*wr^2+g*wr^2-a+1-k);
psir=dnum/(dprime);
tr=wr*y/v444;
tnr=imax*tr/t(imax);
dis(tnr)=20;

```

```
% Temporal convolution of sslw and gaussian
```

```

cs=dis(1);
ce=dis(imax)*exp(-((t-imax*deltau).^2)/.07);
cnvs=0;
for i=2:imax-1;
    cnv=2*dis(i)*exp(-((t-i*deltau).^2)/.00077);
    cnvs=cnvs+cnv;
end;
cnvs=1.42e-8*(cnvs+cs+ce)*deltau/2;

```

```

ttt=[0:1:2326]*2e-3;
plot(ttt,un29-1e-3);
hold
plot(tt*y/(v444),(-cnvs*10e6)*1.3,'b');

```

**Program Offepi2**

% This m-file Calculates the displacement for zinc for observation directions that  
 % are off the epicentral axis. The Cagniard integration contour must be defined first,  
 % thus the programs Cagniard and Cagn88 must be call before running this program.

% Define elastic constants

```
a=1.57;
b=4.17;
g=2.4;
kk=(1+a*b-g)^.5;
```

```
tint=775;    % Define max number of point for Cagniard contour for long and
```

```
            % shear portion.
```

```
delt=.00025;
maxj=4800;
load wrr;
txx=[0.7944  0.9934  1.0841  1.1766];
```

```
[i,y]=min(abs(imag(wrr(1:1:tint,1))));
```

% Assign each portion of Cagniard Contour to w1 thru w3

```
w1=wrr(1:1:tint,1);
w2=wrr(:,3);
w3=wrr(:,4);
```

% Evaluate derivative of each portion of Cagniard contour

```
for hj1=1:(tint-1)
    dw1(hj1)=(w1(hj1+1)-w1(hj1))/delt;
end
dw1(hj1+1)=dw1(hj1);
```

```
for hj2=1:(maxj-1)
    dw2(hj2)=(w2(hj2+1)-w2(hj2))/delt;
end
dw2(hj2+1)=dw2(hj2);
```

```
for hj3=1:(maxj-1)
    dw3(hj3)=(w3(hj3+1)-w3(hj3))/delt;
end
dw3(hj3+1)=dw3(hj3);
```

```

%%%%%%%%%%%%%%%%%%%%%%%%%%%%%%%%%%%%%%%%%%%%%%%%%%%%%%%%%%%%%%%%%%%%%%%%
% shear & long %%%%%%%%%
%%%%%%%%%%%%%%%%%%%%%%%%%%%%%%%%%%%%%%%%%%%%%%%%%%%%%%%%%%%%%%%%%%%%%%%%

```

```
% Buld kappa array
```

```

k3w11=(g*(w1.^2)+a+1);
k3w12=sqrt(k3w11.^2-4*a*(b*(w1.^4)+(b+1)*(w1.^2)+1));
k3w1=sqrt(k3w11+k3w12)/sqrt(2*a);
k1w11=(g*(w1.^2)+a+1);
k1w12=sqrt(k1w11.^2-4*a*(b*(w1.^4)+(b+1)*(w1.^2)+1));
k1w1=sqrt(k1w11-k1w12)/sqrt(2*a);

```

```
% Build Rayleigh pole array
```

```
d11=2*(1-kk)*(w1.^4+w1.^2)-(g*w1.^2+a).*(w1.^2+1)-a*k1w1.*k3w1;
```

```
% Build A3
```

```

als31=k1w1./((k1w1-k3w1).*d11);
als32=(w1.^2).*(a*k3w1.^2+(kk-1)*w1.^2+(kk-1));
als3=als31.*als32;
dis1=abs(imag(als3)).*(imag(dw1))'+abs(real(dw1)).*real(als3);
[ii,yy]=min(abs(dis1(50:1:tint)));
dis11=dis1(1:1:yy);
dis11(yy+1)=0;
dis11(yy+2:maxj)=zeros(1,maxj-yy-1);

```

```

%%%%%%%%%%%%%%%%%%%%%%%%%%%%%%%%%%%%%%%%%%%%%%%%%%%%%%%%%%%%%%%%%%%%%%%%
% lower hyperbola %%%%%%%%%
%%%%%%%%%%%%%%%%%%%%%%%%%%%%%%%%%%%%%%%%%%%%%%%%%%%%%%%%%%%%%%%%%%%%%%%%

```

```
% Buld kappa array
```

```

k3w21=(g*(w2.^2)+a+1);
k3w22=sqrt(k3w21.^2-4*a*(b*(w2.^4)+(b+1)*(w2.^2)+1));
k3w2=sqrt(k3w21+k3w22)/sqrt(2*a);
k1w21=(g*(w2.^2)+a+1);
k1w22=sqrt(k1w21.^2-4*a*(b*(w2.^4)+(b+1)*(w2.^2)+1));
k1w2=sqrt(k1w21-k1w22)/sqrt(2*a);

```

```
% Build Rayleigh pole array
```

```
d22=2*(1-kk)*(w2.^4+w2.^2)-(g*w2.^2+a).*(w2.^2+1)-a*k1w2.*k3w2;
```

% Build A3

```

au31=k1w2./((k1w2-k3w2).*d22);
au32=(w2.^2).*(a*k3w2.^2+(kk-1)*w2.^2+(kk-1));
au3=au31.*au32;
dis2=(au3.*conj(dw2'));

```

```

%%%%%%%%%%%%%%%%%%%%%%%%%%%%%%%%%%%%%%%%%%%%%%%%%%%%%%%%%%
%%%%%%%%%%%%%%%%%%%%%%%%%%%%%%%%%%%%%%%%%%%%%%%%%%%%%%%%%%
upper hyperbola %%%%%%%%%%%%%%%%%%%%%%%%%%%%%%%%%%%%%%%%%%
%%%%%%%%%%%%%%%%%%%%%%%%%%%%%%%%%%%%%%%%%%%%%%%%%%%%%%%%%%
%%%%%%%%%%%%%%%%%%%%%%%%%%%%%%%%%%%%%%%%%%%%%%%%%%%%%%%%%%

```

% Buld kappa array

```

k3w31=(g*(w3.^2)+a+1);
k3w32=sqrt(k3w31.^2-4*a*(b*(w3.^4)+(b+1)*(w3.^2)+1));
k3w3=sqrt(k3w31+k3w32)./sqrt(2*a);
k1w31=(g*(w3.^2)+a+1);
k1w32=sqrt(k1w31.^2-4*a*(b*(w3.^4)+(b+1)*(w3.^2)+1));
k1w3=sqrt(k1w31-k1w32)./sqrt(2*a);

```

% Build Rayleigh pole array

```

d33=2*(1-kk)*(w3.^4+w3.^2)-(g*w3.^2+a).*(w3.^2+1)-a*k1w3.*k3w3;

```

% Build A4

```

al41=k3w2./((k1w2-k3w2).*d22);
al42=(w2.^2).*(a*k1w2.^2+(kk-1)*w2.^2+(kk-1));
al4=al41.*al42;
dis3=(al4.*(dw3'));

```

% This portion of the program build entire displacement array from  
% the various portions of the integration contour. The main difficulty is  
% putting the displacement array in the correct order.

```

maxjj=round(maxj+txx(1)/delt)-1;
for xxx=1:maxjj
t=delt*(xxx-1);

if t<=txx(1)
dis(xxx)=0;
y1=xxx;

```

```
elseif t>txx(1) & t<=txx(2)
dis(xxx)=(dis11(xxx-y1));
y2=xxx;
```

```
elseif t>txx(2) & t<=txx(3)
dis(xxx)=0;
y3=xxx;
```

```
elseif t>txx(3) & t<=txx(4)
dis(xxx)=(dis11(xxx-y1)+dis2(xxx-y3));
y4=xxx;
```

```
elseif t>txx(4)
dis(xxx)=(dis11(xxx-y1)+dis2(xxx-y3)+dis3(xxx-y4));
end
end
dis=real(dis);
```

```
jk=size(dis);
jk=jk(2);
jkk=jk-1;
t=[0:delt:delt*jkk];
```

```
pause
```

```
% Temporal convolution of sslw and gaussian
```

```
cs=dis(1);
ce=dis(jk)*exp(-((t-jk*delt).^2)/2e-4);
cnvs=0;
for i=2:jk-1;
    cnv=2*dis(i)*exp(-((t-i*delt).^2)/2e-4);
    cnvs=cnvs+cnv;
end;
cnvss=(cnvs+cs+ce)*delt/2;
```

## REFERENCES

1. R.M. White, "Elastic Wave Generation by Electron Bombardment or Electromagnetic Wave Absorption," *Journal of Applied Physics*, **34**, 2123-2130 (1963).
2. R.M. White, "Excitation of Surface Elastic Waves by Transient Surface Heating," *Applied Physics Letters*, **12**, 12-15 (1963).
3. C.B. Scruby, R.J. Dewhurst, D.A. Hutchins and S.B. Palmer, "Quantitative Studies of Thermally Generated Elastic Waves in Laser-Irradiated Metals," *Journal of Applied Physics*, **51** (12), 6210-6216 (1980).
4. H. Lamb, *Philosophical Transaction of the Royal Society*, **A 203**, 1 (1904).
5. L.R.F. Rose, "Point Source Representation for Laser Generated Ultrasound," *Journal of the Acoustical Society of America*, **73**, 723, (1984).
6. L.M. Lyamshev and B.I. Chelnokov, "Sound Generation in a Solid by Penetrating Radiation," *Soviet Physical Acoustics*, **29**, 220-225 (1983).
7. P. Doyle, "On Epicentral Waveforms for Laser-Generated Ultrasound," *Journal of Physics-D: Applied Physics*, **19**, 1613-1623 (1986).
8. K. Telschow and R. Conant, "Optical and Thermal Parameter Effects on Laser Generated Ultrasound," *Journal of the Acoustical Society of America*, **88**, 1494-1502 (1990).
9. C. Sve and J. Miklowitz, "Thermally Induced Stress Waves in an elastic Layer," *Journal of Applied Mechanics*, **40**, 161-167 (1973).
10. S. Campin, E.M. Chesnokov and R.G. Hipkin, "Seismic Anisotropy - The State of the Art: II," *Geophys. J. R. astr. Soc.*, **76**, 1-16, (1984).
11. V.N. Martynov and B.G. Mikhailenko, "Numerical Modeling of Propagation of Elastic Waves in Anisotropic Inhomogeneous Media for the Half-Space and the Sphere," *Geophys. J. R. astr. Soc.*, **76**, 53-63, (1984).
12. D. Bamford and S. Campin, "Seismic Anisotropy - The State of the Art," *Geophys. J. R. astr. Soc.*, **76**, 1-16, (1984).

13. R. Stonely, *Proceeding of the Royal Society of London, Ser. A* **232**, 447-458 (1955).
14. D. Royer and E. Dieulesaint, "Rayleigh Wave Velocity and Displacement in Orthorhombic, Tetragonal, Hexagonal, and Cubic Crystals," *Journal of the Acoustical Society of America*, **76**, 1438-1444, (1984).
15. E.A. Kraut, "Rev. Geophys.," **1**, 401, (1963).
16. L. Cagniard, *Reflection and Refraction of Prog. Seismic Waves*, McGraw-Hill, New York, (1962).
17. A. T. de Hoop, *Applied Scientific Research*, **B8**, pg 349, (1960).
18. M. J. P. Musgrave, *Crystal Acoustics*, Holden-Day, Inc., San Francisco (1970).
19. R. Burridge, "Lamb's Problem for an Anisotropic Half-Space," *Quarterly Journal of Mechanics and Applied Mathematics*, **24**, 81-98, (1970).
20. J. R. Willis and R. J. Bedding, "Arrivals Associated with a Class of Self-Similar Problems in Elastodynamics," *Mathematical Proceedings of the Cambridge Philosophical Society*, **77**, 591-607, (1975).
21. A. Mourad, M. Deschamps, B. Castagnède, Acoustic Waves Generated by a Transient Line Source in an Anisotropic Half-Space, *Acustica*, **82**, 839-851, (1996).
22. R. L. Weaver, W. Sachse, K. Y. Kim, Transient Elastic Waves in a Transversely Isotropic Plate, *J Applied Mech* (1996) **63** 337-346.
23. R.G. Payton, *Elastic Wave Propagation in Transversely Isotropic Media*, Martinus Nijhoff Publisher, The Hague (1983).
24. J. D. Achenbach and G. Hermann, 'Dispersion of Free Harmonic Waves in Fiber- Reinforced Composites,' *Journal of the Acoustical Society of America*, **85**, 2268-2276 (1989).
25. T.T. Wu and Z.H. Ho, "Anisotropic Wave Propagation and its Application to NDE of Composite Materials," *Experimental Mechanics*, 313-318, (1990).
26. A. K. Mal, and S.J. Singh, *Deformation of Elastic Solids*, Prentice-Hall, Englewood Cliffs, NJ, (1991).

27. S.K. Data, A.H. Shah, R.L. Bratton and T. Chakraborty, "Wave Propagation in Laminated Composite Plates," *Journal of the Acoustical Society of America*, **85**, 2020-2026, (1988).
28. A.K. Mal and S. Lih, "Elastodynamic Response of a Unidirectional Composite Laminate to Concentrated Surface Loads: Part I & II," *Journal of Applied Mechanics*, **59**, 878-892 (1992).
29. V.E. Gusev, A. A. Karabutov, *Laser Optoacoustics*, American Institute of Physics Press, New York, NY, (1993).
30. W. B. Gauster and D. H. Habing, *Phys. Rev. Lett.* **18**, 1059-1061, (1967).
31. A. N. Dharamsi, A. B. Hassam, "Cold Shock Waves in Semiconductors and Insulators," *J. Appl. Phys.*, **65**, (1989).
32. S. Dixon, C. Edwards, S.B. Palmer, and D.W. Schindel, "Ultrasound Generation in Single-Crystal Silicon Using a Pulsed Nd:YAG Laser," *J. Phys. D: Appl Phys.*, **29** (1996).
33. *Handbook of optical constants of solids II*, Academic Press, Boston, MA, (1991).
34. M. Dubois, M Choquet, J. Monchalain, F. Enguehard, L. Bertrand, " Absolute Optical Absorption Spectra in Graphite Epoxy by Fourier Transform Infrared Photoacoustic Spectroscopy," *Optical Engineering*, **32**, 2255-2260, (1993).
35. L. Lang, "Absorption Spectra in the Ultraviolet And Visible Region," Academic Press, New York, NY, (1959).
36. *Sprouse collection of infrared spectra, Book 1: Polymers*, Sprouse Scientific Systems, Paoli, PA, (1987)
37. Hetnarski, R. B., "The Generalized d'Alembert Solution to the Coupled Equations of Thermoelasticity. Progress in Thermoelasticity, 121-131. VOOOtj European Mechanics Colloquium, Warsaw (1969).
38. Nowacki, W., *Dynamic Problems of Thermoelasticity*, Polish Scientific Publishers, Warszawa (1975).
38. Ready J.F., *Effects of High-Powered Laser Radiation*, Academic Press, New York, (1971).
40. Graff K.F., *Wave Motion in Elastic Solids*, Dover Publication, Inc., New York, (1975).

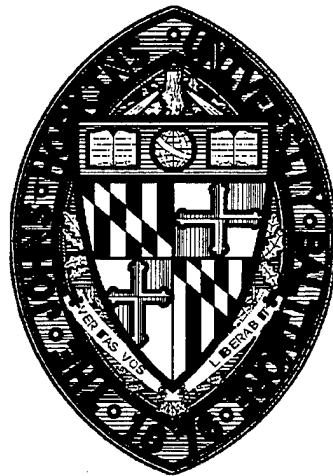
41. Achenbach J. D., *Wave Propagation in Elastic Solids*, North-Holland Publishing Company, New York, (1973).
42. Eringen C. A. and Suhubi E. S., *Elastodynamics*, Academic Press, New York, (1975).
43. G.G.D. Duff, *Boundary Value Problems for Linear Evolution Partial Differential Equations*, Holland, D. Reidel Publishing Co., (1977).
44. Petrowski, I.G., *Rec. Math. [Mat. Sbornik] 17* (1945).
45. Wolf, J. P., "Acoustic Wavefronts in Crystalline Solids," *Physics Today*, 34-40 (Sept. 1995).
46. Scruby, C. B., *Laser Ultrasonics*, Adam Hilger, New York, (1990).
47. Schleichert, U., K.J. Langenberg, W. Arnold and S. Fassbender, "A Quantitative Theory of Laser-Generated Ultrasound," *Review of Progress in Quantitative NDE Vol. 8A* ed. D.E. Chimenti and D.O. Thompson (Plenum Press, New York, 1989) (pp. 489-496).

**VITA**

David Hurley was born in Alexandria, Virginia in 1965. He received his B.S. in Physics from the University of North Carolina-Chapel Hill in 1989, and his M.S. in Mechanical Engineering from Montana State University, in 1992. He is currently a graduate student in the Department of Materials Science and Engineering at Johns Hopkins University, Baltimore, Maryland.

**APPENDIX B**

Laser Interactions with Materials:  
Optimizing the Laser Source for the Generation  
of Acoustic Waves in Laser Ultrasonics Applications



by

Todd William Murray

A dissertation submitted to Johns Hopkins University in  
conformity with the requirements  
for the degree of Doctor of Philosophy

Baltimore, Maryland

1997

## ABSTRACT

Signal detectability is arguably the key parameter to be optimized when designing a laser-based system for remote generation and detection of acoustic signals. The acoustic signal generated by a laser source depends on the thermal, optical, and elastic properties of the specimen and on the characteristics of the laser source. For a given materials system, the laser source parameters, including temporal profile, spatial profile, energy, and wavelength, can be chosen such that the signal-to-noise ratio of the detection system is maximized.

It is well known that the amplitude of a laser generated acoustic waves can be significantly enhanced by increasing the energy in the generation pulse such that surface ablation occurs. The amplitude of acoustic waves generated in the ablative regime is directly related to the surface vaporization process. In this manuscript, the laser vaporization process in vacuum is modeled using an implicit finite difference technique. The surface pressure resulting from vaporization serves as a source for acoustic wave generation. The acoustic displacements generated by a laser source in the ablative regime are calculated. The calculations are then compared to experimentally measured surface displacements in aluminum specimens. Acoustic wave generation is considered for the limited range of vaporization in which absorption of light in the vapor can be neglected. Processes beyond this point are discussed qualitatively. Good agreement is seen between theory and experiment over a limited irradiance range.

A novel technique for laser ultrasonic system sensitivity increase through spatial modulation of the incident laser source is presented. The method uses a transmission mask to generate linearly frequency modulated (chirped) surface waves. The laser source is extended in space allowing for a large amount of laser energy to be utilized in the generation process before the surface damage threshold is exceeded. The received signal is subsequently processed using a matched filter. The application of a matched filter to a linearly frequency modulated signal leads to the compression of the in time. The technique allows for temporal resolution to be maintained while surface damage is avoided.

Temporal modulation of laser sources for the generation of acoustic waves is considered. Methods for controlling the pulse length of a conventional Q-switched laser system are given. The effects of varying incident laser pulse length on the thermoelastic generation of acoustic waves are discussed. For materials exhibiting strong surface absorption, it is found that there exists a pulse length which optimizes the laser generated signal amplitude while avoiding surface damage. A linear systems approach for determination of pulse length effects is presented. This allows for the calculation of acoustic waves with an arbitrary temporal profile based on a theoretically or experimentally determined reference signal. Finally, pulse length effects on two composite specimens are evaluated and the results discussed.

## ACKNOWLEDGMENTS

I am especially grateful to my advisor, Dr. James Wagner, for all of the assistance and support that he has given me in my years at Johns Hopkins. He has been an excellent mentor and his unique way of running his research program has made my graduate study very enjoyable. The work presented here has been done in close collaboration with a number of researchers at Johns Hopkins. In particular, I would like to thank Kevin Baldwin who has been instrumental in this work. His willingness to take time out of his day to assist others in their projects is unparalleled. I would also like to thank Dr. Michael Ehrlich, David Blodgett, Chris Richardson, and Dr. James Spicer for their help in this work, and for the many hours of interesting discussion over the past several years. Additional thanks go out to all of the other students, faculty, and support staff of the Department of Materials Science and Engineering.

Finally, I would like to acknowledge the help and support of my wife, Sylvia Gaylord. She has been encouraging and understanding throughout my graduate studies, and particularly so during the last several months. I greatly appreciate her help in the preparation and editing of this manuscript.

## TABLE OF CONTENTS

|   |     |
|---|-----|
| ABSTRACT .....  | ii  |
| ACKNOWLEDGMENTS .....   | iii |
| LIST OF FIGURES.....  | vi  |
| LIST OF TABLES .....  | x   |
| CHAPTER 1   |     |
| Introduction.....   | 1   |
| References.....   | 7   |
| CHAPTER 2: LASER GENERATION OF ULTRASOUND IN THE<br>ABLATIVE REGIME                     |     |
| 2.1 Introduction .....  | 8   |
| 2.2 Modeling Laser Generation of Ultrasound in the Ablative Regime                      |     |
| 2.2.1 Introduction.....   | 11  |
| 2.2.2 Pressure Induced on the Surface Through Vaporization.....                         | 12  |
| 2.2.3 Expulsion of Melt.....  | 16  |
| 2.2.4 Calculation of Laser Generated Acoustic Waves.....                                | 18  |
| 2.3 Laser Vaporization Solution   |     |
| 2.3.1 Finite Difference Equations .....   | 25  |
| 2.3.2 Temperature Dependence of the Thermal and Optical Properties....                  | 32  |
| 2.3.3 Test of the Model .....   | 36  |
| 2.3.4 Predictions of the Laser Vaporization Model .....                                 | 38  |
| 2.3.5 Spot Size Considerations .....  | 46  |
| 2.3.6 Solution Procedure: Coupling of Vaporization and Acoustic Wave<br>Generation..... | 49  |
| 2.4 Experimental Setup and Procedure  |     |
| 2.4.1 Experimental Setup .....  | 50  |
| 2.4.2 Experimental Procedure .....  | 52  |
| 2.5 Experimental Results/Comparison with Theory   |     |
| 2.5.1 Longitudinal wave amplitude .....   | 54  |
| 2.5.2 Calculated and Experimental Displacement.....                                     | 61  |

|     |   |    |
|-----|---|----|
| 2.6 | Discussion of the Ablative Generation of Ultrasound ..... | 71 |
|     | References.....   | 76 |

**CHAPTER 3: SPATIAL MODULATION OF INCIDENT LASER LIGHT**

|     |                                    |    |
|-----|------------------------------------|----|
| 3.1 | Abstract .....                     | 82 |
| 3.2 | Introduction ...                   | 82 |
| 3.3 | Theory .....                       | 84 |
| 3.4 | System Description .....           | 87 |
| 3.5 | Results and Discussion.....        | 88 |
|     | 3.5.1 Resolution Enhancement ..... | 91 |
|     | 3.5.2 Directionality .....         | 92 |
| 3.6 | Conclusions ...                    | 95 |
|     | References.....                    | 96 |

**CHAPTER 4: TEMPORAL MODULATION OF LASER SOURCES**

|     |  |     |
|-----|--|-----|
| 4.1 | Introduction ...   | 99  |
| 4.2 | Controlling Laser Pulse Length.....                            | 100 |
| 4.3 | Pulse Length Effects on Surface Heating .....                  | 103 |
| 4.4 | Pulse Length Effects on the Generation of Acoustic Waves ..... | 106 |
| 4.5 | Linear Systems Approach to Pulse Length Effects .....          | 111 |
| 4.6 | Linear Systems Approach to Laser Generation in Composites..... | 118 |
| 4.7 | Signal Processing Considerations.....                          | 122 |
|     | References.....  | 126 |

**APPENDIX I: PROGRAM LISTING-LASER VAPORIZATION CODE..... 128**

|          |       |  |
|----------|-------|--|
| Vita ... | ..... |  |
|----------|-------|--|

## LIST OF FIGURES

|             |  |    |
|-------------|--|----|
| Figure 2-1  | Schematic view of laser ablation processes.....  | 11 |
| Figure 2-2  | Melt ejection mechanism given by Allmen.....   | 17 |
| Figure 2-3  | Geometry for elastic wave solution.....  | 19 |
| Figure 2-4  | Description of nodes around melt front.....  | 28 |
| Figure 2-5  | Temperature dependence of thermal conductivity (top) and heat capacity (bottom) in aluminum.....   | 33 |
| Figure 2-6  | Polynomial fitting functions used in the vaporization model for thermal conductivity (top) and heat capacity (bottom).....               | 34 |
| Figure 2-7  | Temperature dependence of the resistivity of aluminum.....   | 35 |
| Figure 2-8  | Laser heating comparison of exact solution with solution obtained through finite difference technique.....                               | 37 |
| Figure 2-9  | Comparison of Gaussian and modified Gaussian laser pulse models with experimentally measured laser pulse.....                            | 39 |
| Figure 2-10 | Calculated surface temperature (top) and melt front position (bottom) as a function of time at 100 and 150 MW/cm <sup>2</sup> .....      | 41 |
| Figure 2-11 | Material removal through surface vaporization and melt flow at 400 (top) and 450 MW/cm <sup>2</sup> as a function of time.....           | 42 |
| Figure 2-12 | Total material removal, and contribution of melt flow and surface vaporization processes as a function of incident laser irradiance..... | 43 |
| Figure 2-13 | Pressure pulses exerted on the surface at various incident laser pulse intensities.....  | 44 |
| Figure 2-14 | Peak pressure exerted on the surface as a function of incident laser irradiance.....   | 44 |
| Figure 2-15 | Maximum surface temperature reached as a function of incident laser pulse radiance.....  | 45 |
| Figure 2-16 | Fraction of energy used for sample heating as a function of incident laser pulse irradiance.....   | 46 |

|             |  |       |
|-------------|--|-------|
| Figure 2-17 | Spatial irradiance distribution of the incident laser pulse (top) and spatial distribution of pressure pulse on the surface with Gaussian fit .....                        | 48    |
| Figure 2-18 | Calculated pressure pulse radius as a function of incident laser pulse irradiance .....  | 49    |
| Figure 2-19 | Experimental setup for vacuum ablation testing.....  | 51    |
| Figure 2-20 | Setup for evaluating generation laser spot size.....   | 53    |
| Figure 2-21 | Peak longitudinal wave amplitude as a function of incident laser irradiance .....  | 55    |
| Figure 2-22 | Longitudinal wave generation efficiency presented as a function of incident laser power density.....   | 57    |
| Figure 2-23 | Experimental and theoretical amplitude of longitudinal wave displacement as a function of incident laser irradiance.....   | 58    |
| Figure 2-24 | Theoretical and experimental longitudinal wave amplitude at .532 $\mu$ m as a function of incident laser power density.....  | 60    |
| Figure 2-25 | Experimentally measured (top) and calculated thermoelastic waveforms used in ablation model.....   | 62    |
| Figure 2-26 | Theoretical ablative signals predicted in aluminum.....  | 64-67 |
| Figure 2-27 | Experimental signals measured in aluminum .....  | 67-69 |
| Figure 2-28 | Theoretical and experimental waveforms at 300 MW/ cm <sup>2</sup> .....  | 70    |
| Figure 2-30 | Comparison of waveforms generated in air and vacuum at a) 284 MW/cm <sup>2</sup> and b) 660 MW/cm <sup>2</sup> .....   |       |
| Figure 3-1  | Experimental setup for the generation of FM surface waves .....  | 88    |
| Figure 3-2  | Comparison of a) theoretical and experimental chirped surface waves and b) the compressed waveforms after autocorrelation .....  | 89    |
| Figure 3-3  | a) Single shot FM surface waveform and b) the waveform after matched filtering showing a 15-fold increase in signal to noise ratio and compression of the wave packet..... | 90    |

|             |  |     |
|-------------|--|-----|
| Figure 3-4  | Overlapping FM and narrowband surface wave packets (a, c). Matched filtering allows for resolution of individual arrivals in the chirped case (b) but not in the narrowband case (d) ..... | 93  |
| Figure 3-5  | a) Single shot waveform on an aluminum block. Matched filtering with the “forward chirp” and “reverse chirp” (b, c).....   | 94  |
| Figure 4-1  | Effects of varying laser cavity length, pumping rate, and output coupler reflectivity .....  | 102 |
| Figure 4-2  | Relative amount of absorbed laser energy needed to raise the surface temperature to $T_{max}$ as a function of pulse length .....  | 105 |
| Figure 4-3  | Definition of source-receiver geometry.....  | 107 |
| Figure 4-4  | Relative peak power in laser pulse needed to raise the surface temperature to $T_{max}$ as a function of pulse length.....   | 109 |
| Figure 4-5  | Relative longitudinal wave amplitude possible in thermoelastic regime without exceeding $T_{max}$ as a function of pulse length.....   | 110 |
| Figure 4-6  | Comparison of longitudinal wave displacement as pulse length is varied a) in the regime $t_s \gg t_p$ and b) in the regime $t_s \ll t_p$ .....   | 112 |
| Figure 4-7  | Comparison of longitudinal wave displacement from 20ns .....   | 115 |
| Figure 4-8  | Surface wave amplitude as a function of pulse length.....  | 116 |
| Figure 4-9  | a) Calculated surface wave amplitude from 10ns pulse and 125ns pulse and b) amplitudes have been scaled for analysis of temporal extent .....  | 117 |
| Figure 4-10 | Verification of linear systems approach with epicentral waveforms in a graphite PEEK sample.....   | 118 |
| Figure 4-11 | Epicentral waveforms on two regions of graphite-PEEK sample.....   | 120 |
| Figure 4-12 | Relative amplitude and spatial extent of the incident laser pulses considered showing a) the 10ns and b) the FM pulse .....  | 123 |
| Figure 4-13 | Relative surface heating produced by a) 10ns pulse and b) pulse.....   | 124 |

Figure 4-14 Relative surface displacement produced by a) 10ns pulse and b) FM pulse when surface temperature  $T_{max}$  is reached..... 124

Figure 4-15 Correlation peaks produced through match filtering of the acoustic signal generated by the FM pulse (top) and the 10ns pulse (bottom)..... 125

## LIST OF TABLES

|           |  |    |
|-----------|--|----|
| Table 1-1 | Summary of advantages and disadvantages of laser ultrasonic methods.....               | 2  |
| Table 2-1 | Models of the laser/materials interaction process .....                                | 10 |
| Table 2-2 | Summary of thermal and optical properties of aluminum used in vaporization model ..... | 38 |

## CHAPTER 1

### Introduction

The principles and uses of optical techniques for the generation and detection of ultrasound have been discussed extensively in the literature. The generation of ultrasound through laser heating of a material surface was first considered by White (1963)<sup>1</sup> soon after the advent of the laser. Several excellent reviews of the progress in the field of laser ultrasonics are available.<sup>2,3,4</sup> Laser ultrasonic techniques have several advantages over other inspection methods, making them an attractive option for select applications. A review of some advantages and disadvantages of laser based techniques is presented in Table 1-1. Unfortunately, poor sensitivity and high cost of laser ultrasonic systems are currently limiting industrial application. In general, implementation is limited to situations where laser inspection methods present the only available solution, or the few cases that prove cost effective. The goal of the current work is to increase the sensitivity of optical generation and detection systems. The work focuses on the laser/materials interaction that occurs during the generation of ultrasonic waves, and considers a number of methods by which laser ultrasonic systems can achieve greater sensitivity through control of the laser generation source. In order to help define the detectability limits of interferometer systems, the signal-to-noise ratio (SNR) can be evaluated. For the purposes of this discussion, the SNR is defined as:

| ADVANTAGES   | DISADVANTAGES  |
|--|--|
| 1. Non-contacting<br>(couplant problems eliminated and no surface loading) | 1. Sensitivity<br>(optical techniques generally have significantly lower sensitivity than other methods) |
| 2. Remote<br>(access to hostile environments)                              | 2. Relatively Expensive  |
| 3. Rapid Scanning Capability   | 3. Sample Surface Condition Important for Interferometry   |
| 4. Allow Operation on Geometrically Awkward Specimens                      | 4. Requires Laser Safety Precautions   |

|   |  |
|---|--|
| 5. Can be used as an Ultrasonic Point Source                          |  |
| 6. Broadband (ultra-high frequency generation and detection possible) |  |
| 7. Reproducible Source  |  |
| 8. Laser Interferometry Offers an Absolute Calibration Standard       |  |

Table 1-1 Summary of advantages and disadvantages of laser ultrasonic methods.

$$\text{SNR} = \frac{s_o^2(t_m)}{n_o^2(t)} \quad (1.1)$$

where  $s_o(t_m)$  is the maximum signal amplitude and  $n_o^2(t)$  is the mean squared noise amplitude.

Several sources of noise exist in the detection laser, photodetectors, and processing electronics of an optical detection system. Amplitude and wavelength fluctuations in the laser source contribute to noise. Room vibrations and relaxation of optical components can introduce additional noise into the system. Finally, noise in the optical detector and associated electronics include 1/f noise, thermal noise, and shot noise. Most of these noise sources can be controlled through, for example, reducing system bandwidth, decreasing component temperatures, and employing electronic noise rejection schemes. Ultimately, the SNR of an optical detection system is limited by shot noise. Shot noise is unique among the noise sources given in that it depends on signal amplitude. Consequently, shot noise limited performance of an optical detection system can be achieved easily by increasing the light incident on the detector such that the shot noise grows to dominate all other noise sources.<sup>5</sup>

Expressions for the SNR of several optical detection techniques, including optical beam deflection, and path stabilized, heterodyne, and Fabry-Perot interferometry, have been presented in the literature.<sup>5,6</sup> For all of these systems, assuming shot noise limited detection, the following relation holds:

$$\text{SNR} \propto \frac{\delta_m^2 P}{B} \quad (1.2)$$

where  $\delta_m$  is the maximum amplitude of the signal to be detected,  $P$  is the optical power incident on the detector, and  $B$  is the bandwidth of the detection system. By maximizing this quantity, the ability of a laser ultrasonic system to detect acoustic signals can be optimized.

The SNR can be increased through the use of a stable high-power laser in the detection system. If interferometric detection techniques are used on optically rough or highly absorbing surfaces, only a fraction of the laser light incident on the material will make it back to the detection system. The remainder of the light is lost to scattering or absorption processes. The SNR increase that can be achieved through increasing  $P$  is dictated by the power of the detection laser and the ability of the interferometric detection system to collect scattered light. The limit is generally set by the cost and availability of stable high-power laser sources.

Further enhancement requires refinement of the laser generation process, such that either the amplitude of the laser generated ultrasonic signals is increased or the bandwidth decreased. In the former case, the limit on the amplitude of laser generated ultrasonic systems is generally dictated by the damage tolerance of the surface under inspection. If damage is to be avoided, then generation must take place in the thermoelastic regime. The amount of laser energy that can be used for acoustic wave generation can not exceed that which heats the surface above the vaporization temperature. If a certain amount of surface damage is acceptable, the amplitude of laser generated acoustic signals may be further enhanced through generation in the ablative regime. In order to achieve SNR increase through bandwidth reduction of the optical detection system, the bandwidth of the laser generated acoustic waves must also be decreased to match that of the detection system. This requires control of the laser generation source in time and/or space in such a way that narrow bandwidth acoustic signals are generated.

Signal processing techniques offer another means by which SNR increase may be obtained. In the simplest case, signal averaging can be performed. This may be a viable option when generating ultrasound with a high repetition rate pulsed laser. Filtering techniques may also be used. If the noise is white, as is the case for a shot noise limited optical detection system, the SNR can be maximized by using a matched filter. The maximum SNR is given by:

$$\text{SNR}_{\text{max}} = \frac{2E}{N_o} \quad (1.3)$$

where  $E$  is the total signal and  $N_0/2$  is the noise spectral density. This indicates that the SNR can be enhanced by increasing the energy in the signal to be detected. The Wiener filter has also been used for the filtering of laser ultrasonic signals.<sup>7</sup> This filter minimizes the mean squared error between the detected signal and a reference signal. Signal averaging, matched filtering, and Wiener filtering are three examples of signal processing techniques that can be used to enhance the detectability of laser generated acoustic signals. Other established signal processing techniques will invariably be incorporated into future laser based inspection systems.

The acoustic signal generated by a laser source depends on the thermal, optical, and elastic properties of the specimen, and on the characteristics of the laser source. For a given materials system, the laser pulse parameters can be chosen such that the SNR of the detection system is maximized. There are four laser pulse parameters to consider: temporal profile, spatial profile, energy, and wavelength. Of these, wavelength probably offers the least flexibility, although harmonic crystals do provide some choice in wavelength for a given Q-switched laser system. Wavelength considerations are not discussed at length in the present work. Various aspects of temporal and spatial modulation of laser light used for the generation of acoustic waves will be presented. Also, the effects of increasing laser pulse energy beyond the point at which surface vaporization is initiated will be considered. A brief outline of the coming chapters is presented below.

Chapter 2 presents an analysis of laser generation of acoustic waves in the ablative regime. The process of laser vaporization in vacuum is modeled using an implicit finite difference technique. As a surface is heated beyond the melting point, the surface melts and the melt front propagates into the material. Continued heating brings the material to the vaporization temperature. The vaporization process exerts a force on the material surface which serves as a source for acoustic wave generation. The changes in the thermal and optical properties of materials with temperature are discussed. Acoustic wave generation is considered for the limited range of vaporization in which absorption of light in the vapor can be neglected. Processes beyond this point are discussed qualitatively. The amplitude of acoustic waves generated in the ablative regime is directly related to the surface vaporization process. A greater understanding of this relationship may allow for the acoustic signal to be used simultaneously for elastic property determination or materials inspection and surface damage monitoring.

Chapter 3 presents a novel technique for laser ultrasonic system sensitivity increase through spatial modulation of the incident laser source. The method uses a transmission mask to generate linearly frequency

modulated (chirped) surface waves. The laser source is extended in space allowing for a large amount of laser energy to be utilized in the generation process before the surface damage threshold is exceeded. The received signal is subsequently processed using a matched filter. The application of a matched filter to a linearly frequency modulated signal leads to the compression of this signal in time. The advantage of this technique is that it allows for the incident laser source to be distributed over a large area in space and subsequently compressed in time upon reception through application of the matched filter. Temporal resolution is maintained while surface damage is avoided. The SNR is maximized through matched filtering in accordance with Eq. (1.3).

Chapter 4 deals with the temporal modulation of laser sources for the generation of acoustic waves. Methods of controlling the pulse length of a conventional Q-switched laser system are first described. The effects of varying incident laser pulse length on the thermoelastic generation of acoustic waves is considered. For materials exhibiting strong surface absorption, it is found that there exists a pulse length which optimizes the laser generated signal amplitude while avoiding surface damage. A linear systems approach for determination of pulse length effects is presented. This allows for the calculation of acoustic waves with an arbitrary temporal profile based on a theoretically or experimentally determined reference signal. Finally, pulse length effects on two composite specimens are evaluated and the results discussed.

## REFERENCES

- <sup>1</sup> R.M. White, "Generation of elastic waves by transient surface heating," *J. Appl. Phys.* **24** (12) 3559-3567 (1963)
- <sup>2</sup> C.B. Scruby and L.E. Drain, *Laser Ultrasonics, Techniques and Applications*, Adam Hilger, N.Y. (1990)
- <sup>3</sup> S.J. Davies, C. Edwards, G.S. Taylor and S.B. Palmer, "Laser-generated ultrasound: its properties, mechanisms, and multifarious applications," *J. Phys. D.* **26** 329-348 (1993)
- <sup>4</sup> D.A Hutchins, "Mechanisms of pulsed photoacoustic generation," *Can. J. Phys.* **64** 1247-1264 (1986)
- <sup>5</sup> J.W. Wagner, "Optical Detection of Ultrasound," in *Physical Acoustics Vol. XIX*, Academic Press, N.Y. (1990)
- <sup>6</sup> J.W. Wagner and J.B. Spicer, "Theoretical noise-limited sensitivity of classical interferometry," *Opt. Soc. Am. B*, **4** 1316-1326 (1987)

<sup>7</sup> J.B. Deaton Jr. and J.W. Wagner, "Wiener filtering of laser-generated multiple pulse narrow-band ultrasound for enhanced detectability by a laser interferometer," *Ultrasonics*, **32** (3) 187-193 (1994)

## Laser Generation of Ultrasound in the Ablative Regime

### 2.1 Introduction

In this chapter, the effects of increasing the incident laser irradiance on the generation of acoustic waves are examined. Laser generation of acoustic waves in the thermoelastic regime has been well characterized.<sup>1,2,3,4</sup> In the low irradiance regime, before vaporization takes place, the amplitude of laser generated acoustic waves shows a linear increase with pulse energy.<sup>5</sup> The laser generation process is somewhat less well characterized in the ablative regime. Experimentally, it is well known that there is a large enhancement in the amplitude of the longitudinal wave generated in the ablative regime. Qualitative models have been presented which indicate that the shape of the ablative waveform can be understood as being a superposition of a thermoelastic (point expansion) source and a force acting normal to the surface.<sup>5,6</sup> The physical origin of the normal force is the momentum transfer from the evaporating species. These papers also show that the time dependence of the normal force, at low irradiance ablation, follows that of the incident laser pulse. At high irradiance ablation, the forcing function assumes a step function time dependence. Although the shape of the displacements predicted in the literature agrees well with experiment, indicating that the assumed forcing functions are correct, the amplitude and shape of the normal forcing function is deduced qualitatively without solution of the laser vaporization problem.

A more quantitative analysis of the generation of acoustic waves in the ablative regime was recently presented.<sup>7</sup> Many of the important issues concerning laser vaporization were addressed. Still, assumptions made considering, for example, the distribution of forces exerted within the laser spot, indicate the need for further study in this area. Unfortunately, there are few comparisons of experimental and theoretical displacements and the agreement between experiment and theory presented is only moderate.

An understanding of laser generation of acoustic waves in the ablative regime is important for several reasons. Generating in the thermoelastic regime, it is often important to use as much laser energy as possible while remaining below the vaporization threshold. Thus it is desirable to be able to predict the laser irradiance at which a detectable amount of vaporization takes place. Next, there are many ultrasonic inspection applications in which a small amount of surface damage can be tolerated. In these cases, it is important to have a good understanding of the vaporization process to take advantage of the large acoustic wave enhancement possible in the ablative regime. This may allow for the generation of high amplitude acoustic signals, while staying below some specified damage tolerance level. If the relationship between acoustic signals produced in the ablative regime and surface damage incurred is well characterized, then the acoustic signature can be used simultaneously for process monitoring / inspection and surface damage monitoring. It also allows for the possibility of using acoustic signals for direct monitoring of the laser/material interaction region to track vaporization, surface temperature, etc.

Laser-material interactions have been discussed extensively in the literature.<sup>8,9,10,11</sup> The interaction involves the coupling of laser energy into a material, resulting in melting and vaporization; ejection of ions, molecular species, and fragments; shock waves; plasma initiation and expansion; and a

| <u>Author</u>                        | <u>Results</u>   |
|--------------------------------------|--|
| Ready <sup>12</sup> (1965)           | material removal by vaporization                                     |
| Anisimov <sup>13</sup> (1969)        | discontinuities across Knudsen layer in vacuum                       |
| Allman <sup>14</sup> (1976)          | material removal by vaporization and melt flow                       |
| Knight <sup>15</sup> (1979)          | discontinuities across Knudsen layer as function of flow Mach number |
| Rosen et.al. <sup>16</sup> (1982)    | thermal and impulse coupling of laser energy                         |
| Chan et. al. <sup>17</sup> (1987)    | material removal by vaporization and melt flow                       |
| Zweig (1991) <sup>18</sup>           | laser drilling depth and recoil (medical)                            |
| Vertes et.al. <sup>19</sup> (1994)   | laser ablation of Cu, processes in vapor                             |
| Aden and Kreutz <sup>20</sup> (1996) | material removal and plasma dynamics                                 |
| Anisimov et.al. <sup>21</sup> (1996) | three dimensional model of plume expansion                           |

Table 2-1 Models of the laser/materials interaction process.

hybrid of these and other processes. There are many laser ablation models in the literature used for the analysis of such processes as laser drilling, pulsed laser deposition of thin films, removal and patterning of thin films, laser fusion, and inductively coupled plasma atomic emission spectroscopy (IES-AES). For a given application (laser irradiance and thermal and optical properties of the material under illumination), it is important to consider the relevant processes and to model the situation accordingly. A brief history of several laser/material interaction models is presented in Table 2-1. A more complete historical development is given in references 8-11 and the references therein.

## 2.2 Modeling Laser Generation of Ultrasound in the Ablative Regime

### 2.2.1 Introduction

A schematic view of the laser ablation process is given in Figure 2-1. The surface is first heated to the melting point, at which time the melt front begins to propagate into the material. Continued heating brings the material to the vaporization point. Adjacent to the surface is a thin layer (on the order of a few

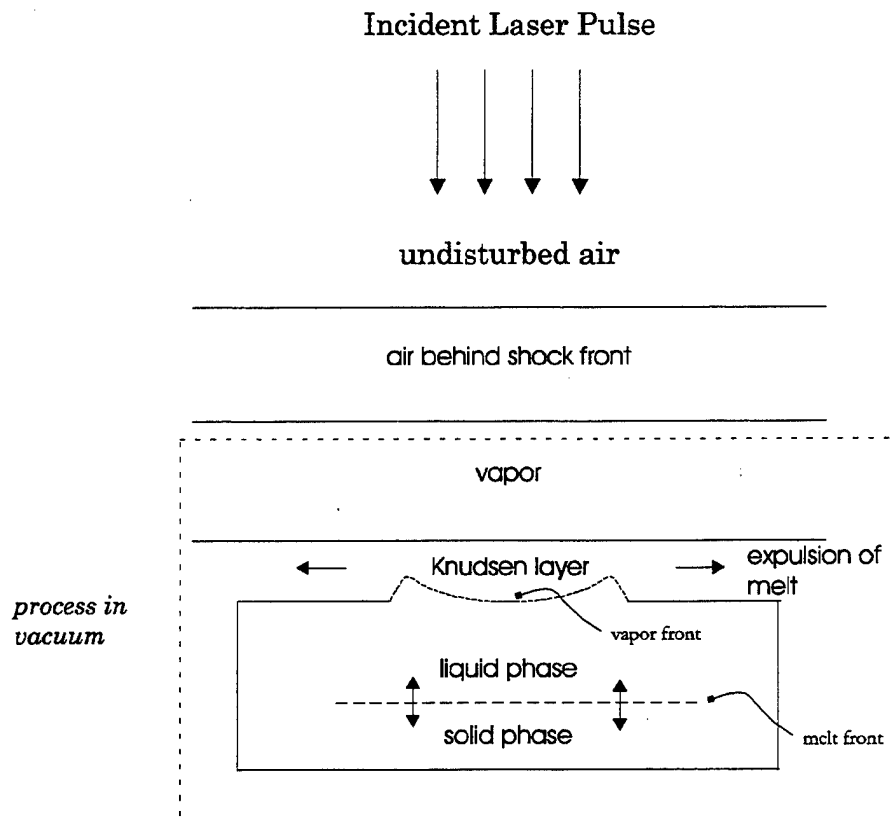


Figure 2-1

Schematic view of laser ablation processes.

molecular mean free paths) known as a Knudsen layer, where the vapor is not in translational equilibrium. Across this layer, there are discontinuities in temperature, pressure, and density. Beyond the Knudsen layer is a region of expanding vapor. In this analysis it is assumed that vaporization takes place in vacuum. In this case, the gas dynamic processes outside of the Knudsen layer need not be considered and the vapor expands freely into vacuum. Continued heating well beyond the vaporization point will lead to vapor breakdown and absorption of the incoming laser light through photo-ionization and inverse bremsstrahlung processes. For simplicity, vapor breakdown is not considered in this model, although it will be discussed in the results section. Thus the applicability of the model holds up to the point when laser light absorption by the vapor becomes significant.

### 2.2.2 Pressure Induced on the Surface Through Vaporization

The core vaporization model to be presented has seen widespread use in the study of various laser ablation phenomena. The relevant physical processes outlined below are generally accepted and numerous examples can be found in the literature. For example, apart from several of the references in Table 2.1, models showing reasonable similarities have been presented recently by Fahler<sup>22</sup> (1996), Svendsen<sup>23</sup> (1995), and Tsui<sup>24</sup> (1994). The model describes laser heating of a finite plate and is limited to the case where plasma processes do not play an important role.

The heating induced by a Q-switched laser can be described by the heat equation with a source term to include light absorption:

$$\rho_i(T)C_{p_i}(T)\frac{\partial T_i(x,t)}{\partial t} = \frac{\partial}{\partial x}(K_i(T)\frac{\partial T_i(x,t)}{\partial x}) + I_0(t)\alpha(T)(1 - R(T))\exp(-\alpha(T)x)$$

$i = 1,2$  (2.1)

where  $\rho$  is the mass density,  $C$  is the heat capacity,  $K$  is the thermal conductivity,  $I$  is the incident laser power density,  $R$  is the reflectivity, and  $\alpha$  is the absorption coefficient. The subscript  $i$  is 1 for the solid phase and 2 for the liquid. The temperature dependence of the thermal and optical properties of the material is shown. One dimensional heating is assumed. This approximation, neglecting radial heat flow from the illuminated region, holds reasonably well as long as the laser spot size is sufficiently large in comparison to the characteristic heat flow distance or thermal diffusion length in the material on the time scale of interest. The thermal diffusion length is given by:

$$L_{\text{thermal}} = (4\kappa t)^{0.5}$$

(2.2)

where  $\kappa$  is the thermal diffusivity and  $t$  is the time scale over which heating will be calculated. In the present case, the time scale may be taken as the laser pulse length. The thermal diffusion length in aluminum ( $\kappa = 1.12 \text{ cm}^2/\text{sec}$ ) heated with a Q-switched laser pulse ( $t = 15\text{ns}$ ) is found to be equal to  $2.59\mu\text{m}$ . Therefore the one dimensional model can be expected to hold reasonably well as long as the incident laser spot size is sufficiently greater than  $2.59 \mu\text{m}$ .

Considering the heating of a plate in vacuum, Eq. (2.1) is augmented by the condition that no heat flows across either bounding surface. This is given as:

$$\frac{\partial T}{\partial x} = 0 \quad \text{at} \quad x = 0, L \quad (2.3)$$

where  $L$  is the plate thickness. The boundary condition between the solid and liquid phases (at the melt front) is included as:

$$-K_s \frac{\partial T_1}{\partial x} + K_l \frac{\partial T_2}{\partial x} = L_1 \frac{\partial s}{\partial t} \quad (2.4)$$

where  $K_s$  is the thermal conductivity of the solid at temperature  $T_1$  at the interface,  $K_l$  is the thermal conductivity of the liquid at temperature  $T_2$ ,  $L_1$  is the latent heat of melting and  $ds/dt$  is the interface velocity.

When the surface temperature exceeds the equilibrium vaporization temperature at a given pressure, ablation begins. In this model, the ablation mechanism is treated simply as thermal evaporation from a hot surface. Assuming a Maxwellian velocity distribution for the vapor particles, the vaporization front velocity is given by:<sup>11</sup>

$$\frac{\partial s_v}{\partial t} \approx \frac{V_1 p(T)}{(2\pi MRT_s)^{\frac{1}{2}}} \quad (2.5)$$

where  $V_1$  is the molar volume,  $p(T)$  is the equilibrium vapor pressure at the surface temperature  $T_s$ ,  $M$  is the molar mass, and  $R$  is the universal gas constant. The equilibrium vapor pressure may be found from consideration of the Clausius-Clapeyron equation as follows:

$$p(T) = p_o \exp(L_v \left( \frac{T_s - T_{lv}}{RT_s T_{lv}} \right)) \quad (2.6)$$

where  $T_{lv}$  is the equilibrium vaporization temperature at ambient pressure  $p_o$ , and  $L_v$  is the latent heat of vaporization. The boundary condition to be evaluated at the liquid-vapor interface is given as:

$$K_1 \frac{\partial T_1}{\partial x} = L_v \frac{\partial s_v}{\partial t} \quad (2.7)$$

The vapor near the vapor-solid interface is not in translational equilibrium. This is achieved within a few mean free paths by collisions between particles in a Knudsen layer region. The Knudsen layer is analyzed by treating this region as a gas dynamic discontinuity across which conservation of mass, momentum, and energy are applied.<sup>13,15</sup> This process has previously been modeled for the vacuum case (Anisimov<sup>13</sup>, 1969) as well as for cases when the surface is surrounded by air at various pressures (Knight<sup>15</sup>, 1979). For the present analysis, in order to calculate the pressure applied to the sample surface, it is only necessary to know the pressure jump across the Knudsen layer under vacuum conditions. This has been found to be:<sup>13,15</sup>

$$\frac{P_{\text{vapor}}}{P_{\text{sat}}} = 0.206 \quad (2.8)$$

where  $p_{\text{sat}}$  is the saturated vapor pressure. The pressure exerted on the surface can now be found by consideration of the momentum- flux through the Knudsen layer as follows:<sup>18</sup>

$$p_{\text{surface}} = p_{\text{vapor}} (1 + \gamma M_v^2) \quad (2.9)$$

where  $\gamma$  is the ratio of specific heats in the vapor and  $M_v$  is the flow Mach number outside of the Knudsen layer. For the case of a monatomic gas evaporating into vacuum we have  $\gamma = 5/3$  and  $M_v = 1$ . Combining Eqs. (2.8) and (2.9) under these conditions, the relation between the saturated vapor pressure and the pressure exerted on the specimen surface is:

$$p_{\text{surface}} = 0.549 p_{\text{sat}} \quad (2.10)$$

### 2.2.3 Expulsion of Melt

The analysis above allows for the calculation of material removed from the material surface through surface vaporization. Vaporization pressure induced melt flow can provide another significant means of material removal and, in fact, is the primary source of material removal in laser cutting processes with long (non Q-switched) laser pulses. Several models of vaporization induced melt flow have been reported in the literature.<sup>14,17,18</sup> In order to simply approximate the extent of melt flow induced by a Q-switched laser pulse in the irradiance range of interest, the model of Allmen<sup>14</sup> (1976) has been adopted. A sketch of the

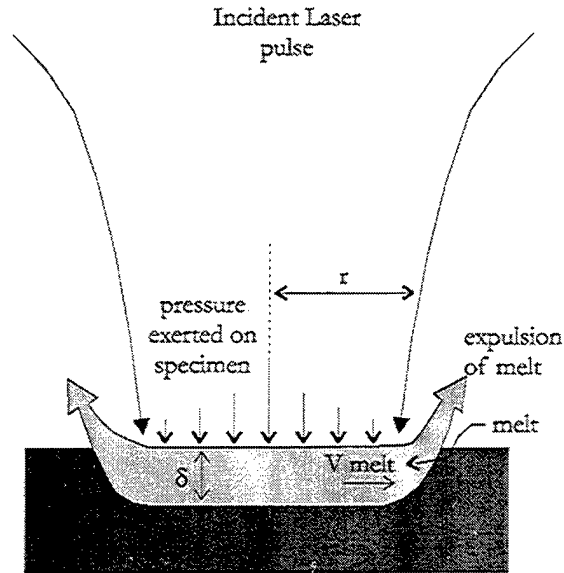


Figure 2-2

Melt ejection mechanism given by Allmen (after Allmen<sup>11</sup>)

process is given in Figure 2-2. The vaporization pressure is assumed to act as a piston on the melt layer of thickness  $\delta_{melt}$ . From volume work considerations this pressure causes the melt to flow with a velocity given by:

$$v_{melt} = (2p / \rho)^{0.5} \quad (2.11)$$

where  $p$  is the surface pressure and  $\rho$  is the density. The melt is assumed to be expelled from the edge of the illuminated spot leading to the following approximation for surface recession velocity due to melt expulsion:

$$F_{\text{melt}} = \frac{2\delta v_{\text{melt}}}{r} \quad (2.12)$$

where  $\delta$  is the melt thickness and  $r$  is the laser spot radius. The melt begins to flow when the radial pressure force exceeds the surface tension of the liquid metal. Eq. (2.12) can only be expected to give an order of magnitude approximation for the amount of melt flow. It will be shown that melt flow is not predicted to be a primary source of material removal for Q-switched laser sources. Under other conditions, especially when ablating with long pulse lasers at moderate power levels, closer attention must be paid to the flow of melt if accurate material removal rates are to be calculated.

#### 2.2.4 Calculation of Laser Generated Acoustic Waves

The above analysis allows for the calculation of pressure exerted on the surface of a material due to vaporization. The laser generated acoustic signal, in the ablative regime, can be considered the superposition of an acoustic signal resulting from the thermoelastic expansion of the material and an acoustic signal resulting from material ablation. In the present analysis, the thermoelastic component of the acoustic signal is calculated using a model directly following that of Spicer.<sup>2</sup> This model has shown excellent agreement with experiment for the laser generation of acoustic waves in the thermoelastic regime.<sup>2</sup> The force exerted on the surface due to vaporization is assumed to act as a normal point force with an amplitude and time dependence determined with the vaporization model outlined above.

The axially symmetric elastic wave problem is set up in cylindrical

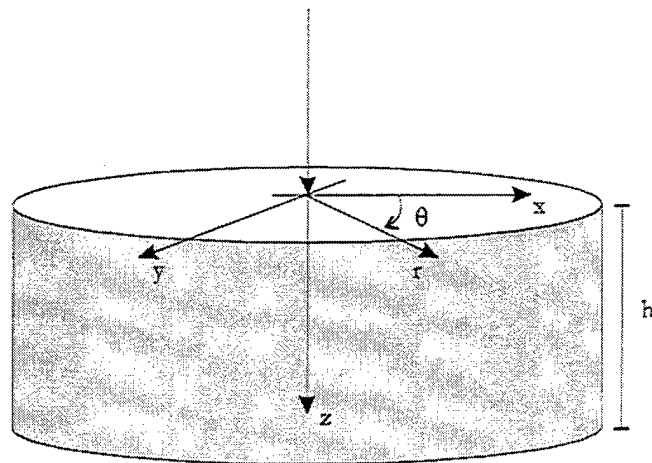


Figure 2-3 Geometry for elastic wave solution.

coordinates for both the thermoelastic and ablative source calculation, with the geometry illustrated in Figure 2-3. The calculation is performed on an infinite plate of thickness  $h$ . The decomposition of the displacement vector is written as:<sup>25</sup>

$$\begin{aligned}
 u &= \frac{\partial \phi}{\partial r} - \frac{\partial \psi}{\partial z} \\
 w &= \frac{\partial \phi}{\partial z} + \frac{1}{r} \frac{\partial(rz)}{\partial r}
 \end{aligned}
 \tag{2.13}$$

where displacement components in the  $r$ ,  $\theta$ , and  $z$  directions are given by  $u$ ,  $v$ , and  $w$  respectively. The vector potential is given by  $\psi$  ( $\theta$  component) and the scalar potential by  $\phi$ . The two potentials satisfy the following wave equations:

$$\frac{\partial^2 \phi}{\partial r^2} + \frac{1}{r} \frac{\partial \phi}{\partial r} + \frac{\partial^2 \phi}{\partial z^2} = \frac{1}{c_L^2} \frac{\partial^2 \phi}{\partial t^2}$$

$$\frac{\partial^2 \psi}{\partial r^2} + \frac{1}{r} \frac{\partial \psi}{\partial r} + \frac{\partial^2 \psi}{\partial z^2} - \frac{\psi}{r^2} = \frac{1}{c_T^2} \frac{\partial^2 \psi}{\partial t^2}$$
(2.14)

Where  $C_L$  and  $C_T$  are the longitudinal and shear wave speeds respectively.

The stress-displacement relations are given as:

$$\tau_z = (\lambda + 2\mu) \frac{\partial w}{\partial z} + \frac{\lambda}{r} \frac{\partial (ru)}{\partial r}$$

$$\tau_{rz} = \mu \left( \frac{\partial u}{\partial z} + \frac{\partial w}{\partial r} \right)$$
(2.15)

Where  $\lambda$  and  $\mu$  are the Lamé constants. These equations are augmented by the initial conditions. If the plate is at rest prior to  $t = 0$  then:

$$\phi(r, z, 0) = \dot{\phi}(r, z, 0) = \psi(r, z, 0) = \dot{\psi}(r, z, 0) = 0$$
(2.16)

Equations (2.13)-(2.16) specify the elastic wave problem under consideration and must now be supplemented by the appropriate stress boundary conditions. It has been shown that, under certain conditions, the thermoelastic source can be modeled as an equivalent elastic boundary source.<sup>2</sup> These conditions are given as 1) the point of observation is outside the volume defined by significant thermal diffusion 2) the plate is optically and thermally thick on the time scales of interest 3) optical energy is converted to heat close to the irradiated

boundary and 4) the thermal propagation speed in the material is equal to the longitudinal wave speed. Assuming these conditions hold, then following Hankel-Laplace transformed boundary conditions may be used:<sup>2</sup>

$$\tau_{zz}(H-L)_{z=0} = \frac{\rho}{b^2} \left( -\frac{\kappa(\beta^2 + p^2)}{s\varepsilon} \right) \gamma Q_0 Q(P)Q(S)$$

$$\tau_{rz}(H1-L)_{z=0} = \frac{\rho p}{b^2} \left( -\frac{2\kappa}{s} \right) \gamma Q_0 Q(P)Q(S)$$

$$\tau_{zz}(H-L)_{z=h} = \tau_{rz}(H1-L)_{z=h} = 0$$

where:

$$\beta^2 = b^2 s^2 + p^2$$

$$\varepsilon^2 = \frac{s}{\kappa} + a^2 s^2 + p^2$$

(2.17)

where H and H1 denote Hankel transforms of zero and first order respectively, L denotes the Laplace transform, p is the Hankel variable, s is the Laplace variable, Q(P) and Q(S) are the Hankel transform of the incident laser pulse spatial profile and Laplace transform of the laser pulse temporal profile respectively, a and b are the reciprocal of the longitudinal and sheer wave speeds,  $\kappa$  is the thermal diffusivity,  $Q_0$  is the absorbed laser energy, and  $\gamma = Ba^2\alpha/\rho$  where B is the bulk modulus and  $\alpha$  is the coefficient of thermal expansion.

The system of Eqs.(2.13-2.16) is solved using a transform technique. A Laplace transform is performed with respect to the temporal variable and a Hankel transform with respect to the radial component of displacement. The resulting ordinary differential equations [Eqs. (2.14)] are then solved subject to the boundary conditions given in Eq. (2.17). Detailed expressions for the Hankel-Laplace transformed potentials have been presented elsewhere<sup>2</sup> and will not be

repeated here. The displacement components at the point of observation are found by numerically inverting the transformed solution.

The component of displacement resulting from the vaporization of the free surface is found using the same set of Eqs. (2.13-2.16) subject to the following boundary conditions:

$$\begin{aligned}\tau_{zz}|_{z=0} &= -Q\delta(t)\frac{\delta_r}{2\pi r} \\ \tau_{rz}|_{z=0} &= \tau_{rz}|_{z=h} = \tau_{zz}|_{z=h} = 0\end{aligned}\tag{2.18}$$

where  $Q$  in this case indicates the magnitude of the forcing function. The system of Eqs. (2.13-2.16, 2.18) is then solved using the same Laplace-Hankel transform technique outlined for the thermoelastic case, with the Laplace-Hankel transformed boundary conditions given in this case by:

$$\begin{aligned}\tau_{zz}(H-L)_{z=0} &= \frac{-Q}{2\pi} \\ \tau_{rz}(H-L)_{z=0} &= 0 \\ \tau_{zz}(H-L)_{z=h} &= \tau_{rz}(H-L)_{z=h} = 0\end{aligned}\tag{2.19}$$

The solution is convolved with the temporal and spatial dependence of the forcing function as indicated by the vaporization routine. It is assumed that the spot size over which the pressure acts on the surface is much smaller than the specimen thickness. Under this assumption, the pressure can be integrated over the spot yielding a force,  $Q$ , which acts at a point on the surface. Thus the spatial extent of the ablative source is ignored. At present, only the epicentral solution is

considered in which case simplifications allow for the normal displacement component to be expressed analytically. Solutions for other points on the plate may be obtained numerically using a routine analogous to that used for the thermoelastic case but replacing Eq. (2.17) with Eq. (2.19). Finally, only the first longitudinal and shear wave arrivals will be considered, making the solution valid for the time range given by:

$$t \leq \frac{3h}{C_L} \quad (2.20)$$

where  $h$  is the plate thickness and  $C_L$  is the longitudinal wave speed.

The epicentral displacement component normal to the surface and valid in the time frame indicated above is given by:<sup>6</sup>

$$u_{\text{epicenter}} = f(t) * \frac{Q}{\pi \mu h C_T^2} \left( \frac{\partial g_L}{\partial t} + \frac{\partial g_S}{\partial t} \right)$$

where:

$$g_L = \frac{(S_L^2 + C_L^{-2})(2S_L^2 + C_T^{-2})^2}{[(2S_L^2 + C_T^{-2})^2 - 4S_L^2(S_L^2 + C_T^{-2})^5(S_L^2 + C_T^{-2})^5]^2} H\left(t - \frac{h}{C_L}\right)$$

$$g_S = \frac{-4S_S^2(S_S^2 + C_L^{-2})(S_S^2 + C_T^{-2})}{[(2S_S^2 + C_T^{-2})^2 - 4S_S^2(S_S^2 + C_L^{-2})^5(S_S^2 + C_T^{-2})^5]^2} H\left(t - \frac{h}{C_T}\right)$$

$$S_L^2 = \left( \frac{t^2}{h^2} - \frac{1}{C_L^2} \right)$$

$$S_S^2 = \left( \frac{t^2}{h^2} - \frac{1}{C_T^2} \right)$$

(2.21)

where  $\mu$  is the shear modulus,  $C_L$  and  $C_T$  are the longitudinal and shear wave speeds, and  $f(t)$  is the normalized temporal dependence of the forcing function.

The final epicentral displacement is taken as the superposition of the displacements calculated from the thermoelastic and ablative acoustic response as follows:

$$u_{\text{total}} = u_{\text{thermoelastic}} + u_{\text{ablative}} \quad (2.22)$$

The model used for calculation of the thermoelastic response assumes that the process is linear. Although this approximation neglects the variation in thermal and optical properties with temperature, it will be kept for the sake of tractability in the present analysis. In the ablative regime, the absorbed energy is divided into the energy used for material heating and the energy spent on material vaporization. This is expressed as follows:

$$Q_{\text{absorbed}} = Q_{\text{vaporation}} + Q_{\text{heating}} \quad (2.23)$$

The amplitude of the thermoelastic signal is assumed to scale linearly with the laser energy used for material heating,  $Q_{\text{heating}}$ , while the remainder of the energy is expended in the vaporization process.

## 2.3 Laser Vaporization Solution

### 2.3.1 Finite Difference Equations

The one dimensional laser vaporization problem is solved numerically using an implicit finite difference program. Finite difference techniques involve splitting time and space into finite temporal and spatial steps, and approximating the differential equation with a difference equation at each of these points.<sup>26,27</sup> Truncation error is inherent in finite difference techniques and stems from the replacement of the differential equation with a difference equation. The difference equations are derived from a Taylor series expansion of the derivatives about spatial and temporal points of observation. Simple finite difference schemes (i.e. the simple implicit and simple explicit techniques) have a truncation error corresponding to  $O(\Delta t) + O(\Delta x)^2$  where  $\Delta t$  is the time step and  $\Delta x$  is the space step chosen. Smaller truncation error leads to faster convergence of the approximate solution to the exact solution.

Explicit techniques, characterized by the fact that at each time level there is a single unknown that can be solved for, are extremely simple to implement but also suffer from stability criterion which limits the size of the steps that can be chosen. Implicit techniques are characterized by the fact that at every time step a system of  $i$  equations must be solved simultaneously, where  $i$  refers to the number of space steps chosen. In the thermal case, these equations are generally obtained from  $i-2$  internal nodes and supplemented by two boundary conditions. Implicit techniques, though slightly more difficult to implement, do not suffer from stability criterion limitations and thus the space and time steps may be freely chosen.

Finite difference techniques are commonly used for the solution of heat conduction problems.<sup>25</sup> They are also one of the most common techniques for the

numerical evaluation of laser heating problems, with numerous examples appearing in the literature. The finite difference method chosen was presented by Richtmeyer<sup>26</sup> and utilized for laser heating problems by Singh and Narayan<sup>28</sup> (1989). It is a higher order implicit method with a truncation error of  $O(\Delta t)^2 + O(\Delta x)^4$  leading to much faster convergence than the simple explicit or simple implicit method. The solution approach closely follows that of Singh and Narayan.<sup>27</sup>

The thermal conductivity equation and melt front boundary condition are made non-dimensional by introducing the following quantities

$$x_1 = \frac{x}{l} \quad s_1 = \frac{s}{l} \quad \theta = \frac{T - T_m}{T_m} \quad t_1 = \frac{T_m K_2 t}{L l^2} \quad (2.24)$$

where  $T_m$  is the melting temperature of the material,  $L$  is the latent heat of melting, and  $l$  and  $K_2$  are constants having units of length and thermal conductivity respectively. These constants can now be substituted into the thermal conductivity equation (2.1) yielding the non-dimensional form:

$$\frac{\partial \theta}{\partial t_1} = \sigma(T) \left( \frac{\partial^2 \theta}{\partial x_1^2} + \frac{1}{K(T)} \frac{\partial K(T)}{\partial x_1} \frac{\partial \theta}{\partial x_1} \right) + \frac{I_0 (1-R) e^{-\alpha x} L^2}{T_m^2 K_2 C_v(T)}$$

where:

$$\sigma(T) = \frac{K(T)L}{K_2 C_v(T) T_m} \quad (2.25)$$

where  $C_v$  is the volume heat capacity given by  $\rho(T)C_p(T)$ . The melt boundary condition may also be expressed in non-dimensional form as:

$$\frac{\partial s_1}{\partial t} = \frac{K_s \partial \theta_2}{K_2 \partial x_1} - \frac{K_1 \partial \theta_1}{K_2 \partial x_1} \quad (2.26)$$

In order to solve the differential equation the time and space variables are separated into small steps ( $\Delta t$  and  $\Delta x$ ) as follows:

$$\begin{aligned} x_1 &= i \Delta x \quad i = 0, 1, 2, \dots, N \\ t_1 &= n \Delta t \quad n = 0, 1, 2, \dots, M \end{aligned} \quad (2.27)$$

The position of the melt front interface is followed explicitly and is given by:

$$s_1 = q \Delta x + \epsilon \Delta x \quad -0.5 < \epsilon < 0.5 \quad (2.28)$$

where  $q$  is a whole number corresponding to a nodal point and  $\epsilon$  is the fractional distance to the nodal point as illustrated in Figure 2-4.

The position of the vaporization front is not tracked explicitly but is instead followed through energy balance considerations. In this approach the heat flux carried away by the vapor is regarded as a surface heat sink in the same manner as the laser pulse is considered a heat source. The velocity of the vaporization front is determined at every time step [Eq. (2.5)] providing a distance over which the vaporization front moves given by:

$$s_v = \frac{\partial s_v}{\partial t} \Delta t \quad (2.29)$$

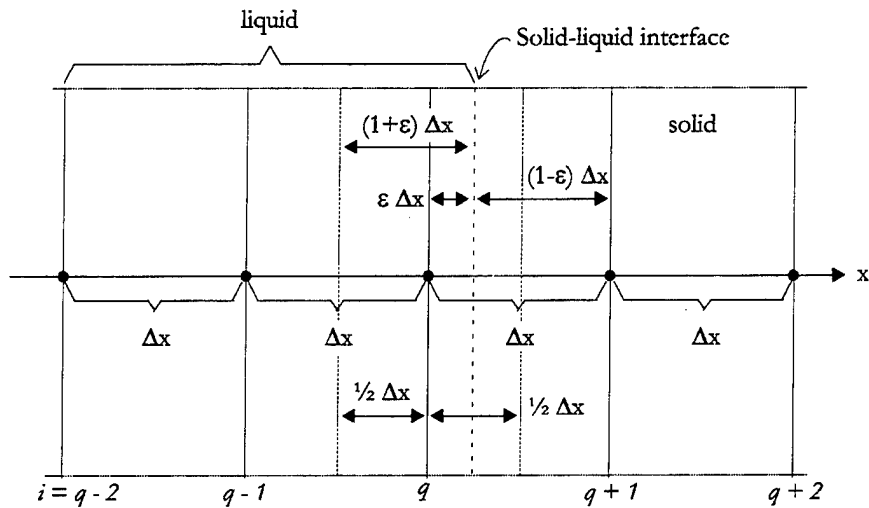


Figure 2-4 Description of nodes around melt front.

The major expenditure of energy during the vaporization process is through the latent heat of vaporization. A more complete description of energy expenditure includes additional terms given by the latent heat of melting, the enthalpy of the vapor, and the kinetic energy of the vapor. These may be summarized in an effective latent heat of vaporization given by:

$$\Delta H_{lv}^* = \Delta H_{lv} + \Delta H_{lm} + H_v + \frac{Mv_v^2}{2} \quad (2.30)$$

where  $H_v$  is the enthalpy of the vapor and the final term represents the kinetic energy of the vapor. Eq. (2.30) is dominated by the latent heat of vaporization

while the kinetic energy term is quite small and can be neglected. The vaporization energy loss mechanisms are considered in the model and although the vaporization front is not tracked explicitly, an effective vaporization front is monitored. This gives a reasonable estimation for laser induced vaporization depth. At every time step, the pressure exerted on the specimen is also tracked using Eqs. (2.6) and (2.10) allowing for the melt flow calculation. The energy lost to melt flow is much less than the energy lost to vaporization and is also neglected in the model.

The finite difference expressions have been outlined in the literature<sup>27</sup>, but as they form the core of the vaporization model solution they will be repeated here for completeness. A detailed account of various higher order implicit finite difference techniques, and the derivation of the particular technique used, is given in Richtermeyer.<sup>26</sup> The material is divided into  $i$  spatial nodes as indicated by Eq. (2.27). Of these nodes, expressions must be derived for  $i-4$  general nodes or nodes that are not adjacent to a boundary. Complementing these, expressions must be derived for each of the four boundaries considered. These include the front and back surface boundary conditions and the boundary conditions at each side of the melt front. For the general nodes, Eq. (2.25) is expressed in finite difference form by:

$$\begin{aligned} \frac{\theta_{i+1}^{n+1}}{\sigma_{i+1}} \left( \frac{1}{6} - R_{i+1} \right) + \frac{\theta_{i-1}^{n+1}}{\sigma_{i-1}} \left( \frac{1}{6} - R_{i-1} \right) + \frac{\theta_i^{n+1}}{\sigma_i} \left( \frac{5}{3} + 2R_i \right) = \\ \frac{\theta_{i+1}^n}{\sigma_{i+1}} \left( \frac{1}{6} + a_i R_{i+1} \right) + \frac{\theta_{i-1}^n}{\sigma_{i-1}} \left( \frac{1}{6} + b_i R_{i-1} \right) + \frac{\theta_i^n}{\sigma_i} \left( \frac{5}{3} - 2R_i \right) + \Delta t (I_i^{n+1} + I_i^n) \end{aligned} \quad (2.31)$$

where:

$$I = \frac{I_0(1-R)e^{-\alpha x} L^2}{T_m^2 K_2 C_v(T)} \quad R_i = \frac{\sigma_i \Delta t}{(\Delta x)^2} \quad a_i, b_i = \left\{ 2K_i \pm \frac{K_{i+1} - K_{i-1}}{2K_i} \right\}$$

The left side of Eq. (2.31) contains three unknowns which are the temperatures of three nodal points at the time step  $n+1$ . At each time step, Eq. (2.31) is written as a series of linear equations for all  $i$ . The boundary conditions at the front and back surfaces of the plate are applied simply by forcing the temperature at imaginary nodes adjacent to the interface to have the same temperature as those at the interface, eliminating the driving force for heat flow across the boundary. These conditions are given as:

$$\theta_{-1}^n = \theta_0^n \quad \theta_{N+1}^n = \theta_N^n \quad (2.32)$$

These equations state that at for time ( $n$ ) the temperature nodes adjacent to the plate boundaries are kept at the same temperature as the boundary nodes. If the position of the melt front is some distance  $\varepsilon$  from the nodal point  $q$ , where  $\varepsilon$  was defined above, then boundary conditions are also necessary for the nodal points  $q-1$  and  $q+1$ . If the melt front is taken to be at the melting point, then the temperature of the node corresponding to the interface is known and  $\theta_q = 0$ . The boundary conditions at nodes  $q-1$  and  $q+1$  are then given by:

(node  $q-1$ )

$$\begin{aligned} \theta_{q-2}^{n+1} \left( \frac{1}{3(2 + \varepsilon^n)} - \frac{2(\Delta t)\sigma_{q-2}}{(\Delta x)^2(2 + \varepsilon^{n+1})} \right) + \theta_{q-1}^{n+1} \left( 2 - \frac{1}{3(1 + \varepsilon^n)} + \frac{2(\Delta t)\sigma_{q-1}}{(\Delta x)^2(1 + \varepsilon^{n+1})} \right) = \\ \theta_{q-2}^n \left( \frac{1}{3(2 + \varepsilon^n)} + \frac{2(\Delta t)\sigma_{q-2}}{(\Delta x)^2(2 + \varepsilon^n)} \right) + \theta_{q-1}^n \left( 2 - \frac{1}{3(1 + \varepsilon^n)} - \frac{2(\Delta t)\sigma_{q-1}}{(\Delta x)^2(1 + \varepsilon^n)} \right) + \text{source} \end{aligned} \quad (2.33)$$

(node q+1)

$$\begin{aligned} & \theta_{q+2}^{n+1} \left( \frac{1}{3(2-\varepsilon^n)} - \frac{2(\Delta t)\sigma_{q+2}}{(\Delta x)^2(2-\varepsilon^{n+1})} \right) + \theta_{q+1}^{n+1} \left( 2 - \frac{1}{3(1-\varepsilon^n)} + \frac{2(\Delta t)\sigma_{q+1}}{(\Delta x)^2(1-\varepsilon^{n+1})} \right) = \\ & \theta_{q+2}^n \left( \frac{1}{3(2-\varepsilon^n)} + \frac{2(\Delta t)\sigma_{q+2}}{(\Delta x)^2(2-\varepsilon^n)} \right) + \theta_{q+1}^n \left( 2 - \frac{1}{3(1-\varepsilon^n)} - \frac{2(\Delta t)\sigma_{q+1}}{(\Delta x)^2(1-\varepsilon^n)} \right) + \text{source} \end{aligned} \quad (2.34)$$

The final expression necessary to solve the finite difference routine is an equation describing the movement of the melt at subsequent time steps. This expression is found by applying the finite difference scheme to the melt front boundary condition [Eq. (2.26)] and is given as follows:

$$\begin{aligned} s_1^{n+1} - s_1^n &= \frac{(\Delta t)K_s}{2(\Delta x)K_2} \left( \theta_{q+1}^{n+1} \frac{2-\varepsilon^{n+1}}{1-\varepsilon^{n+1}} - \theta_{q+2}^{n+1} \frac{1-\varepsilon^{n+1}}{2-\varepsilon^{n+1}} + \theta_{q+1}^n \frac{2-\varepsilon^n}{1-\varepsilon^n} - \theta_{q+2}^n \frac{1-\varepsilon^n}{2-\varepsilon^n} \right) + \\ & \frac{(\Delta t)K_1}{2(\Delta x)K_2} \left( \theta_{q-1}^{n+1} \frac{2+\varepsilon^{n+1}}{1+\varepsilon^{n+1}} - \theta_{q-2}^{n+1} \frac{1+\varepsilon^{n+1}}{2+\varepsilon^{n+1}} + \theta_{q-1}^n \frac{2+\varepsilon^n}{1+\varepsilon^n} - \theta_{q-2}^n \frac{1+\varepsilon^n}{2+\varepsilon^n} \right) \end{aligned} \quad (2.35)$$

Equations (2.29)-(2.35) are solved using a numerical routine written in C included in Appendix 1. These equations are also supplemented by the equations describing the vaporization and melt flow processes [Eqs. (2.5)-(2.12)]. The solution allows for the calculation of the temperature at any point in the plate (within the 1-D approximation), the position of the melt front, an approximation for the flow of melt from the illuminated region, the position of the vaporization front, the pressure exerted on the specimen due to vaporization, and the division of energy between the heating and vaporization processes. In the vaporization

model, an effort has been made to address all of the physical processes that are expected to play a dominant role.

### 2.3.2 Temperature Dependence of the Thermal and Optical Properties

Accurate solution of the thermal problem presented requires that the temperature dependence of the thermal and optical properties of the material under investigation be considered. In the present study, the vaporization of pure (99%) aluminum is evaluated. The physical properties of aluminum showing the strongest temperature dependencies are the thermal conductivity and heat capacity. The temperature dependence of these properties can be included in the finite difference program so long as the property can be represented as a continuously differentiable function of temperature. The nature of the solution technique presented does allow for discontinuities in the functions at the melting temperature.

Values for the thermal conductivity and heat capacity as function of temperature up to the critical temperature are available in the literature<sup>29</sup> and have been plotted in Figure 2-5. The thermal conductivity shows a decrease from room temperature to the melting point, at which point there is a significant drop. The heat capacity shows a strong rise up until the melting point, followed by an abrupt drop to a constant value recommended throughout the melt region. The data have been approximated as follows:

#### Thermal Conductivity

*Below melting point: average value = 2.287 W/cmK*

*Above melting point =  $.549 + (5.249e-4)T - (1.338e-7)T^2 + (7.941e-12)T^3$  W/cmK*

#### Heat Capacity

*Below melting point =  $3.728 + (.0105)T - (1.482e-5)T^2 + (9.142e-9)T^3$  cal/molK*

*Above melting point: constant = 7.59 cal/molK*

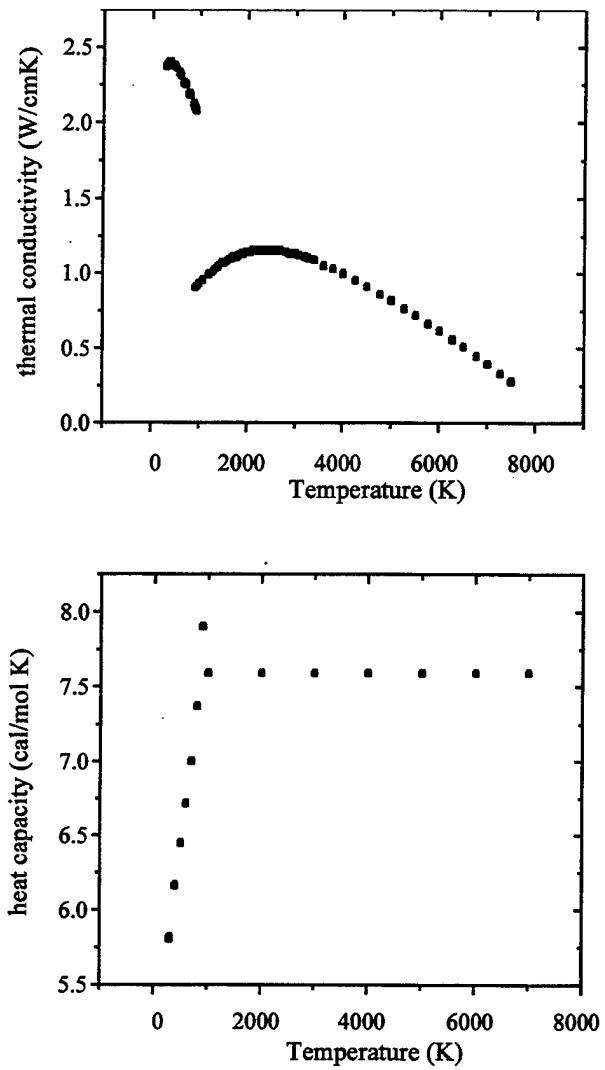


Figure 2-5. Temperature dependence of thermal conductivity (top) and heat capacity (bottom) in aluminum.

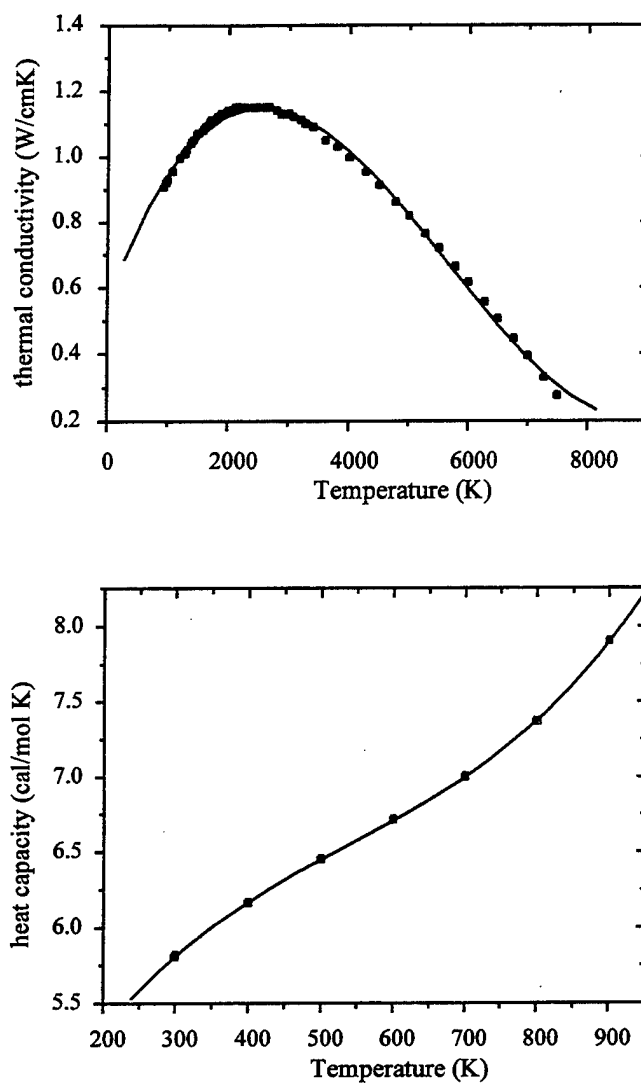


Figure 2-6 Polynomial fitting functions used in the vaporization model for thermal conductivity (top) and heat capacity (bottom).

The polynomial fits given above are plotted in Figure 2-6 against the recommended values.

The density change with temperature is quite small, going from about 2.6 g/cm<sup>3</sup> in the solid to about 2.3 g/cm<sup>3</sup> in the liquid state and decreasing slightly with temperature from that point on.<sup>28</sup> This change has been neglected in the

calculations. Data on the optical properties of aluminum as a function of temperature have proven more difficult to find. The resistivity of aluminum as a function of temperature has been included in Figure 2-7 with the data below the melting point taken on a 99.9% Al, .05% Si 5 mil wire and the data above the melting point taken in 99.99% pure Al.<sup>28</sup> The resistivity rises markedly in aluminum with temperature with a strong positive jump occurring at the melting point. Under the assumptions of the Drude model it can be shown that the absorptivity is proportional to the square-root of the resistivity. Over the limited range of temperatures given in Figure 2-7, a fourfold increase in absorptivity from the room temperature value is estimated using this model.

Unfortunately, the absorptivity is also a strong function of surface condition and reported values differ quite substantially. The American Institute of Physics Handbook<sup>30</sup> reports values of room temperature reflectivity at the  $1\mu\text{m}$

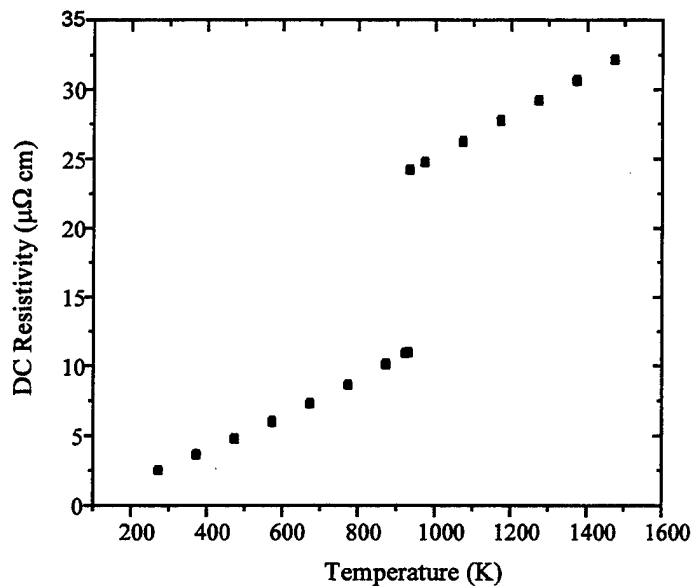


Figure 2-7

Temperature dependence of the resistivity of aluminum.

wavelength as .912 (calculated), .940 (evaporated mirror coating), and .733 (polished). Another source reports specular reflectance from 70% to above 90% for polished aluminum at room temperature.<sup>28</sup> In the work of Tsui et.al.<sup>24</sup> (1994), the reflectivity of sputter coated aluminum films at .248 $\mu\text{m}$  was measured to be 83% at room temperature and calculations were performed assuming reflectivity of the melt was between 40% and 80%. Theoretically, the room temperature reflectivity at .248 $\mu\text{m}$  should be similar to that at 1 $\mu\text{m}$ .<sup>29</sup> Difficulties encountered determining the temperature dependence of the reflectivity have led to the use of a constant reflectivity in the vaporization model. The value used should be considered an average reflectivity over the heating cycle that the surface goes through. Currently, the reflectivity is estimated and used as a fitting parameter in the model, with the values chosen held within the reasonable ranges indicated above. Finally, the absorption depth is not expected to change significantly with temperature and the temperature dependence is thus ignored.

### 2.3.3 Test of the Model

In order to verify the working of the finite difference routine, a test was performed to compare the output of the model with a simple laser heating problem which was solved analytically. The case chosen was the one dimensional heating of a half space by a constant amplitude laser pulse turned on at  $t = 0$ . The solution to this problem may be found simply with the surface temperature given as follows:

$$T_{\text{surface}} = \frac{2I\sqrt{kt}}{K\sqrt{\pi}} - \frac{I}{K\alpha} + \frac{I}{K\alpha} \exp(\alpha^2 kt)(1 - \text{erf}(\alpha\sqrt{kt}))$$

(2.36)

where  $I$  is the incident laser pulse power density,  $\kappa$  is the thermal diffusivity given by  $\kappa=K/\rho C$  where  $C$  is the heat capacity, and  $\alpha$  is the absorption depth. The following room temperature values for aluminum were used: thermal conductivity  $K=2.37$  W/cmK, heat capacity  $C = .90$  J/gK, absorption coefficient  $\alpha = 10$ nm, reflectivity  $R = 80\%$ , and incident laser pulse irradiance  $I = 20$ MW/cm<sup>2</sup>. The resulting plot of the analytical solution [Eq. (2.36)] and the finite difference solution is plotted in Figure 2-8. The finite difference solution shows excellent convergence to the exact solution indicating that the core of the finite difference is working appropriately. It should be noted that two other simpler finite difference schemes were implemented prior to choosing the current technique; the simple explicit method and an implicit method known as the Crank-Nicholson method. These methods failed to achieve the level of convergence displayed by the current

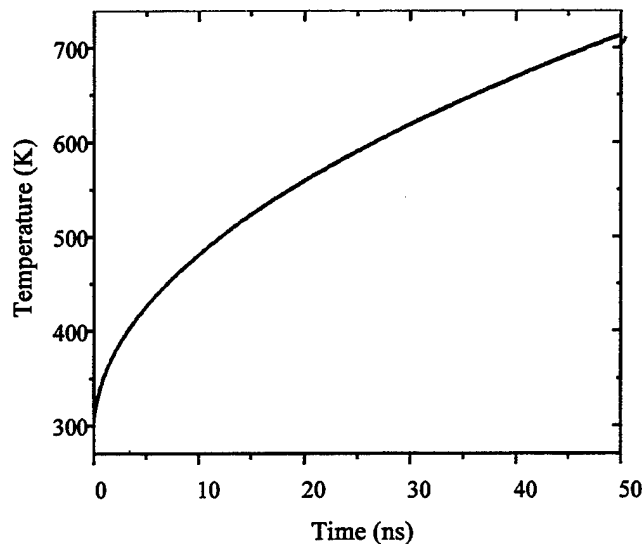


Figure 2-8 Laser heating comparison of exact solution with solution obtained through finite difference technique.

technique. This test was run a number of times with various thermal and optical properties input into the routine.

Further testing of the model is difficult, as the numerical technique was chosen because of the lack of availability of analytical solutions to the problem considered. This test is taken as evidence that the finite difference scheme was programmed properly and indeed converges to the exact solution in simple cases.

#### 2.3.4 Predictions of the Laser Vaporization Model

The thermal and optical constants used in the vaporization model are summarized in Table 2-2. The temporal profile of the laser pulse is assumed to be Gaussian with the FWHM of the pulse chosen to match that of the laser pulse used experimentally. In the program examples to be given in this section, the FWHM of

|                                    |   |
|------------------------------------|---|
| Absorption depth                   | 10 nm   |
| Melting Temperature                | 933K  |
| Vaporization Temperature           | 1785 @ pressure of $1.013e5 \text{ g/sec}^2\text{m}$      |
| density                            | $2.69 \text{ g/cm}^3$                                     |
| atomic weight                      | $26.98 \text{ g/mol}$                                     |
| latent heat of melting             | $10790 \text{ J/mol}$                                     |
| heat capacity ( $T < T_m$ )        | $3.72 + 0.01T - 1.48e-5T^2 + 9.14e-9T^3 \text{ cal/molK}$ |
| heat capacity ( $T > T_m$ )        | $7.59 \text{ cal/molK}$                                   |
| Thermal Conductivity ( $T < T_m$ ) | $2.28 \text{ W/cmK}$                                      |
| Thermal Conductivity ( $T > T_m$ ) | $.549 + 5.24e-4T - 1.33e-7T^2 + 7.54e-12T^3$              |
| Reflectivity                       | .6 - .9 (variable)  |
| latent heat of vaporization        | $293420.0 \text{ J/mol}$                                  |

Table 2-2 Summary of thermal and optical properties of aluminum used in vaporization model.

the laser pulse is taken as 16ns. It is noted here that the temporal shape of the pulse used in the thermoelastic acoustic wave generation program is that of a modified Gaussian presented by Schleichert et.al.<sup>31</sup> (1988) The difference between these two forms is slight and is expected to have negligible effects on the theoretical results. A comparison of these two pulses with the experimentally measured laser pulse is given in Figure 2-9. Reasonable agreement is seen between the theoretical and experimentally measured laser pulse shapes.

Figure 2-10(top) shows the calculated surface temperature of the aluminum specimen at incident intensities of 100 and 150 MW/cm<sup>2</sup>. In this case, the reflectivity was taken to be 80%. Both of these pulses heat the surface beyond the melting point. When the surface temperature reaches the melting point, the melt front begins to propagate into the material. At some point in the material, towards

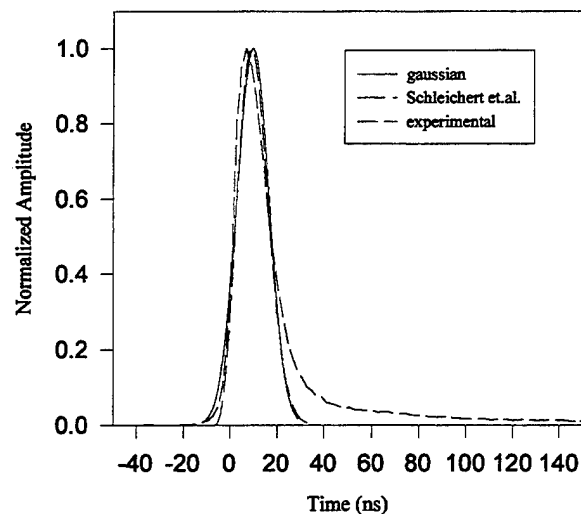


Figure 2-9 Comparison of Gaussian and modified Gaussian laser pulse models with experimentally measured laser pulse.

the end of the laser pulse, the melt front velocity slows to zero and the direction of propagation reverses. As the melt front recedes back towards the surface, the temperature of the melt approaches the melting temperature. Thus the entire liquid layer approaches the equilibrium melting temperature and the driving force for thermal diffusion away from the surface ceases. This is the origin of the flat region in the heating curves, at which the temperature remains at the melting point. When the melt front makes it back to the surface and solidification is complete, surface cooling proceeds. The position of the melt front as a function of time is given in Figure 2-10(bottom). As expected, the higher amplitude pulse begins to melt the surface sooner with the melt front propagating significantly further into the material.

Figure 2-10 shows that the surface temperature remains below the vaporization temperature for the  $100 \text{ MW/cm}^2$  pulse while slightly exceeding the vaporization temperature for the  $150 \text{ MW/cm}^2$  pulse. Although the equilibrium vaporization temperature is exceeded at this irradiance, much higher temperatures must be reached for a significant amount of vaporization to occur. Material removal through melt expulsion and surface vaporization are compared in Figure 2-11 at an incident laser intensities of 400 and  $450 \text{ MW/cm}^2$ . The material removal is quite rapid and ceases immediately after the laser pulse ends. The major contribution to material removal is predicted to be surface vaporization. At  $400 \text{ MW/cm}^2$  about 70% of total material removed is from surface vaporization while at  $450 \text{ MW/cm}^2$  this figure increases to about 80%.

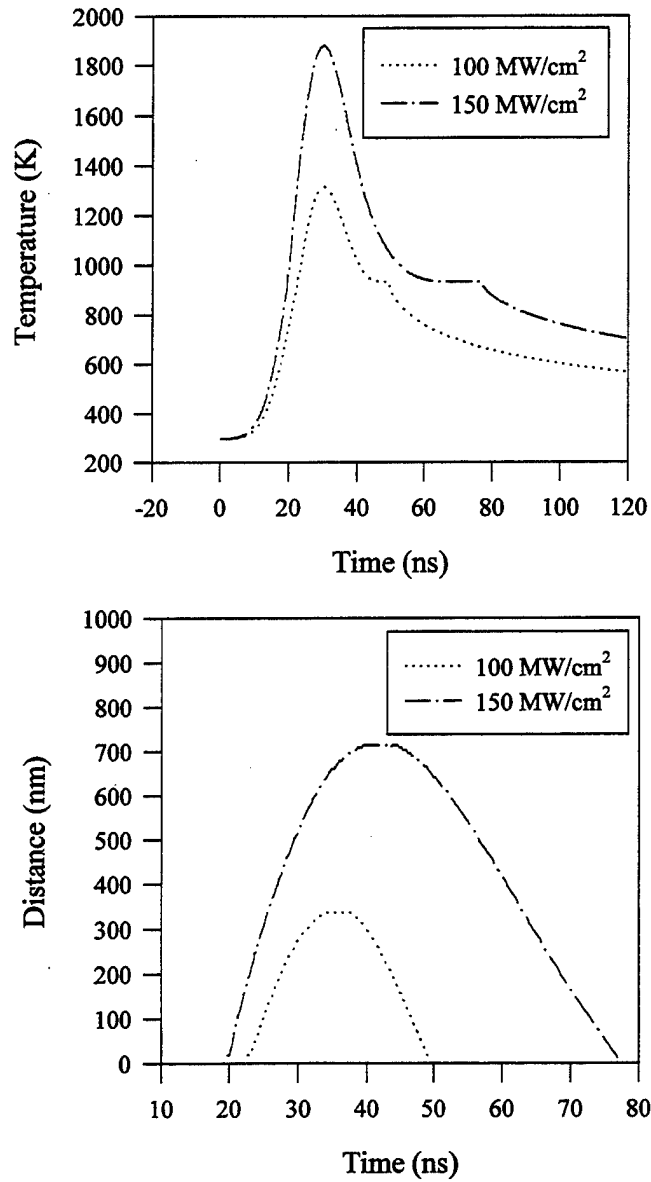


Figure 2-10 Calculated surface temperature (top) and melt front position (bottom) as a function of time at 100 and 150 MW/cm<sup>2</sup>.

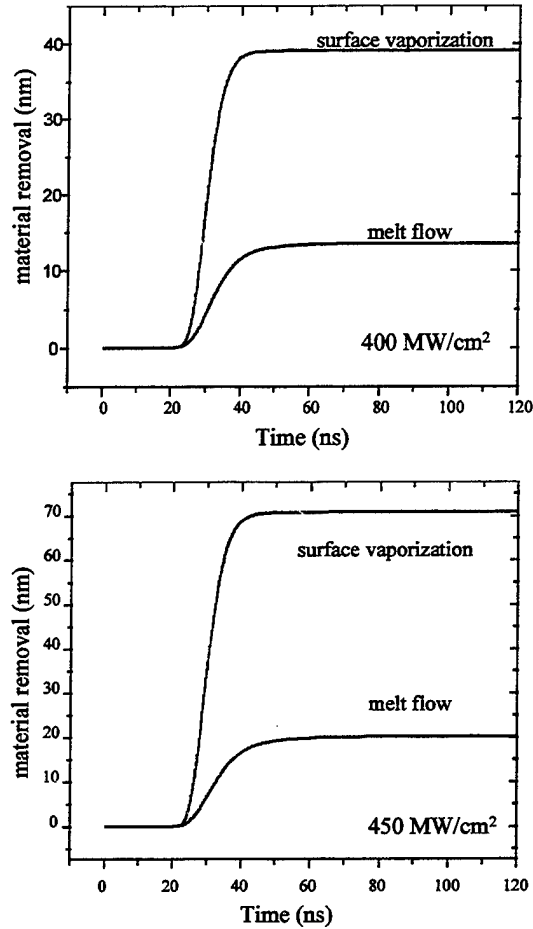


Figure 2-11 Material removal through surface vaporization and melt flow at 400 (top) and 450 MW/cm<sup>2</sup> as a function of time.

The total predicted ablation depth, and contributions of both melt flow and surface vaporization, is summarized in Figure 2-12. The material removal or ablation depth indicated in Figure 2-12 represents the maximum ablation depth expected. The would occur at the center of the incident laser spot where the

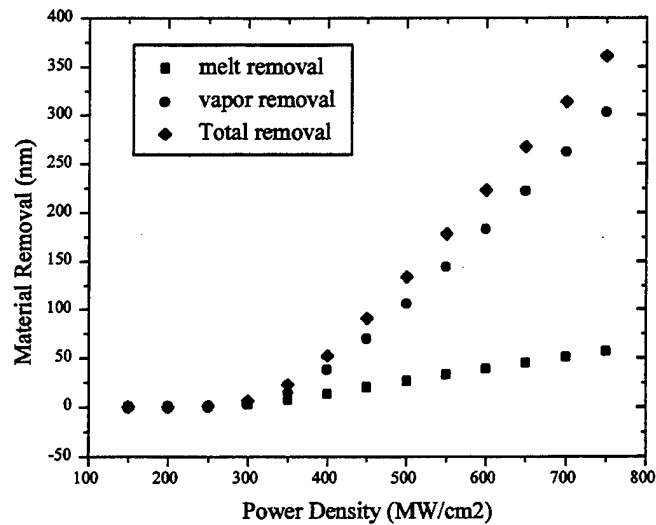


Figure 2-12 Total material removal, and contribution of melt flow and surface vaporization processes as a function of incident laser irradiance

irradiance is the highest. On aluminum specimens, and in the power density range considered here, the amount of material removal is not expected to exceed 400nm. The general trend indicated by the model is that contribution of the melt flow mechanism to the total material removed decreases with increasing laser pulse power density. This is in qualitative agreement with the work of Chan and Mazumder<sup>17</sup> (1987) showing a similar trend. Direct comparison with these results are difficult as they were calculated using a steady state model for long pulse laser heating in the kW power regime.

As discussed earlier, laser vaporization exerts a surface pressure on the material. Through Eqs. (2.6) and (2.10), this pressure can be related to surface temperature. Assuming radial melt flow induced by the vaporization, reasonable results should be possible without considering any additional forces exerted by

the melt. The pressure exerted on the specimen at 300, 400, and 450 MW/cm<sup>2</sup> is given

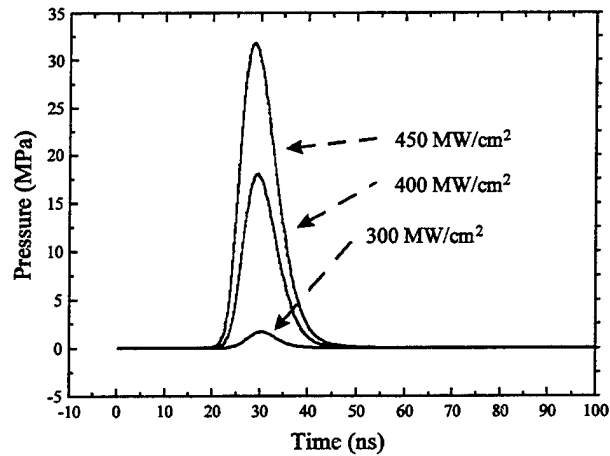


Figure 2-13 Pressure pulses exerted on the surface at various incident laser pulse intensities.

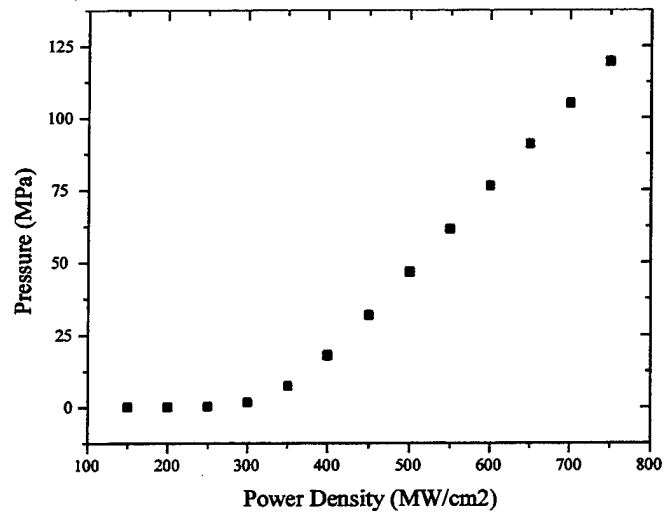


Figure 2-14 Peak pressure exerted on the surface as a function of incident laser irradiance.

in Figure 2-13. The first observation of note is that the pressure pulse amplitude is a very strong function of surface temperature, increasing sharply with incident laser irradiance. The second observation of interest is that the temporal extent of the pressure pulse is a function of incident laser irradiance. For an incident laser pulse with a 16ns FWHM, the FWHM of the pressure pulse increases from about 8ns at 200MW/cm<sup>2</sup> to about 13ns at 800MW/cm<sup>2</sup>. The principle mechanism accounting for this is simply that the surface is held well above the vaporization point for a longer amount time for high irradiance laser pulses. The peak pressure exerted on the specimen surface is given as a function of irradiance in Figure 2-14. The peak pressure is expected to be on the order of tens of MPa reaching a maximum of about 150 MPa at an incident laser power density of 750 MW/cm<sup>2</sup>.

The final demonstration of the calculated results involves the division of energy between the heating and vaporization of the sample. Significant amount of energy can be utilized in the vaporization process, especially in the high irradiance laser vaporization regime. Two plots illustrating this point are given in Figures 2-15 and 2-16. Figure 2-15 shows the maximum surface temperature reached as a function of incident laser irradiance. At low irradiance illumination,

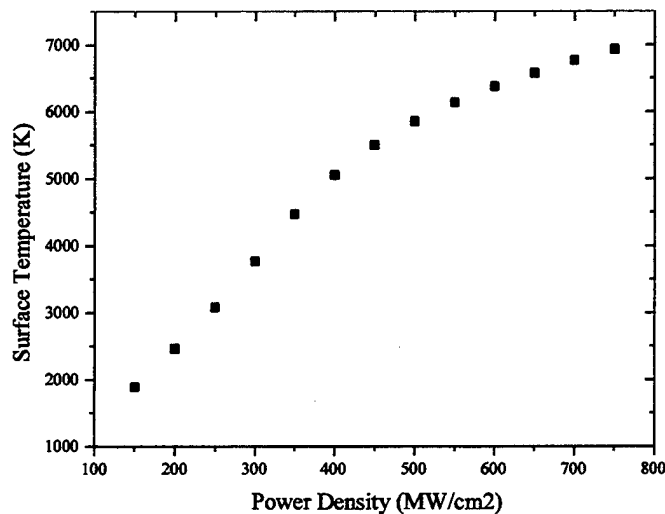


Figure 2-15 Maximum surface temperature reached as a function of incident laser pulse irradiance.

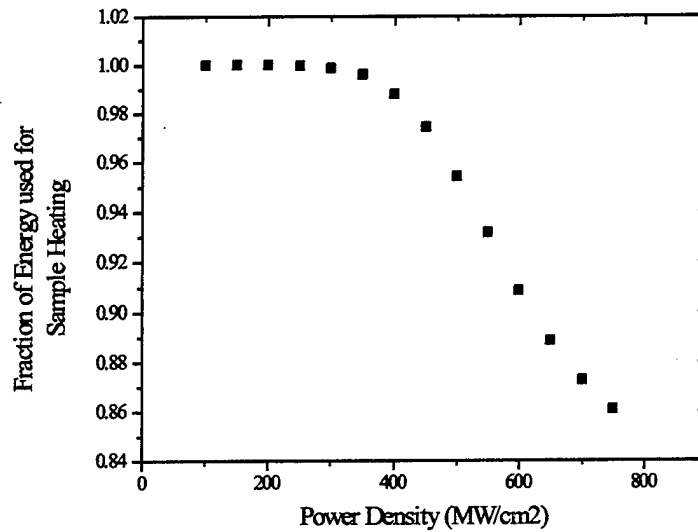


Figure 2-16 Fraction of energy used for sample heating as a function of incident laser pulse irradiance.

the curve is essentially linear, with all of the absorbed laser energy being used for sample heating. At higher irradiance illumination, there is a marked shift in the curve illustrating the effect of energy removal through vaporization. Figure 2-16 gives the fraction of energy used for sample heating. It can be seen that at the highest power density levels considered here, up to about 15% of the absorbed energy is utilized for vaporization.

### 2.3.5 Spot Size Considerations

The fact that the vaporization model is one dimensional presents some difficulty in calculating the force exerted in the surface during vaporization with an incident laser pulse which has a Gaussian irradiance distribution in space.

Under the assumptions of this model, the incident laser pulse is thermally large but acoustically small. This essentially means that the laser spot is large with respect to the thermal diffusion length but small compared to the thickness of the specimen. The acoustic approximation allows for the laser to be considered a point source in space. Under this approximation, the pressure exerted on the surface must be integrated over the spatial distribution of this pressure on the surface. This yields the total force exerted on the specimen. In general, unless the irradiance of the laser is constant over the surface of the specimen, the spatial distribution of the pressure pulse does not follow the spatial distribution of the incident laser pulse. This follows from the nonlinear nature of the vaporization process. If the incident laser irradiance is small and the spatial distribution is Gaussian, vaporization may take place at the center of the illuminated spot giving a spatially sharp pressure pulse. If it is larger, the pressure pulse will act over a broader area.

In order to determine accurately the force exerted on the specimen, the spatial distribution of the pressure pulse must be calculated as a function of peak laser irradiance. The peak pressure exerted on the specimen as a function of peak irradiance is first calculated. This is subsequently mapped to the Gaussian irradiance distribution over space. A point is chosen within the laser spot, the power density seen at that point calculated, and the pressure exerted on that point determined. This gives the spatial distribution of the pressure pulse over the surface. This distribution is then fit to a Gaussian and the spot size of the pressure pulse estimated. Once the Gaussian spot size is determined it needs only be integrated to arrive at the amplitude of the forcing function. The incident laser pulse profile is given in Figure 2-17(top) with the pressure pulse profile and corresponding Gaussian fit given in Figure 2-17(bottom) for an incident laser pulse irradiance of  $750\text{MW}/\text{cm}^2$ . The gaussian fit for the pressure is satisfactory and should give a reasonable estimate for the total force exerted on the specimen.

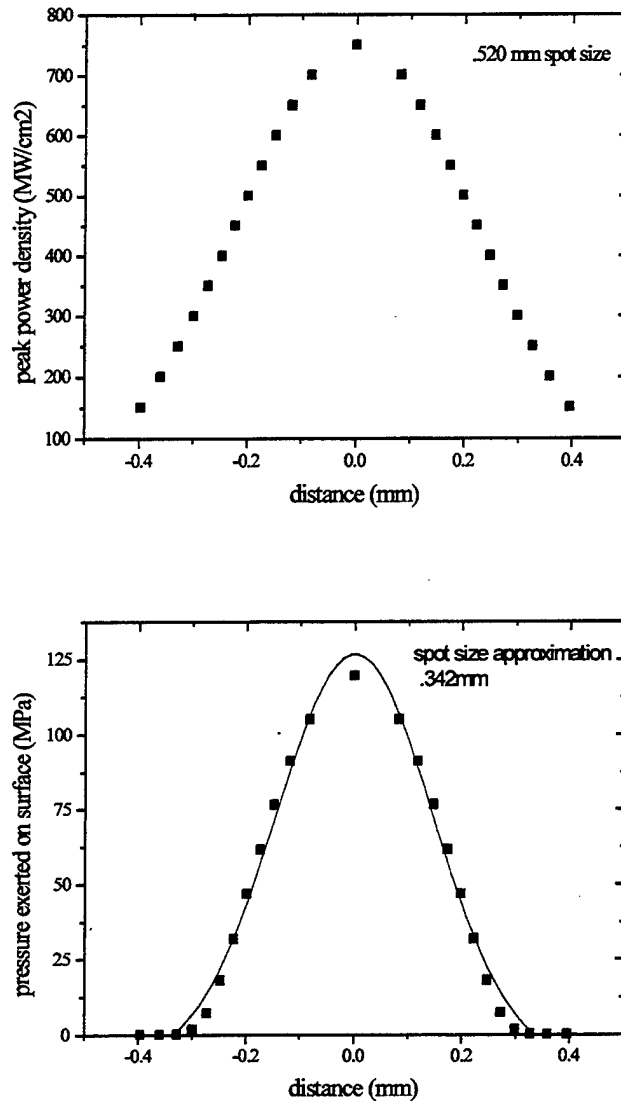


Figure 2-17 Spatial irradiance distribution of the incident laser pulse (top) and spatial distribution of pressure pulse on the surface shown with Gaussian fit.

The importance of taking spot size considerations into account is illustrated in Figure 2-18 showing the effective pressure pulse spot size estimations as a function of incident laser power density.

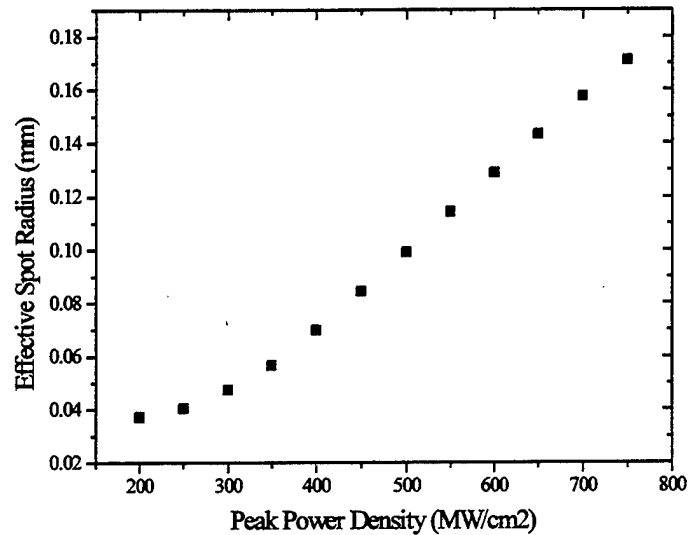


Figure 2-18 Calculated pressure pulse radius as a function of incident laser pulse irradiance

### 2.3.6 Solution Procedure: Coupling of Vaporization and Acoustic Wave Generation

The final solution for acoustic wave generation in the ablative regime requires a coupling of the vaporization program with the elastic wave solutions presented previously. The procedure used for this calculation is outlined below:

1. The vaporization program was run at a number of peak laser power density levels and the spatial distribution of the pressure pulse at each level is computed.
2. The normal force Green's function [Eq. (2.21)] is computed with the derivatives taken numerically.

3. The force exerted on the surface is calculated by integration of the temporal profile of the pressure pulse at a given power level over the spatial profile of the pressure pulse.
4. The surface displacement caused by vaporization is calculated through the convolution of the forcing function computed in step (3) and the Green's function from step (2).
5. The surface displacement caused by thermoelastic expansion is calculated through a program modeled after that given by Spicer<sup>2</sup> (1991).
6. The surface displacement caused by thermoelastic expansion is scaled according to the amount of absorbed laser energy used for sample heating.
7. The surface displacements from the thermoelastic expansion and vaporization processes are summed giving the final output.

## 2.4 Experimental Setup and Procedure

### 2.4.1 Experimental Setup

The basic experimental setup used is presented in Figure 2-19. A Continuum Surelite Nd:YAG laser operating at 1064nm and 532nm was used for the generation of ultrasound. The pulse length was in the 7-16ns range (depending on pump energy). The laser pulse was sent through a variable attenuator consisting of a half wave-plate and a polarizer. The polarization of the light was kept fixed with the energy throughput controlled by the rotation of the wave-plate. The pulse was then sampled using a partially reflecting (20% R) Nd:YAG laser mirror. The sampled light was directed to a Molectron energy meter.

The vacuum chamber was constructed using a T-section vacuum fitting. Optical ports were fit on two sides allowing for specimen interrogation by the

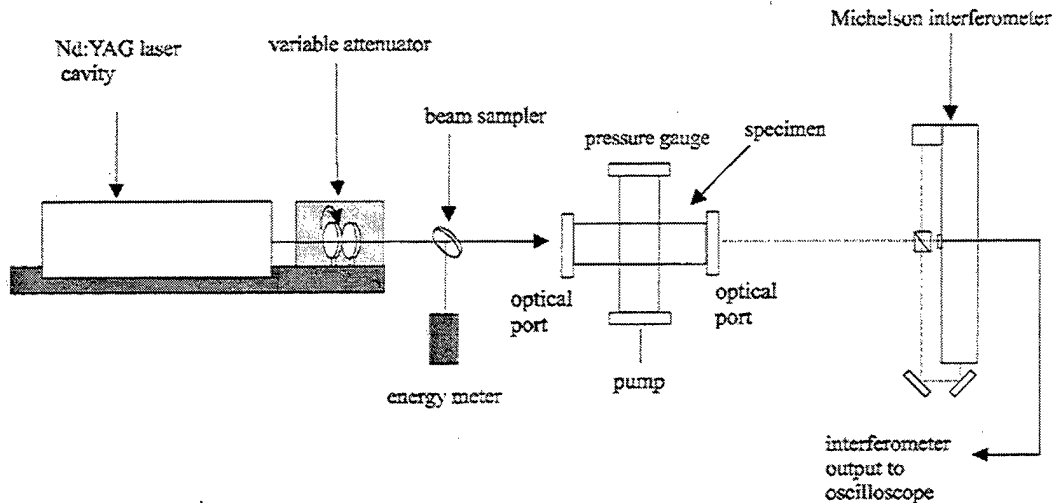


Figure 2-19 Experimental setup for vacuum ablation testing.

laser pulses. The other ports attached to the vacuum pump and a thermocouple pressure gauge. A DV-4D thermocouple was used, with the pressure readout performed with a Kurt J. Lesker 500TC digital meter. The specific vacuum pump used only allowed for experimentation in rough vacuum. The minimum pressure in the chamber did not get below about 0.2 torr. The vacuum chamber was mounted on a translation stage allowing for laser sampling across the surface of the specimen.

The surface displacement was detected using a stabilized Michelson interferometer. The operation of this type of interferometer is well known<sup>32</sup> and will not be described in detail here. The light source for this interferometer was a

CW Coherent laser operating at 532nm with a maximum power output of approximately 100mW. The photodetectors used in the interferometer were Thor Labs (model # FDS010) with a specified rise time of less than 1ns. The signal from the photodetectors was amplified using a Comlinear (model # E201) with a specified bandwidth of 95 MHz. The amplified signal was captured with Lecroy9354 Digital Oscilloscope with a sample rate of 500MHz. The bandwidth limit on the Michelson Interferometer was set by the Comlinear amplifier and is assumed to be approximately 95 MHz.

#### 2.4.2 Experimental Procedure

The aluminum samples were 6mm thick 99% Al purchased from Alpha Aesar Chemical. The samples were cut to 1" disks and hand polished down to 1 $\mu$ m diamond suspension. The room temperature specular reflectivity of the polished sample was measured with a He-Ne laser operating at 632nm. The laser was reflected at near-normal incidence into a Newport (model # 805) power meter and the power reading compared with the total output from the laser. The specular reflectivity was determined to be approximately 77%. Although the profile of the reflected beam appeared show a strong specular component, this measurement should be taken as only a rough approximation of the room temperature reflectivity, as the diffusely reflected light was not collected.

One of the most critical parameters necessary for the calculation of the surface displacement caused by laser vaporization is the spatial profile of the incident laser pulse. At the beginning of each experiment, the generation and detection lasers were first aligned to be co-linear at the specimen surface. The specimen was then removed from the chamber and a knife-edge inserted at the position of the back surface of the specimen as shown in Figure 2-20. The fraction of total energy making it past the knife edge was then recorded as it was

scanned, in 20  $\mu\text{m}$  steps, across the laser spot. Assuming a single transverse mode laser pulse, the spatial distribution of the incident laser pulse is Gaussian and the amount of energy making it past the knife-edge is given simply as:

$$E_{\text{measured}} = \frac{E_{\text{total}}}{w\sqrt{\frac{\pi}{2}}} \int_{k-\infty}^{\infty} \exp\left(\frac{-2(x^2 + y^2)}{w^2}\right) dx dy \quad (2.37)$$

where the knife edge is perpendicular to the y direction at a position given by k and moves through the spot in the positive y direction. The variable w in this expression describes the spot size with the FWHM being given by approximately  $w/0.849$ . Eq. (2.37) must be inverted in order to solve for the laser spot size. The solution for w follows the method of Khosrofian and Garetz<sup>33</sup>(1983).

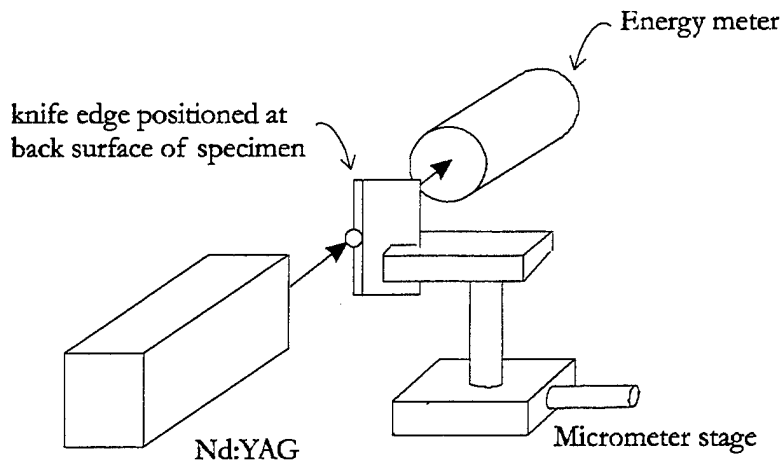


Figure 2-20 Setup for evaluating generation laser spot size.

After the spot size was determined, the fraction of incident energy sampled by the energy meter was measured and the energy meter calibrated. The vacuum chamber was then pumped down to approximately 0.2 torr. The interferometer was adjusted for maximum detection sensitivity. The generation pulse was fired three times at the specimen surface prior to data collection in order to "clean" the surface and remove any surface contamination. The signal was then averaged 5 to 10 times and transferred to a PC for analysis. The specimen was translated between shots such that a new region of the surface was sampled at each energy level. The temporal laser pulse profile (as illustrated in Figure 2-9) was recorded at the conclusion of each experiment.

## 2.5 Experimental Results/ Comparison with Theory

### 2.5.1 Longitudinal wave amplitude

The goal of this work was to relate the acoustic waves generated in the ablative regime (and corresponding surface displacement) to the physical processes occurring at the surface during the ablation process. All of the surface displacements measured experimentally were taken on epicenter through 6 mm thick aluminum (99%) specimens. All theoretical calculations were done using the thermal and optical parameters summarized in Table 2-2, and assuming a constant reflectivity of 67%. The reflectivity was essentially used as a fitting parameter with 67% considered to be a reasonable choice, although somewhat lower than expected, based on the considerations of Section 2.3.

The displacement corresponding to the longitudinal wave arrival gives a direct indication of the validity of the model in predicting the vaporization force

exerted on the surface. Although there is a small normal force exerted during thermoelastic generation, as modeled through Eq. (2.17), the normal force exerted by the vaporization process becomes dominant quite soon after vaporization is initiated. Thus when generating in the ablative regime, the amplitude of the displacement corresponding to the longitudinal wave arrival is almost completely dictated by the vaporization force as modeled through the vaporization routine.

Figure 2-21 shows the maximum longitudinal wave amplitude as a function of incident laser irradiance as measured with two different specimens (both having undergone the same polishing procedure). The data sets are both included to show the relative consistency of the experimental procedure. The spot size measured in each of these cases was  $520\mu\text{m}$ . The amplitudes measured in each experiment are relatively consistent, with the variations in the data sets most likely caused by slight differences in the surface condition of the samples. The

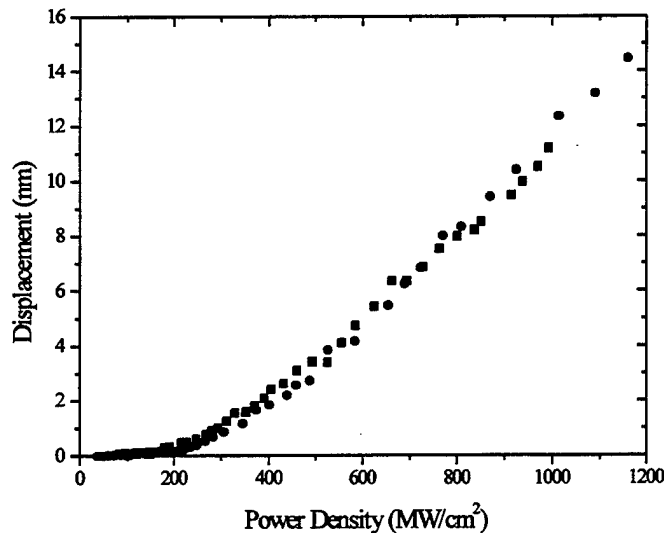


Figure 2-21 Peak longitudinal wave amplitude as a function of incident laser irradiance. Data taken in two sets of experiments presented.

curves show a low amplitude linear region up until about  $200 \text{ MW/cm}^2$  corresponding to laser generation in the thermoelastic regime. This is followed by a rapid rise in amplitude which, at high power densities, appears to show a linear relationship with irradiance and corresponds to laser generation in the ablative regime. In general, plots related to Figure 2-21 are quite common in the literature.<sup>45</sup> Unfortunately, the experimental procedure usually consists of increasing the power density through the translation of a focusing lens. This changes the spot size at each step and is not expected to give a curve similar to the one presented here. Also, the fact that this experiment was performed in vacuum makes it difficult to compare to other results presented in the literature.

The coupling of pulsed lasers with materials is often described through the use of thermal and impulse coupling coefficients. The thermal coupling coefficient is defined as the fraction of laser pulse energy incident on the specimen which is retained as heat. The impulse coupling coefficient is defined as the ratio of the impulse delivered to the specimen to the laser pulse energy. Impulse coupling coefficients have are commonly measured using a ballistic pendulum arrangement,<sup>16,34</sup> although reported methods also include measurement of the acoustic signal through contact piezoelectric transducers<sup>35</sup> and interferometry<sup>36</sup>. In order to interpret the results of Figure 2-21 more closely, it is instructive to consider a quantity, analogous to the impulse coupling coefficient, in the present case. The coupling coefficient chosen represents the generation efficiency and is in units of surface displacement /irradiance. This is plotted in Figure 2-22 verses incident laser irradiance. Although this is simply another way of presenting the data, it accentuates certain features. Through the relationship between the force exerted on the surface and the displacement caused by the longitudinal wave, this quantity represents the amount of force exerted on the

specimen (per unit of incident irradiance) at each incident irradiance level. This gives an effective efficiency of ultrasonic wave generation at each irradiance

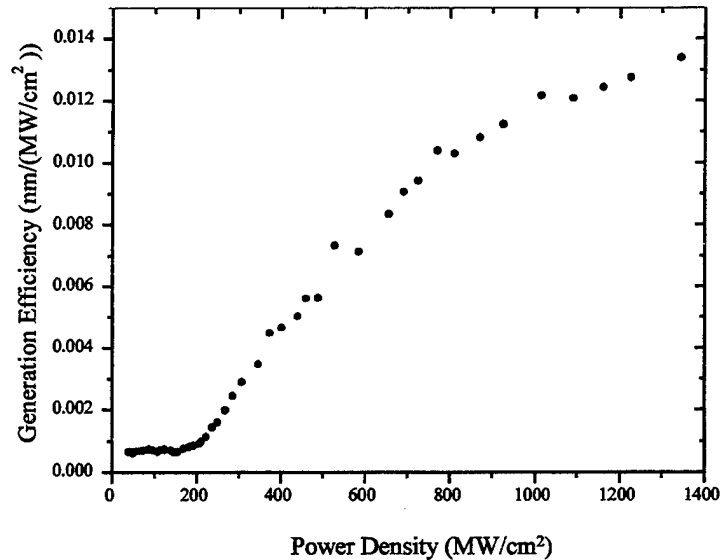


Figure 2-22 Longitudinal wave generation efficiency presented as a function of incident laser power density.

level. The curve is a constant for generation in the thermoelastic regime as shown in the low irradiance region. There is then a sharp rise in efficiency corresponding to the beginning of strong vaporization beginning at about 200 MW/cm<sup>2</sup> and lasting until about 400 MW/cm<sup>2</sup>. Beyond this point, the efficiency continues to increase, but at a somewhat slower rate. At the highest power density levels the efficiency appears to be approaching a constant value.

The outlined regimes may be explained through the comparison of experimental and theoretical longitudinal wave amplitudes as a function of irradiance as given in Figure 2-23. The theoretical and experimental curves are

seen to compare well in functional form up until about 300 MW/cm<sup>2</sup>. It is believed that this is the point at which processes in the vapor start to become important. The current model does not take into account processes in the vapor and is limited to the low power laser ablation regime. In both Figures 2-22 and 2-23, there is evidence of a linear region where thermoelastic generation occurs, a vaporization region in which plasma processes do not play an important role, and a high irradiance region where plasma processes play an important role.

In order to correctly interpret the break between experiment and theory seen in Figure 2-23, a more detailed discussion of processes occurring in the vapor will be given. During strong vaporization, the temperature in the vapor can rise to a point where excited atoms and free electrons exist in the vapor in relatively high concentrations. These species are capable of absorbing laser light directly. Ground state aluminum in the vapor is not able to absorb laser light

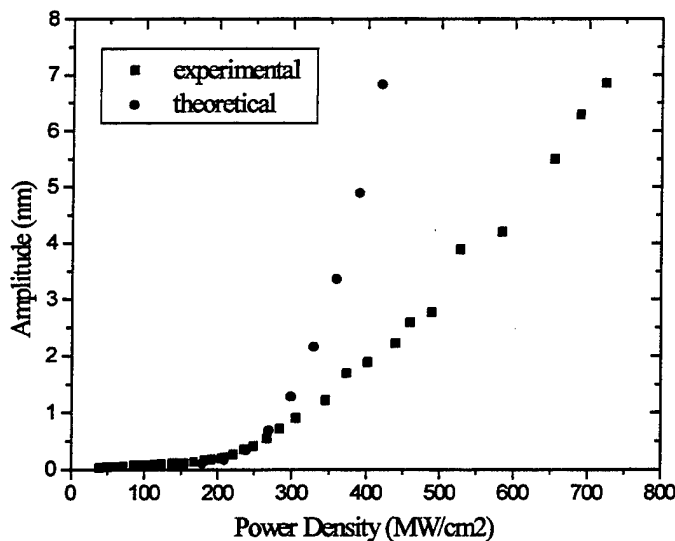


Figure 2-23 Experimental and theoretical amplitude of longitudinal wave displacement as a function of incident laser irradiance.

directly, as the photon energy considered here is below the ionization threshold. There are two dominant absorption mechanisms in aluminum: absorption of free electrons through the inverse bremsstrahlung process and photoionization of an excited state. The absorption coefficient from the inverse bremsstrahlung process is given by:<sup>37</sup>

$$\beta = (1.35)(10^{-35})\lambda^3 T_e^{-5} N_e \left( N_e + \frac{N_{AL}}{200} \right) \quad (2.38)$$

where  $\beta$  is the inverse absorption length,  $\lambda$  is the laser wavelength,  $T_e$  is the electron temperature,  $N_{AL}$  and  $N_e$  are the neutral atom and electron number densities respectively. The absorption cross section for photoionization of an excited state is given approximately by:<sup>37</sup>

$$\sigma = (7.9)(10^{-18}) \left( \frac{E}{h\nu} \right)^3 \left( \frac{I_H}{E} \right)^5 \quad (2.39)$$

where  $E$  is the energy of ionization of the excited state,  $I_H$  is the hydrogen ionization potential, and  $\nu$  is the frequency of laser radiation. The total power deposited in the vapor may then be given as:

$$P = (\beta + N^* \sigma) I_{ave} \quad (2.40)$$

where  $N^*$  is the density of excited atoms and  $I_{ave}$  is the average irradiance of laser radiation in the vapor.

Equations (2.38)-(2.40) require a detailed treatment of the processes occurring in the vapor in order to determine the concentration of various species present, as well as the distribution of these species in space. This is beyond the scope of the present work. One interesting observation, though, is the strong wavelength dependence of the absorption processes. In order to determine the effect of wavelength on the generation of acoustic waves in the ablative regime, the experiment was repeated at a wavelength of 532nm. The results of this experiment and comparison with theory are presented in Figure 2-24. The spot size was measured to be 520 $\mu$ m (the same as for the 1064 nm case). Unfortunately, the laser pump energy had to be increased and, combined with the nonlinear conversion of the doubling crystal used, resulted in a pulse width of 10ns. The data was fit to a reflectivity of 65%, showing an expected decrease from the value fit at 1064 nm.

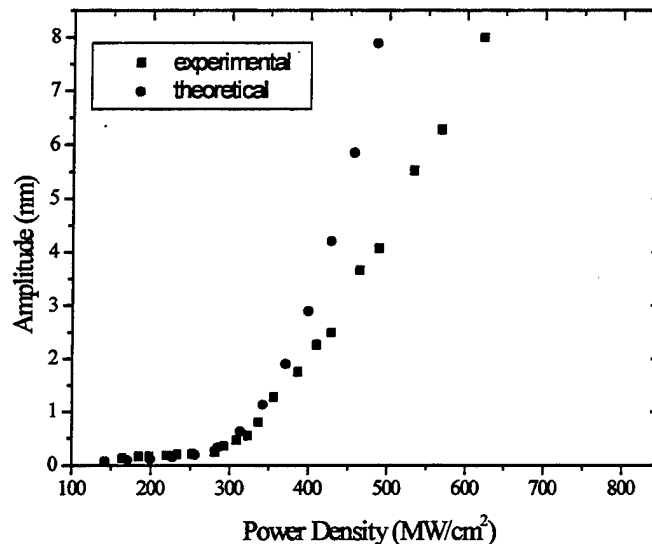


Figure 2-24 Theoretical and experimental longitudinal wave amplitude at .532 $\mu$ m as a function of incident laser power density.

The theoretical results (run with 10ns pulse width,  $R=.65$ ) agree better with the experimental results at this wavelength indicating a reduction of absorption in the vapor at 532nm. The functional form of the curves agrees until a higher longitudinal wave amplitude indicating that stronger vaporization must take place at this wavelength before processes in the vapor become important. This provides further evidence of the ability of the model to evaluate laser vaporization processes in the transparent vapor regime.

### 2.5.2 Calculated and Experimental Displacement

There are several difficulties involved in the estimation of the shape of acoustic waves generated in the ablative regime. The first arises in the calculation of the thermoelastic displacement. This calculation is done with a program modeled after that of Spicer<sup>2</sup> (1991) which does not accommodate the temperature dependence of the thermal properties or any changes in generation conditions resulting from surface melting. Other than the temperature dependence of the heat capacity and thermal conductivity described in detail in Section 2.3, there is also a large increase in the coefficient of thermal expansion between room temperature ( $\alpha_{AL}=23 \times 10^{-6}$ ) and the melting point ( $\alpha_{AL}=37 \times 10^{-6}$ ). The room temperature values for the physical properties were used in the model, with the exception of thermal conductivity for which the average solid value used in the vaporization model was incorporated. The resulting waveform was approximately a factor of two smaller in amplitude than observed experimentally. As the shape of this waveform was similar to the experimental observation, and the focus of this work was not to solve the difficult problem of thermoelastic wave generation with temperature dependent physical parameters, the waveform was simply scaled to fit the observed waveform in the thermoelastic regime. This is equivalent to

adjusting the thermal conductivity and thermal expansion coefficient, both of which have a linear relationship with amplitude. The agreement in shape between the experimental and theoretical signals indicate that the effects of surface melt are not critical to the calculation.

The experimental and theoretical results for generation in the thermoelastic regime are given in Figure 2-25. These show reasonable agreement

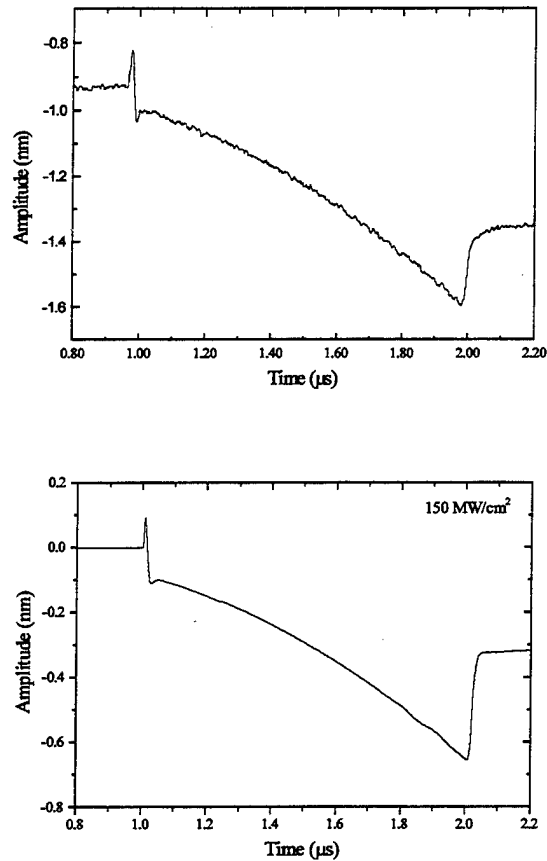


Figure 2-25 Experimentally measured (top) and calculated thermoelastic waveforms used in ablation model.

in shape with the exception of the amplitude of the step occurring at the shear wave arrival time of  $2\mu\text{s}$  which is somewhat smaller in the experimental case. The thermoelastic displacement given in Figure 2-25 was used in the calculation of all of the theoretical waveforms. The amplitude was scaled with the amount of energy incorporated for sample heating. As previously discussed, this equals the incident laser energy minus the energy used in the vaporization process.

The calculated surface displacements for the power density range from  $180\text{-}450\text{ MW/cm}^2$  are given in Figure 2-26. The displacement corresponding to the longitudinal wave arrival grows rapidly, becoming the dominant feature at high power levels. This arrival is also seen to broaden somewhat as the power is increased. This development can be compared to the experimental displacements measured ( $1.064\ \mu\text{m}$ ) in the power range  $200\text{-}800\text{ MW/cm}^2$  given in Figure 2-27. Although the development of strong vaporization in the transparent vapor model is much more rapid than is observed experimentally, the general development of the shape of the waveforms is quite similar. Notable differences include the amplitude of the negative going spike after the longitudinal wave arrival, which is larger in the experimental case. Also contrasting somewhat is the amplitude of the shear step which is diminished in the experimental case.

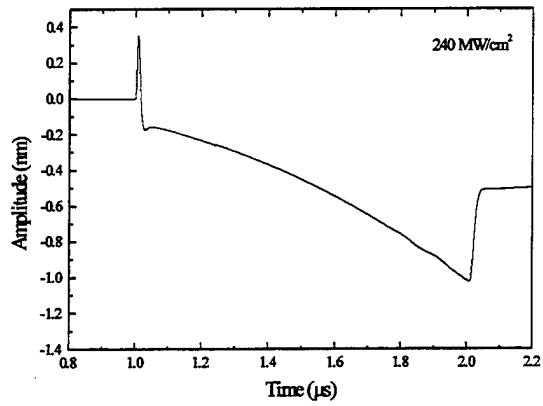
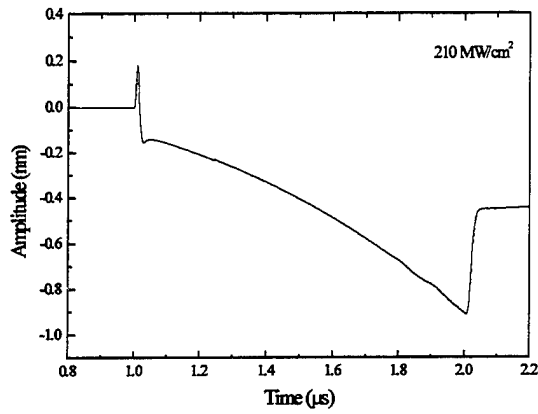
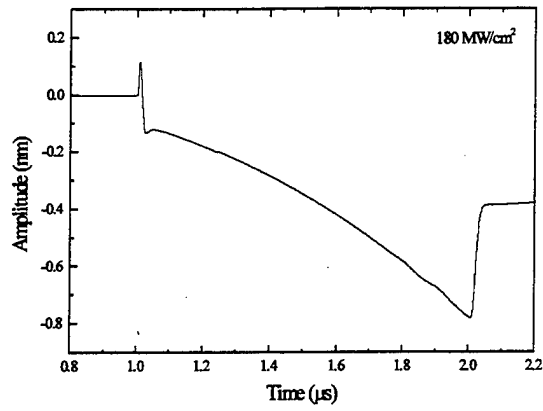


Figure 2-26 Theoretical ablative signals predicted in aluminum

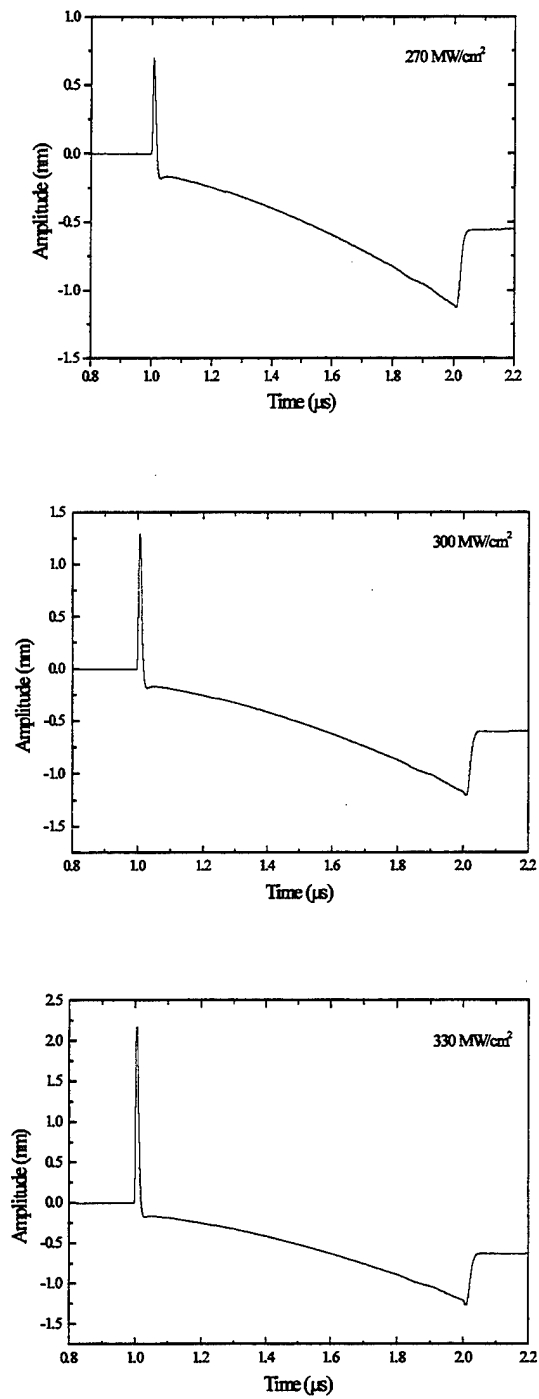


Figure 2-26 Theoretical ablative signals predicted in aluminum (continued)

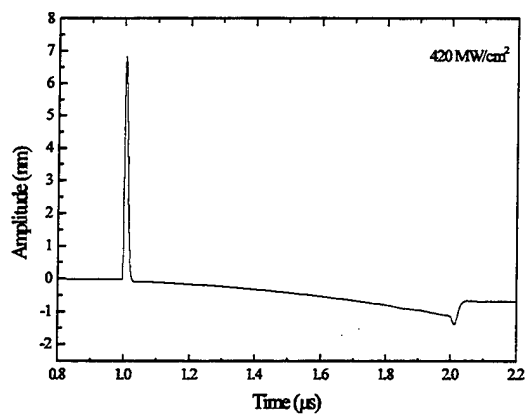
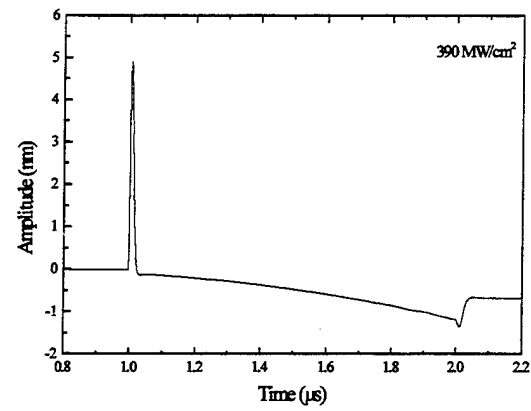
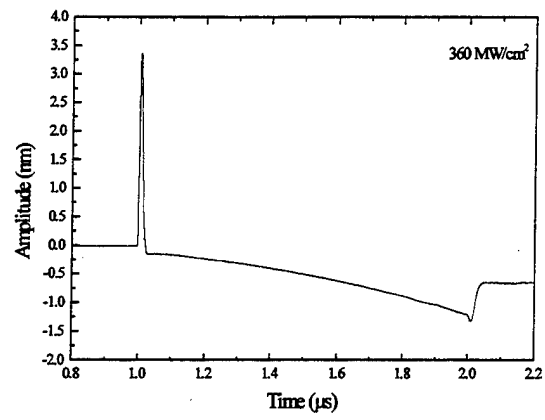


Figure 2-26 Theoretical ablative signals predicted in aluminum (continued)

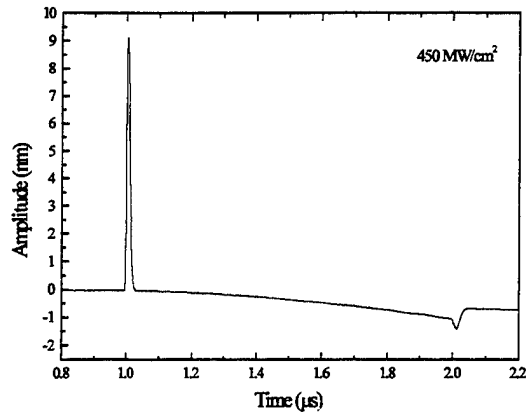


Figure 2-26 Theoretical ablative signal predicted in aluminum. (continued)

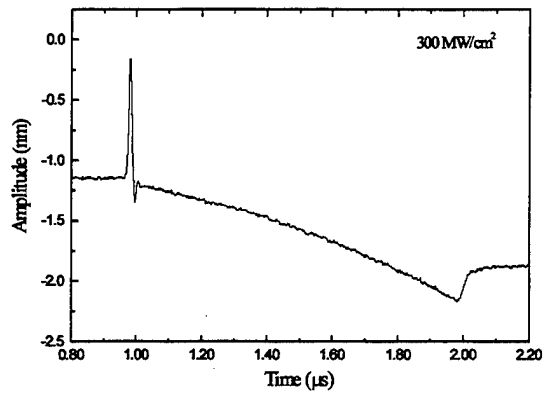
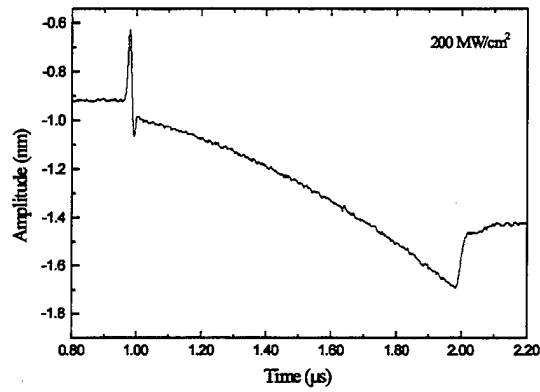


Figure 2-27 Experimental signals measured in aluminum.

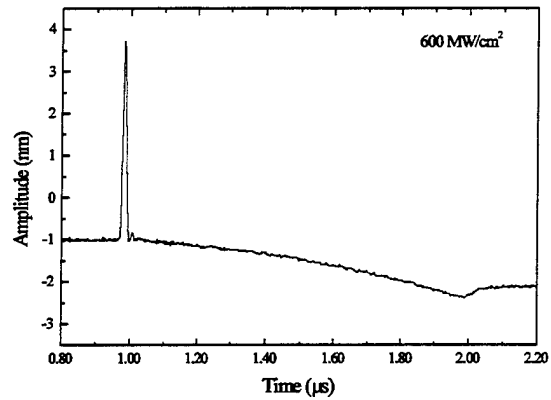
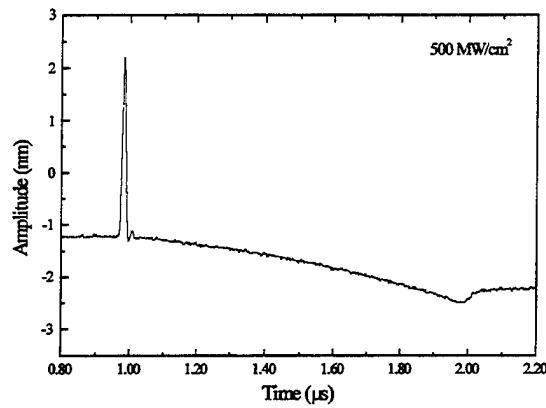
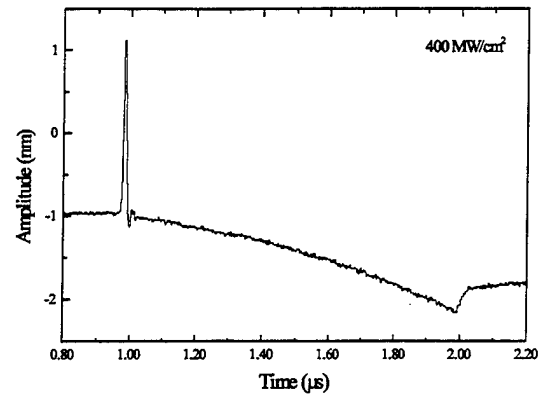


Figure 2-27 Experimental signals measured in aluminum. (continued)

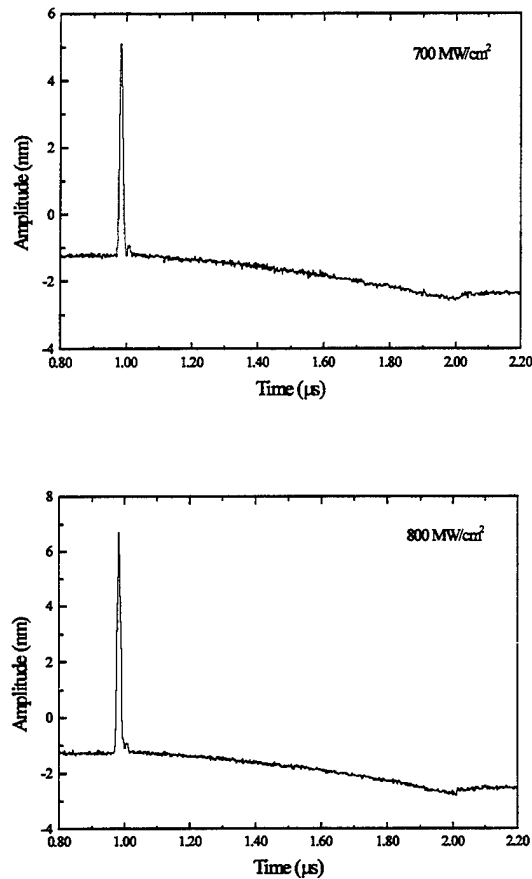


Figure 2-27 Experimental signals measured in aluminum. (continued)

A direct comparison of experiment and theory at  $300 \text{ MW/cm}^2$  is given in Figure 2-28. The shape of the waveforms, including the temporal extent of the longitudinal arrival, agree reasonably well. The theoretical signal is slightly larger in amplitude. It is interesting to note here that the theoretical and experimental results both indicate that the FWHM of the first longitudinal arrival is somewhat narrower than the FWHM of the incident laser pulse (approximately 75% narrower at  $300 \text{ MW/cm}^2$ ). It will also be noted that in the high irradiance region, after vapor processes become important, the shape of the waveforms still agree well. Figure 2-29 gives a comparison of the waveform calculated at  $420 \text{ MW/cm}^2$  with the waveform taken experimentally at  $700 \text{ MW/cm}^2$ . Although the model

greatly underestimates the power density at which this waveform is generated, the essential features of the waveform match those seen experimentally. The implications of this will be discussed in the following section.

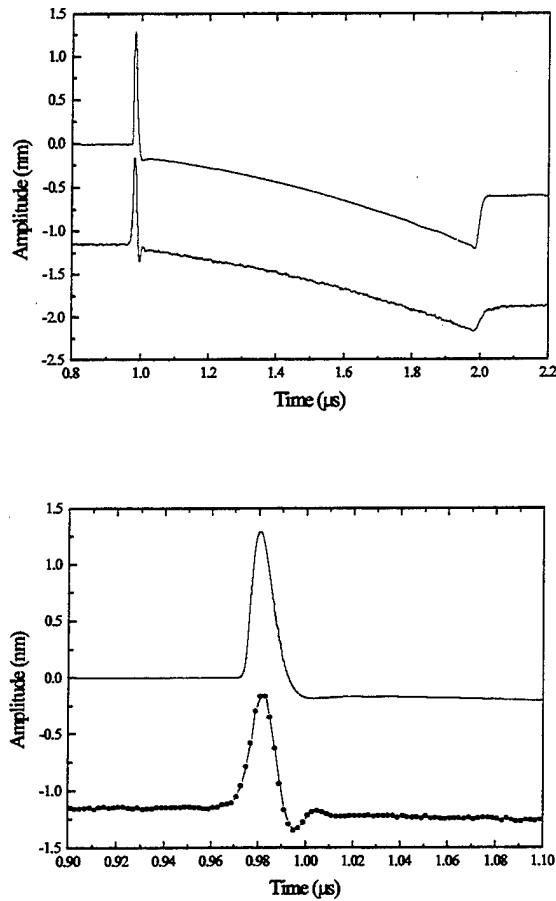


Figure 2-28 Theoretical and experimental waveforms at 300 MW/cm<sup>2</sup>. The bottom figure shows a comparison of the first longitudinal arrival.

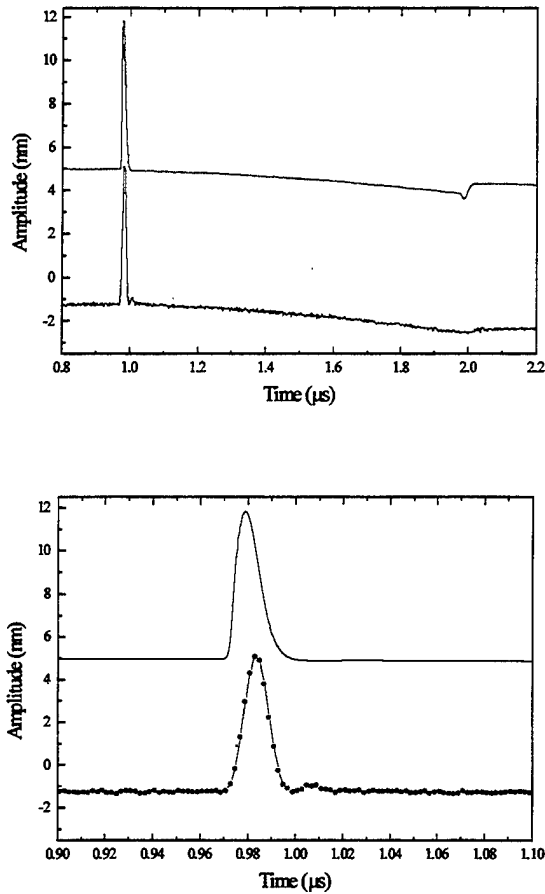


Figure 2-29 Theoretical ( $420 \text{ MW/cm}^2$ ) and experimental ( $700 \text{ MW/cm}^2$ ) waveforms. The bottom figure shows a comparison of the first longitudinal arrival.

## 2.6 Discussion of Ablative Generation of Ultrasound

The laser generation of ultrasound in the ablative regime is a complex process. The results presented show reasonable agreement with experiment in the low irradiance regime. Although the model presented is still somewhat qualitative, as the sample reflectivity was estimated through the evaluation of experimental results, the agreement between theory and experiment indicate that

the primary physical processes involved are modeled appropriately. The reflectivity chosen at  $1.064\mu\text{m}$  (67%) seems quite low and, although it may be reasonable based on the discussion of Section 2.3, the reflectivity as a function of temperature of a given sample has to be evaluated in order for the vaporization routine to be used in a completely quantitative fashion. The shape of the ablative waveforms, and the evolution of the shape as a function of irradiance, perhaps show the most promising results at present.

The vaporization model, as presented, can be coupled to a model describing processes occurring in the vapor. In vacuum, these processes can be modeled independently with the only effect of the vapor being the shielding of the sample surface from incoming laser radiation. There are a number of models of vapor processes available in the literature, some of which have been given in Table 2-1. In the simplest case, the vapor can be described as column that expands at a given rate above the surface and has a given optical density. In this case, the effect of the vapor is to attenuate incoming radiation according to:

$$I_{\text{surface}} = I_{\text{incident}} \exp(-\alpha d) \quad (2.41)$$

where  $\alpha$  is the absorption coefficient in the vapor and  $d$  is the vapor thickness. Both  $d$  and  $\alpha$  are expected to be a strong function surface temperature. The results of Figure 2-29 are somewhat surprising in that the waveform predicted at  $420 \text{ MW/cm}^2$  agrees very well with the experimental waveform measured at  $700 \text{ MW/cm}^2$ . This indicates that vapor processes which are shielding the incident radiation do not have an abrupt onset, at least not that can be observed through the acoustic signal generated, suggesting that vaporization in the high irradiance regime may be approximated by:

$$I_{\text{surface}} = c(I_{\text{max}})I_{\text{incident}} \quad (2.42)$$

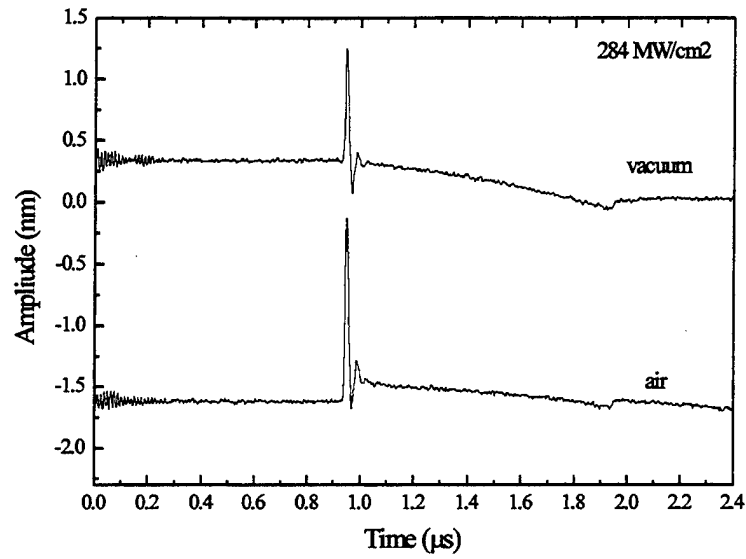
where  $c(I_{\text{max}})$  is a fraction dependent on only the maximum power density. This essentially states that the incident laser is smoothly attenuated by the vapor with the attenuation coefficient determined by the peak irradiance of the laser pulse. This is obviously an approximation, as the attenuation of the vapor must evolve as the surface is heated, but Figure 2-29 indicates that it may be a reasonable one in the irradiance range considered.

One implication of the previous approximation is that the vaporization model, as presented, may be able to be used for vacuum process monitoring at irradiance levels higher than those corresponding to vapor shielding initiation. For instance, the amplitude of the longitudinal arrival could be measured and compared to theoretical values. A match of theoretical and experimental amplitudes indicates a certain amount of light absorption at the surface, independent of plasma processes in the vapor or the surface condition (reflectivity) of the sample. The model can be used in a quantitative fashion, with no variable parameters, to monitor vaporization rate, melt front position, or surface temperature. Possible applications for this type of remote vacuum sensing include process monitoring in laser drilling and cutting operations, inductively coupled plasma atomic emission spectroscopy (ICP-AES), and laser deposition of thin films.

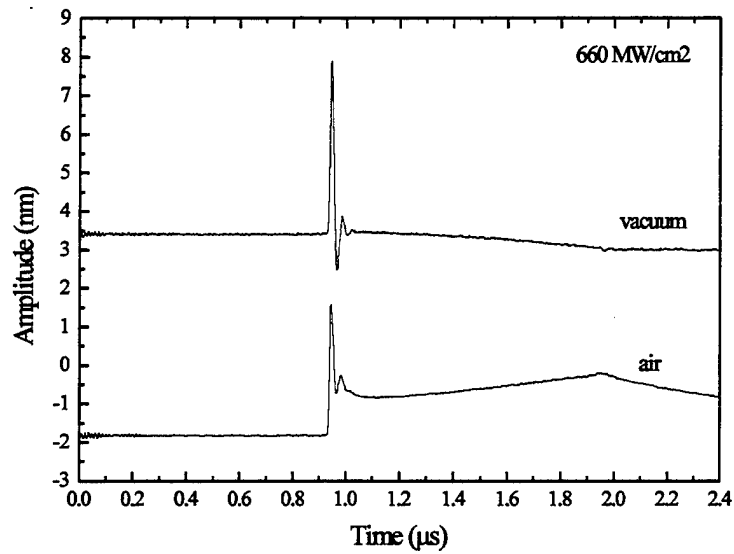
Another development in the model would be the inclusion of processes occurring in the air under atmospheric conditions. The vacuum model presented here used the jump conditions across the Knudsen layer originally presented by Anisimov (1968). These conditions only hold in the strong vaporization limit where the flow just outside the Knudsen layer is sonic. This limits the model to cases where the vapor pressure is large compared to the atmospheric pressure.

The jump conditions for cases where this approximation breaks down are treated by Knight (1979). Vaporization in the presence of a backing gas is expected to increase the pressure exerted on the surface relative to vaporization in vacuum. The other effect that can be significant is that there can be an increase in the back-flow of evaporating species. Anisimov predicts only 18% of the evaporating species will not make it through the Knudsen layer in vacuum, but this percentage can increase substantially in the presence of a backing gas. This may limit the amount of material removed from the surface when irradiating in the presence of a backing gas.

Laser generated ultrasonic signals in air are more complex to evaluate than those in vacuum. Direct comparisons between waveforms generated in air and vacuum are presented in Figure 2-30. This experiment was performed in aluminum with a spot size of approximately 350  $\mu\text{m}$ . The spot size was not measured with the knife edge technique, but rather estimated from examination of the surface damage site under an optical microscope. The experimental setup was not changed between the vacuum and air data sets, with the chamber pumped down to 0.2 torr prior to the experiment in vacuum. Figure 2-30a shows a comparison of signals generated in air and vacuum under relatively low irradiance. A larger longitudinal wave displacement is seen in air. It is also noted that after the longitudinal wave arrival, the signal in air does not return to the baseline as it does in the vacuum case. The force exerted on the specimen is seen to approach the temporal dependence of a step function under strongly ablative conditions. This is shown in Figure 2-30b, comparing waveforms generated in air and vacuum at higher laser irradiance. Figure 2-30b also indicates that, at high irradiance levels, the amplitude of the longitudinal wave displacement in vacuum is significantly larger than that in air. It is proposed that the lower amplitude signal observed in air is a result of increased plasma shielding from the breakdown of air above the surface.



a)



b)

Figure 2-30 Comparison of waveforms generated in air and vacuum at a)  $284 \text{ MW/cm}^2$  and b)  $660 \text{ MW/cm}^2$ .

Figure 2-30b illustrates that, for highly ablative generation of ultrasound in air, pressure is exerted on the surface for a significant amount of time after the laser pulse ends. This was previously assumed to be a result of the vaporization process continuing for a substantial period of time after illumination.<sup>5,6</sup> This effect was not observed in vacuum and the present results indicate that strong vaporization occurs, even at high intensities, only during the time of illumination. The surface cools quite rapidly at the conclusion of the pulse. Thus the step function time dependence of the forcing function observed in high irradiance laser ablation experiments is apparently due to the presence of the backing gas and most likely caused by the ignition of a laser supported combustion wave or laser supported detonation wave in the plasma.<sup>11,38,39</sup> A detailed discussion of these high irradiance phenomena is beyond the scope of this work and the reader is referred to the given references.

## REFERENCES

- <sup>1</sup> L.R.F. Rose, "Point-Source Representation for Laser Generated Ultrasound," *J. Acoust. Soc. Am* **75** (3), 723-732 (1984)
- <sup>2</sup> J.B. Spicer, "Laser Ultrasonics in Finite Structures: Comprehensive Modeling with Supporting Experiment," Ph.D. Dissertation, The Johns Hopkins University (1991)
- <sup>3</sup> F.A. McDonald, "Practical quantitative theory of photoacoustic pulse generation," *Appl. Phys. Lett.*, **54** (16) 1504-1506 (1989)
- <sup>4</sup> J.C. Cheng, S.Y. Zhang, and L. Wu, "Excitations of thermoelastic waves in plates by a pulsed laser," *Applied Physics A*, **61**, 311-319 (1985)
- <sup>5</sup> R.J. Dewhurst, D.A. Hutchins, S.B. Palmer, and C.B. Scruby, "Quantitative measurements of laser generated acoustic waves," *J. Appl. Phys.*, **53** (6) 4064-4071 (1982)

- 
- <sup>6</sup> J.D. Aussel, A. Le Brun, and J.C. Baboux, "Generating acoustic waves by Laser: theoretical and experimental study of the emission source," *Ultrasonics* **27** 165-177 (1988)
- <sup>7</sup> A. Hoffman and W. Arnold, "Calculation and measurement of the ultrasonic signals generated by ablating material by a Q-switched laser pulse," *Applied Surface Science*, **96-98** pp.71-75 (1996)
- <sup>8</sup> J.F. Ready, *Effects of High-Power Laser Radiation*, Academic Press, N.Y. (1971)
- <sup>9</sup> W.W. Duley, *Laser Processing and Analysis of Materials*, Plenum Press, N.Y. (1983)
- <sup>10</sup> J.C. Miller (Ed.), *Laser Ablation- principles and applications*, Springer Series in Materials Science 28, Springer-Verlag, N.Y. (1994)
- <sup>11</sup> M. von Allmen and A. Blatter, *Laser-Beam Interactions with Materials- physical principles and applications*, Springer Series in Materials Science, Springer N.Y. (1995)
- <sup>12</sup> J.F. Ready, *J. Appl. Phys.* **36** p.462 (1965)
- <sup>13</sup> S.I. Anisimov, "Vaporization of Metal Absorbing Laser Radiation," *Soviet Physics, JETP* **27(1)** 182-183 (1968)
- <sup>14</sup> M. von Allmen, "Laser drilling velocity in metals," *J. Appl. Phys.* **47(12)** 5460-5463 (1976)
- <sup>15</sup> C.J. Knight, "Theoretical modeling of rapid surface vaporization with back pressure," *AIAA Journal* **17(5)** 519-523 (1979)
- <sup>16</sup> D.I. Rosen, D.E. Hastings, and G.M. Weyl, "Coupling of pulsed 0.35 $\mu$ m laser radiation to titanium alloys," *J. Appl. Phys.* **53(8)** 5882-5890 (1982)

- 
- <sup>17</sup> C.L. Chen and J. Mazumder, "One-dimensional steady state model for damage by vaporization and liquid expulsion due to laser-material interaction," *J. Appl. Phys.* **62**(11) 4579-4586 (1987)
- <sup>18</sup> A.D. Zweig, "A thermo-mechanical model for laser ablation," *J. Appl. Phys.* **70** (3) 1684-1691 (1991)
- <sup>19</sup> A. Vertes, R.W. Dreyfus, D.E. Platt, "Modeling of the Thermal-to-plasma transitions for Cu photoablation," *IBM J. Res. and Development* **38** (1) (1994)
- <sup>20</sup> M. Aden and E.W. Kreutz, "Material removal and plasmadynamics during pulsed laser deposition by eximer and CO<sub>2</sub> laser radiation," *Applied Surface Science* **96-98** pp. 39-44 (1996)
- <sup>21</sup> S.I. Anismov, B.S. Lukyanchuk, and A. Luches, "An analytical model for three-dimensional laser plume expansion into vacuum in hydrodynamic regime," *Applied Surface Science* **96-98** pp. 24-32 (1996)
- <sup>22</sup> S. Fahler and H. Krebs, "Calculations and experiments of material removal and kinetic energy during pulsed laser ablation of metals," *Applied Surface Science* **96-98** p. 61-65 (1996)
- <sup>23</sup> W. Svendsen, J. Schou, B. Thestrup, and O. Ellegaard, "Ablation from metals induced by visible and UV laser irradiation," *Applied Surface Science* **96-98** p. 518-521 (1996)
- <sup>24</sup> Y.Y. Tsui, J. Santiago, Y.M. Li, R. Fedosejevs, "Melting and damage of aluminum surfaces by 80ps KrF laser pulses," *Optics Communications* **111** 360-369 (1994)
- <sup>25</sup> J.D. Achenbach, *Wave Propagation in elastic solids*, Elsevier Science Publishers, The Netherlands (1975)
- <sup>26</sup> M.N. Ozisik, *Finite Difference Methods in Heat Transfer*, CRC Press, Ann Arbor (1994)
- <sup>27</sup> R.D. Richtmyer, *Difference Methods for Initial Value Problems*, Interscience Publishers, N.Y. (1957)

- 
- <sup>28</sup>R.K. Singh and J. Narayan, "A novel method for simulating laser-solid interactions in semiconductor and layered structures," *Materials Science and Engineering*, **B3** 217-230 (1989)
- <sup>29</sup> J.E. Hatch, *Aluminum-properties and physical metallurgy*, American Society for Metals, Metals Park Ohio (1984)
- <sup>30</sup> D.E. Gray (Ed.), *American Institute of Physics Handbook*, McGraw-Hill, N.Y. (1972)
- <sup>31</sup> U. Schleichert, M. Paul, B. Hoffman, K.J. Langanberg, and W. Arnold, "Theoretical and experimental investigations of broadband thermoelastically generated ultrasonic pulses" in *Photoacoustic and Photothermal Phenomena*, Ed. P. Hess and J. Pelzl, 262-268, Springer-Verlag, N.Y. (1988)
- <sup>32</sup> J.W. Wagner, "Optical Detection of Ultrasound", in *Physical Acoustics Vol. XIX*, 201-266 Academic Press, N.Y. (1990)
- <sup>33</sup> J.M. Khosroffian and B.A. Garetz, "Measurement of a Gaussian laser beam diameter through the direct inversion of knife edge data," *Applied Optics* **22**(21) 3406-3410 (1983)
- <sup>34</sup> C.R. Phipps Jr., T.P. Turner, R.F. Harrison, G.W. York, W.Z. Osborne, G.K. Anderson, X.F. Corlis, L.C. Haynes, H.S. Steele, K.C. Spicochi, and T.R. King, "Impulse Coupling to targets in vacuum by KrF, HF, and CO<sub>2</sub> single-pulse lasers," *J. Appl. Phys.* **64** (3) 1083-1096 (1988)
- <sup>35</sup> M.A. Shannon, X.L. Mao, A. Fernandez, W. Chan, and R.E. Russo, "Laser ablation mass removal versus incident power density during solid sampling for inductively coupled plasma atomic emission spectroscopy," *Anal. Chem.* **67**, 4522-4529 (1995)
- <sup>36</sup> L.R. Hettche, T.R. Tucker, J.T. Schriempf, R.L. Stegman, and S.A. Metz, "Mechanical response and thermal coupling of metallic targets to high-intensity 1.064 radiation," *J. Appl. Phys.* **47** (4) 1415-1421 (1976)
- <sup>37</sup> D.I. Rosen, J. Metteldorf, G. Kothandaraman, A.N. Pirri, and E.R. Pugh, "Coupling of pulsed .35mm radiation to aluminum alloys," *J. Appl. Phys.*, **53** (4) (1982)

---

<sup>38</sup> P.E. Nielsen, "Hydrodynamic calculations of surface response in the presence of laser-supported detonation waves," *J. Appl. Phys.* **46**(10) 4501-4505 (1975)

<sup>39</sup> B.S. Holmes and D.C. Erlich, "Surface pressures from laser supported detonations," *J. Appl. Phys.* **48** (6) 2396-2403 1977

### **Spatial Modulation of Incident Laser Light**

As will be discussed, there has been a considerable amount of work presented in the literature on spatial modulation of laser sources for the generation of acoustic waves. A new technique has recently been developed which builds upon the existing work. This technique has been summarized in a manuscript entitled "Laser Ultrasonic Chirp Sources for Low Damage and High Detectability without Loss of Temporal Resolution."<sup>1</sup> This manuscript is presented in its entirety in the current chapter.

### 3.1 Abstract

Linear frequency modulated (chirped) acoustic signals have been generated using a pulsed laser spatially modulated by an absorption mask at the surface of a test material. By distributing the laser energy over an area, instead of focusing it to a point or line source, the peak power density of the laser source can be kept below the damage threshold of the material. The corresponding chirped ultrasonic surface wave packet produced by the source, although extended in time, is detected and processed using a matched filtering technique which compresses the packet into a pulse, thus preserving temporal resolution for accurate time-of-flight measurements. Matched filter processing of the chirped wave packet has been compared with the same processing applied to a narrowband tone burst wave packet. Processing of the chirped signal permits easy separation of overlapped return echoes which could not be resolved when narrowband signals were used. Finally, by compressing the energy within a chirped signal to a single detection spike, an apparent 15-fold enhancement in signal-to-noise ratio is observed.

### 3.2 Introduction

Signal detectability is arguably the key parameter to be optimized when designing a laser-based system for remote generation and detection of ultrasonic signals. The dependence of signal-to-noise ratio upon signal amplitude, signal bandwidth, and laser brightness (both for generating and detecting sound) are well understood.<sup>2,3,4,5,6</sup> Increasing the ultrasonic signal amplitude directly improves signal-to-noise ratio and, correspondingly, the detectability of a laser

ultrasonic system. There are limits, however, to increasing source laser power as a means of generating large ultrasonic amplitudes. In some configurations and for particular materials systems, it may not be possible to achieve a satisfactory signal-to-noise ratio at laser power densities below the damage threshold for the material being tested. As an alternative to single pulse excitation, phased array systems have been proposed and demonstrated which can enhance surface and bulk wave amplitudes to acceptably high levels without requiring any individual element of the array source to exceed the material ablation threshold.<sup>7,8,9,10</sup> Alternatively, periodic spatial arrays<sup>11,12,13,14,15</sup> and temporal modulation of a single source<sup>16,17</sup> have been demonstrated to produce tone burst acoustic signals to which a receiving detector can be tuned, thus providing enhanced immunity to broadband noise. Among these three methods for modifying the laser source for enhanced detectability, the spatial array methods for generation of narrowband, tone burst ultrasound are the simplest and least expensive to implement. The disadvantage of these narrowband methods, however, is that the temporal extent of the wave packet generated by such sources can lead to uncertainty in time-of-flight measurements important for many practical laser inspection and measurement applications.

A new laser ultrasonic generation technique has been investigated which uses a spatial mask in a manner similar to that which may be employed for generation of narrowband, tone burst ultrasound. Instead of periodic spatial modulation at the surface of a test object, however, the mask employed for this technique is linearly frequency modulated as a function of position and correspondingly generates ultrasonic wave packets which are linearly frequency modulated (FM) as a function of time (chirped). Although the chirped mask launches an ultrasonic wave packet which is extended in time, not unlike an ultrasonic tone burst, the nature of the chirped signal is such that once detected, it

can be processed by a matched filter algorithm which generates a single narrow spike corresponding to the time of arrival of the wave packet.

Pulse compression techniques were originally developed to overcome system power limitations in radar applications.<sup>18,19,20,21</sup> These same concepts have been used in the field of ultrasonic NDT. Conventional contact piezoelectric systems using pulse compression methods such as linear FM<sup>22</sup>, random noise<sup>23</sup>, and Barker and Golay codes<sup>24,25</sup> have been demonstrated. Pulse compression techniques have also been successfully applied to electromagnetic-acoustic transducer (EMAT) systems.<sup>26</sup> More recently, ultrasonic pulse compression has been applied to medical imaging systems.<sup>27,28</sup> In all of the above applications, the use of pulse coding techniques provides a means of circumventing peak power limitations in the transducer (or in the system under inspection) while maintaining high temporal resolution and signal-to-noise ratio (SNR). In the present work, the use of linear FM pulse compression is extended to laser ultrasonic NDT where sensitivity issues are often a major obstacle limiting the use of such systems in practical NDT applications. Furthermore, the power limitation (ablation threshold) encountered in the laser ultrasonic generation can be quite severe as it is dictated by the thermal and optical properties of the material under inspection. Thus the use of linear FM, as well as other pulse compression techniques, may provide a means of extending the range of laser ultrasonic systems to cases where low ablation threshold and poor sensitivity may have proven prohibitive.

### 3.3 Theory

In filtering surface wave data, considerations include signal to noise ratio as well as extraction of useful information, such as arrival time and amplitude, from the signals arriving at the detection point. For many applications, it is not

necessary that the shape of the waveform be preserved in the filtering process as long as amplitude and time-of-flight information can be extracted from the filtered signals. Taking this into account the signal-to-noise ratio (SNR) that is to be maximized at some (arbitrary) instant in time ( $t_m$ ) may be given as:

$$\left(\frac{S}{N}\right) = \frac{s_o^2(t_m)}{n_o^2(t)} \quad (3.1)$$

where  $s_o(t_m)$  is the maximum signal amplitude and  $n_o^2(t)$  is the mean squared noise amplitude. If the noise is white, as would be the case for a shot noise limited interferometric detection system, the SNR can be maximized using a matched filter.<sup>29</sup> The output of a matched filter is obtained by cross-correlating the received signal with the generated signal. The maximum SNR is given as

$$\left(\frac{S}{N}\right)_{\max} = 2E/N_o \quad (3.2)$$

where  $E$  is the total signal energy and  $N_o/2$  is the noise spectral density.

In the laser ultrasonic generation case, the energy in the acoustic waveform is proportional to the incident laser energy.<sup>4</sup> When generating surface waves with a Q-switched laser pulse, the surface wave frequency content is determined primarily by the spot size of the generation pulse. A small spot size will give rise to a high frequency surface wave while a broad generation spot will give rise to a low frequency surface wave. Thus to achieve high resolution and SNR, the energy in the incident pulse could be increased and focused to a sharp point or line. Unfortunately, the energy density of the input pulse is limited, though, by the ablation threshold of the material. One scheme to circumvent this

difficulty is to distribute the generating pulse over a large area on the surface of a specimen. This allows for generation to remain in the thermoelastic regime while at the same time increasing the total energy in the acoustic signal, and thus increasing the SNR. In order to distribute the laser energy over a large area and still maintain good signal resolution, the energy can be modulated over the extent of the illuminated region.

Narrowband surface waves have been obtained by illuminating the specimen with a sinusoidal intensity pattern with the generation laser.<sup>11-14</sup> When using narrowband signals in a matched filter arrangement, the output of the matched filter consists of a sinusoidal signal of twice the duration of the input signal and modulated by a triangular envelope. The use of narrowband generation has drawbacks in that ambiguities exist at multiples of the signal period (at the sidelobes) and difficulties arise when detecting multiple signals in cases where the correlation envelopes overlap. These problems can be overcome by using pulse coding techniques, examples of which include the use of amplitude or frequency modulated signals, or pseudo random signals.<sup>18-28</sup> By imposing these pulse compression techniques, the effective bandwidth of the signal is increased and the width of the envelope of the signal, after matched filtering, is decreased.

Linear frequency modulation (FM) signals have been used extensively in radar and ultrasonics applications. Such signals are especially useful in cases where a short duration, high energy pulse cannot be generated or transmitted. The signal energy may then be distributed over a large period of time and then be compressed into a short pulse, after reception, with a matched filter system. In the laser ultrasonics case, this consists of generating a FM surface wave pulse train with a spatially broad laser source and, after interferometric detection, compressing the wave train into a sharp spike through matched filtering. The general expression for a linear FM pulse is given by:

$$W(t) = \cos[\omega_0 t + bt^2] \quad (3.3)$$

This produces a chirp pulse in which the angular frequency is linearly swept from  $\omega_0$  to  $\omega_0 + 2bT$ , where  $T$  is the temporal pulse duration and  $2b$  is the linear frequency sweep rate. The pulse width obtained after match filtering a linear FM pulse is inversely proportional to the FM pulse bandwidth,  $bT/\pi$ .

### 3.4 System Description

The experimental configuration is shown in Figure 3-1. To generate a linear FM acoustic wave, a transmission mask was placed near the surface of the specimen and was illuminated with an expanded beam from a pulsed Nd:YAG source. The mask was constructed by taking the desired linear FM waveform (Eq. 3.2) as a template and then thresholding about the zero value. The resulting mask is shown in the lower left hand corner of Figure 3-1. The dimensions of the active area of the mask are 1.1cm wide by 2.5 cm long. The incident laser pulse was expanded to over 1.1cm in diameter in an attempt to achieve relatively uniform illumination over the entire width of the mask. The laser pulse width was 13ns and the total energy transmitted by the mask was 30mJ (approximately 25% of the laser energy incident on the mask). The laser pulse energy was low enough to ensure that generation took place in the thermoelastic regime. All surface waves were generated on an aluminum specimen with multiple surface wave arrivals corresponding to reflections off of the edges. The acoustic waves were detected using a path-stabilized skewed Michelson interferometer. The waveforms were transferred to a personal computer for digital filtering.

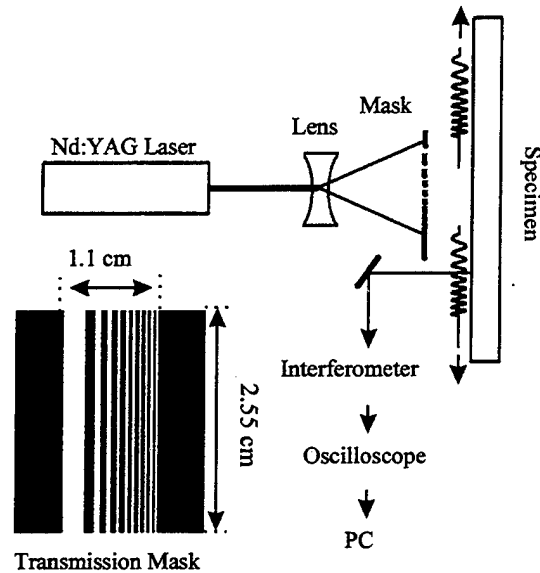


Figure 3-1 Experimental setup for the generation of FM surface waves. The transmission mask is shown in the lower right hand corner.

### 3.5 Results and Discussion

This technique launches acoustic waves that are very similar in form to the linear FM template, as is shown in Figure 3-2a comparing the theoretical chirped signal to an experimental chirped surface wave which was signal averaged 100 times. The pulse compression obtained from the experimental and the theoretical FM waveform are in good agreement as is illustrated in Figure 3-2b. Note that although the theoretical and experimental waveforms have some

slight differences, the pulse compression achieved with the experimental signal is sufficient to prove that this technique performs adequately. A typical single shot

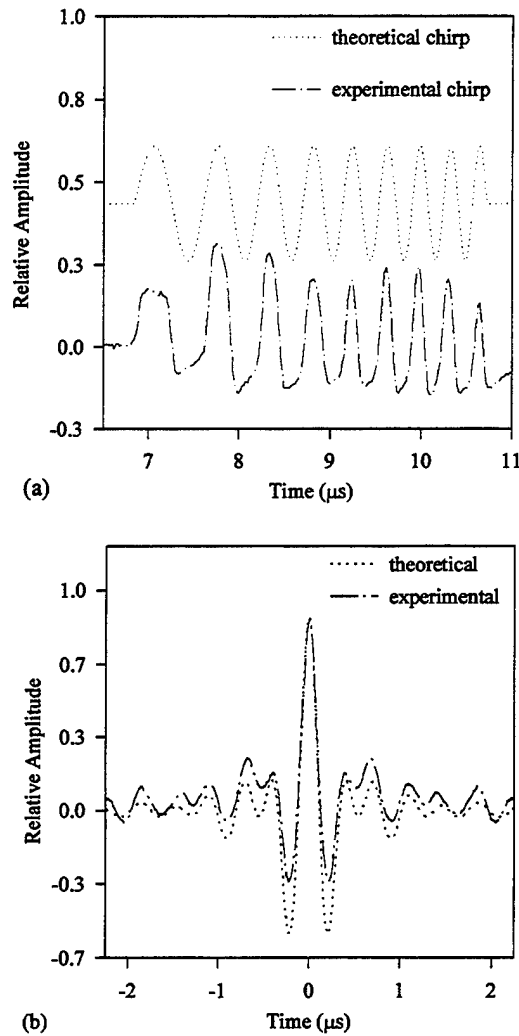


Figure 3-2 Comparison of a) theoretical and experimental chirped surface waves and b) the compressed waveforms after autocorrelation.

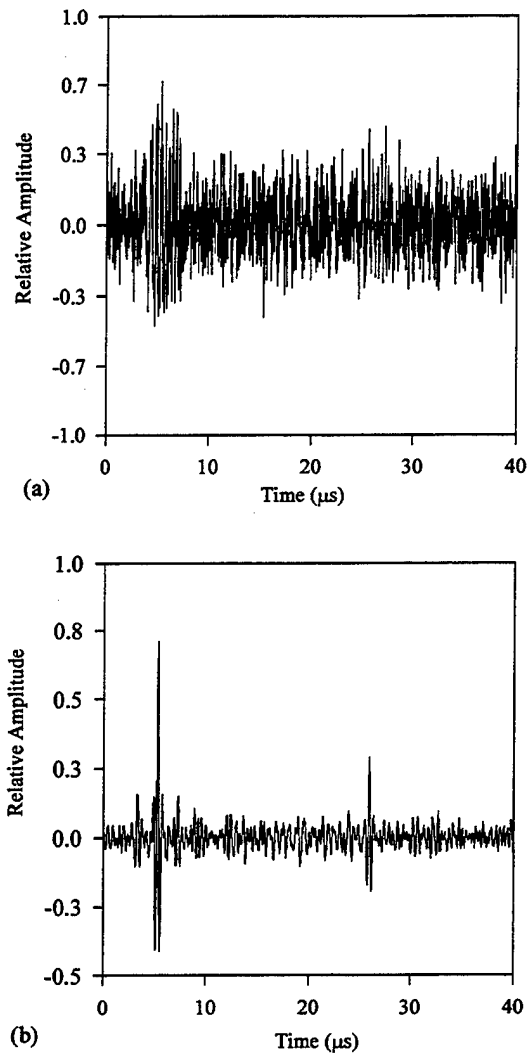


Figure 3-3 a) Single shot FM surface waveform and b) the waveform after matched filtering showing a 15-fold increase in signal to noise ratio and compression of the wave packet.

signal waveform using a linear FM mask is shown in Figure 3-3a. This signal was then processed using a matched filter based upon the template linear FM waveform. The resulting output is shown in Figure 3-3b. An apparent 15-fold increase in SNR (based on Eq. 2.1) is observed in the filtered waveform.

### 3.5.1 Resolution Enhancement

Analogous to the radar case, it becomes difficult to resolve distinct pulses in the output of a matched filter if the pulses are separated by less than the full width half maximum (FWHM) of their envelopes. In the narrow band case, the envelope function is given by:<sup>19</sup>

$$1 - \frac{|t|}{T}, |t| < T \quad (3.4)$$

where  $T$  is the duration of the pulse train.

In the linear FM case, the envelope is given by:

$$\frac{\sin(bt)}{bt} \left[ 1 - \frac{|t|}{T} \right], |t| < T \quad (3.5)$$

As can be seen from the functional forms, the FWHM of the narrow band case is  $T$  and the FWHM of the linear FM case is  $\pi/bT$ . The linear FM signal

essentially 'compresses' the envelope of the narrowband signal by a factor of  $b/\pi$ .

The benefits of this compression effect are apparent in Figure 3-4. Figure 3-4a shows a single shot ultrasonic signal containing two overlapping linear FM signals in noise. Figure 3-4b shows the result of using a linear FM matched filter. In this case, the compression of the envelopes allows the two signals to be easily resolved. Figure 3-4c shows a single shot ultrasonic signal composed of two overlapping narrow band signals in noise. Figure 3-4d shows the output of a matched filter based on a noise free signal. Here, the width of the envelopes poses a problem in resolving the individual signals.

### 3.5.2 Directionality

Using the mask, a FM array of line sources generates a corresponding FM acoustic pulse train. Considering the surface wave directivity for a line source, large amplitude surface waves are generated perpendicular to illuminating lines.<sup>30</sup> These two FM pulse trains are phased reversed. Using a matched filter, the received signal can be correlated with a forward or reversed chirp signal. The acoustic signal launched to the left of the mask is phase reversed from that emitted to the right and thus will only correlate with a reversed chirp (see Figure 3-1). This concept is illustrated in Figure 3-5. Figure 3-5a shows the single shot data. Figure 3-5b shows the correlation with the forward chirp, with the peaks corresponding to surface waves originally launched to the right of the mask. Figure 3-5c shows the correlation with the reverse chirp, with the peaks corresponding to surface waves originally launched to the left of the mask. Note that in Figure 3-5c there is some noise corresponding to a degree of correlation between the reverse chirp and the large amplitude surface wave pulse train

originally launched to the right of the mask, but the broad nature of this noise (it is not compressed) allows it to be distinguished from the other arrivals. The

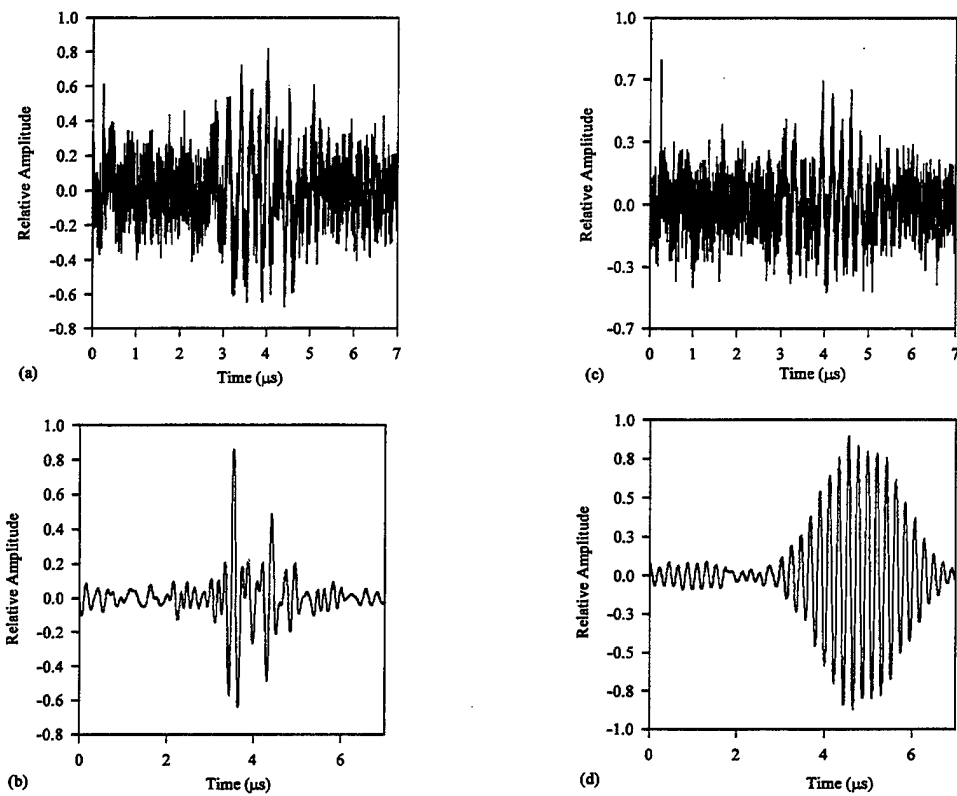


Figure 3-4 Overlapping FM and narrowband surface wave packets (a,c). Matched filtering allows for resolution of individual arrivals in the chirped case (b) but not in the narrowband case (d).

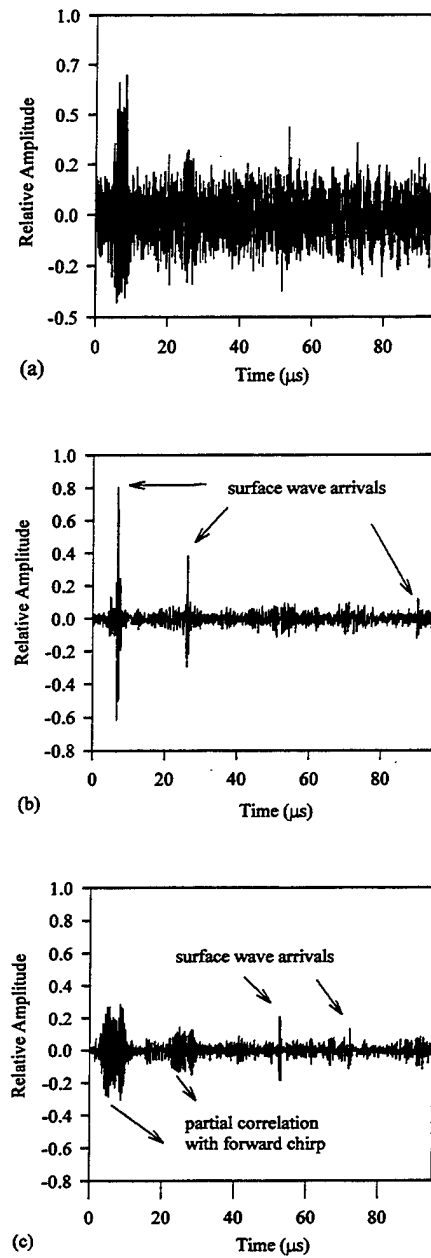


Figure 3-5 a) Single shot waveform on an aluminum block. Matched filtering with the “forward chirp” and “reverse chirp” (b,c).

asymmetry of the chirp pulse can prove useful when, for example, locating a crack when several arrivals are present.

### 3.6 Conclusions

A new technique has been presented which allows for greater temporal resolution and enhanced detectability of laser generated surface waves. The laser energy is spread over an area of the surface allowing for more laser energy to be used in the generation of acoustic waves while remaining in the thermoelastic regime. Spatial frequency modulation of the laser source over the illuminated region allows for the compression of the generated surface wave packet upon reception by matched filtering. Matched filtering gives the maximum SNR possible in the white noise case. The filtered FM surface wave signals showed a 15-fold increase in SNR over the unfiltered waveforms. The advantages of using a FM technique over a narrowband generation process, such as increased ability to resolve overlapping signals, have been discussed and experimentally verified.

The transmission mask used to generate the FM pulse train was placed in close proximity to the specimen. In practical inspection systems, where remote generation of surface waves is required, other means of producing a FM intensity distribution on the surface of the component to be inspected may be utilized. The transmission mask may be imaged onto the surface of the specimen using a simple imaging system. A binary phase grating, similar to that previously employed for narrowband surface wave generation,<sup>11</sup> may also be employed for the same purpose.

## REFERENCES

- <sup>1</sup> T. W. Murray, K. C. Baldwin, and J. W. Wagner, "Laser Ultrasonic Chirp Sources for Low Damage and High Detectability without Loss of Temporal Resoultion," *J. Acoust. Soc. Am.*, in press
- <sup>2</sup> C.B. Scruby and L.E. Drain, *Laser Ultrasonics, Techniques and Applications*, Adam Hilger, Bristol (1990)
- <sup>3</sup> D.A. Hutchins, "Ultrasonic Generation by pulsed lasers", in *Physical Acoustics*, edited by W.P. Mason and R.N. Thurston (Academic Press, New York, 1988), Vol. XVIII, pp. 21-143
- <sup>4</sup> R.J. Dewhurst, D.A. Hutchins, S.B. Palmer, and C.B. Scruby, "Quantitative studies of thermally generated elastic waves in laser irradiated metals," *J. Appl. Phys.* **51**(12), 6210-6216 (1980)
- <sup>5</sup> J.W. Wagner, "Optical detection of ultrasound," in *Physical Acoustics*, edited by Ed Pierce (Academic Press, New York, 1990) Vol. XIX, pp. 201-266
- <sup>6</sup> J.W. Wagner and J.B. Spicer, "Theoretical noise-limited sensitivity of classical interferometry," *J. Opt. Am. B* **4**, 1316-1326 (1987)
- <sup>7</sup> M-H. Noroy, D. Royer, and M. Fink, "The laser-generated phased array: Analysis and experiments," *J. Acoust. Soc. Am.* **94**(4) 1934-1943 (1993)
- <sup>8</sup> T.W. Murray, J.B. Deaton Jr., and J.W. Wagner, "Experimental evaluation of enhanced generation of ultrasonic waves using an array of laser sources", *Ultrasonics* **34**, 69-77 (1996)
- <sup>9</sup> J.S. Steckenrider, T.W. Murray, J.W. Wagner, and J.B. Deaton Jr., "Sensitivity enhancement in laser ultrasonics using a versatile laser array system", *J. Acoust. Soc. Am.* **97**(1), 273-279 (1995)
- <sup>10</sup> Y. Yang, N. DeRidder, C. Ume, and J. Jarzynski, "Noncontact optical fibre phased array generation of ultrasound for non-destructive evaluation of materials and processes," *Ultrasonics* **31**, 387-394 (1993)

- 
- <sup>11</sup> J. Huang, S. Krishnaswamy, and J.D. Achenbach, "Laser generation of narrow-band surface waves," *J. Acoust. Soc. Am.* **92**, 2527-2531 (1992)
- <sup>12</sup> S. Nagai and H. Nakano, "Laser generation of antisymmetric lamb waves in thin plates," *Ultrasonics* **29**, 230-234 (1991)
- <sup>13</sup> A. Harata, H. Nishimura, T. Sawada, "Laser-induced surface acoustic waves and photothermal surface gratings generated by crossing two pulsed laser beams," *Appl. Phys. Lett.* **57** (2), 132-134 (1990)
- <sup>14</sup> H. Nishino, Y. Tsukahara, Y. Nagata, T. Koda, and K. Yamanaka, "Excitation of high frequency surface acoustic waves by phase velocity scanning of a laser interference fringes," *Appl. Phys. Lett.* **62** (17), 2036-2038 (1993)
- <sup>15</sup> A.D.W. McKie, J.W. Wagner, J.B. Spicer, and C.M. Penny, "Laser generation of narrowband and directed ultrasound," *Ultrasonics* **27**, 323-330 (1989)
- <sup>16</sup> J.W. Wagner, J.B. Deaton Jr., and J.B. Spicer, "Generation of ultrasound by repetitively Q-switching a pulsed Nd:YAG laser," *Applied Optics* **27**(22) 4696-4700 (1988)
- <sup>17</sup> J.B. Deaton Jr., A.D.W. McKie, J.B. Spicer, and J.W. Wagner, "Generation of narrowband ultrasound with a long cavity mode-locked Nd:YAG laser," *Appl. Phys. Lett.* **56**, 2390-2392 (1990)
- <sup>18</sup> C.E. Cook, "Linear f-m Pulse Compression," in *Modern Radar*, Edited by R.S. Berkowitz (John Wiley and Sons, Inc, New York, 1965) pp. 216-241
- <sup>19</sup> H. Urkowitz, "Ambiguity and Resolution," in *Modern Radar*, Edited by R.S. Berkowitz (John Wiley and Sons, Inc, New York, 1965) pp. 197-213
- <sup>20</sup> A.W. Rihaczek, *Principles of High Resolution Radar*, McGraw-Hill, New York (1969)

- 
- <sup>21</sup> C.E. Cook and M. Bernfeld, *Radar Signals*, Academic Press, New York (1967)
- <sup>22</sup> F.K. Lam and J. Szilard, "Pulse Compression techniques in ultrasonic non-destructive testing," *Ultrasonics* **14**, 111-114 (1976)
- <sup>23</sup> E.S. Furgason, V.L. Newhouse, N.M. Bilgutay and G.R. Cooper, "Application of random signal correlation technique to ultrasonic flaw detection," *Ultrasonics* **13**, 11-17 (1975)
- <sup>24</sup> W.H. Chen and D.L. Deng, "Ultrasonic non-destructive testing using Barker code pulse compression techniques," *Ultrasonics* **26**, 23-26 (1988)
- <sup>25</sup> B.B. Lee and E.S. Furgason, "High-speed digital Golay code flaw detection system," *Ultrasonics* **21**, 153-161 (1983)
- <sup>26</sup> H.M. Frost, "Electromagnetic-Ultrasound Transducers: Principles, Practice, and Applications," in *Physical Acoustics* Vol.14, Edited by W.P. Mason and R.N. Thurston, (Academic Press, NY. 1979) pp. 179-276
- <sup>27</sup> J.Y. Chapelon, "Pseudo-random correlation imaging and systems characterization," in *Progress in Medical Imaging*, Edited by V.L. Newhouse, (Springer-Verlag, 1988) Chap.6
- <sup>28</sup> N.A.H.K. Rao, "Investigation of a pulse compression technique for medical ultrasound: a simulation study", *Med. & Biol. Eng. & Comp.*, **32**, 181-88 (1994)
- <sup>29</sup> A.D. Whalen, *Detection of Signals in Noise*, Academic Press Inc., Florida, (1971) pp. 167-175
- <sup>30</sup> A.M. Aindow, R.J. Dewhurst, and S.B. Palmer, "Laser generation of directional surface acoustic wave pulses in metals," *Opt. Comm.* **42**(2) 116-120 (1982)

## Temporal Modulation of Laser Sources

### 4.1 Introduction

In this chapter, the dependence of laser generated acoustic waves on the temporal extent of the laser source will be evaluated. It is assumed that laser generation takes place in the thermoelastic regime. If surface vaporization is to be avoided, the generating pulse must not heat the surface beyond the vaporization threshold temperature. This controls the amount of energy that may be absorbed at the specimen surface and limits the amplitude of the acoustic waves that may be generated. One method of circumventing this problem is to alter the temporal profile of the incident radiation. This technique has been successful in a number of cases reported in the literature. Temporal modulation of laser sources has been achieved through repetitive Q-switching of a Nd:YAG laser<sup>1</sup>, mode locking of a long cavity Nd:YAG laser<sup>2</sup>, a White cell optical delay line arrangement<sup>3</sup>, and the use of an array of laser sources.<sup>4,5</sup> Temporal modulation through optical fiber delay line arrangements has also been demonstrated.<sup>6,7</sup> The primary benefit of temporal modulation is that it allows for more energy to be coupled to the specimen before the vaporization temperature is reached. The spatial and temporal distribution of this acoustic energy can be optimized in several ways. First, the modulation of laser sources at a single point allows for the concentration of this energy into a narrow frequency band to which

the detection systems can be tuned and sensitivity increased. Next, if spatial and temporal modulation are possible, the sources may be arranged such that superposition of the acoustic waves occurs at the detection point.

Laser ultrasonic system sensitivity enhancement has been demonstrated using the temporal modulation techniques mentioned above. The present work first considers the effects of modifying the pulse length from a single laser source on the generation of acoustic waves. The problem of controlling the pulse length of a Q-switched laser is addressed. Pulse length effects in homogeneous, isotropic, materials can be determined theoretically through analysis of the thermal and acoustic processes involved. In complex materials systems, the prediction of pulse length effects may be complicated by elastic and thermal anisotropy. A linear systems model is presented which simplifies the prediction of temporal modulation effects in these materials, and may prove useful in the design of laser ultrasonic systems for specific applications.

#### 4.2 Controlling Laser Pulse Length

Commercial Q-switched Nd:YAG laser systems generally have fixed pulse lengths in the 5-30 ns range. In order to adjust this, the dependence of the pulse length on various laser cavity parameters must be found. Q-switching can be modeled using coupled rate equations:<sup>8</sup>

$$\begin{aligned}\frac{\partial \eta}{\partial \tau} &= (\beta - 1)\eta \\ \frac{\partial \beta}{\partial \tau} &= -2\beta\eta\end{aligned}$$

(4.1)

where  $\eta$  is the ratio of the cavity photon density to the threshold photon population inversion density,  $\beta$  is the ratio of the population inversion to the threshold inversion, and  $\tau$  is a dimensionless time variable given by:

$$\tau \approx \frac{c(1-R)t}{L} \quad (4.2)$$

where  $L$  is the cavity length,  $c$  is the speed of light, and  $R$  is the output coupler reflectivity.

Through numerical solution of these rate equations, the output laser pulse shape can be estimated, and its dependence on cavity parameters evaluated. In general, there are two ways of increasing the pulse length in a given Q-switched laser system. The first is to increase the photon lifetime in the cavity. The photon lifetime is a characteristic time constant which describes the decay of optical radiation in the laser cavity and is given by:

$$t_c = \frac{\tau}{t} \approx \frac{L}{c(1-R)} \quad (4.3)$$

Increasing the photon lifetime essentially traps the light in the laser cavity, spreading the light out in time. From Eq. (4.3), this can be accomplished through either lengthening the laser cavity or increasing the reflectivity of the output coupler. The second method of increasing the pulse length is by decreasing the laser pump energy. This broadens the laser pulse by allowing stimulated emission to occur over a longer period of time. The effects of increasing cavity length, increasing output coupler reflectivity, and decreasing pump rate were found

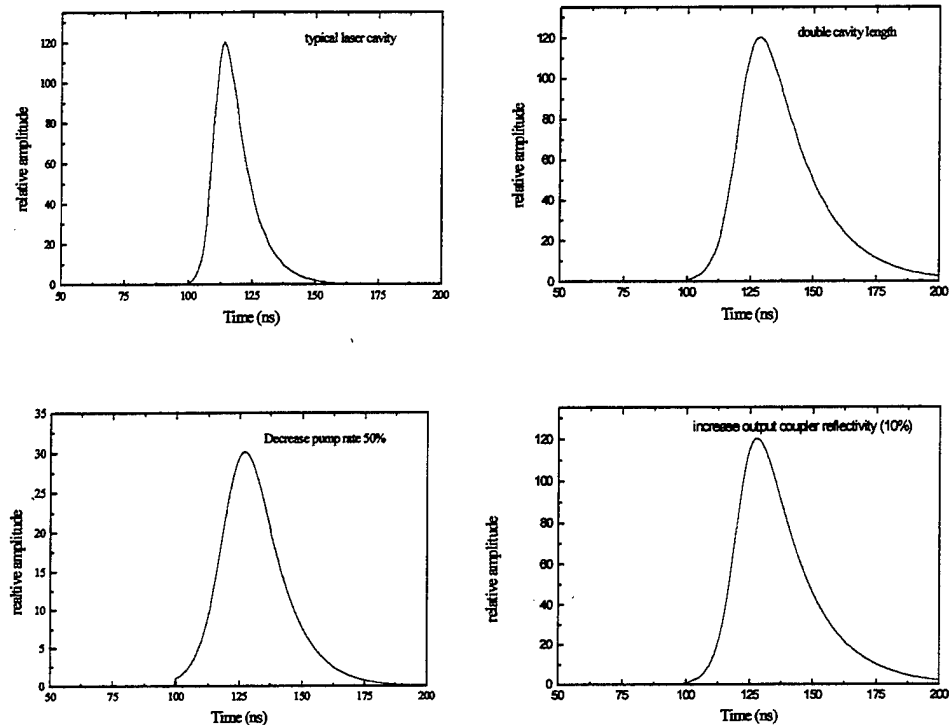


Figure 4-1 Effects of varying laser cavity length, pumping rate, and output coupler reflectivity. All of the changes indicated lead to a lengthening of the laser pulse.

through a numerical solution of the rate equations and are illustrated in Figure 4-1. All of these effects can be readily used to control the output pulse length of a given laser system.

Experiments with a Lasermetrics Q-switched Nd:YAG laser system have shown that the pulse length of this system could be controlled through adjustment of the pump energy and laser cavity length. The pulse length could be adjusted from about 10ns to over 200ns. Controlling the pump energy was the easiest method of controlling pulse width. Unfortunately, decreasing the laser pump energy results in a decrease in the energy of the output pulse. In order to ensure

adequate energy in the output pulse, the cavity length or output coupler reflectivity may have to be adjusted in conjunction with the pump energy.

#### 4.3 Pulse Length Effects on Surface Heating

For thermoelastic generation of acoustic waves, there exists some temperature ( $T_{\max}$ ) which the sample surface is to be kept below. For a given generation laser pulse length ( $t_p$ ), this limits the maximum amount of energy ( $E_{\max}$ ) that may be absorbed at the sample surface. At present, the case of a strongly absorbing surface will be considered. The three dimensional solution of the heat equation for a spatially Gaussian laser source (surface absorber) with an arbitrary time dependence is given by:<sup>9</sup>

$$T_{\text{Gaussian}} = \frac{F_{\max} d^2 \sqrt{\kappa}}{K \sqrt{\pi}} \int \frac{p(t-t_1) dt_1}{\sqrt{t_1} (4\kappa t_1 + d^2)} \exp\left(-\frac{z^2}{4\kappa t_1} - \frac{r^2}{4\kappa t_1 + d^2}\right) \quad (4.4)$$

where  $F_{\max}$  is the absorbed power per unit area at the center of the Gaussian spot,  $\kappa$  is the thermal diffusivity,  $K$  is the thermal conductivity, and  $d$  is the beam radius. This solution does not take into account the temperature dependence of the thermal and optical properties of the material which may be substantial (as discussed in Chapter 2), but nevertheless gives a reasonable approximation for pulse length effects.

It is assumed that the pulse length is adjusted through the variation of laser cavity parameters. Eq. (4.4) was solved with the pulse shape  $p(t)$  calculated through the laser rate equations. The pulse length was increased, in the numerical

routine, by increasing the laser cavity length. Figure 4-2 shows the relative amount of energy absorption needed to raise the surface to the maximum allowable temperature,  $T_{\max}$ , as a function of pulse length. The spot size was taken as 2.5mm and the calculation was performed using the thermal properties of aluminum. Figure 4-2 illustrates a square-root dependence of  $E_{\max}$  on the pulse length.

Typically, the laser spot sizes used for the generation of ultrasound are significantly large such that radial diffusion of heat from the generation spot can be ignored. If the surface temperature is evaluated over an extended period of time or if the laser spot size is very small, then the three dimensional heat conduction problem must be considered. In the cases presented below, the laser spot size is sufficiently larger than the thermal diffusion length and the assumption of one dimensional heating holds.

If one dimensional heating is assumed, the relationship between  $E_{\max}$  and  $t_p$  can be easily found. Consider the case of one-dimensional heating of a half space by a constant amplitude laser pulse. The solution to this problem is given as follows:

$$T_{\text{surface}} = \frac{2I\sqrt{kt}}{K\sqrt{\pi}} - \frac{I}{K\alpha} + \frac{I}{K\alpha} \exp(\alpha^2 kt)(1 - \text{erf}(\alpha\sqrt{kt})) \quad (4.5)$$

where  $I$  is the incident laser pulse power density and  $\alpha$  is the absorption coefficient. With strong surface absorption, as is the case in metals,  $\alpha$  approaches infinity and this expression reduces to:

$$T_{\text{surface}} = \frac{2I\sqrt{kt}}{K\sqrt{\pi}}$$

(4.6)

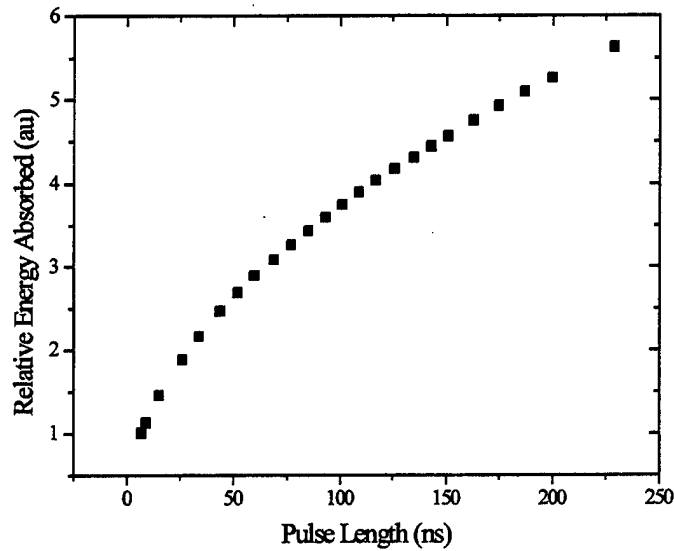


Figure 4-2 Relative amount of absorbed laser energy needed to raise the surface temperature to  $T_{\max}$  as a function of pulse length.

Eq. (4.6) shows explicitly the dependence of surface temperature on heating time. The relation between  $E_{\max}$  and  $t_p$  is expressed as follows:

$$E_{\max} \propto \sqrt{t_p} \quad (4.7)$$

The simple result given in Eq. (4.7) provides the incentive for pulse length consideration in the generation of ultrasound. The amount of laser energy that may be absorbed by a material without causing damage can be increased by

increasing the laser pulse length. This, in turn, should increase the energy in the acoustic signal generated.

#### 4.4 Pulse Length Effects on the Generation of Acoustic Waves

The frequency content of laser generated ultrasonic signals (in the absence of material dependent losses) is determined, to a large extent, by the temporal frequency content of the incident laser pulse, the spatial frequency content of the generation spot, the source-receiver geometry, and the optical absorption depth. For strongly absorbing materials, the influence of the optical absorption depth on the frequency content of the acoustic signal is negligible. This leaves the temporal and spatial frequency content of the generation pulse and the source-receiver geometry to be evaluated.

For discussion purposes, a characteristic time constant describing the spatial extent of the source and the source-receiver geometry will be introduced. The geometry under consideration is illustrated in Figure 4-3. In this configuration,  $d_s$  is the difference in propagation distance from the center of the laser spot and the Gaussian radius of the laser spot to the detection point. The characteristic spatial time constant ( $t_s$ ) is given by:

$$t_s = \frac{d_s}{c_m}$$

$$d_s = d_2 - d_1 = \sqrt{h^2 + (d+r)^2} - \sqrt{h^2 + d^2} \quad (4.8)$$

where  $c_m$  is the acoustic velocity of the mode under consideration. Considering bulk wave generation, Eq. (4.8) gives characteristic spatial time constants for

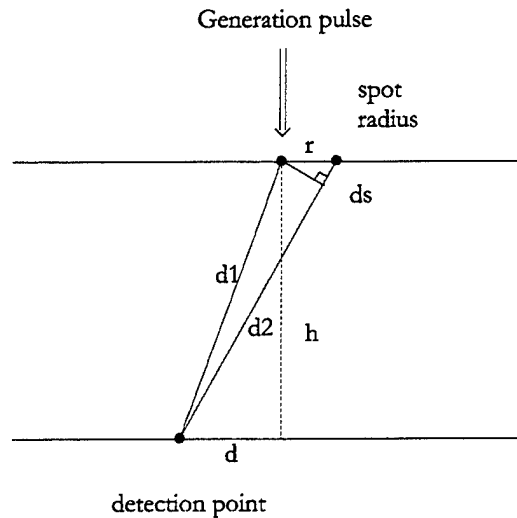


Figure 4-3 Definition of source-receiver geometry.

surface, longitudinal, and shear waves.

The results of Section 4.3 indicated that longer pulses should permit more energy absorption by the specimen before  $T_{\max}$  is reached. The energy in the resulting acoustic waves is also expected to increase. The amplitude of the acoustic waves generated, though, depends on the relationship between the characteristic spatial time constant  $t_s$  and the laser pulse temporal width  $t_p$ . There are two limiting cases of interest which will be discussed.

If  $t_s \gg t_p$ , then the frequency content of the generated signal is controlled by the spatial extent of the source. In this case, broadening the laser pulse should have little effect on the shape of resulting the acoustic wave. An increase in acoustic wave amplitude directly proportional to the increase in absorbed energy should be observed. In general, from the relationship between absorbed energy

and pulse width, and in the limit  $t_s \gg t_p$ , the expected amplitude gain ( $g$ ) through pulse length increase is given by:

$$g \approx \sqrt{\frac{t_{p2}}{t_{p1}}} \quad (4.9)$$

where  $t_{p2}$  and  $t_{p1}$  are the pulse widths of the longer and shorter pulse respectively.

In the other limit, if  $t_s \ll t_p$ , the expected behavior is quite different. In this case, the frequency content of the generated signal is controlled by the temporal extent of the laser source. For a given laser spot size, the amplitude profile of the generated acoustic signals will follow the temporal *power* profile of the incident laser pulse. For a constant spot size and pulse width, this leads to the linear relationship between absorbed energy and acoustic wave amplitude observed in the thermoelastic regime. Increasing the laser pulse width, at constant energy, leads to a proportional decrease in peak power. The maximum absorbed energy  $E_{\max}$  shows a square root dependence on pulse length and cannot offset the decrease in peak power, which has a linear dependence on pulse length. This is illustrated in Figure 4-4 showing the peak power in the incident laser pulse as a function of pulse length. It is expected that the amplitude of acoustic waves generated in the limit  $t_s \ll t_p$  will show an effective amplitude gain of:

$$g \approx \frac{(\sqrt{t_{p2}})t_{p1}}{(\sqrt{t_{p1}})t_{p2}} = \frac{\sqrt{t_{p1}}}{\sqrt{t_{p2}}} \quad (4.10)$$

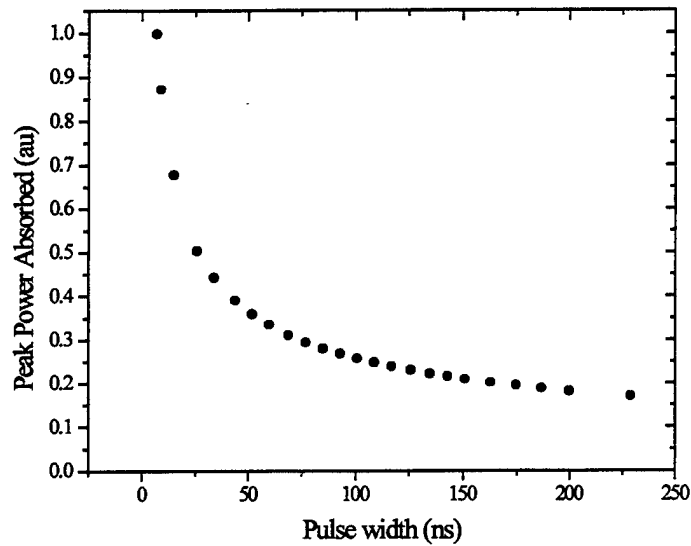


Figure 4-4 Relative peak power in laser pulse needed to raise the surface temperature to  $T_{\max}$  as a function of pulse length.

In this limit, Eq. (4.10) is found to be the reciprocal of Eq. (4.9) and predicts an amplitude decrease with increasing pulse length.

Equations (4.9) and (4.10) predict the effects of increasing the laser pulse length on the laser generation of acoustic waves in the thermoelastic regime in two limiting cases. In the general case, the behavior is expected to fall somewhere between these two conditions with Eq. (4.9) giving the maximum possible gain and Eq. (4.10) indicating the greatest loss. As mentioned in Chapter 2, thermoelastic generation of ultrasound has been extensively modeled.<sup>10,11,12,13</sup> The predictions of Eqs. (4.9) and (4.10) will now be evaluated using the model for acoustic wave generation in the thermoelastic regime described in Chapter 2 and adapted from that of Spicer.<sup>12</sup> This program has shown excellent agreement with experiment.<sup>12</sup> The model was run for a 6mm thick aluminum specimen with the detection point 3mm off of epicenter. The incident laser spot size was 2mm. The

displacement was calculated as a function of incident laser energy and the allowed energy then scaled according to Eq. (4.7). Figure 4-5 shows a plot of maximum longitudinal wave amplitude versus pulse length. The functional dependencies given by Eqs. (4.9) and (4.10) are over-plotted for comparison.

The behavior of the thermoelastic generation model subject to the input energy constraints of Eq. (4.7) agrees well with the predicted trends. The disagreement at the longer pulse lengths is most likely caused by the influence of a negative-going displacement which occurs after the arrival of the longitudinal wave. This becomes superimposed on the longitudinal wave arrival when the laser pulse length is substantially broadened. For short laser pulses, the pulse shape is dictated mostly by the spatial extent of the laser source. In this region, an increase

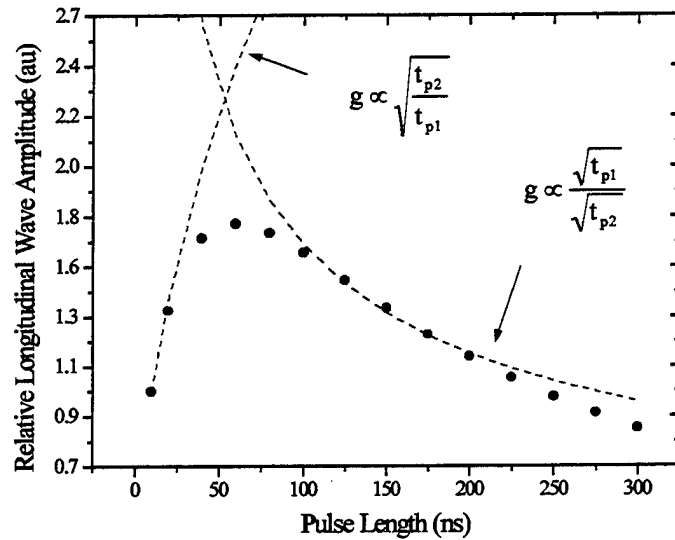


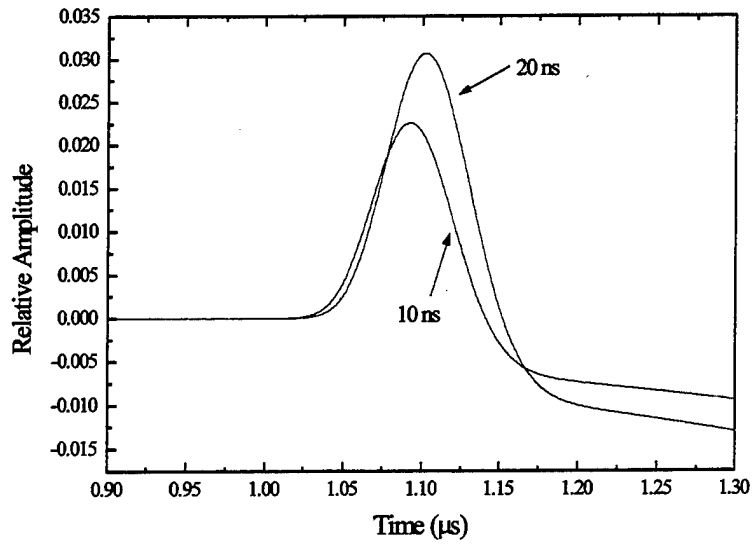
Figure 4-5 Relative longitudinal wave amplitude possible in thermoelastic regime without exceeding  $T_{max}$  as a function of pulse length.

in longitudinal wave amplitude proportional to  $(t_p)^{0.5}$  is seen. For longer laser pulses, the pulse shape is dictated by the temporal extent of the source and a decrease in signal amplitude proportional to  $1/(t_p)^{0.5}$  is observed. The first longitudinal arrivals in the two outlined regimes are illustrated in Figure 4-6. Figure 4-6a shows a comparison of predicted displacements with 10 and 20ns pulses and illustrates that, although there is some broadening, the width of the arrival does not increase substantially. The amplitude gain when going from a 10 to a 20 ns pulse is 1.36 which compares favorably with the 1.41 predicted by Eq. (4.9). Figure 4-6b shows a comparison of longitudinal arrivals from 100ns and 200ns pulses. In this case, the temporal extent of the arrival is dictated mainly by the input laser pulse length. The broadening of the longitudinal wave arrival directly follows that of the incident laser pulse. A decrease in amplitude is seen with increasing pulse length, with the longitudinal wave generated with the 200 ns pulse reduced by a factor of 0.713. This again compares very well with the predicted 0.707 through Eq. (4.10).

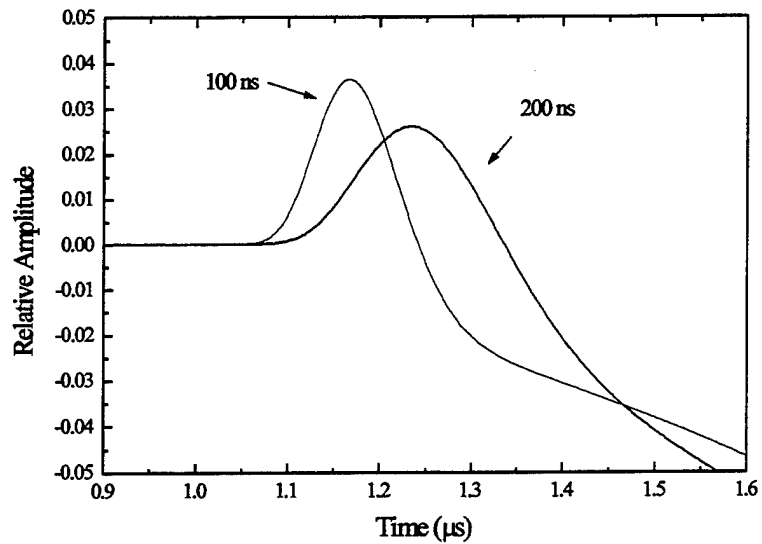
Figure 4-5 indicates that there is an optimal laser pulse length for acoustic wave generation in a given experimental arrangement. For the particular case treated, a pulse length of about 60ns allowed for optimization of the longitudinal wave amplitude. A gain of approximately 1.8 is seen over the longitudinal wave generated with a 10ns pulse. Curves analogous to Figure 4-5 can be produced for longitudinal, shear, and surface wave generation.

#### 4.5 Linear Systems Approach to Pulse Length Effects

The thermoelastic generation model used is computationally intensive and the calculation of pulse length effects on the generation of all of the acoustic



a)



b)

Figure 4-6 Comparison of longitudinal wave displacement as pulse length is varied a) in the regime  $t_s \gg t_p$  and b) in the regime  $t_s \ll t_p$ .

modes, in a number of experimental configurations, can prove quite time intensive. As such, a significantly faster and easily applied technique for predicting acoustic waves generated by temporally modulated laser sources will be presented.

The thermoelastic generation of ultrasound can be modeled as a linear system. The excellent agreement of theory and experiment given in the literature has shown that linear equations are sufficient, in most cases, for describing the process. If greater accuracy is required, the temperature dependence of the thermal and optical properties may need to be taken into account, resulting in the breakdown of the linear assumption. In the approach taken here, it is assumed that the entire process is linear.

The premise is quite simple. At the shortest incident laser pulse length of interest, a single reference signal is either theoretically calculated or experimentally measured. Although the impulse response is not known, this signal provides enough information to give an exact solution for calculation of the displacement for any arbitrary laser intensity modulation on the surface, so long as the frequency content of the modulated pulse does not exceed the frequency content of the reference pulse. This provides an extremely useful tool for the evaluation of pulse length effects, as well as other temporal modulation schemes of interest. This technique can be used to analyze the response of composite materials and other complex systems to temporal modulation of the generation pulse based solely on experimental data acquired with conventional Q-switched laser systems.

Let  $s(t)$  be the reference pulse used to generate the reference signal  $r(t)$ . The transfer function  $h(t)$  describing the material response (as well as the response of the detection system) may be found through the deconvolution of:

$$r(t) = s(t) * h(t) \quad (4.11)$$

The frequency spectrum of  $s(t)$  is finite and thus the material/instrumentation response is only determined over the spectral range of this pulse. From this information, the material/instrumentation response to an arbitrary input laser pulse,  $k(t)$ , can be determined, as long as the spectral range of  $k(t)$  falls within the spectral range of  $s(t)$ . For smooth laser pulses of similar shape, this generally means that the pulse width of  $k(t)$  is greater than that of  $s(t)$ . Let  $m(t)$  be the theoretical ultrasonic response to generation with  $k(t)$ . The following relation holds:

$$m(t) = k(t) * h(t) \quad (4.12)$$

Using Eqs. (4.11) and (4.12), the ultrasonic signal generated in a material by an arbitrary laser pulse  $k(t)$  can be predicted through the relation:

$$m(t) = F^{-1}\{M(f)\} = F^{-1}\left\{\frac{R(f)K(f)}{S(f)}\right\} \quad (4.13)$$

Equation (4.13) is valid as long as all other parameters, including spot size, source location, and receiver location are held constant. This provides a method for evaluating pulse modulation techniques for various applications which is very easy to implement and computationally very fast.

A comparison between the linear systems approach and the predictions of the thermoelastic generation model was performed with the results given in Figure 4-7. The same geometry was used as was given in the previous Section

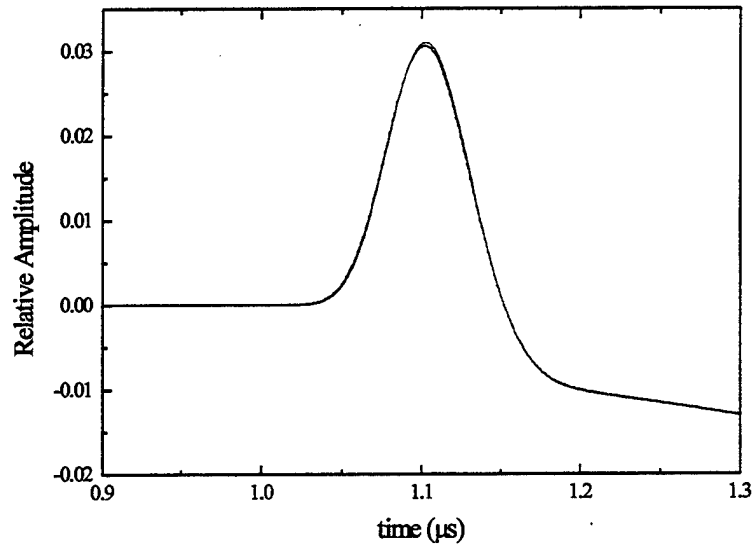


Figure 4-7 Comparison of longitudinal wave displacement from 20ns. Incident laser pulse calculated through thermoelastic generation model and linear systems model.

(calculation of Figure 4-5) with the reference pulse taken as a 10ns pulse and the reference signal calculated through the model. The material response to a 20 ns pulse is calculated using the linear systems approach and compared to the waveform calculated with the model. Agreement is excellent, with approximately 1% error in the amplitude prediction.

In another case, the reference signal was calculated using a 10ns pulse and the linear systems approach was used to determine pulse length effects on surface wave generation in aluminum. The surface is not allowed to heat above  $T_{max}$  and

the spot size used in the calculation was 1.5mm. The maximum surface wave amplitude is plotted as a function of laser pulse length in Figure 4-8. The functional dependence predicted by Eqs. (4.9) and (4.10) is again over-plotted for comparison. The peak surface wave amplitude occurs at about 125ns. This gives an amplitude gain of about 2.7 over the surface wave generated with a 10ns pulse. The surface waves generated by 10ns and 125ns pulses are shown in Figure 4-9a. These waveforms have been scaled to equal amplitude in Figure 4-9b for easy comparison of the temporal extent of the signals. The increase in incident laser pulse width, in this case, does not cause significant broadening of the signals. The surface wave generated by the 125 ns is shifted later in time because the time coordinate is centered on the start of the pulse, rather than the peak. It is apparent that the frequency content of these signals is dictated mainly by the laser pulse spot size, rather than the temporal extent of the generation pulse.

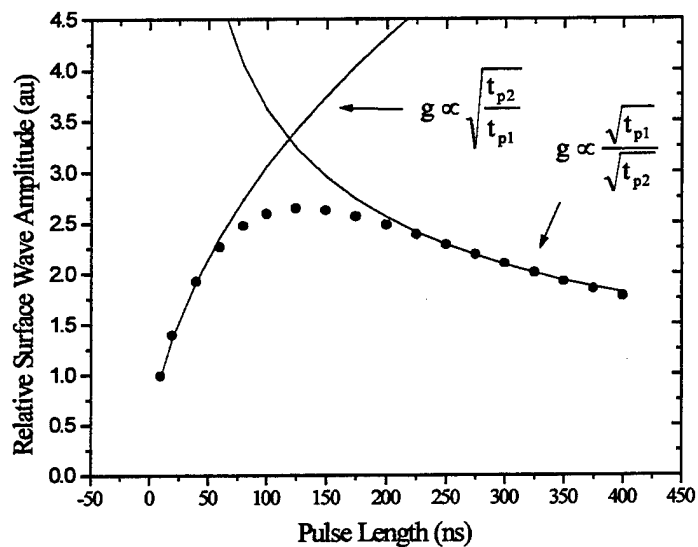


Figure 4-8 Surface wave amplitude as a function of pulse length. Calculation performed for case where surface is not heated above  $T_{max}$ .

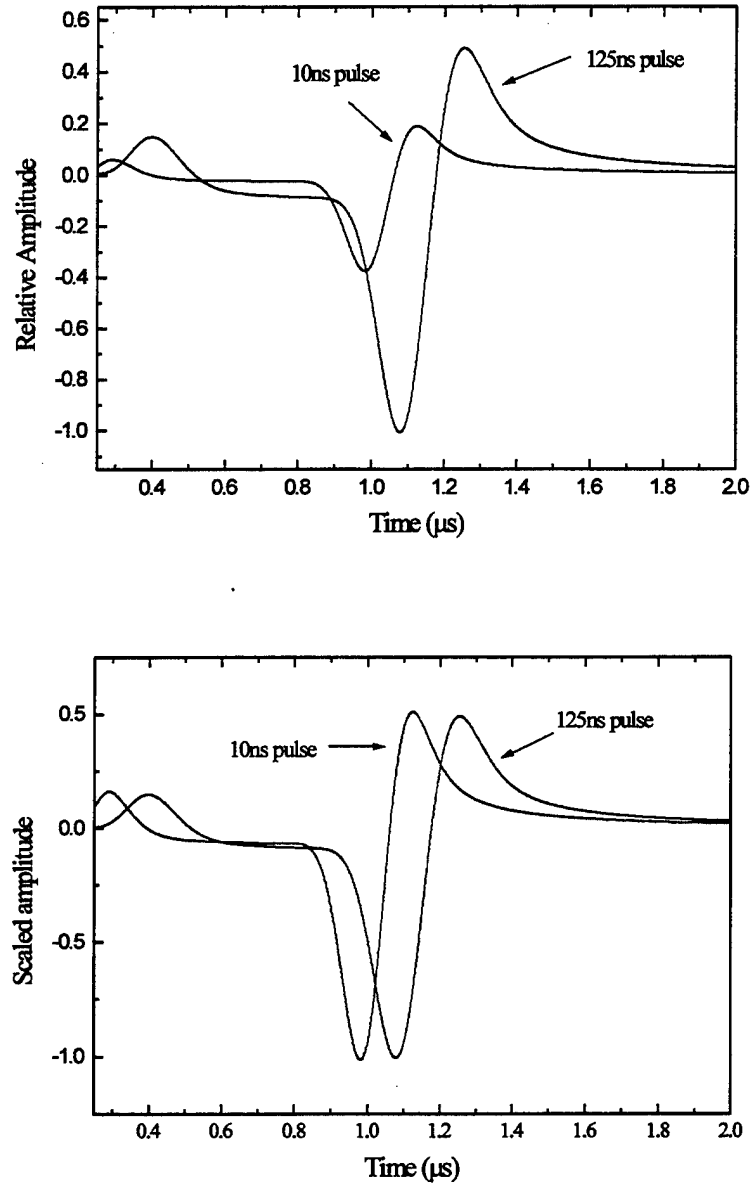


Figure 4-9 a) Calculated surface wave amplitude form 10ns pulse and 125ns pulse and b) amplitudes have been scaled for analysis of temporal extent.

#### 4.6 Linear Systems Approach to Laser Generation in Composites

One of the advantages of the linear systems approach is that the effects of pulse length modification can be evaluated without solving the elastic wave equations for wave propagation in the media of interest. This is particularly useful in composite materials, where the wave propagation problem is complicated by anisotropy. Pulse length effects have been evaluated in graphite-PEEK and graphite-epoxy specimens. In order to check the linearity of the laser ultrasonic generation process, an experimental check of the linear systems approach was performed. A reference signal was generated on epicenter with an 86 ns laser source. The material response to a 211ns pulse was then calculated using Eq. (4.13) and compared to the experimentally measured waveform at 211 ns. The

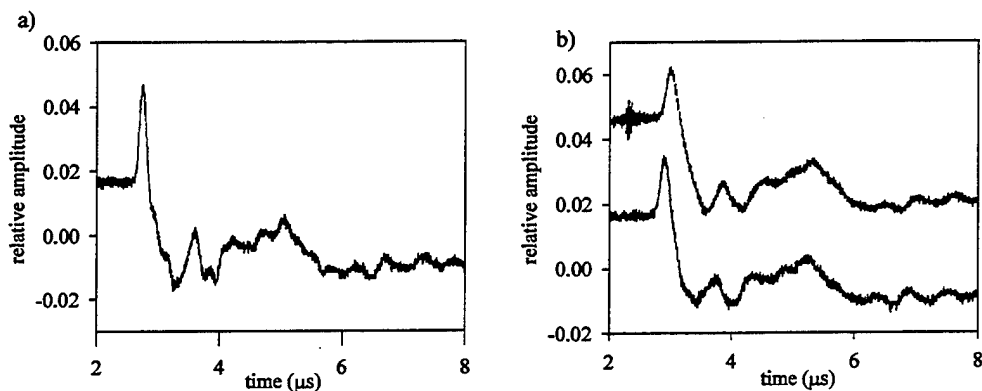


Figure 4-10 Verification of linear systems approach with epicentral waveforms in a graphite-PEEK sample. a) reference waveform taken with a 86ns pulse and b) predicted (top) and experimental (bottom) waveform from 210ns pulse.

pulse length of the Nd:YAG laser was controlled by adjusting the cavity length and pumping rate. Other experimental parameters, including spot size, pulse energy, and source-receiver geometry, were held constant at each pulse length. The results of this experiment are presented in Figure 4-10. The linear systems technique is seen to agree well with experiment, indicating that the assumption of linearity holds reasonably well in this material.

Figure 4-11 shows epicentral waveforms taken at two different locations on the graphite-PEEK specimen. The signal generated with a 11ns laser source is taken as the reference signal. The response to 100 and 178ns laser pulses are predicted through the linear systems technique. The difference in the signals observed at the two locations illustrates the inhomogeneous character of the specimen. The two cases also show different responses to the longer laser pulses. The waveform in Figure 4-11a shows little change when the pulse length is increased, while that in Figure 4-11b shows a marked decrease in the amplitude of the high frequency features.

The signals in Figures 4-10 and 4-11 were calculated using constant energy in the incident laser pulses, and spreading that energy out in time as the pulse length was increased. This information needs to be augmented by the relation between pulse length ( $t_p$ ) and damage threshold energy ( $E_{max}$ ). The graphite-polymer specimens have a very complex structure, making predictions based on analytical solution difficult. The relationship between threshold energy and pulse width was thus determined experimentally through surface inspection under an optical microscope. The onset of visible damage was monitored as the pulse length was increased, at constant energy, from 10ns to 200ns. There was no

detectable change in the damage threshold over this pulse length range for either the graphite-PEEK or graphite-epoxy specimens.

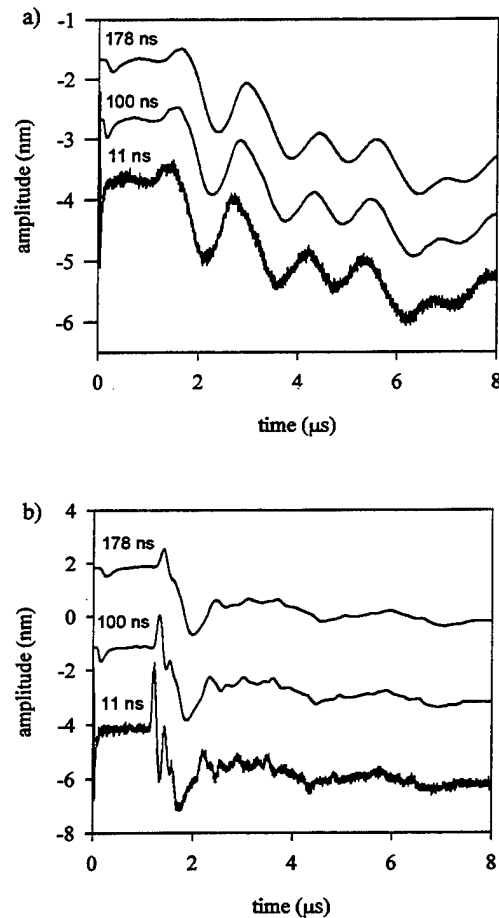


Figure 4-11 Epicentral waveforms on two regions of graphite-PEEK sample. The 11ns waveforms were taken experimentally and the longer pulse waveforms were predicted using linear systems theory.

The fact that no change in  $E_{\max}$  was observed indicates pulse lengthening is not an effective method of increasing the amplitude of acoustic waves generated

in these materials. The energy  $E_{\max}$  is simply spread out in time as the pulse length is increased. This leads to either little change in waveform shape (Figure 4-11a) or a decrease in the amplitude of high frequency features (Figure 4-11b), depending on the frequency content of the reference signal.

The results on the composite specimens indicate that the thermal diffusion length is small compared to the spatial extent of the illuminated region. The square-root dependence of  $E_{\max}$  on  $t_p$  given in Eq. (4.7) holds only for the case of strong surface absorption. If the absorption coefficient is small compared to the thermal diffusion length, then the approximate dependence of  $E_{\max}$  on pulse length can be found through evaluation of Eq. (4.5). The exponential terms are first expanded, and Eq. (4.5) is approximated by:

$$T_{\text{surface}} \approx \frac{2I\sqrt{\kappa t}}{K\sqrt{\pi}} - \frac{I}{K\alpha} + \frac{I}{K\alpha} (1 + \alpha^2 \kappa t) \left( 1 - \frac{2}{\sqrt{\pi}} \int_0^{\alpha\sqrt{\kappa t}} (1-x^2) dx \right) \quad (4.14)$$

Neglecting higher order terms in  $\alpha$ , Eq. (4.14) can be further approximated as:

$$T_{\text{surface}} \approx \frac{I\alpha\kappa t}{K} \quad (4.15)$$

Equation (4.15) states that, as  $\alpha$  gets very small with respect to the thermal diffusion length, there is no means by which heat can escape from the illuminated volume. The terms  $I\alpha t$  define the energy input from the laser source in units of  $J/cm^3$ . This energy heats the specimen according to the specific heat of the illuminated material ( $\kappa/K = 1/\rho C$ ). In this limit, the temperature of the volume is

only a function of the total amount of energy absorbed, and not a function of how this energy is distributed in time. This is one possible explanation for the behavior observed in the composite specimens.

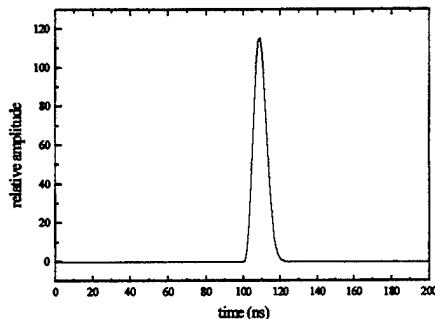
This explanation does not account for the specific interaction of the incident laser light with the graphite-polymer composites. Most polymers are weak absorbers of visible and near IR laser radiation. It has been shown that, when generating with a Nd:YAG laser in a graphite-epoxy specimen, a significant portion of the laser energy is absorbed by the graphite fibers.<sup>14</sup> If the laser induced damage mechanism originates in the fibers, or at the fiber-matrix interface through heating of the fibers, then the present results suggest that heat flow in the fibers was not sufficient to remove heat from the illuminated volume during the nanosecond time-scale of the incident laser pulse. The damage mechanism in graphite-epoxy and graphite-PEEK polymers has not been quantified. Optical microscopy of laser damaged regions, though, indicates that the polymer matrix material is vaporized first and bare graphite fibers are left at the surface.

#### 4.7 Signal Processing Considerations

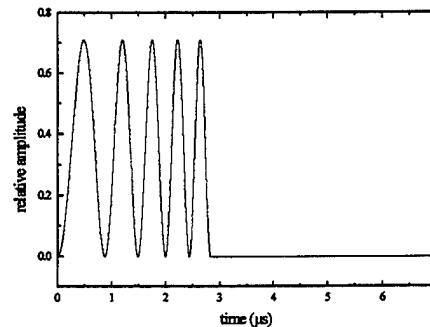
The primary issue of increasing laser ultrasonic system sensitivity depends not only on the amplitude of acoustic signals generated, but also on the energy in these signals. This was discussed in detail in Chapter 3. When the SNR is maximized through match filtering, the result does not depend on signal amplitude, but instead on total signal energy. Increasing the incident laser pulse length can prove useful, even if the amplitude of the acoustic signal generated with the longer laser pulse is not enhanced. One problem, though, is that in the limit as  $t_s \ll t_p$  the acoustic signal is broadened in direct proportion to the incident

laser pulse. This broadening of the acoustic signals limits the temporal resolution of the laser ultrasonic system.

A chirp technique, analogous to that presented in Chapter 3, has recently been presented.<sup>15</sup> In this method, though, the incident laser pulse is frequency modulated in time rather than in space. Temporal modulation techniques such as this may prove very useful in increasing the sensitivity of laser ultrasonic systems. The linear systems approach for determining the acoustic response as a function of the incident laser pulse shape provides a straightforward method for evaluation of temporal modulation methods. As an example, the effects of generating ultrasound with a linearly frequency modulated laser source will be presented. The reference signal is taken as a surface wave calculated with the thermoelastic model. The same input parameters as given in Section 4.6 are used for the calculation. The reference laser pulse shape is given in Figure 4-12a. The goal is to determine the response to the linearly frequency modulated (FM) signal presented in Figure 4-12b, under the constraint that each pulse heats the surface to the same temperature,  $T_{\max}$ . The signals shown in Figure 4-12 have been normalized such that the total energy in the pulses is equal. Heating curves for the two pulses, having the same amount of total energy, are presented in Figures 4-13a and 4-13b.



a)



b)

Figure 4-12 Relative amplitude and spatial extent of the incident laser pulses considered showing a) the 10ns pulse and b) the FM pulse.

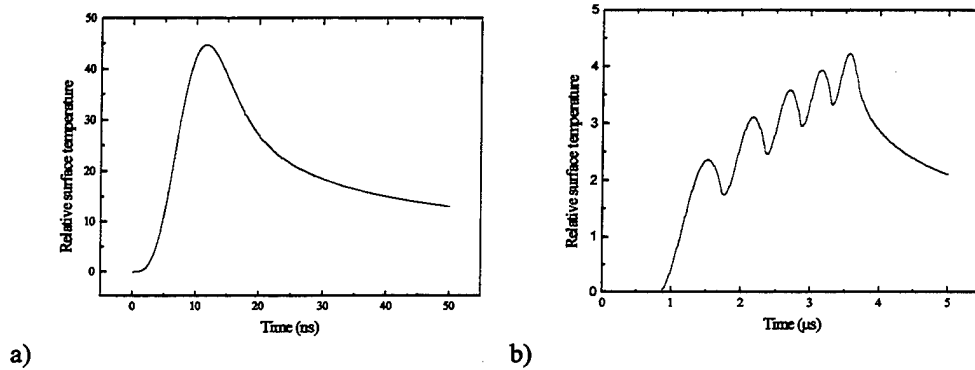


Figure 4-13 Relative surface heating produced by a) 10ns pulse and b) FM pulse.

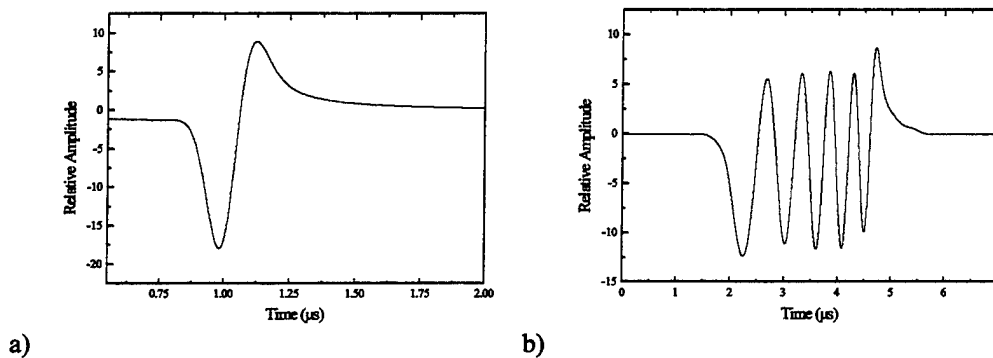


Figure 4-14 Relative surface displacement produced by a) 10ns pulse and b) FM pulse when surface temperature  $T_{max}$  is reached.

The surface heating was calculated through numerical integration of Eq. (4.4) with the functional dependence of each laser pulse included as  $p(t)$ . It can be seen

that the reference laser pulse heats the surface to a temperature about 10.5 times higher than the FM pulse. This allows 10.5 times more energy to be used for acoustic wave generation using the FM laser pulse.

The reference waveform is given in Figure 4-14a and the material response to the FM pulse, as calculated using linear systems theory, is given in Figure 4-14b. It can be seen that, even with 10.5 times more energy, the amplitude of the FM generated acoustic wave is still well below that of the reference pulse signal. The energy is also spread out substantially in time.

The signal processing methodology to be used is identical to that given in Chapter 3. It is assumed that the SNR is maximized using a matched filter. For the case of a perfect matched filter on a noise free signal, this amounts to an autocorrelation of each of the waveforms in Figure 4-14. The resulting signals are presented in Figure 4-15. The amplitude of the correlation peak is approximately 4 times higher for the FM signal over that of the short pulse illustrating the increase in SNR possible. The FM waveform also shows the effects of pulse compression. Frequency modulation of the generation laser pulse allows for an increase in SNR without the sacrificing the temporal resolution of the detection system.

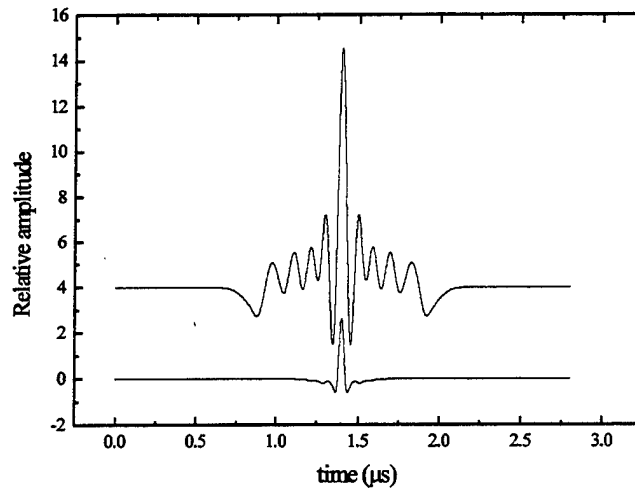


Figure 4-15 Correlation peaks produced through match filtering of the acoustic signal generated by the FM pulse (top) and the 10ns pulse (bottom).

The linear systems technique presented for analysis of the effects of temporally modulating the incident laser light in the generation of acoustic waves is relatively easy to implement. It may prove useful in the optimization of a given laser ultrasonic generation scheme. The same methodology can be used to evaluate any arbitrary generation laser pulse shape, including the effects of generating ultrasound with multiple pulses as well as sinusoidal modulation techniques.

## REFERENCES

<sup>1</sup> J.W. Wagner, J.B. Deaton Jr., and J.B. Spicer, "Generation of ultrasound by repetitively Q-switching a Nd:YAG laser," *Applied Optics* **27** (22) 4696-4700 (1988)

<sup>2</sup> J.B. Deaton Jr., A.D.W. McKie, J.B. Spicer, and J.W. Wagner, "Generation of narrow-band ultrasound with a long cavity mode-locked Nd:YAG laser," *Appl. Phys. Lett.* **56** (24) 2390-2392 (1990)

- 
- <sup>3</sup> J.S. Steckenrider, T.W. Murray, and J.W. Wagner, "Sensitivity enhancement in laser ultrasonics using a versatile laser array," *J. Acoust. Soc. Am.* **97**(1) 273-279 (1995)
- <sup>4</sup> T.W. Murray, J.B. Deaton Jr. And J.W. Wagner, "Experimental evaluation of enhanced generation of ultrasonic waves using an array of laser sources," *Ultrasonics* **34** 69-77 (1996)
- <sup>5</sup> M-H Noroy, D. Royer, and M. Fink, "The laser-generated ultrasonic phased array: Analysis and experiments," *J. Acoust. Soc. Am.* **94** (4) 1934-1943 (1993)
- <sup>6</sup> J. Jarzynski and Y. Berthelot, "The use of optical fibers to enhance the laser generation of ultrasonic waves," *J. Acoust. Soc. Am.* **85** (1) 158-162 (1989)
- <sup>7</sup> J. Yang, N. Deridder, C. Ume, and J. Jarzynski, "Non-contact optical fiber phased array generation of ultrasound for non-destructive evaluation of materials and processes," *Ultrasonics* **31** (6) 387-394 (1993)
- <sup>8</sup> P.W. Maloney and J.H. Eberly, *Lasers*, John Wiley and Sons, N.Y. (1988)
- <sup>9</sup> J.F. Ready, *Effects of High-Power Laser Radiation*, Academic Press, N.Y. (1971)
- <sup>10</sup> L.R.F. Rose, "Point-Source Representation for Laser Generated Ultrasound," *J. Acoust. Soc. Am.* **75**(3), 723-732 (1984)
- <sup>11</sup> F.A. McDonald, "Practical quantitative theory of photoacoustic pulse generation," *Appl. Phys. Lett.*, **54** (16) 1504-1506 (1989)
- <sup>12</sup> J.B. Spicer, "Laser Ultrasonics in Finite Structures: Comprehensive Modeling with Supporting Experiment," Ph.D. Dissertation, The Johns Hopkins University (1991)
- <sup>13</sup> J.C. Cheng, S.Y. Zhang, and L. Wu, "Excitations of thermoelastic waves in plates by a pulsed laser," *Applied Physics A* **61**, 311-319 (1995)
- <sup>14</sup> A.D.W. McKie and R.C. Addison Jr., "Practical considerations for the rapid inspection of composite materials using laser-based ultrasound", *Ultrasonics* (1994)
- <sup>15</sup> J-P. Monchalain and D. Drolet, "Laser ultrasonics with a single laser for generation and detection," 8<sup>th</sup> International Symposium on Nondestructive Characterization of Materials, (Ed. R.E. Green), in press (1997)

**Implicit Finite Difference Solution to Melting and Vaporization Problem  
Occurring in Vacuum. Physical Constants set up for Calculation in Aluminum**

```

#include <math.h>
#include <stdio.h>
#include <stddef.h>
#include <stdlib.h>
#include <malloc.h>

void main ( )
{
double *allocate_double_vector (int l,int y);
void free_double_vector (double *v, int l);
int i, j, m, q, cnt, n, tot, melting, num1, starter, ji, nm;
double c, p, I, a, dt, dz, I1, I2, cp, L, K2, st1, st2, ds, gs, power1;
double beta, po, A, R0, Ts, Hv, Tlv, density, flux, flux1, totflux, vsurface, R1;
double cvsurface, dsurface, totsurface, enout, marker, pressure;
double l1, Tm, Rf, I11, I12, I21, I22, I23, kip;
char string[80]; char string2[80];
double expulsion, expdist, totexpul, power, IA, CT;
double *TP, *s, *u, *z, *R, *b, *Q, *STP, *k, *ka, *kb;
FILE *lp, *mp, *np;

lp=fopen("alum150.dat","w");

STP=allocate_double_vector(1,5100);
TP=allocate_double_vector(1,5100);
s=allocate_double_vector(1,5100);
u=allocate_double_vector(1,5100);
z=allocate_double_vector(1,5100);
R=allocate_double_vector(1,5100);
Q=allocate_double_vector(1,5100);
b=allocate_double_vector(1,5100);
k=allocate_double_vector(1,5100);

```

```

ka=allocate_double_vector(1,5100);
kb=allocate_double_vector(1,5100);

/* INITIALIZE VARIOUS VALUES TO ZERO */

totexpul=0.0;expulsion=0.0;starter=1;nm=0;totsurface=0.0;
enout=0.0;marker=0.0; kip=0.0; pressure=0.0;

/* INPUT POWER DENSITY AND OUTPUT FILE NAMES */

printf("Enter the power density in MW/cm2: ");
scanf("%lf",&power);
printf("\n");
printf("The power density is %lf\n",power);
printf("\n");

printf("Enter the ablation file name with no spaces:");
    cscanf("%s", string);
    printf("\n");
printf("Enter the thermal file name with no spaces:");
    cscanf("%s", string2);
    printf("\n");
printf ("The name of the ablation file is:%s\n",string);
printf ("\n");
printf ("The name of the thermal file is:%s\n",string2);
mp=fopen (string2,"w");
np=fopen (string,"w");

        /* PHYSICAL CONSTANTS */

a=1.0e6; /* 1/CM ABSORPTION DEPTH */

power=(power*1e6); /* CONVERT POWER DENSITY MW/CM2 */

ds=0.0; /* INITIAL MOVEMENT OF MELT FRONT */

l1=2e-5; /* THICKNESS (CM)- DIMENSIONLESS LENGTH CONSTANT
          DZ (ACTUAL)= (DZ)(L1) */

dz=.03; /* DIMENSIONLESS SPACE STEP */

Tm=933.0; /*MELTING TEMPERATURE */

L=(10790/26.98)*2.69; /* LATENT HEAT J/CM3 */

K2=.23061106e1; /*DIMENSIONLESS CONSTANT W/CMK */

melting=0; /* MELTING=1.0 WHEN MELT FRONT STARTS TO PROPAGATE */

st1=0.0; st2=0.0; /* TWO VARIABLES FOR DEFINING POSITION OF MELT FRONT */

```

```

dt=.03; /* DIMENSIONLESS TIME STEPS */

tot=1300; /* TOTAL NUMBER OF SPACE STEPS */

m=1300; /* NUMBER OF SPACE STEPS BEFORE MELT FRONT */

n=tot-m; /* NUMBER OF SPACE STEPS AFTER MELT FRONT */

cnt=0; /* COUNTER FOR WRITE TO FILE */

/* CONSTANTS FOR VAPORIZATION CALCULATION */

A=26.98; /* ATOMIC WEIGHT g/mol */

po=.001*1.013e8; /* AMBIENT PRESSURE g/(sec2 m) */

R1=8.314e3; /* GAS CONSTANT (UNITS) g m2/(sec2 mol K) */

Tlv= 1785.0; /* VAPORIZATION TEMPERATURE K */

beta=1.0; /* COUPLING CONSTANT */

density=2.69*100*100*100; /* g/m3 */

Hv=293430.0; /* LATENT HEAT J/mol */

R0=8.314; /* GAS CONSTANT (UNITS) J/ mol K */

/* INITIAL TEMPERATURE DISTRIBUTION (corresponds to 300K)*/
  for(i=1;i<=tot+100;i++) {TP[i]=(-.684800);}

/* J GIVES TOTAL NUMBER OF TIME STEPS */

  for (j=1;j<=20000;j++){

n=tot-(m+1);          /* n= number of space steps behind front */

/* TERMS FOR HEAT EQUATION */

  for(i=1;i<=tot+5;i++) {
    if (TP[i]>0.0) /* melt properties */
      {
        CT=TP[i]*Tm+Tm;
        k[i]= .54976+5.24994e-4*CT1.33889e-7*CT*CT
      }
  }

```

```

+7.94112e-12*CT*CT*CT; /* J/cmKs */
cp=(7.59*4.184/26.98)*2.69; /* J/cm3K */
    }

else /* solid properties */
{
CT=TP[i]*Tm+Tm;
cp=3.72883+0.01057*CT-1.48277e-5*CT*CT
+9.14297e-9*CT*CT*CT; /* J/cm3K */
cp=(cp*4.184/26.98)*2.69;
k[i]=2.28706;
}

Q[i]=(k[i]*L)/(cp*Tm*K2);
R[i]=Q[i]*dt/(dz*dz);

}

if (j==1) {
for(i=1;i<=tot+4;i++) {
    ka[i]=1.0;
    kb[i]=1.0;
}}

/* weighting fnc, not used- very small variation of
K spatially at every time step. approx=1*/

/* REFLECTIVITY */

if (TP[1]>0.0) {Rf=.80;} else {Rf=.80;}

/* BOUNDRY CONDITION- FRONT SURFACE */

s[1]=(1.0/6.0-R[1]+5.0/3.0+2.0*R[1])/Q[1];
u[1]=((1.0/6.0-R[2])/Q[2])/s[1];

/* INTERNAL NODES */

for (q=2;q<=m-1;q++){

    b[q]=(1.0/6.0-R[q-1])/Q[q-1];
    s[q]=(5.0/3.0+2.0*R[q])/Q[q]-b[q]*u[q-1];

```

```

u[q]=((1.0/6.0-R[q+1])/Q[q+1])/s[q];
}

/* MELT FRONT -LEFT SIDE- BOUNDARY CONDITION */

if (melting==1){
b[m]=1.0/(3.0*Q[m-1]*(2.0+st1))-2.0*dt/(dz*dz*(2.0+st2));

s[m]= 2.0/Q[m]-1.0/(3.0*Q[m]*(1.0+st1))+(2.0*dt)/(dz*dz*(1.0+st2))-b[m]*u[m-1];
}

/* BACK SURFACE BOUNDARY CONDITION */

else {

b[m]=(1.0/6.0-R[m-1])/Q[m-1];

s[m]=((1.0/6.0-R[m]+5.0/3.0+2.0*R[m])/Q[m])-b[m]*u[m-1];
}

cnt=cnt+1; if (cnt==45) {cnt=0;} /* Counter-write to file when counter = 0 */

/* LASER SOURCE FIRST LAYER */

gs=((j*dt*L*I1*I1)/(Tm*K2)-25e-9)/6.0e-9* /*9.6 for 16ns pulse (FWHM) */
((j*dt*L*I1*I1)/(Tm*K2)-25e-9)/6.0e-9;
I=power*exp(-1.0*gs);
I1=(1.0-Rf)*I*exp(-1.0*(0.0)*(a*dz*I1));
I2=(I1*(1.0-exp(-a*dz*I1))*2.0*dt*I1*I1)/(k[1]*dz*Tm*I1);

/* SOURCE TERM FOR FRONT SURFACE*/

if (melting==1){
z[1]=(((1.0/6.0+ka[1]*R[1]+5.0/3.0-2.0*R[1])/Q[1])*TP[1]
+((1.0/6.0+kb[1]*R[2])/Q[2])*TP[2]+I2-enout)/s[1];}

else {
z[1]=(((1.0/6.0+ka[1]*R[1]+5.0/3.0-2.0*R[1])/Q[1])*TP[1]
+((1.0/6.0+kb[1]*R[2])/Q[2])*TP[2]+I2)/s[1];}

/* CALCULATE TEMPERATURE FOR INTERNAL NODES */

for(i=2;i<=m;i++) {

```

```

gs=((j*dt*L*11*11)/(Tm*K2)-25e-9)/6.0e-9*
((j*dt*L*11*11)/(Tm*K2)-25e-9)/6.0e-9;
I=power*exp(-1.0*gs);
I1=(1.0-Rf)*I*exp(-1.0*(i-1)*(a*dz*11));
I2=(I1*(1.0-exp(-a*dz*11))*2.0*dt*11*11)/(k[i]*dz*Tm*11);

/* BOUNDRY CONDITION - FIRST MELT BOUNDARY */

    if (i==m) { if (melting==1){
        z[i]= (TP[i-1]*(1.0/(3*Q[i-1]*(2+st1))+
        (2*dt)/(dz*dz*(2.0+st1)))+TP[i]*
        (2.0/Q[i]-1/(3*Q[i]*(1+st1))-2.0*dt/
        (dz*dz*(1.0+st1)))+I2-b[i]*z[i-1])/s[i];
    }

    else {

        z[i]=(((1.0/6.0+R[i])/Q[i])*TP[i]+((5.0/3.0-2.0*R[i])/Q[i])*TP[i]
        +((1.0/6.0+R[i-1])/Q[i-1])*TP[i-1]-b[i]*z[i-1]+I2)/s[i];

    }

    }

    else{
        z[i]= (((1.0/6.0+ka[i]*R[i+1])/Q[i+1])*TP[i+1]+
        ((5.0/3.0-2.0*R[i])/Q[i])*TP[i]+((1.0/6.0+kb[i]*R[i-1])/Q[i-1])
        *TP[i-1]-b[i]*z[i-1]+I2)/s[i];

    }

}

/* COMPLETE ALGORITHM -SOLVE FOR TEMPERATURE AT ALL NODES*/

TP[m]=z[m];

for(i=m-1;i>=1;i--){TP[i]=z[i]-u[i]*TP[i+1];}

/*.....CALCULATION BEHIND THE MELT FRONT.....*/

if (melting==1){

/* BOUNDARY CONDITION- BEHIND MELT FRONT */

```

```

s[1]=2.0/Q[1+(m+1)]-1.0/(3.0*Q[1+(m+1)]*(1.0-st1))+2.0*dt/(dz*dz*(1.0-st2));
u[1]=(1.0/(3.0*Q[2+(m+1)]*(2.0-st1))-2.0*dt/(dz*dz*(2.0-st2)))/s[1];

/* INTERNAL NODES */

for (q=2;q<=n-1;q++){
    b[q]=(1.0/6.0-R[q-1+(m+1)])/Q[q-1+(m+1)];
    s[q]=(5.0/3.0+2.0*R[q+(m+1)])/Q[q+(m+1)]-b[q]*u[q-1];
    u[q]=((1.0/6.0-R[q+1+(m+1)])/Q[q+1+(m+1)])/s[q];
}

/* BACK SURFACE BOUNDARY CONDITION */

b[n]=(1.0/6.0-R[n-1+(m+1)])/Q[n-1+(m+1)];
s[n]=((1.0/6.0-R[n+(m+1)]+5.0/3.0+2.0*R[n+(m+1)])/Q[n+(m+1)]-b[n]*u[n-1];

/* LASER SOURCE- BACK OF MELT FRONT */

gs=((j*dt*L*I1*I1)/(Tm*K2)-25e-9)/6.0e-9*
((j*dt*L*I1*I1)/(Tm*K2)-25e-9)/6.0e-9;
I=power*exp(-1.0*gs);
I1=(1.0-Rf)*I*exp(-(m+1)*a*dz);
I2=(I1*(1.0-exp(-a*dz*I1))*dt*2.0*I1*I1)/(Tm*k[1+m+1]*dz*I1);

/* SOURCE TERM AT BACK MELT BOUNDARY*/

z[1]=(TP[2+(m+1)]*(1.0/(3*Q[2+(m+1)]*(2-st1))+2*dt/(dz*dz*(2.0-st1)))+
TP[1+(m+1)]*(2.0/Q[1+(m+1)]-1/(3*Q[1+(m+1)]*(1-st1))-
2.0*dt/(dz*dz*(1.0-st1)))+I2)/s[1];

/* CALCULATE TEMPERATURE FOR INTERNAL NODES */

for(i=2;i<=n;i++) {
    gs=((j*dt*L*I1*I1)/(Tm*K2)-25e-9)/6.0e-9*
((j*dt*L*I1*I1)/(Tm*K2)-25e-9)/6.0e-9;
I=power*exp(-1.0*gs);
I1=(1.0-Rf)*I*exp(-1.0*(i-1+(m+1))*(a*dz*I1));

```

```

I2=(I1*(1.0-exp(-a*dz*11))*2.0*dt*11*I1)/(k[i+m+1]*dz*Tm*11);

    if (i==n) {
        z[i]=(((1.0/6.0+R[i+(m+1)])/Q[i+(m+1)])*TP[i+(m+1)]+
        ((5.0/3.0-2.0*R[i+(m+1)])/Q[i+(m+1)])*TP[i+(m+1)]
        +((1.0/6.0+R[i-1+(m+1)])/Q[i-1+(m+1)])
        *TP[i-1+(m+1)]-b[i]*z[i-1]+I2)/s[i]; }

    else{

z[i]=(((1.0/6.0+ka[i+m+1]*R[i+1+(m+1)])/Q[i+1+(m+1)])*TP[i+1+(m+1)]+
((5.0/3.0-2.0*R[i+(m+1)])/Q[i+(m+1)])*TP[i+(m+1)]+((1.0/6.0+
kb[i+m+1]*R[i-1+(m+1)])/Q[i-1+(m+1)])*TP[i-1+(m+1)]-b[i]*z[i-1]+I2)/s[i];}
    }

/* COMPLETE ALGORITHM- CALCULATE TEMPERATURE AT ALL NODES BEHIND
MELT*/

    TP[n+(m+1)]=z[n];

    for(i=n-1;i>=1;i--){TP[i+(m+1)]=z[i-u[i]*TP[i+1+(m+1)]};}

/* CALCULATE NEW TEMPERATURE AT NODE CLOSEST TO MELT FRONT */

    gs=((j*dt*L*11*11)/(Tm*K2)-25e-9)/6.0e-9*
    ((j*dt*L*11*11)/(Tm*K2)-25e-9)/6.0e-9;
    I=power*exp(-1.0*gs);
    I1=(1.0-Rf)*I*exp(-1.0*(m+1)*(a*dz*11));
    I2=(I1*(1.0-exp(-a*dz*11))*2.0*dt*11*11)/(k[m+1]*dz*Tm*11);

TP[m+1]= (((1.0/6.0+ka[m+1]*R[m+2])/Q[m+2])*STP[m+2]+
((5.0/3.0-2.0*R[m+1])/Q[m+1])*STP[m+1]
+((1.0/6.0+kb[m+1]*R[m])/Q[m])*STP[m]
+I2-((1.0/6.0-ka[m+1]*R[m+2])/Q[m+2])*TP[m+2]-
((1.0/6.0-kb[m+1]*R[m])/Q[m])*TP[m])*Q[m+1]/(5.0/3.0+2.0*R[m+1]);

/* CALCULATE HOW FAR MELT FRONT MOVES */

ds=(dt*k[m+2]/(2.0*dz*K2))*(TP[m+2]*((2.0-st2)/(1.0-st2))-
TP[m+3]*((1.0-st2)/(2.0-st2))+STP[m+2]*((2.0-st1)/(1.0-st1))-
STP[m+3]*((1.0-st1)/(2.0-st1)))+(dt*k[m]/(2.0*dz*K2))*(TP[m]*((2.0+st2)/(1.0+st2))-
TP[m-1]*((1.0+st2)/(2.0+st2))+STP[m]*((2.0+st1)/(1.0+st1))-STP[m-1]*((1.0+st1)/(2.0+st1)));

/* CALCULATE WHERE THE NEW MELT FRONT POSITION LIES */

    if (fabs(st1*dz+ds)<=(dz/2.0)) {
        st1=(st1*dz+ds)/dz;
        st2=(st1*dz+2.0*ds)/dz;

```

```

    }

else {
    if (st1*dz+ds>dz/2){

        num1=(int)((st1*dz+ds)-dz/2)/dz);
        m=m+(num1+1);
        if (m==4){starter=2;}
        st1=(-(num1+1)*dz+(st1*dz+ds))/dz;
        st2=(-(num1+1)*dz+(st1*dz+2.0*ds))/dz;

    }

    else {
        num1=(int)((fabs(st1*dz+ds)-dz/2)/dz);
        m=m-(num1+1);
        st1=((num1+1)*dz+(st1*dz+ds))/dz;
        st2=((num1+1)*dz+(st1*dz+2.0*ds))/dz;
        if(starter==1) {m=2;st1=st2=0.0;}
        else if(m==1){melting=2; m=tot;}
    }

}

Ts=TP[1]*Tm+Tm; /* REAL SURFACE TEMPERATURE */

flux= beta*po/(pow(2.0*3.1415*A*R1*Ts,.5));

flux1=exp((Hv*(Ts-Tlv))/(R0*Ts*Tlv));

pressure=(po/1000.0)*flux1; /* SATURATED VAPOR PRESSURE */

/* CALCULATE VAPORIZATION BOUNDARY MOVEMENT DUE TO EXPULSION */

expulsion=((m*6e-9)*2.0/260e-6)*pow((po*flux1)/density,.5)*100.0
*((L*11)/(Tm*K2));
expdist=expulsion*dt;
totexpul=totexpul+expdist;

/* CALCULATE VAPORIZATION FRONT MOVEMENT FROM SURFACE
VAPORIZATION */

totflux=flux*flux1;
vsurface= ((totflux*A)/density)*100.0; /* velocity in cm/sec */
cvsurface= (vsurface)*((L*11)/(Tm*K2)); /* convert to dimless velocity */
dsurface=cvsurface*dt;

/* Total distance vaporation interface has moved-dimless */
totsurface=totsurface+dsurface+expdist;

```

```

        marker=marker+dsurface; /* tracks surface vaporization only */

/* CALCULATE ENERGY REMOVED FROM FIRST NODE- USED IN VAPORIZATION
PROCESS */

        if(((TP[1]*Tm+Tm)-Tlv)>=0.0){

                enout=vsurface*((293430.0+10790.0)/26.98)*2.69+
                vsurface*((5.82*4.184/26.98)*2.69)*((TP[1]*Tm+Tm)-300.0);

        }
        else {enout=0.0;}

/* TRACK ENERGY LOST AND CONVERT TO FORM TO BE INPUT BACK INTO
PROGRAM */

power1=enout;
enout=(enout*((2.0*dt*11*11)/(k[1]*dz*Tm*11))); /* adjust units */

/* ERROR CHECK*/

        if (totsurface>=dz){
                totsurface=(totsurface-dz);
                for (i=1;i<=tot;i++){ TP[i]=TP[i+1];}
                if (totsurface>=dz) { printf("error in evaporation routine");}
                m=m-1;
                nm=nm+1;
        }

if(TP[1]*Tm+Tm>=Tlv){kip=TP[1]*Tm+Tm-Tlv;}
else {kip=0.0;}

} /* END OF PROCESSES OCCURRING IN THE MELT */

/* SAVE PREVIOUS TEMPERATURE VALUES IN ARRAY */

for (i=1;i<=tot;i++) {STP[i]=TP[i];}

/* CHECK FOR MELT FRONT PROPAGATION - MELT FRONT STARTED NODE NEXT
TO BOUNDARY TO AVOID CALCULATION OF THERMAL GRADIENTS AT
BOUNDARY */

if (TP[2]>=0.0&&melting==0){melting=1;m=3;}

/* PRINT RESULTS TO FILE WHEN COUNTER INDICATES */

```

```

    if(cnt==0){

        printf("%1.4e %lf %i %e %1.4e\n",j*dt*L*11*11)/
        (Tm*K2),TP[1]*Tm+Tm,m,pressure,marker*11);

        fprintf(lp,"%1.4e %1.4e %i %1.4e %1.4e %1.4e\n",j*dt*L*11*11)/
        (Tm*K2),TP[1]*Tm+Tm,m*6,pressure,totexpul*11,marker*11);

        fprintf(mp,"%1.4e\n",I-power1); /* output energy balance at surface */

        fprintf(np,"%1.4e\n",pressure); /* output pressure exerted on surface */

    }

}

    free_double_vector(TP,1);
    free_double_vector(s,1);
    free_double_vector(z,1);
    free_double_vector(u,1);

    free_double_vector(Q,1);
    free_double_vector(R,1);
    free_double_vector(b,1);
    free_double_vector(k,1);

}

/* Subroutines */

void system_error(char error_message[])
{
    void exit(int);

    printf("%s",error_message);
    exit(1);
}

void free_double_vector(double *v, int l)
{
    /* Frees a real vector of range [l..u]. */

    free((char*) (v+l));
}

```

```
double *allocate_double_vector(int l, int u)
{
    /* Allocates a real vector of range [l..u]. */

    void system_error(char *);
    double *p;

    p=(double *)calloc((unsigned) (u-l+1),sizeof(double));
    if (!p) system_error("Failure in allocate_real_vector.");
    return p-l;
}
```

## VITA

Todd William Murray was born on January 15, 1970 in Schenectady, New York. He received a Bachelor of Science degree in Biomedical Engineering in 1992 from Johns Hopkins University in Baltimore, Maryland. He received a Master of Science degree in Materials Science and Engineering in 1994 from Johns Hopkins University. Since 1992 he has been a graduate student in the Department of Materials Science and Engineering at Johns Hopkins University.